Università degli Studi di Torino
Doctoral School of Sciences and Innovative Technologies
PhD Programme in Chemical and Materials Sciences XXX Cycle

Photoreactions of significance for the chromophoric dissolved organic matter in surface waters

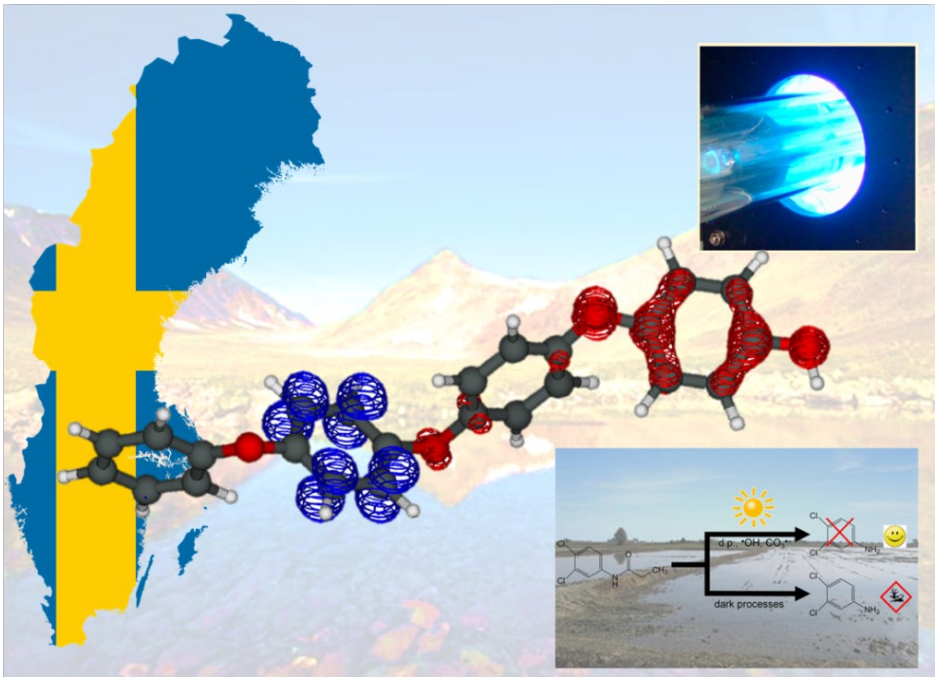

Francesco Barsotti

Supervisor:
Prof. Davide Vione

Università degli Studi di Torino

Doctoral School of Sciences and Innovative Technologies

PhD Programme in Chemical and Materials Sciences XXX cycle

Photoreactions of significance for the chromophoric dissolved organic matter in surface waters

Candidate: **Francesco Barsotti**

Supervisor: Prof. **Davide Vione**

Jury Members:

Prof. **Marcello Brigante**
Université Clermont-Auvergne (France)
Institut de Chimie de Clermont-Ferrand

Prof. **Birgit Koehler**
Uppsala Universitet (Sweden)
Department of Ecology and Genetics

Prof. **Anssi Vähätalo**
University of Jyväskylä (Finland)
Department of Biological and Environmental Science

Head of the Doctoral School: Prof. Massimo Maffei
PhD Programme Coordinator: Prof. Mario Chiesa

Torino, 2018

Table of Contents

List of pubblications

- Berto, S., Isaia, M., Sur, B., De Laurentiis, E., **Barsotti, F**., Buscaino, R., Maurino, V., Minero, C., Vione, D., "UV-Vis spectral modifications of water samples under irradiation: Lake vs. subterranean water" *Journal of Photochemistry and Photobiology: A Chemistry* (2013) **251**, 85−93 https://dx.doi.org/10.1016/j.jphotochem.2012.10.019

- **Barsotti, F**., Brigante, M., Sarakha, M., Maurino, V., Minero, C., Vione, D. Photochemical processes induced by the irradiation of 4-hydroxybenzophenone in different solvents. *Photochemical & Photobiological Sciences* (2015) **14(11)**, 2087-2096. https://dx.doi.org/10.1039/c5pp00214a

- **Barsotti, F**., Ghigo, G., Vione, D. "Computational assessment of the fluorescence emission of phenol oligomers: a possible insight into the fluorescence properties of humic-like substances (HULIS)." *Journal of Photochemistry and Photobiology A: Chemistry* (2016) **315**, 87-93. https://dx.doi.org/10.1016/j.jphotochem.2015.09.012

- Bertinetti, S., Minella, M., **Barsotti, F**., Maurino, V., Minero, C., Özensoy, E., Vione, D. "A Methodology to Discriminate Between Hydroxyl Radical-induced Processes and Direct Charge-transfer Reactions in Heterogeneous Photocatalysis". *Journal of Advanced Oxidation Technologies*, (2016) **19(2)**, 236-245. https://doi.org/10.1515/jaots-2016-0207

- Minella, M., Sappa, E., Hanna, K., **Barsotti, F**., Maurino, V., Minero, C., Vione, D. "Considerable Fenton and photo-Fenton reactivity of passivated zero-valent iron." *RSC Advances*, (2016) **6(89)**, 86752-86761 https://dx.doi.org/10.1039/c6ra17515e

- Carena, L., Minella, M., **Barsotti, F**., Brigante, M., Milan, M., Ferrero, A., Berto, S., Minero, C., Vione, D. "Phototransformation of the herbicide propanil in paddy field water." *Environmental Science & Technology,* (2017) **51(5)**, 2695-2704. https://dx.doi.org/10.1021/acs.est.6b05053

- Barsotti, F., Bartels-Rausch, T., De Laurentiis, E., Ammann, M., Brigante, M., Mailhot, G., Maurino, V., Minero, C., Vione, D. "Photochemical Formation of Nitrite and Nitrous Acid (HONO) upon Irradiation of Nitrophenols in Aqueous Solution and in Viscous Secondary Organic Aerosol Proxy." *Environmental Science & Technology,* (2017). **51(13)**, 7486-7495. https://dx.doi.org/10.1021/acs.est.7b01397

- Koehler, B., **Barsotti, F**., Minella, M., Landelius, T., Minero, C., Tranvik, L. J., Vione, D. "Simulation of photoreactive transients and of photochemical transformation of organic pollutants in sunlit boreal lakes across 14 degrees of latitude: A photochemical mapping of Sweden." *Water research*, (2018). **129**, 94-104. https://dx.doi.org/10.1016/j.watres.2017.10.064

Introduction

The uptake of light energy by organic compounds may cause subsequent photophysical or photochemical events. Photophysical processes include emission of energy (light or heat), whereas photochemical reactions produce new compounds by transformation pathways that include isomerization, bond cleavage, rearrangement, or intermolecular reactions .[1]

In the environment, photochemical processes can be important transformation pathways for organic compounds of both natural and anthropic origin. They involve most notably biologically refractory xenobiotics, such as pesticides, industrial chemicals, pharmaceuticals and personal care products (PPCPs), most of them being emerging contaminants.[2-3] Some of these compounds are directly released into the environment, as in the case of pesticides, which may reach surface waters through different routes including soil runoff and groundwater contamination, followed by transport from ground to surface water.[4-5] In contrast, PPCPs are usually found in wastewater and their release to environmental waters depends on the ability to escape removal by wastewater treatment plants .

It is possible to highlight many different photochemical processes that involve several reactive species, in different compartments of the hydrosphere, each species being characterized by a specific chemical reactivity (see Table 1)[6].

Environment	Water components	Photogenerated species
Marine and fresh waters	DOM	$^3CDOM^*$
		$^1O_2$
		$ROO^\bullet$
		$R^\bullet$
	NO_3^- / NO_2^-	$NO_2^\bullet$ $NO^\bullet$ $OH^\bullet$
	Br^- / Cl^-	$Br_2^{\bullet-}$ $Cl_2^{\bullet-}$
	CO_3^{2-} / HCO_3^-	$CO_3^{\bullet-}$
Marine waters	CH_3I	$I^\bullet$
	I^-	$I^\bullet$
	MnO_2 (colloidal)	Mn_{aq}^{2+}
	Cu(II)	Cu(I)Cl
	Cu(II)-organic complex	
Fresh waters	Fe(III)-organic complex	Fe(II)
	Fe(III)-organic-PO_4 complex	

Table 1 Examples of photoprocesses taking place in natural waters

In surface waters, photochemical reactions take place in the photic zone where many other biotic and abiotic processes also occur. Transport, phase transfers and biological pathways (including aquatic primary productivity) are usually more intense in this area than in deeper waters. [6]

In addition to their environmental importance, surface waters are also the receptacle for many liquid, solid, and airborne wastes. At the same time, surface waters are essential for recreation, aesthetics, transportation, food, and as sources of irrigation water, drinking water and water for industrial or urban use. It is thus important to understand the processes connected with the transformation of compounds that occur in surface waters and particularly in their photic zone.[6]

Reactions induced by sunlight are receiving increasing attention because of their potential importance in the removal of the parent molecules. Many organic pollutants such as polycyclic aromatic hydrocarbons, some pesticides, many pharmaceuticals and their transformation intermediates are refractory to biological degradation. In these cases, abiotic processes (including most notably photochemical reactions) can represent major removal pathways from surface waters.[7] Furthermore, several biorefractory pollutants can become bioavailable after some degree of abiotic processing, with the consequence that the combination of abiotic and biotic degradation can lead to the complete mineralization of organic matter.[8] Unfortunately, in some cases the xenobiotics can undergo photochemical transformation with production of harmful secondary pollutants.[9]

The main photochemical pathways occurring in surface waters are the direct photolysis and the reaction with transient species that are photochemically produced, such as the triplet states of chromophoric dissolved organic matter (^{3}CDOM*), the radicals $^{\bullet}OH$ (hydroxy) and $CO_3^{-\bullet}$ (carbonate) and singlet oxygen, $^1O_2$. Such species are involved in the transformation of xenobiotics and they are generated upon absorption of sunlight by nitrate, nitrite and CDOM, in the presence of bicarbonate and carbonate as far as $CO_3^{-\bullet}$ generation is concerned. [10,]

The photochemical fate in surface waters of organic compounds depends on the complex interaction between molecules and ecosystems. The phototransformation kinetics is linked to both substrate-related and environment-related variables, for which reason different molecules could follow different phototransformation pathways in the same water body, and the same molecule could undergo different processes in different water bodies.

To unravel the complex molecule-ecosystem interactions, a multicomponent approach has to be used. Considering substrates and natural water systems, it is necessary to take into account:

I. The direct photolysis quantum yield of each relevant compound and its reaction rate constants with the photogenerated transients. In the case of ^{3}CDOM*, reactivity can be studied by use of proxy molecules that simulate the photochemical behavior of natural CDOM;
II. Water chemical composition and penetration of sunlight inside the water body (which is also affected by the irradiance, spectral quality, and spatial-temporal distribution of sunlight) [11,12];

III. The photochemical behavior of naturally-occurring photosensitizers, and most notably of CDOM that is by far the less know photoactive component of surface waters.

The difficulty to generalize the results obtained in single studies is an obstacle to the prediction of the photochemical fate of a certain compound in a definite ecosystem. This difficulty, which is mainly related to the challenge of complexity, hampers a better understanding of the photochemical processes in surface waters. However, the problem can be addressed by combining studies of ecosystem photochemical functioning, laboratory measures of substrate reactivity including elucidation of the photochemistry of CDOM proxies, and photochemical modeling with a comparison between model results and field data regarding the time evolution of the compound in a specific water body.

Photochemical processes in surface waters

Abiotic transformation reactions can be important for the degradation of biorecalcitrant organic pollutants in surface waters, and of biorecalcitrant intermediates deriving from microbial processes [13]. Interestingly, non-biodegradable organic compounds can become bioavailable after some degree of abiotic processing.[14]. An example is the addition of hydroxyl groups to biorecalcitrant aromatic rings upon reaction with photochemically produced hydroxyl radicals. Usually the biotransformation kinetics of hydroxylated substrates is orders of magnitude faster than that of the original compounds [15].

Abiotic transformation in surface waters includes a large variety of reactions such as hydrolysis and oxidation mediated by dissolved species or by metal oxides such as Fe(III) and Mn(III,IV) (hydr)oxides. Hydrolysis will often produce bond cleavage, which in many cases results in the loss of a lateral functional chain. Hydrolytic reactions are usually acid- or base-catalyzed, but at the pH values around neutrality that are typical of surface waters the effects of catalysis may be limited [16].

Among the abiotic processes, light-induced reactions play a key role in the degradation of non-biodegradable compounds [17]. Contaminants can undergo phototransformation by absorption of solar radiation (via direct photolysis) or by the action of photoactive components present in environmental waters (photo-induced or photosensitized processes). Direct photolysis is affected by the ability of the contaminant to absorb sunlight and by the photolysis quantum yield. Indirect photolysis depends on the reactive species produced by excitation of the photosensitizers (e.g. CDOM, nitrate and nitrite) and on the ability of these species to react with the contaminants. Both direct and indirect photolysis are affected by the water column depth, because sunlight irradiance decreases as the depth increases due to absorption and scattering phenomena.[10]

In the case of direct photolysis, the absorption spectrum and quantum yield are strictly dependent on the substrate and they may vary significantly. Accordingly, direct photolysis should be studied separately for each compound and the results cannot be generalized even within homogeneous compound classes.

Direct Photolysis

To be operational in surface waters, the direct photolysis process requires that a compound is able to absorb sunlight. Moreover, the absorption of sunlight has to trigger some kind of transformation. In other words, the direct photolysis process depends on the substrate absorption spectrum (and on the extent by which it overlaps with the spectrum of sunlight) and on its photolysis quantum yield. Typical processes that can follow sunlight absorption are photoionization, bond breaking, intra-molecular rearrangement, and the formation of excited states (singlet, triplet) that can undergo peculiar reaction pathways[18]. For instance, the direct photolysis of 2-chlorophenol causes ring contraction via the singlet state and dechlorination upon triplet reactivity.[19-20]

Among the environmental features that can affect the direct photolysis process, the main ones are the irradiance and the spectrum of sunlight, water depth and the water absorption spectrum. The irradiance of sunlight depends on the time of the day, on seasonality, on latitude and on weather issues. Weather is predictable with difficulty, but the mid-latitude sunlight irradiance would be maximum on midday during fair-weather summertime (specifically, at the summer solstice). Sunlight irradiance typically increases as latitude decreases but, in the tropical belt, the summer solstice is no longer the day of maximum irradiance. For instance, at the equator the irradiance is maximum in the spring and fall equinox under fair-weather conditions. The higher is the total sunlight irradiance, the higher is usually also the UV radiation intensity in both absolute and relative terms. The UV irradiance has key importance for many xenobiotics that absorb sunlight prevalently or exclusively in the UV region.[21-22]

Differently from ultra-pure water, natural waters absorb sunlight and this absorption process interferes with the direct photolysis reactions by decreasing the available irradiance. The absorption spectrum of surface waters, in particular in the environmentally significant wavelength range above 300 nm, is largely coincident with the absorption spectrum of CDOM.[23] Only at elevated visible wavelengths (> 500 nm) there may be important contributions from chlorophylls and water itself to absorption. The spectral region above 500 nm, while very important in the determination of the water color that has implications for e.g. satellite measurements,[24-25] is usually of little importance for the photochemistry of surface waters. Photochemical reactions are mainly linked with radiation in the 300-500 nm wavelength range, where CDOM is by far the main absorber.[26] Nitrate can account for the majority of light absorption around 200-230 nm, but this range is not environmentally significant.[27] CDOM is a very complex mixture of compounds of both allochthonous (soil runoff, atmospheric deposition) and autochthonous origin (aquagenic processes, mostly biologic), and its absorption spectrum is usually characterized by an almost featureless exponential decay of the absorbance with increasing wavelength.[23] Therefore, the absorption spectra of both natural waters and CDOM at 300-500 nm (and often a bit beyond) can be conveniently approximated with an exponential function of the form:

$$A_1(\lambda) = A_o\, e^{-S\lambda} \quad (1),$$

where λ is the wavelength, $A_1(\lambda)$ is the water absorbance referred to an optical path length of 1 cm, and A_o is a constant that depends on several issues including most notably the amount of organic matter in the water body (measured as the dissolved organic carbon, DOC). The quantity S is the so-called spectral slope, which is usually inversely proportional to the molecular weight of CDOM.[28] This means that high molecular weight CDOM tends to absorb long-wavelength sunlight to a larger extent than the low molecular weight fraction. A closer look at S has suggested that it can undergo small but not negligible variations with wavelength, which may suggest peculiar features connected with CDOM nature and transformation.[11-29]
Largely due to the water absorption spectrum, the water depth highly affects photochemical reactions because of the attenuation of sunlight as the depth increases. The consequence is that the lower depths of water bodies are scarcely illuminated by sunlight, differently from the surface layer where the photoreactions reach the highest rates. Therefore, photochemistry is most effective in shallow water bodies.[30] Because CDOM absorbs short-wavelength sunlight to a higher extent than long-wavelength sunlight (e.g. the UVB more than the UVA and the visible), the penetration depth of sunlight is shorter at shorter wavelengths.[31] Water depth has thus a negative impact on all the photochemical reactions but, most notably, on the reactions that are triggered by short-wavelength radiation.

Indirect Photochemistry

Several photosensitizers occur in surface waters and produce reactive species upon absorption of sunlight. The best known photosensitizers are nitrate (NO_3^-), nitrite (NO_2^-) and CDOM. Nitrate absorbs sunlight in the UVB and (to a lesser extent) UVA regions, and the light absorption triggers the production of $^\bullet OH$ radicals with quantum yield $\Phi \sim 0.01$. Note that the equilibrium $^\bullet OH \leftrightarrows O^{-\bullet} + H^+$ has pKa ~ 12, thus the production of $^\bullet OH$ via reactions (2) and (3) in typical surface-water conditions is not really pH-dependent.[32-33] However, a dependence of $^\bullet OH$ photoproduction from pH might arise from the photoisomerization of nitrate to peroxynitrite ($ONOO^-$,see reaction (4)), which is not a $^\bullet OH$ source while its conjugated acid HOONO (peroxynitrous acid, pKa ~ 7) partially is. As a consequence, the production of $^\bullet OH$ upon nitrate photolysis decreases with increasing pH.[34]

$$NO_3^- + h\nu \rightarrow O^{-\bullet} + {}^\bullet NO_2 \quad (2)$$
$$O^{-\bullet} + H^+ \leftrightarrows {}^\bullet OH \quad (3)$$
$$NO_3^- + h\nu \rightarrow ONOO^- \quad (4)$$
$$ONOO^- + H^+ \leftrightarrows HOONO \quad (5)$$
$$HOONO \rightarrow NO_3^- + H^+ \quad (6)$$
$$HOONO \rightarrow {}^\bullet OH + {}^\bullet NO_2 \quad (7)$$

Nitrite absorbs UVB and, most notably, UVA radiation to a larger extent than nitrate, and radiation absorption by nitrite induces the photogeneration of $O^{-\bullet}$/$^{\bullet}OH$ as well. Nitrite can also be oxidized by $^{\bullet}OH$ to produce $^{\bullet}NO_2$ (see reaction (10)). Due to UVA vs. UVB absorption and higher photolysis quantum yield, the environmental photochemistry of nitrite is more efficient than that of nitrate and often compensates (or even more than compensates) for the lower concentration values that nitrite reaches in surface waters compared to nitrate.[35] Moreover, absorption at higher wavelengths ensures that nitrite photochemistry is operational at lower depths compared to that of nitrite. In addition to $^{\bullet}OH$ photoproduction, nitrate and nitrite both yield $^{\bullet}NO_2$ (reactions (1) and (8-10)) that is a nitrating agent, responsible for instance for the photogeneration of toxic nitroaromatic compounds in particular environments.[36-37]

$$NO_2^- + h\nu \rightarrow O^{-\bullet} + {}^{\bullet}NO \quad (8)$$
$$O^{-\bullet} + H^+ \leftrightarrows {}^{\bullet}OH \quad (9)$$
$$NO_2^- + {}^{\bullet}OH \rightarrow NO_2^{\bullet} + OH^- \quad (10)$$

The photochemistry of CDOM is much more complex compared to that of nitrate and nitrite. Moreover, CDOM is a source of several photoinduced transients and not only of $^{\bullet}OH$. Among CDOM chromophores, there are several groups (e.g. aromatic carbonyls and quinones) that easily undergo inter-system crossing (ISC) to yield the triplet states with elevated quantum yield, which is at the basis of the rather efficient production of ^{3}CDOM*. The transients ^{3}CDOM* can undergo vibrational deactivation, reaction with dissolved compounds (e.g. the xenobiotics) or with dissolved O_2 to produce singlet oxygen ($^1O_2$).[38]

$$CDOM + h\nu\ (via\ ISC) \rightarrow {}^3CDOM^* \quad (11)$$
$$^3CDOM^* + O_2 \rightarrow CDOM + {}^1O_2^{\bullet} \quad (12)$$

The generation of $^{\bullet}OH$ by irradiated CDOM is much more controversial as far as the actual pathways are concerned. A first issue is that CDOM yields H_2O_2 under irradiation (see reactions 13 and 15, where HR is a dissolved organic compound), which can produce $^{\bullet}OH$ by direct photolysis or *via* the Fenton reaction.[39-40] Moreover, there is also a H_2O_2-independent (and still largely unknown) generation pathway of $^{\bullet}OH$ from irradiated CDOM.[41-42]

$$^3CDOM^* + H\text{–}R \rightarrow CDOM\text{–}H^{\bullet} + R^{\bullet} \quad (13)$$
$$CDOM\text{–}H^{\bullet} + O_2 \rightarrow CDOM + HOO^{\bullet} \quad (14)$$
$$2\ HOO^{\bullet} \rightarrow H_2O_2 + O_2 \quad (15)$$
$$H_2O_2 + h\nu \rightarrow 2\ {}^{\bullet}OH \quad (16)$$
$$Fe^{2+} + H_2O_2 \rightarrow Fe^{3+} + OH^- + {}^{\bullet}OH \quad (17)$$

Finally, the carbonate radical ($CO_3^{-\bullet}$) is produced upon oxidation of carbonate and bicarbonate by $^{\bullet}OH$ and of carbonate by ^{3}CDOM*.[43] In addition to the generation reactions, the scavenging processes of the photoinduced transients are also

important for the photochemistry of surface waters. The radical •OH is a strong oxidant and reacts at near diffusion-controlled rates with many dissolved compounds.[44] In surface waters, •OH is mainly produced by irradiation of CDOM, nitrate and nitrite and it is mainly consumed by reaction with dissolved organic matter (DOM, which also includes the chromophoric fraction CDOM) and inorganic carbon (the latter process yields $CO_3^{-\bullet}$). In brackish/saline waters, bromide is usually the main •OH scavenger.[9-45] The reaction with DOM is also the main removal process for $CO_3^{-\bullet}$, while $^1O_2$ mainly undergoes deactivation to O_2 upon collision with the water solvent and ^{3}CDOM* mainly undergoes vibrational deactivation and reaction with O_2.[9-46] The main processes involving photosensitizers and transients in surface waters are summarized in Figure 1.

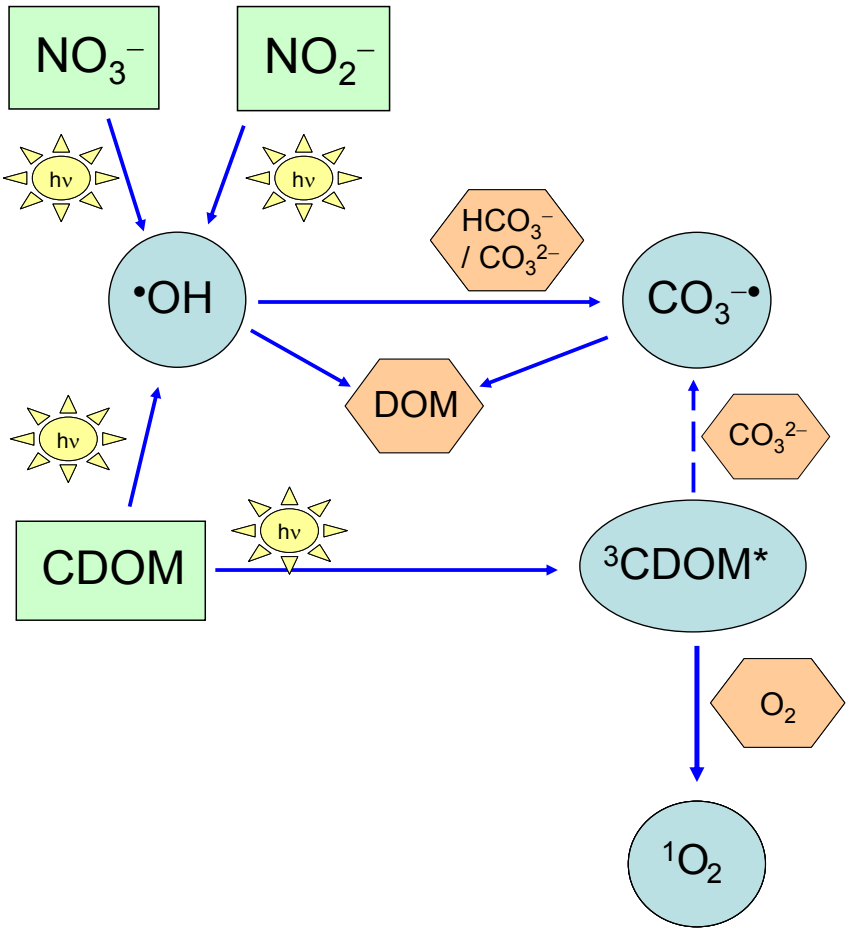

Figure 1 Schematic of the main indirect photochemistry processes taking place in surface waters and involving photosensitizers (represented by rectangles) to produce reactive transient species (circles). The main scavengers are represented by the hexagons.

Xenobiotic phototransformation: Some examples

The ability of a given compound to undergo direct photolysis and/or one or more of the indirect photochemistry reaction pathways depends on the features of both the compound itself and the surrounding environment. The compound reactivity towards the different photochemical pathways is quantitatively assessed by its direct photolysis quantum yield and the second-order reaction rate constants with the photogenerated transients. For instance, the fungicide dimethomorph would mainly undergo indirect photodegradation by $^{\bullet}OH$ in waters that are poor in organic matter, and by $^{3}CDOM^{*}$ in DOM-rich waters. In the same water conditions, the solar filter 2-ethylhexyl 4-(dimethylamino)benzoate would mainly undergo direct photolysis independently of the organic matter content.[47-48]

Among PPCPs, the direct photolysis may be irrelevant for β-blockers but it may be important for some β-lactam antibiotics (e.g. amoxicillin and cefazolin), sulfonamides (e.g. sulfamethoxazole and sulfisoxazole), for some fluoroquinolones, as well as for some non-steroidal anti-inflammatory drugs such as diclofenac, ibuprofen and naproxen.[2] The direct photolysis may also be an important or even the main phototransformation pathway in the case of solar filters.[48-49] It is unfortunately not easy to make predictions about the importance of direct photolysis, even among compounds that share a related chemical structure. For instance, in the case of phenylurea herbicides, photolysis may be quite important for chlortoluron, fairly important for isoproturon, metoxuron and diuron, and irrelevant for fenuron.[50]

The radical $CO_3^{-\bullet}$ is poorly reactive toward most organic compounds, but there are major exceptions concerning some easily oxidized substrates. Therefore, $CO_3^{-\bullet}$ may be important for the phototransformation of aromatic amines, of sulfur-containing molecules such as organic sulfides and mercaptans, as well as phenolates.[51-52] Singlet oxygen often shows limited reactivity, too, but it is for instance the main environmental reactant for the phototransformation of chlorophenolates.[53] Many knowledge gaps still exist concerning the reactivity of $^{3}CDOM^{*}$, which might be involved in the phototransformation of a wide variety of substrates. Anyway, triplet sensitization (i.e., reaction with $^{3}CDOM^{*}$) is thought to play an important role in the degradation of several phenols, phenylurea herbicides and some sulfonamide antibiotics.[38] Finally, $^{\bullet}OH$ is very reactive but its role is partially limited by the very low steady-state concentrations that it reaches in most surface-water environments. Its importance tends to be higher for the degradation of compounds (e.g., toluene or nicotine) that are poorly reactive toward other phototransformation pathways.[54]

Effect of water chemical composition on photochemical reactions

Hydroxyl and carbonate radicals

Water chemistry is a major environmental factor that promotes or inhibits particular phototransformation pathways. The direct photolysis processes involving xenobiotic compounds are typically inhibited by the presence of CDOM, which competes with the pollutants for sunlight irradiance.[2-55] Considering that CDOM (similarly to DOM) typically occurs to a higher extent in waters with elevated levels of dissolved organic carbon (DOC), the direct photolysis processes are usually inhibited in high-DOC waters. As mentioned before, the $^{\bullet}OH$ radical is photogenerated by irradiation of nitrate, nitrite and CDOM and it is mainly scavenged by reaction with DOM. Considering that (C)DOM is an important $^{\bullet}OH$ source but, at the same time, its main scavenger, the steady-state [$^{\bullet}OH$] is usually lower as the DOC is higher. Other factors that affect [$^{\bullet}OH$], although to a usually lesser extent than the DOC, are the concentration values of nitrate and nitrite ($^{\bullet}OH$ sources, which positively correlate with [$^{\bullet}OH$]) and those of carbonate and bicarbonate ($^{\bullet}OH$ sinks, which negatively correlate with [$^{\bullet}OH$]).[9] The DOC trend of [$CO_3^{-\bullet}$] is even more marked compared to that of [$^{\bullet}OH$], because the organic matter both scavenges $CO_3^{-\bullet}$ and inhibits its formation by consuming $^{\bullet}OH$ (most of $CO_3^{-\bullet}$ is in fact formed by reaction of $^{\bullet}OH$ with carbonate and bicarbonate). Therefore, the $CO_3^{-\bullet}$ reactions are typical processes that are favored in low-DOC waters.[56] Another issue is that the formation of $CO_3^{-\bullet}$ from $^{\bullet}OH$ requires bicarbonate and most notably carbonate, which has a considerably higher reaction rate constant with the hydroxyl radical compared to bicarbonate. As a consequence, $CO_3^{-\bullet}$ occurs to a higher extent as the water pH and the inorganic carbon content are higher.[9-43] Finally, there is usually a positive correlation between [$^{\bullet}OH$] and [$CO_3^{-\bullet}$], which is understandable when considering that $CO_3^{-\bullet}$ mostly derives from $^{\bullet}OH$. For this reason, [$CO_3^{-\bullet}$] is often higher in waters that are rich in nitrate and nitrite.[9]

^{3}CDOM and $^1O_2$*

The triplet excited states of CDOM and singlet oxygen are generated by irradiated CDOM and they are scavenged, respectively, by dissolved oxygen (with a minor role of internal conversion, which becomes important in anoxic waters) and by collision with the solvent. Therefore, the steady-state [3CDOM*] and [1O2] are typically higher in high-DOC waters. Furthermore, [3CDOM*] is higher in anoxic waters and [1O2] in oxygenated ones. Among all the water chemistry parameters, the DOC is certainly the most important one that enhances or inhibits the different photochemical reactions.9 A schematic of the pathways that tend to prevail at different DOC values is provided in Figure 2. Of course, the figure reports a general view of the possible processes. Those that really prevail under definite conditions also depend on the reactivity of a given substrate toward each pathway (for instance, if a

xenobiotic does not undergo direct photolysis, the relevant pathway will never be important irrespective of the water DOC value).

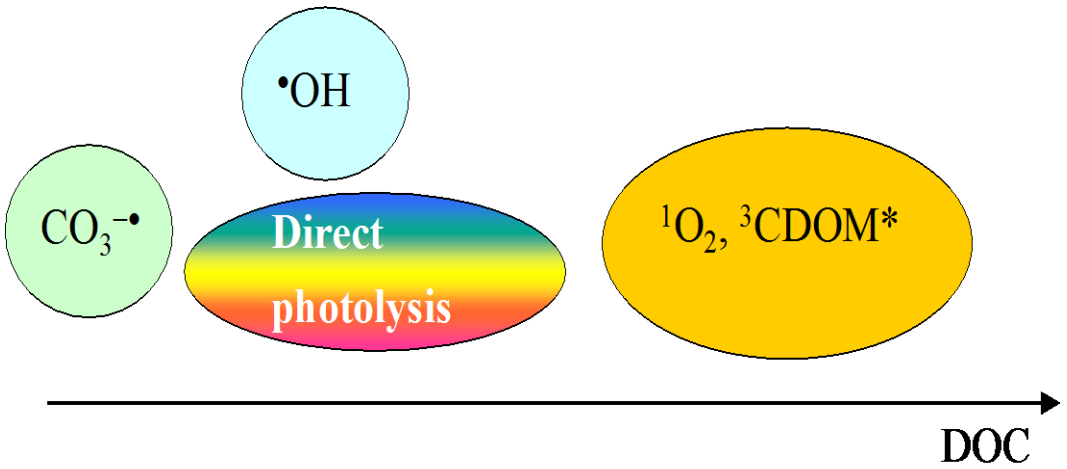

Figure 2 Schematic indication of the different photochemical processes that tend to be favored at different levels of the dissolved organic carbon (DOC). The direction of the DOC increase is shown by the arrow.

With the above-cited limitations, Figure 2 can be read as follows (provided that a given pathway is relevant for a particular xenobiotic): reactions with $CO_3^{-\bullet}$ are most favored in low-DOC waters, while intermediate DOC values (e.g., around 2 mg C L^{-1}) may enhance •OH reactions and the direct photolysis. Direct photolysis and •OH reactions are actually inhibited at high DOC, but to a lower extent than the $CO_3^{-\bullet}$ processes; moreover, DOM usually inhibits the •OH-induced reactions to a higher extent than CDOM inhibits the direct photolysis. Therefore, if •OH reaction and direct photolysis are the only operational pathways, •OH usually predominates at low DOC and direct photolysis at high DOC.[50-57] Finally, high-DOC waters tend to favor the processes induced by ^{3}CDOM* and $^1O_2$.[9-38]

Photochemical production of harmful intermediates

Photochemical transformation can lead to the attenuation of xenobiotics but it can also induce the production of harmful compounds. Typically, different photochemical pathways produce different intermediates, and/or the same intermediates with different yields. For instance, phenylurea herbicides are known to produce toxic N-formyl compounds upon reaction with $^{\bullet}$OH. Moreover, similarly or equally toxic compounds can also be formed by direct photolysis of the phenylureas metoxuron and diuron. In contrast, the reaction between phenylureas and ^{3}CDOM* should not produce toxic intermediates.

These considerations, together with the discussion reported in the previous section, suggests that the photochemical generation of toxic species from phenylureas would be inhibited in high-DOC waters.[50] A similar conclusion is afforded for the toxic intermediate 2-methyl-4-chlorophenol, which is produced from the herbicide 2-methyl-4-chlorophenoxyacetic acid (MCPA), in similar yields, by direct photolysis and reaction with $^{\bullet}$OH radical.[58]

Another example is the formation of toxic isobutylacetophenone (IBAP) from ibuprofen. Production of IBAP with fairly elevated yields (25-30%) takes place upon direct photolysis and ^{3}CDOM* reaction, while the IBAP yield from ibuprofen and $^{\bullet}$OH is very low. Therefore, toxic IBAP would be typically formed in high-DOC waters.[59]

The photochemical formation of mutagenic acridine from carbamazepine occurs with similar yields (3-3.5%) upon both direct photolysis and $^{\bullet}$OH reaction. The two processes are also the main transformation pathways of carbamazepine in surface waters, which suggests that acridine would be formed photochemically in low but constant yield under variable environmental conditions.[60]

Gemfibrozil is known to produce a strongly mutagenic species upon direct photolysis.[61]-[62] On the basis of the scheme reported in Figure 2, one could hypothesize that the mutagenic compound would be formed preferentially at intermediate DOC values. A similar prediction could be made for the production of toxic species by direct photolysis of the antibiotic cefazolin.[57]-[63] The basic form of the antimicrobial agent triclosan (5-chloro-2-(2,4-dichlorophenoxy)phenol) is known to produce a potentially harmful dioxin by direct photolysis and ^{3}CDOM* reaction, in the latter case with even higher yield. One could hypothesize that dioxin formation is enhanced at high DOC, where the ^{3}CDOM* processes are favored, but this is little relevant because the direct photolysis is usually the main phototransformation pathway of triclosan. In this case the key water parameter is actually the solution pH, because protonated triclosan (which prevails at pH < 8) does not yield dioxins upon photochemical transformation.[64]-[65]

The above examples suggest that water chemistry (most notably, DOC and pH) could be a major factor that directs the photochemical formation of harmful intermediates, with the notable exception of the production of acridine from carbamazepine. The examples were taken from literature papers in which the formation of the intermediates was differentiated on the basis of the actual phototransformation pathways. Although the reported cases are only exemplary and not exhaustive, this "phototoxicology" approach is still relatively rare and such details about the

photochemical pathways are presently known for just a limited number of compounds. A more extended knowledge would be very helpful to elucidate the impact of xenobiotics as a function of the environmental conditions.

Time trends of water chemistry

As previously reported, water chemistry may play a very important role in the phototransformation of xenobiotics and in the production of harmful transformation intermediates. The chemical composition of surface waters can undergo seasonal changes because of biological and chemical processes. For instance, nitrate often has winter maxima because it is consumed by algae during summer, while the consumption of CO_2 by photosynthesis produces summer maxima of pH in the surface water layer. Calcium and alkalinity often have summer minima because of $CaCO_3$ precipitation in warm water, while the DOC may be high in summer due to the elevated biological productivity.[66] Superposed to the seasonal changes there may be long-term trends that can be directly or indirectly associated with human impact. An example of a direct impact is the discharge of nutrients into water bodies, which causes eutrophication and often increases the values of DOC and possibly those of inorganic nitrogen (e.g. nitrate and nitrite, unless nitrogen is the limiting factor for algal growth). If nutrient inputs change over time, the water chemistry and, as a consequence, its photochemistry may be affected significantly. Controls on discharges could for instance decrease the nutrient inputs, often decreasing the water DOC and shifting photochemistry from $^3CDOM^*/^1O_2$ to $CO_3^{-\bullet}/^\bullet OH$ processes.[67]
Another cause of long-term modification is climate change. In the case of lake water, increases in alkalinity and pH are often the main indices that climate change is operating on water chemistry. The rationale is the enhanced dissolution of salts such as $CaSO_4$ in warmer water, where Ca^{2+} can be up-taken but it is not transformed by biota while sulfate is transformed into organic sulfur species with H^+ consumption. A pH increase may lead to higher dissolution of CO_2, thereby increasing the levels of carbonate and bicarbonate.[68] Higher alkalinity and higher pH would favor the reactions induced by $CO_3^{-\bullet}$, but such changes could be easily offset by variations in the DOC that is a major $CO_3^{-\bullet}$-controlling factor.[56] The DOC is a key water photochemistry parameter and it is affected by climate, but its variations are not easily predictable. In nordic environments, warming would likely produce an increased export of organic matter from soil to surface waters, with consequent "brownification" and DOC increase.[69] In this case, climate change would shift photochemical processes towards $^3CDOM^*/^1O_2$ reactions. In sub-tropical environments, desertification might produce a long-term decrease of organic matter in soil and, as a consequence, in surface waters, which would rather favor $^\bullet OH/CO_3^{-\bullet}$-induced photoprocesses. In temperate areas, climate-related DOC variations are often small and they could be easily offset by other human impacts such as changes in nutrient inputs. It is clear that much additional work is still needed to elucidate the impact of climate on surface-water photochemistry.

Section I- Photochemistry and Photophysics of CDOM proxies

Dissolved organic matter represents a substantial portion of the total organic carbon found in aquatic ecosystems ranging from freshwater lakes to the open ocean. Photochemical reactions are induced by the absorption of solar radiation by water components, primarily in the ultraviolet region.[70] Photochemical reactions in aquatic ecosystems can alter the chemical structure and optical properties of DOM due to the UV absorption by certain DON moieties, termed chromophores. Because DOM is heterogeneous in nature, only a portion of it may be chromophoric and thus responsible for photochemical reactions.[71]
Although it is possible to characterize DOM composition in terms of its molecular mass spectrum, stable carbon isotopic composition, and elemental composition, these measures are time consuming and typically require sample preparation procedures that can modify DOM composition.[72] Moreover, these techniques have had limited success in defining the relationship between compositional differences in DOM and the metabolic activity of heterotrophic bacteria.
In recent years, there has been a renewed interest in exploring the potential uses of fluorescence spectroscopy to characterize DOM composition.[73]
Fluorescence spectroscopy is an ideal method to identify certain compounds in a complex mixture, provided that they fluoresce at characteristic emission wavelengths and in this case the fluorescence intensity is typically proportional to the concentration. Two main types of DOM fluorescence have been described in natural waters: a humic-like or gelbstoff signal, and an amino acid–like signal attributed to tyrosine and tryptophan as fluorophores.[74]

This first thesis section aims at investigating some compounds that show fluorescence signals in the humic-like region. They include 4-carboxybenzophenone and molecules derived from the *para*-oligomerization of phenol.

The case of 4-carboxybenzophenone

Benzophenones are important chromophores and photosensitizers occurring in chromophoric dissolved organic matter (CDOM) in natural waters, and particularly in humic substances.[75] Recent evidence has provided additional arguments regarding photo-oxidation reactions [76] and charge transfer processes[77] that remark the important role played by benzophenones in the optical and photochemical properties of CDOM and humic materials.[75] A major feature of benzophenones is the fact that the energy levels of their first excited singlet (S_1) and triplet (T_1) states are very near. This issue, combined with the fact that their S_1 and T_1 states are strongly coupled by spin–orbit interactions, favors the inter-system crossing (ISC) from S_1 to T_1 that has elevated (often near-unity) quantum yields. Therefore, light absorption that excites the electrons from S_0 to S_1 is followed to a large degree by relaxation of the excited benzophenones into T_1, which triggers important triplet-sensitized processes.[78] In the case of unsubstituted benzophenone (BP), both S_1 and T_1 have n–π * configuration. The n–π* configuration favors both the ISC and the reactivity of T_1, thereby enhancing the triplet sensitization. Interestingly, the π–π* configurations of both S_1 and T_1 are associated with longer excited-state lifetimes, lower ISC quantum yields and reduced photochemical reactivity.[78] In the case of 4-hydroxybenzophenone (4BPOH), the n–π* and π –π* configurations of T_1 are relatively near in energy. Indeed, the ground state of 4BPOH is a weak acid with $pK_a < 8$,[79] while the excited singlet and triplet states are strong acids. This issue significantly affects the photoluminescent and photochemical behavior of 4BPOH in protic solvents and particularly in aqueous solution, where undissociated 4BPOH absorbs radiation and its excited states undergo quick deprotonation, to give at some stage the anionic species $4BPO^-$ in its ground state. The latter is readily protonated to produce the starting compound 4BPOH. [80]

Although very attractive (see the above survey of literature findings), the description of the excited states as a single configuration generated by only one electronic excitation from an occupied molecular orbital to a virtual molecular orbital is too coarse. The excited states often show a multiconfigurational nature: they are described by several electronic configurations, each corresponding to different excitations from occupied to virtual orbitals (where the HOMO-LUMO transition is only one of them). In this thesis, the electronic structure of the excited states was analyzed with a more accurate approach, considering the changes of the electronic density when going from the ground to the excited states by using a computational approach (TD-DFT methods). Indeed, with this approach it is possible to predict the fluorescence properties of 4BPOH.

The most important findings concerning the photophysics and photochemistry of 4BPOH are as follows: (i) the fluorescence intensity of 4BPOH is much higher in aprotic solvents than in water, as explained hereafter;[81] (ii) the first excited triplet state of 4BPOH is easily detected by laser flash photolysis in aprotic solvents, but it is not detected in aqueous solution;[82] (iii) 4BPOH is a rather efficient photosensitizer that induces the photodegradation of other compounds in aprotic or weakly protic solvents, but its photosensitizing ability is lost in aqueous solution. [81-83] Interestingly, most of the cited aqueous-solution studies have been carried out at neutral pH.

Another interesting feature of 4HOBP is that its fluorescence spectrum shows a peak in the excitation wavelength region of 310-360 nm and emission wavelength region of 450-530 nm,[81] which remarkably overlaps with the so-called "peak C" of humic substances, as shown hereafter. The fluorescence properties of humic compounds are widely used to characterize surface water samples and to assess the origin and environmental processing of the organic matter they contain,[84] but the actual reasons behind the fluorescence emission of the humic material are still very elusive. Fluorescence emission wavelengths around 500 nm could be accounted for by phenol oligomers, as shown below, but it is clear that any compound with fluorescence emission in the same region as the humic substances deserves particular attention. Indeed, a detailed understanding of the relevant photophysical pathways can help elucidating the nature of the transitions behind humic fluorescence. Another reason that could make 4BPOH an interesting model compound for the photochemistry of humic substances is that the latter are probably aggregates of smaller molecules,[85] where the most hydrophilic ones are located at the surface in contact with water, while the hydrophobic ones form a waterless inner core. The hydrophobic cores of humic substances are locations where an unusually elevated concentration of O_2 occurs, which could play an important role in the photochemical degradation of hydrophobic pollutants.[86] There is evidence that part of the reason for the elevated $^1O_2$ concentration in hydrophobic cores is that the lifetime of $^1O_2$ is higher in waterless environments.[87] However, a compound such as 4BPOH is interestingly able to produce $^1O_2$ when irradiated in aprotic or weakly protic solvents, but no $^1O_2$ photoproduction takes place in water.[81] Considering that benzophenone derivatives are quite common in natural humic material,[88] a compound such as 4BPOH might contribute to elevated $^1O_2$ levels in hydrophobic environments and its photoreactivity would be quenched at the interface with water.

4-hydroxybenzophenone behavior in different solvents

As presented in the previous section, an experimental investigation of 4BPOH has been carried out in order to understand the behavior of this compound in different natural environments such as bulk water and hydrophobic cores, simulated in laboratory by using a protic polar solvent (water), a protic but less polar solvent (2-propanol), and an aprotic solvent (acetonitrile).
For each solution prepared in a different solvent, several measurements were performed: fluorescence measurement, by recording the EEM Matrix; steady irradiation experiments, followed by HPLC measurements in order to define the photochemical properties of 4BPOH; and Laser Flash Photolysis (LFP) experiments to investigate the excited-state properties of 4BPOH.

Fluorescence Measurements

The excitation–emission matrix (EEM) fluorescence spectra were taken with a VARIAN Cary Eclipse fluorescence spectrophotometer, with an excitation range from 200 to 400 nm at 10 nm steps, and an emission range from 200 to 600 nm with a scan rate of 1200 nm min^{-1}. Excitation and emission slits were both set at 10 nm. Spectra were taken in a fluorescence quartz cuvette (Hellma) with 1 cm optical path length. The Raman signal of water was taken as a reference for the lamp intensity and signal stability within different measurements.

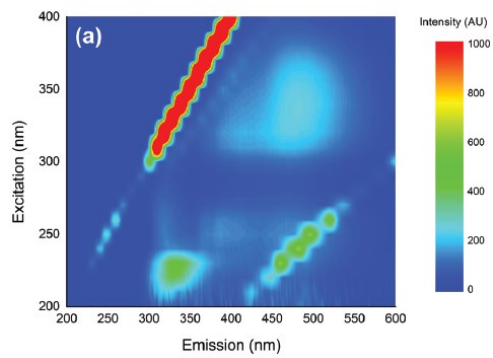

Figure 3a

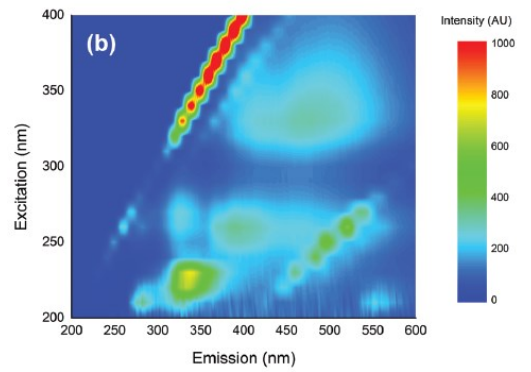

Figure 3b

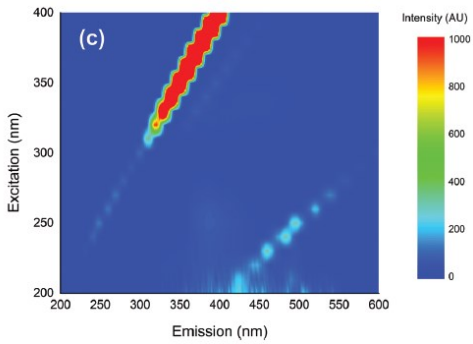

Figure 3c

Figure 3. EEM fluorescent spectra of 0.1 mM 4BPOH in acetonitrile (a), 2-propanol (b), and water (c)

Figure 3 shows the fluorescence EEM spectra of 0.1 mM 4BPOH in different solvents (acetonitrile, 2-propanol and water, the latter at the natural pH ~ 6). Considering first the fluorescence spectra in the organic solvents, one can notice a band at Ex/Em ~225/325 nm that is included in the region of phenolic compounds (which is consistent with the OH group on the aromatic ring of 4BPOH).[74] More interestingly, the band with Ex/Em ~ 325/475 nm overlaps with peak C of humic substances.[74] Because benzophenones are known chromophores/photosensitizers occurring in CDOM, the fact that a compound of this class shows fluorescence in the humic region deserves certain attention. In contrast to the results obtained in organic solvents, the fluorescence spectrum of 4BPOH in water shows little or no fluorescence emission. This issue is consistent with literature reports that the excited states of 4BPOH (including the excited singlet state(s)) undergo rapid (radiationless) deactivation by deprotonation in aqueous solution.[89]

Laser Flash Photolysis (LFP) Experiments

LFP experiments were carried out using the third harmonic (λ_{exc}= 355 nm) of a Quanta Ray GCR 130-01 Nd:YAG laser system instrument, used in a right-angle geometry with respect to the monitoring light beam. The single pulses were ca. 9 ns in duration, with an energy of ~ 45 mJ/pulse. Individual cuvette samples (3 mL volume) were used for a maximum of four consecutive laser shots. The transient absorbance at the pre-selected wavelength was monitored by a detection system consisting of a pulsed xenon lamp (150 W), monochromator and a photomultiplier (1P28). A spectrometer control unit was used for synchronizing the pulsed light source and programmable shutters with the laser output. The signal from the photomultiplier was digitized by a programmable digital oscilloscope (HP54522A). A 32 bits RISC-processor kinetic spectrometer workstation was used to analyzed the digitized signal.

An appropriate volume of stock solutions was mixed before each experiment to obtain the desired concentrations. The pH was adjusted by using $HClO_4$, and deoxygenated and oxygen-saturated solutions were used (when necessary) after 20 min of bubbling with argon or pure oxygen, respectively. The second-order rate constant between 4BPOH-T_1 (hereafter, ^{3}4BPOH*) and quenchers was calculated from the regression line of the absorbance logarithm decay against the quencher concentration. The error bars were derived at the 3σ level from the scattering of the experimental data. All the experiments were performed at room temperature (295 ± 2 K).

The laser excitation of 4BPOH in acetonitrile produces a transient spectrum with absorption maxima at 330 and 520 nm, with the characteristic features of ^{3}4BPOH* (showed in Figure 4d). The transient spectra taken at relatively long times (about 0.30 μs) show the occurrence of a small peak between 550 and 600 nm, which might be consistent with the ketyl radical of 4BPOH (4BPOH($H^\bullet$)). The latter could arise upon reaction between ^{3}4BPOH* and ground-state 4BPOH, according to the following reaction:

$$^3\text{4BPOH*} + \text{4BPOH} \rightarrow \text{4BPOH}(H^\bullet) + \text{4BPO}^\bullet \qquad (18)$$

In contrast, the reaction between ^{3}4BPOH* and acetonitrile is rather unlikely.[90] The first-order decay constant of the signal measured at 520 nm (k_{520nm}) is in the range of 10^7 s^{-1} in aerated solutions. Coherently with the triplet state assignment, k_{520nm} depends on the content of dissolved oxygen. In fact, k_{520nm} increased when passing from an Ar-bubbled system to an aerated and an O_2-bubbled one. The concentration of dissolved oxygen was assessed based on the published data of its solubility in acetonitrile. [91] From the plotted data (Reported in the Appendix I) one obtains a second-order reaction rate constant of (3.6 ± 0.1) × 10^9 M^{-1} s^{-1} between ^{3}4BPOH* and O_2, with the likely formation of $^1O_2$ that is typical of triplet-state reactivity.[92]

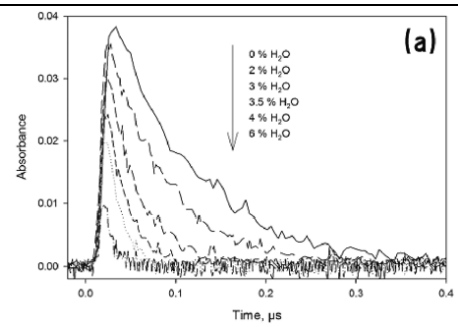

Figure 4a

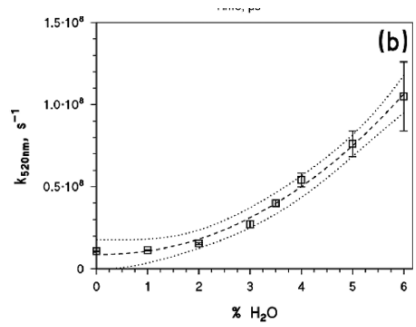

Figure 4b

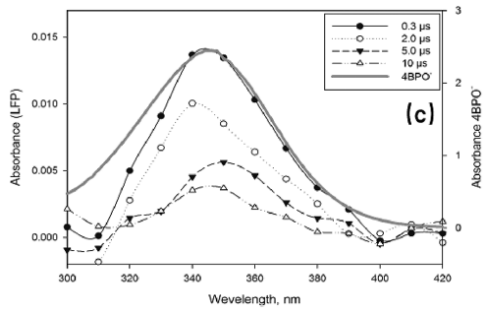

Figure 4c

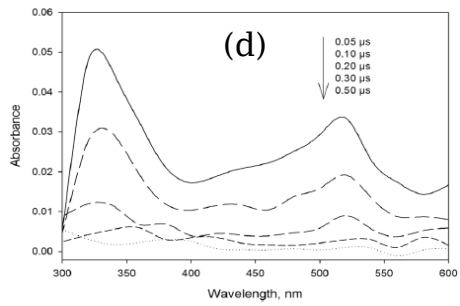

Figure 4d

Figure 4 (a) Trace decay at 520 nm as a function of the percentage of water in CH_3CN. The transients were obtained upon LFP irradiation (355 nm, 94 mJ) of 0.1 mM 4BPOH in aerated solution. (b) Trend of the first-order decay constant of the absorbance at 520 nm, as a function of the percentage of water in binary mixtures of H_2O/CH_3CN. It ws used 4BPOH 0.1 mM, laser excitation at 355 nm, 94 mJ per pulse. The fit curve (dashed) is a polynomial, the dotted ones are the 95% confidence bands of the fit. (c) Time trend of the transient absorption spectrum obtained upon LFP (355 nm, 94 mJ) excitation of 4BPOH (0.1 mM) in an aerated H_2O solution. The gray solid line shows the UV-vis spectrum of anionic 4BPOH (4BPO−, 0.1 mM) in water at pH 10.5. (d) Time trend of the transient absorption spectrum obtained upon LFP (355 nm, 94 mJ) excitation of 4BPOH (0.1 mM) in aerated CH_3CN solution.
All the measurement were carried out at room temperature (295 ± 2 K).

Figure 4a shows the decay traces of the transient absorbance at 520 nm in water/acetonitrile mixtures, as a function of the volume percentage of water (up to 6%). One can observe that the trace absorbance just after the laser pulse is lower in the presence of higher percentages of water, and that the trace decay becomes faster when increasing the water content. This result can be accounted for by the deprotonation of both the singlet and the triplet states of 4BPOH,[82-89] which would both be favored in the presence of higher percentages of water. The deprotonation of the singlet state would compete with the formation of the triplet state, thereby decreasing the triplet absorbance just after the laser pulse. The deprotonation of the triplet state would enhance the relevant trace decay, as reported in Figure 4b which shows that k_{520nm} increases when increasing the volume percentage of water. In the presence of pure water as the solvent, the

signal corresponding to the triplet state of 4BPOH could no longer be observed. Most likely, ^{3}4BPOH* is not formed in water because the deprotonation of the excited singlet state is much faster than the ISC. Moreover, even if formed to some extent in water, or in water–acetonitrile mixtures with a rather elevated water content, ^{3}4BPOH* is expected to undergo very fast deprotonation.[90]

The excited-state deprotonation is known to yield an anionic species with an absorption maximum around 350 nm.[80-82] In both water and water–acetonitrile mixtures we observed the formation of a transient with maximum absorbance at 350 nm, which was longer-lived compared to the triplet state. The transient absorption spectrum is very similar to that of the anionic form of 4BPOH (hereafter, 4BPO$^-$), as shown above in Figure 4c. This finding justifies the identification of the observed species with ground-state 4BPO$^-$. Interestingly, k_{350nm} (the pseudo-first order decay constant of 4BPO$^-$) increases linearly when increasing the volume percentage of water, which may suggest an acid–base process involving 4BPO$^-$ (see the Appendix). Considering that the decay of the 350 nm signal brings the absorbance back to its initial value (namely the value observed before the laser pulse, in the presence of 4BPOH alone), the most likely decay process is the protonation of 4BPO$^-$ back to 4BPOH. Such a deprotonation–protonation sequence would be accounted for by the fact that the triplet state ^{3}4BPOH (pKa < −2) is a much stronger acid than the corresponding ground-state 4BPOH (pKa ~ 8.5).[82] The above hypothesis is further confirmed by the fact that k_{350nm} depends on pH (see the Appendix). The pH trend is consistent with a reaction between 4BPO– and H_3O^+ at pH < 5, while at pH > 5 the prevailing reaction would take place with water.

The triplet states of benzophenones often behave as effective photosensitizers for the transformation of phenolic compounds.[88] The reactivity between ^{3}4BPOH* and phenol was assessed by studying the effect of phenol concentration on the value of k_{520nm} in acetonitrile. The value of k_{520nm} increases linearly with increasing phenol (see the Appendix), from which trend a second-order rate constant $k_{^3\text{4BPOH*,phenol}} = (6.6 \pm 0.3) \times 10^7$ M^{-1} s^{-1} can be obtained between ^{3}4BPOH* and phenol. The reaction yields a species with an absorption maximum around 380 nm, which is longer-lived compared to ^{3}4BPOH*. Based on its absorption spectrum this species is reasonably assigned to a phenoxy radical,[93] which suggests that ^{3}4BPOH* would react with phenol by hydrogen abstraction (or by electron transfer followed by deprotonation, which does however look unlikely in aprotic acetonitrile). The formation of phenoxy radicals has indeed been reported upon reaction between carbonyl triplets and phenols.[83]

Additional experiments of laser irradiation showed that negligible reaction would take place between ^{3}4BPOH* and furfuryl alcohol (FFA). Considering that the latter is a $^1O_2$ probe,[94] it would be possible to use FFA to assess the formation of $^1O_2$ from irradiated 4BPOH (as explained in the following paragraph), without the potential bias of a reaction between FFA and ^{3}4BPOH*.

As an additional solvent, 2-propanol was chosen because it has intermediate proticity between aprotic acetonitrile and water.[95] The initial absorbance of the triplet state after the laser pulse decreased linearly with the increasing percentage of 2-propanol in acetonitrile (see the Appendix), which suggests that a lesser amount of ^{3}4BPOH* would be formed in the presence of the alcohol. This result is consistent with the deprotonation of the excited singlet state in the presence of 2-propanol. Moreover, the first-order rate constant of ^{3}4BPOH* decay (k_{520nm}) increased linearly with increasing 2-propanol (see the appendix), coherently with a reaction between ^{3}4BPOH* and the alcohol. The corresponding second-order rate constant, derived as the slope of the plot of k_{520nm} vs. 2-propanol, is $k_{^3\text{4BPOH*,2-propanol}} = (3.4 \pm 0.3) \times 10^6\ M^{-1}\ s^{-1}$. The relevant process could be an acid–base and/or a redox reaction, and the literature shows an important disagreement over this issue. While some authors assume that ^{3}4BPOH* is able to abstract hydrogen from alcohols including 2-propanol,[82] others explicitly exclude this possibility and only consider an acid–base process where the alcohol acts as a H^+ acceptor for the deprotonation of ^{3}4BPOH*.[96] For instance, no hydrogen abstraction is reported to take place between ^{3}4BPOH* and ethanol in ethanol solution.[97]

To gain insight into the process details, the reaction with 2-propanol was also studied by laser irradiation of benzophenone (BP), which differs from 4BPOH due to the absence of the OH group on the aromatic ring. In this case, it is well known that the BP triplet state abstracts a H atom from the alcohol to form the ketyl radical of BP,[98] which has a comparable lifetime as the BP triplet state and partially overlaps with its absorption spectrum.[99] The laser irradiation of BP was carried out in a system containing 50% acetonitrile and 50% 2-propanol. Figure 5a shows, as a function of the wavelength, the first-order decay constant of the flash photolysis traces (k_{decay}, upper graph), as well as the maximum absorbance value reached by each trace, soon after the laser pulse (lower graph). The maximum trace absorbance gives insight into the absorption spectrum of the transient(s) formed by laser irradiation. The absorbance peaks around 320 and 520 nm can be assigned to the triplet state of BP;[99-100] interestingly, these peaks correspond to the values of $k_{decay} \sim 4 \times 10^6\ s^{-1}$. However, the decay constant shows different values in other wavelength intervals, and in particular it is $k_{decay} \sim 1 \times 10^7\ s^{-1}$ at around 450 and 600 nm. These variations of k_{decay} suggest that the reported maximum trace absorbance is the result of the contribution of more than one species. Literature data indicate that the transient absorption upon laser irradiation of BP and 2-propanol results from both the triplet state and the ketyl radical of BP.[99] Because the BP triplet state absorbs radiation around 320 and 520 nm,[100] one can identify the species with $k_{decay} \sim 4 \times 10^6\ s^{-1}$ as the triplet state of BP and that with $k_{decay} \sim 1 \times 10^7\ s^{-1}$ as the ketyl radical. The latter would thus absorb radiation at around 450 and 600 nm. Interestingly, the ketyl radical is not formed upon laser irradiation of BP in pure acetonitrile.

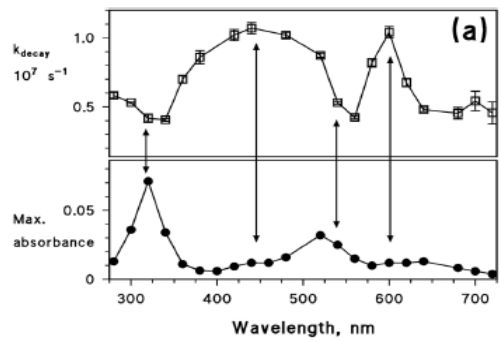

Figure 5a

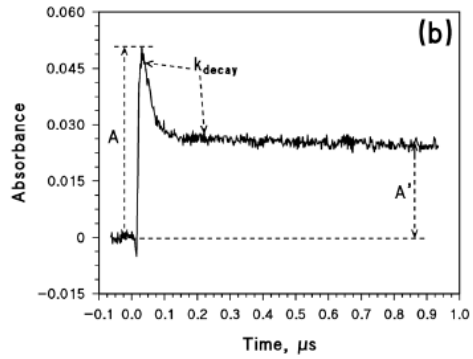

Figure 5b

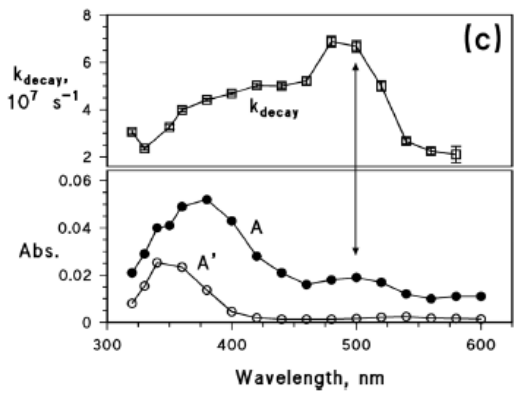

Figure 5c

Figure 5 (a) Upper plot: first-order decay constant (k_{decay}) of the laser trace as a function of wavelength, upon irradiation (355 nm, 94 mJ per pulse) of 0.1 mM benzophenone in 1 : 1 2-propanol : acetonitrile. Lower plot: maximum absorbance of the laser trace under the same conditions. (b) Laser trace (350 nm) upon irradiation of 0.1 mM 4BPOH in 1 : 1 2-propanol : acetonitrile (355 nm, 94 mJ per pulse). The absorbance values A and A' and the time interval used to determine k_{decay} are also highlighted. (c) Upper plot: first-order decay constant (k_{decay}) of the laser trace as a function of wavelength, upon irradiation (355 nm, 94 mJ per pulse) of 0.1 mM 4BPOH in 1 : 1 2-propanol : acetonitrile. Lower plot: wavelength trends of A and A' under the same conditions

The above-discussed laser irradiation of BP in 50% acetonitrile + 50% 2-propanol yielded transient traces that, after an exponential decay, went back to the absorbance value observed before the laser pulse. The situation changed considerably upon laser irradiation of 4BPOH in the same solvent mixture. In this case, the trace reached a maximum (A) and then decayed exponentially down to a constant value (A') that was higher than the initial absorbance (see Figure 5b). This issue means that a longer-lived species was formed in the presence of 4BPOH, while the exponential decay itself is silent as to the occurrence of one or more short-lived transients. The plot shown in Figure 5c was obtained under similar conditions as that of Figure 5a, the only difference being that it is referred to 4BPOH instead of BP. In this case as well, the solvent was a 1 : 1 mixture of acetonitrile and 2-propanol. Also in this case there is evidence of the occurrence of more than one species. First of all, the transient absorption spectrum (A) shows two maxima (around 380 and 500 nm) that, differently from the case of ^{3}4BPOH* alone (see Figure 4d), have quite different absorbances. Secondly, k_{decay} varies from ~2 × 10^7 to ~7 × 10^7 s^{-1}. The plateau absorbance A' has a maximum around 350 nm, which agrees with the absorption spectrum of $4BPO^-$. The latter

species is reported to be formed in alcoholic solvents such as ethanol.[97] Further evidence in favor of the identification of the longer-lived species with $4BPO^-$ is its decay kinetics, which is very slow in 2-propanol and is accelerated upon addition of water traces (see the Appendix). It is reasonable that $4BPO^-$, once formed, undergoes protonation that would be much faster in water compared to 2-propanol. Figure 5c suggests that in addition to $4BPO^-$ that is relatively long-lived, two transient species with shorter and similar lifetimes occur in the system. The triplet state ^{3}4BPOH* is known to absorb at ~330 and ~500–520 nm,[100] thus it should be the species with $k_{decay} \sim 7 \times 10^7\ s^{-1}$. The other species would account for the observed $k_{decay} \sim 2 \times 10^7\ s^{-1}$ at around 575 nm, and possibly also around 320 nm. In analogy with the results obtained with BP, the second species might be the ketyl radical of 4BPOH (4BPOH($H^\bullet$)). This radical is reported to have an absorption maximum at 560 nm,[90] which would be reasonably consistent with the observed wavelength trend of k_{decay}. If the identification of the second species with 4BPOH($H^\bullet$) is correct, there would be support for the possibility of an electron-transfer reaction between ^{3}4BPOH* and 2-propanol.

The following Scheme 1 shows the hypothesized processes involving irradiated 4BPOH. Excited-state deprotonation and $4BPO^-$ protonation would be faster in water than in 2-propanol.

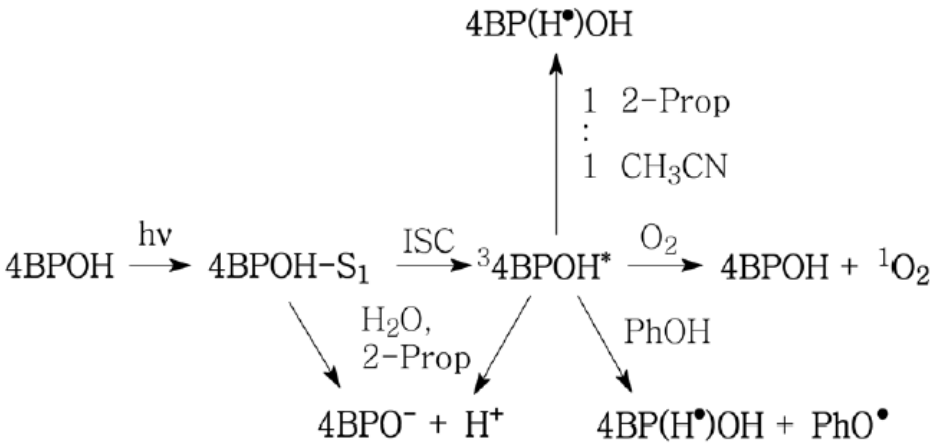

Scheme 1 Hypothesized reaction pathways involving irradiated 4BPOH

Steady Irradiation Experiments

Solutions (5 mL volume) containing 0.1 mM 4BPOH and other reagents (when necessary, such as 0.1 mM phenol or 0.1 mM FFA) were placed in cylindrical Pyrex glass cells (4.0 cm diameter, 2.5 cm height, with a lateral neck tightly closed with a screw cap).

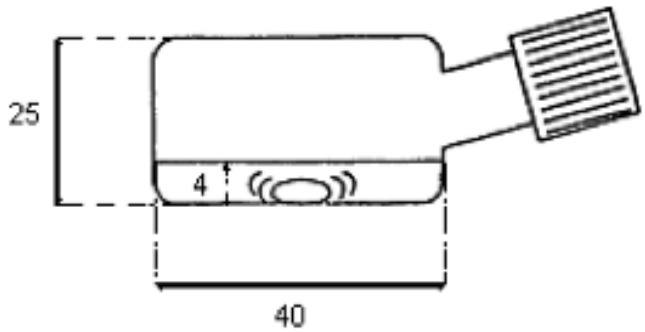

Figure 6 Reaction cell used for the irradiation experiments (the dimensions are expressed in mm)

The solvent was either water, acetonitrile, or 2-propanol. Irradiation of the cells took place under a Philips TL 01 (20 W) lamp with an emission maximum at 313 nm. The solutions in the cells were irradiated from the top and the optical path length was 0.4 cm. The lamp irradiance over the solutions was 2.6 ± 0.1 W m^{-2}, measured with a CO.FO.ME.GRA (Milan, Italy) power meter equipped with a UV-sensitive probe (290–400 nm). The lamp emission spectra (spectral photon flux density $p°(\lambda)$, given in Einstein L^{-1} s^{-1} nm^{-1}) were obtained by combining spectrophotometric measures (CCD spectrophotometer Ocean Optics USB 2000, calibrated with a DH-2000-CAL radiation source) with chemical actinometry using 2-nitrobenzaldehyde. The detailed procedure to determine $p°(\lambda)$ is described in detail elsewhere.[94] Einstein is a measure unit that indicates 1 mol of photons.
Figure 7 shows the spectral photon flux density of the lamp, together with the absorption spectra of 4BPOH (molar absorption coefficients) in both acetonitrile and 2-propanol. The latter were taken with a Varian Cary 100 Scan double-beam UV-vis spectrophotometer, using quartz cuvettes (Hellma, optical path length 1 cm). The main reason for the higher absorption coefficient of 4BPOH in 2-propanol above 300 nm is that the absorption maximum in this solvent, compared to acetonitrile, is shifted from 285 to 295 nm (bathochromic shift). In contrast, the absorbance at the maximum is similar in both cases.

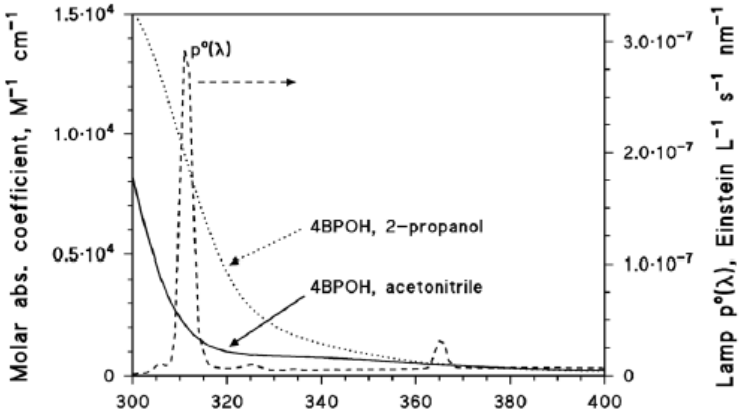

Figure 7 Absorption spectra (molar absorption coefficients) of 4BPOH in acetonitrile and 2-propanol. Emission spectrum (spectral photon flux density) of the lamp used for the steady irradiation experiments.

After the scheduled irradiation times, the cells were withdrawn from the lamp. Measured aliquots of the irradiated solutions (2 mL) were diluted with an equal volume of water and analyzed by high-performance liquid chromatography with diode-array detection (HPLC-DAD). A VWR-Hitachi Elite instrument, equipped with a L-2300 autosampler (25 µL injection volume), a L-2130 quaternary pump for low-pressure gradients, a Duratec DDG-75 online degasser, a L-2300 column oven (operated at 40 °C), a L-2445 DAD detector and a column RP-C18 LiChroCART packed with a LiChrospher 100 RP-18 material (VWR, 4 mm × 125 mm × 5 µm particle size) was used. The eluent was a mixture of 3.5 mM H_3PO_4 in water (A) and of methanol (B). Gradient elution (1 mL min^{-1} flow rate) was as follows: from 5% B to 70% B in 15 min, maintained at 70% B for 7 min, back to 5% B in 5 min and maintained at 5% B for an additional 5 min (post-run equilibration). The detection wavelengths were 290 nm for 4BPOH, 210 nm for phenol, and 230 nm for FFA. The retention times were 15.5 min for 4BPOH, 9.0 min for phenol and 5.3 min for FFA. The column dead time was 1.4 min. Additional runs were carried out to measure the formation of 4-phenoxyphenol (4PP) from 1 mM phenol + 1 mM 4BPOH in acetonitrile and 2-propanol. Isocratic elution (1 mL min^{-1} flow rate) used 50% A and 50% B, with 229 nm detection wavelength and 10.2 min retention time for 4PP. The time evolution data of 4BPOH, phenol and FFA were fitted with pseudo-first order kinetic functions of the form $C_t = C_0\, e^{-kt}$, where C_t is the concentration of the substrate at the time t, C_0 its initial concentration and k the pseudo-first order degradation rate constant. The initial transformation rate was calculated as $R_0 = kC_0$. The uncertainty in the rates is reported as ±σ and it mainly depends on the uncertainty in k, which represents the goodness of the fit of the exponential functions to the experimental data. The reproducibility of replicated experiments was around 15%. The calculation of the quantum yields of 4BPOH and phenol degradation

was based on the photon flux absorbed by the photosensitizer, 4BPOH (P_a^{4BPOH}). The latter was calculated as follows: [101]

$$P_a^{4BPOH} = \int_\lambda p^0(\lambda)\left(1 - 10^{-\varepsilon_{4BPOH}(\lambda) b\,[4BPOH]}\right) d\lambda \qquad \text{(Eq. 1)}$$

where $p^0(\lambda)$ is the spectral photon flux density of the lamp, $\varepsilon_{4BPOH}(\lambda)$ the molar absorption coefficient of 4BPOH, b = 0.4 cm the optical path length in solution, and [4BPOH] =1 × 10^{-4} M the initial concentration of the photosensitizer.

The ability of 4BPOH to photosensitize the degradation of phenol was tested in water, acetonitrile and 2-propanol. The transformation rates R_S of the two substrates (S =4BPOH or phenol, both at 0.1 mM initial concentration) under different conditions are shown in Fig. 6a. Fig. 6b shows the relevant quantum yields of transformation (calculated as $\Phi_S = R_S(P_a^{4BPOH})^{-1}$).
No degradation of either 4BPOH or phenol was observed in water, while both compounds were photodegraded in the organic solvents. Focusing first on the degradation rate of phenol, in aerated solutions it followed the order acetonitrile > 2-propanol > water. An analogous trend was observed for the quantum yields, just with larger differences (compared to the rates) between acetonitrile and 2-propanol: the reason is that 4BPOH absorbs lamp radiation to a higher extent in 2-propanol compared to acetonitrile ($P_a^{4BPOH,2-propanol} > P_a^{4BPOH,CH_3CN}$). Moreover, phenol degradation was enhanced with acetonitrile under a nitrogen atmosphere. These results can be explained easily in the framework of the photochemical processes depicted in the previous Scheme 1, considering that ^{3}4BPOH* would oxidize phenol to the phenoxy radical thereby triggering phenol transformation.
Additional evidence for the formation of the phenoxy radical is the occurrence of the compound 4PP (formed upon dimerization of phenoxyl [102]) upon irradiation of 1 mM phenol + 1 mM 4BPOH in acetonitrile (15–20 μM 4PP was produced for irradiation times over 24 h) and 2-propanol (1–1.5 μM 4PP was formed at the same irradiation time scale).
The lack of phenol degradation in water would be accounted for by the fast deprotonation/quenching of the 4BPOH excited states in this solvent. Indeed, no signal of ^{3}4BPOH* could be detected upon laser irradiation of 4BPOH in aqueous solution. In the case of 2-propanol as the solvent, the reaction between ^{3}4BPOH* and phenol would be in competition with triplet deprotonation and possibly with the oxidation of the solvent (although some evidence of the oxidation of 2-propanol by ^{3}4BPOH* is only available for mixtures with acetonitrile, and not in pure alcohol). These reactions would reduce the availability of ^{3}4BPOH* for the degradation of phenol in 2-propanol, but they would not be as fast as the decay of excited 4BPOH in water. Finally, because ^{3}4BPOH* does not react with acetonitrile, the photosensitized degradation of phenol was fastest in this solvent.

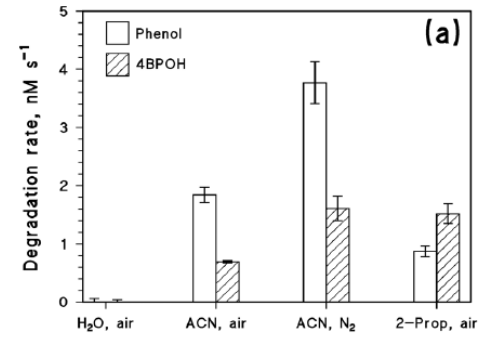

Figure 8a

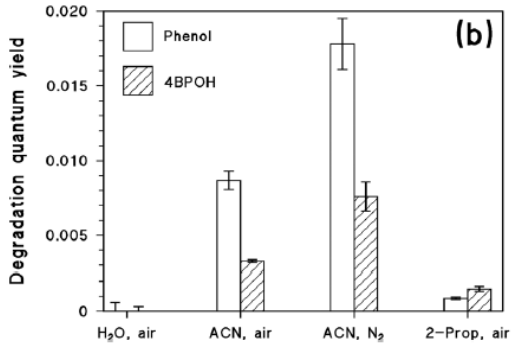

Figure 8b

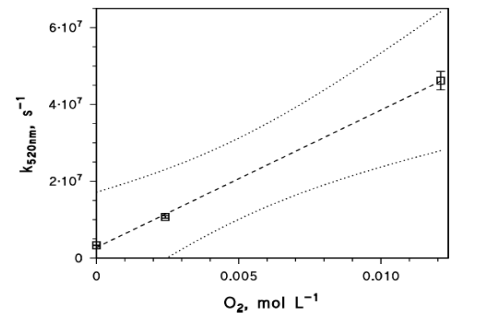

Figure 8c

Figure 8 Degradation rates (a) and degradation quantum yields (b) of phenol and 4BPOH in mixtures (initial concentration 0.1 mM for both compounds), upon UVB irradiation in different solvents (water, acetonitrile and 2-propanol) and different conditions (air or nitrogen atmosphere). The error bars represent ±σ. The rates and quantum yields in water were negligible, and only the related uncertainty (detection limit) is reported. ACN = acetonitrile.
(c) Trend of the first-order decay constant of the absorbance at 520 nm, as a function of the concentration of dissolved oxygen in acetonitrile. 4BPOH 0.1 mM, laser excitation at 355 nm, 94 mJ/pulse.

The faster degradation of phenol in the absence of oxygen (acetonitrile as the solvent, as shown in Figure 8a and 8b), due to the reaction with ^{3}4BPOH*, is accounted for by the quenching of ^{3}4BPOH* by oxygen to yield $^1O_2$. Coherently, Figure 8c suggests that the decay constant of ^{3}4BPOH* in acetonitrile becomes almost double when passing from a deoxygenated to an aerated system. This is fully consistent with the observed degradation kinetics of phenol (which was about twice faster under a nitrogen atmosphere compared to air, see Figure 8), because if ^{3}4BPOH* is deactivated more slowly in N_2 there is more of it available for phenol degradation.
In the aerated system, 0.1 mM phenol would scavenge approximately 0.06% of ^{3}4BPOH*, a percentage that would become approximately double in the absence of oxygen. However, in an aerated solution there would be formation of $^1O_2$ that could also contribute to phenol degradation. The first-order decay constant of $^1O_2$ in acetonitrile is about 2.5×10^4 s^{-1},[103] while the second-order reaction rate constant between phenol and $^1O_2$ seems to be strongly solvent-dependent. Indeed, while phenol-$^1O_2$ rate constants of 10^6–10^7 M^{-1} s^{-1} are reported for water,[104] in organic solvents one has rate constant values of about 10^4 M^{-1} s^{-1}. [105]
The difference could at least in part be explained by the higher reactivity of the phenolate anion toward $^1O_2$, coherently with the fact that the rate constant in water increases with increasing pH.[102] If the reaction rate constants between phenol and $^1O_2$ in acetonitrile were in the range of 10^4 M^{-1} s^{-1}, only ~0.004% of

$^1O_2$ would react with 0.1 mM phenol and the reaction with singlet oxygen would play a secondary role in phenol degradation (~7% of the total). Triplet 4BPOH would thus induce more effective degradation of phenol under a N_2 atmosphere, where triplet quenching by O_2 would not be operational.

Focusing now on the degradation of 4BPOH in different solvents, one observes first of all the absence of transformation in water, which can be explained as per the above discussion. The 4BPOH degradation in acetonitrile was faster in the absence of oxygen, which quenches ^{3}4BPOH* to give back the ground-state molecule in a null cycle of excitation–deactivation:

$$^3\text{4BPOH}^* + O_2 \rightarrow \text{4BPOH} + {}^1O_2 \qquad (19)$$

The degradation rate of 4BPOH was higher in 2-propanol than in acetonitrile (Figure 8a). One should consider that $P_a^{4BPOH,2-propanol} > P_a^{4BPOH,CH_3CN}$ (by a factor of ~4.5) and, as far as the transformation quantum yields are concerned, it was $\Phi_{4BPOH}^{CH_3CN} > \Phi_{4BPOHa}^{2-propanol}$ (Figure 8b). Therefore, while the observed difference in the 4BPOH degradation rates can be accounted for by the higher radiation absorption of 4BPOH in 2-propanol, the lower quantum yield in the alcoholic solvent is consistent with the quenching of ^{3}4BPOH* by an acid–base and possibly also a redox process.

Finally, the formation of $^1O_2$ by irradiated 4BPOH (0.1 mM initial concentration) was assessed in water, acetonitrile and 2-propanol by addition of 0.1 mM FFA. The initial rate of FFA transformation (R_{FFA}) was negligible in water, and it was R_{FFA} =(8.66 ± 0.68) × 10^{-10} M s^{-1} in acetonitrile and R_{FFA} = (1.11 ±0.14) × 10^{-10} M s^{-1} in 2-propanol. Because ^{3}4BPOH* shows negligible reactivity with FFA, as suggested by LFP experiments, the observed degradation of FFA would be accounted for by the production of $^1O_2$ in the irradiated systems. Coherently with the above findings, for which the quenching kinetics of ^{3}4BPOH* follows the order H_2O > 2-propanol > acetonitrile, the photoinduced $^1O_2$ production followed the reverse order acetonitrile > 2-propanol > H_2O.

Considerations concerning the behavior of 4BPOH in different solvents

The singlet and triplet excited states of 4BPOH undergo deprotonation in the presence of water to produce ground-state $4BPO^-$, which quickly adds H^+ to yield back the ground-state 4BPOH. This process quenches the fluorescence and the photosensitizing activity of 4BPOH in aqueous solution. In aprotic acetonitrile, 4BPOH shows significant fluorescence emission with a fluorescence band (Ex/Em ~ 325/475 nm) that overlaps with peak C of humic substances. In this solvent, ^{3}4BPOH* mainly reacts with O_2 to produce $^1O_2$; if phenol occurs in solution, ^{3}4BPOH* is also involved in phenol degradation with a second-order reaction rate constant $k_{^3\text{4BPOH*,phenol}} = (6.6 \pm 0.3) \times 10^7\ M^{-1}\ s^{-1}$. This reaction yields the phenoxy radical, and presumably also the ketyl radical of 4BPOH. With 2-propanol as solvent, which shows some protic properties and can be oxidized, light-excited 4BPOH undergoes partial deprotonation to $4BPO^-$ (but to a considerably lesser extent than in water), and relatively slow reprotonation. There is also some evidence that ^{3}4BPOH* could abstract an H atom from 2-propanol in mixtures of this alcohol with acetonitrile. At the same time, in pure 2-propanol one does not observe ^{3}4BPOH* signals at least because of the fast deprotonation of the 4BPOH triplet state; therefore, this work is silent about the ability of ^{3}4BPOH* to oxidize 2-propanol when the latter acts as the pure solvent. The partial ^{3}4BPOH* quenching in 2-propanol, whatever the actual pathway(s), decreases the photosensitizing ability of 4BPOH compared to acetonitrile as solvent. However, in the solvent 2-propanol the photosensitizer 4BPOH maintains a significant ability to both produce $^1O_2$ and degrade phenol (the latter because of the involvement of ^{3}4BPOH*, while a significant contribution of photogenerated $^1O_2$ to phenol degradation can be excluded). Considering that benzophenones (possibly including 4BPOH) are important constituents of CDOM and particularly of humic substances, the present findings may be significant to better understand the photoactivity of the hydrophobic and hydrophilic humic moieties. Indeed, a compound such as 4BPOH would not be fluorescent and would not produce $^1O_2$ in the presence of water, but it would do so in its absence. Therefore, 4BPOH might contribute to the occurrence of elevated $^1O_2$ levels in the hydrophobic cores of humic materials.

Computational study of 4-hydroxybenzophenone optical properties

As mentioned before, the excited states often show a multi-configurational nature and they are described by several electronic configurations, each corresponding to different excitations from occupied to virtual orbitals. This section reports a description of the electronic structure of the excited states of 4BPOH, based on the analysis of the change of the electronic density when going from the ground to the excited states, by use of TD-DFT methods. Indeed, with this approach it is possible to predict the fluorescence properties of 4BPOH and compare them with the experimental data obtained as described in the previous section.

Computational method

The computational study was performed within the Density Functional Theory (hereafter DFT)[106-107] with the Pople basis set 6-31+G(d).[108-109] Solvent effects (acetonitrile, 2-propanol and water) to the electronic energies were introduced in all calculations (ground and excited state optimizations and single point calculations) by the Polarized Continuum Method (PCM)[110-111] within the universal Solvation Model Density.[112-113] The absorption spectra were obtained with the following procedure: we first optimized the geometries of the ground states, then we calculated the excitation energies with the Time-Dependent DFT (TD-DFT).[114-115] This method provides a reasonable accuracy at reasonable computational costs (time and computing resources).[116-117] On the basis of the literature, and after a few tests on the prediction of the absorption of 4BPOH in acetonitrile (see the Appendix), we decided to use the functional PBE0.[118-119] The excitation energies calculated in this way correspond to the maxima in the absorption spectra, because this approach does not include vibrational contributions or dynamic solvent effects. The simulated absorption spectra of 4BPOH in the three solvents, for direct comparison with the experimental findings, were then obtained through linear combination of gaussian functions centered on the calculated electronic transition frequencies, with relative height defined on the basis of the oscillator strength obtained by calculations. The geometry of 4BPOH was re-optimized in its excited states (singlet and triplet), and the difference between the energies of these states and those calculated for the ground state at the excited-state geometries was taken as emission (fluorescence) energy. For the proton transfer equilibria, the energies were refined through single-point calculations with the 6-311+G(d,p) basis set,[120] and combined with the 6-31+G(d) thermal corrections to the free energy. Calculations were performed using the quantum package Gaussian 09-A.[121]

Absorption and Emission spectra

The absorption spectra of 4BPOH in the three solvents (Figure 9a) were obtained based on the electronic transitions from the ground state (S_0), calculated at the TD-DFT level. The agreement with the experimental data (Figure 9b) is remarkably good. The three main signals observed in acetonitrile (ACN) are well reproduced: the peak found at 283 nm (the literature reports 284 nm)[80] is calculated at 288 nm and corresponds to a $S_0 \rightarrow S_2$ transition (oscillator strength f= 0.405, see the Appendix); the bump found at 249 nm (reported at 250 nm in the literature)[80] is calculated at 252 nm ($S_0 \rightarrow S_5$, f= 0.151); the bump found at 221 nm (222 nm in the literature)[80] is a combination of transitions calculated at 230 ($S_0 \rightarrow S_6$, f= 0.0891) and 220 nm ($S_0 \rightarrow S_7$, f= 0.0684). The strong absorption below 210 nm, well reproduced by the calculations, is a combination of several transitions calculated at 194 and 193 nm (with participation of other less intense transitions, see the Table in the Appendix). A weak absorption (f= 0.005) corresponding to the $S_0 \rightarrow S_1$ transition is also calculated at 327 nm, but the strong band at 283 nm partially hides it. Clear traces of this transition can be found in the tail of the stronger band in the experimental spectrum, so it is possible that the calculation underestimates its oscillator strength.

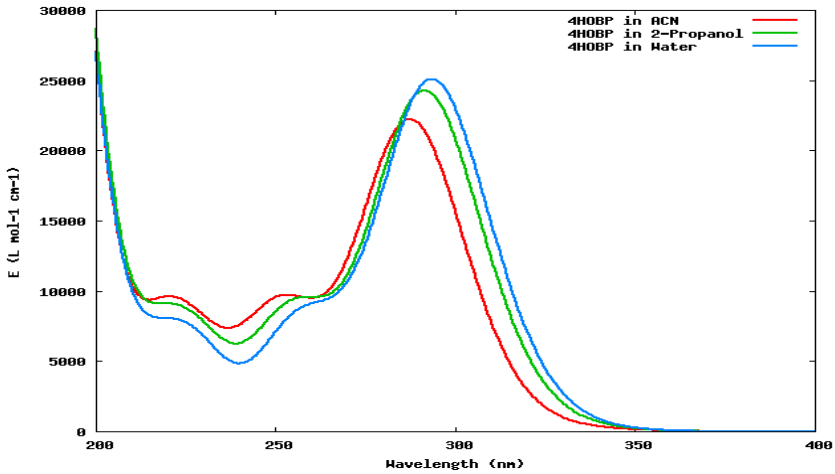

Figure 9a

Figure 9 Calculated (a) and experimental (b) absorption spectra of 4BPOH in acetonitrile (ACN, red line), 2-propanol (green line) and water at pH=1.0 by $HClO_4$ (blue line).

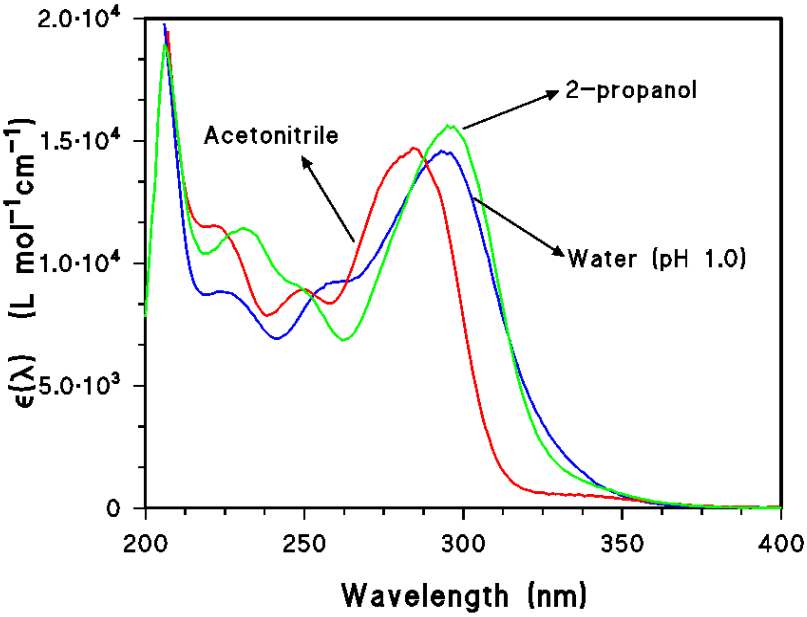

Figure 9b

The bathochromic effect on the lower energy transition, due to protic solvents (2-propanol and water) as shown in the previous section, is also reproduced,.[81] The maxima found at 294 (2-propanol) and 296 nm (water) are calculated with an error of 2 nm, respectively, at 292 and 294 nm (both are $S_0 \rightarrow S_2$ transitions). The bumps found at 249 nm (2-propanol) and 260 nm (water) are calculated at 255 and 257 nm (both $S_0 \rightarrow S_5$ transitions), while those found at 230 nm (2-propanol) and 226 nm (water) are combinations of transitions calculated, respectively, at 230 and 210 nm and at 229 and 218 nm. Similarly to the case of ACN, the $S_0 \rightarrow S_1$ transitions (321 nm in 2-propanol and 317 nm in water) are predicted to be very weak (f=0.008 and 0.011). Indeed, the solvent effect does not seem to be very remarkable (~0.1 eV), but this is possibly due to the fact that the studied solvents are all already quite polar. Larger effects have been observed by comparing pure apolar cyclohexane with alcohol-cyclohexane mixtures.[97]

The optimization in ACN of the structures of the excited states allowed for the calculation of the electronic transitions from these states to the ground state S_0. These transitions should correspond to the emission spectra, and they are calculated as follows: 521 nm from the first triplet state, $T_1 \rightarrow S_0$, 504 nm from the first singlet excited state, $S_1 \rightarrow S_0$, and 337 nm from the second singlet excited state, $S_2 \rightarrow S_0$. For the triplet state T_1 the absorption spectrum was also calculated (see the Table in the appendix), finding two intense transitions at 319 and 498 nm. These calculated transitions are in quite good agreement with the absorption maxima at 330 and 520 nm registered in the laser flash photolysis (LFP) experiments reported in the previous section.

Figure 10 a shows a semi-quantitative picture of the potential energy curves of the S_1, S_2 and T_1 excited states and of the ground state S_0 of 4BPOH. The vertical dashed lines in this figure represent the radiative transitions. Arrows pointing upward are absorptions leading to the excited states and starting from the minimum of the energy curve of S_0. Arrows pointing downwards, starting from the minima of the excited states and reaching the S_0 potential curve, represent the emission transitions. R is an arbitrary parameter representing the geometrical distortion from the equilibrium geometry of the ground state. Although approximate, this picture is related to the actual changes of the optimized structures of the excited states with respect to the starting geometry, which corresponds to the ground state.

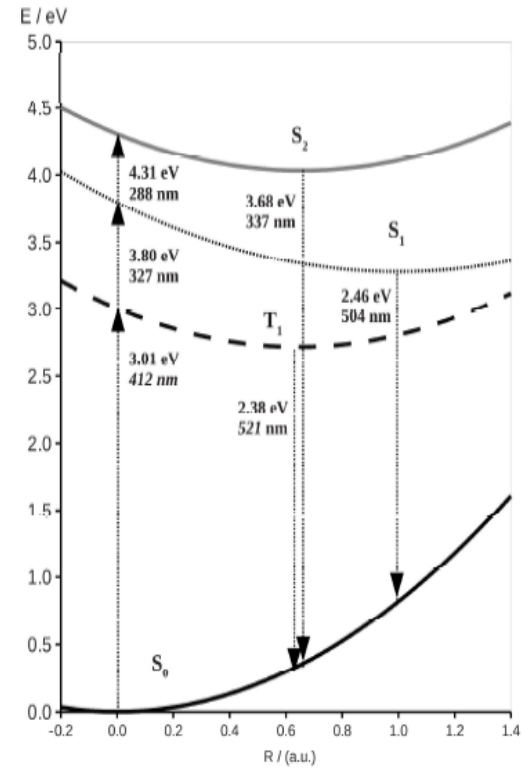

Figure 10a

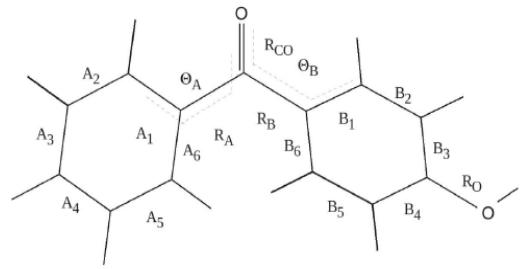

Figure 10b

Figure 10a Potential energy curves (in eV) of the states S_0, S_1, S_2 and T_1, as a function of the arbitrary parameter R (a.u. = arbitrary units), representing the geometrical distortion from the equilibrium geometry of the ground state. Values reported in both eV and nm refer to radiative transitions

Figure 10b Structural parameters of 4BPOH used for the comparison: Θ_A and Θ_B are the dihedral angles between the aromatic rings.

Figure 10b reports the most important geometrical parameters of S_0, S_1, S_2 and T_1; the standard deviations of the geometries of the excited states with respect to S_0 are reported in the Appendix. These values are 0.068 a.u. (atomic units) for T_1 (R is 0.642), 0.083 a.u. for S_2 (R is 0.655), and 0.297 a.u. for S_1 (R is 1). These data confirm that R and the standard deviations are of the same order of magnitude (although not linearly correlated). A precise correlation among the

standard deviations and the parameter R is impossible because the potential energy surfaces are intrinsically multidimensional. However, we can observe that the largest contributions to the structural changes are given by the dihedral angles between the phenyl rings (Θ_A and Θ_B in Figure 10b). In particular, Θ_B changes from -24 in S_0 to -87 in S_1.
The emission spectrum of 4BPOH in ACN shows two main peaks, centered at excitation/emission wavelengths (Ex/Em) of 230/330 nm and 360/480 nm, plus a less intense peak at 280/330 nm. The 230/330 nm peak was much more intense than the 360/480 nm one in dilute 4BPOH solutions (Figure 11a), but the pattern changed and was eventually reversed with varying 4BPOH concentration (Figure 11b). A detailed concentration trend of the peak intensities is reported in Figure 11c.

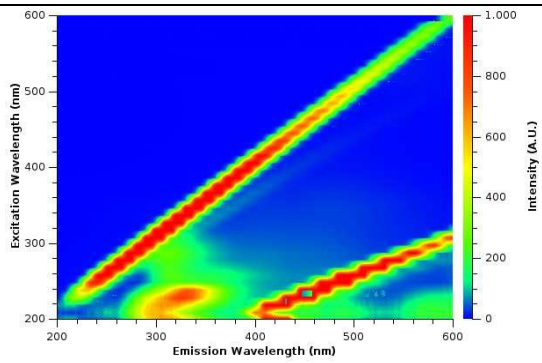

Figure 11a

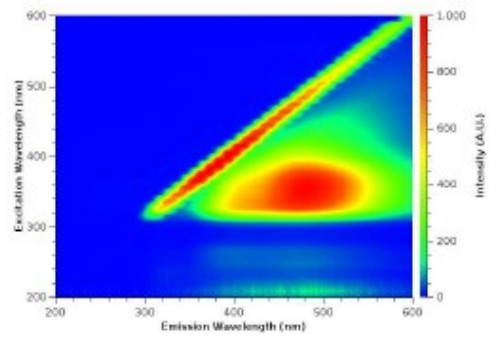

Figure 11b

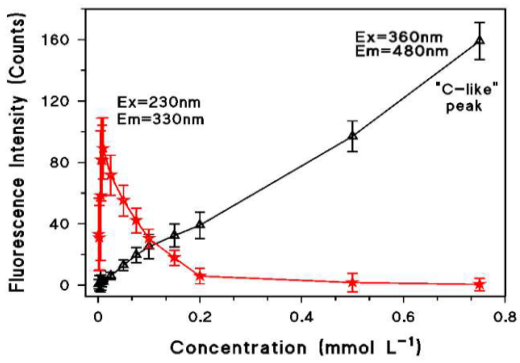

Figure 11c

Figure 11. EEM spectra of 4BPOH in ACN (excitation slit width 10 nm, emission slit width 20 nm) at 4BPOH concentration values of 0.01 mM (a) and 0.5 mM (b).
(c) Fluorescence Intensity vs. Concentration of 4BPOH in ACN solutions, referred to different fluorescence peaks: the black series is the so-called "Humic-Like C peak". In this case, slits were set at 5 nm in excitation and 10 nm in emission. Error bars represent the standard errors of replicate experiments.

The intensity of the 230/330 nm peak (Figure 11c) was deeply influenced by the solution absorbance at 230 nm (see Figure 9b). The spectrofluorimeter does in fact detect the fluorescence emission from a region located in the center of the cuvette, which is reached by the incident (excitation) radiation after it has traveled for ~0.5 cm inside the solution. Over this path length, a 0.01 mM 4BPOH solution has an absorbance of ~0.05 that means that the cuvette center receives ~90% of the incident radiation. In contrast, a 0.1 mM solution has an absorbance

of ~0.5 and the cuvette center receives only ~30% of the incident radiation. After emission, the radiation has to travel for another ~0.5 cm inside the solution, but the solution absorbance at 330 nm is much lower than at 230 nm (Figure 9b) and the inner-filter effect is thus less important on emission than on excitation. The inner-filter effect can explain the maximum in the 230/330 nm fluorescence intensity as a function of 4BPOH concentration, as per Figure 11c. Comparison with TD-DFT computations suggests that the emission found at 330 nm could be assigned to the $S_2 \rightarrow S_0$ transition calculated at 337 nm. To support this hypothesis we must note that, at the variance with state S_1, state S_2 shows a higher oscillator strength (0.472, compared to 0.001) and its geometry is closer to that of the ground state (see Figure 10a and the text above), determining a larger Franck-Condon factor. All these factors should increase the probability of decay from state S_2 through a radiative transition. This is an interesting finding and suggests that 4BPOH does not follow Kasha's rule,[122] according to which the fluorescence emission usually takes place from the lowest excited state (S_1). Although quite uncommon, emissions from excited states upper than S_1 and violating the Kasha's rule have already been observed.[123] The molecule closer to our system is o-hydroxybenzaldehyde, which is reported to show fluorescence emission from the S_2 state.[124]

According to the calculation results reported in Figure 10a, the state S_2 should be reached upon absorption of radiation at 288 nm. However, the described fluorescence peak was centered at an excitation wavelength of 230 nm. Actually, the EEM spectrum of 4BPOH shows a small peak at Ex/Em ~ 280/330 nm (Figure 11a), which is consistent with a $S_0 \rightarrow S_2$ transition in excitation and with a $S_2 \rightarrow S_0$ transition in emission. In contrast, the main peak (Ex/Em = 230/330 nm) is consistent with an excitation to the S_6 state (but also, as an alternative possibility, to a vibrationally excited state of S_2), followed by radiationless decay through internal conversion (or vibrational relaxation) to S_2 and radiative emission from S_2 itself. Differently from the 230/330 nm peak already discussed, the 360/480 nm "C-like" peak (Figure 11b) is observed in an excitation and emission wavelength interval where the radiation absorption by 4BPOH is limited (Figure 9b). For this reason, the peak intensity shows a practically linear increase when increasing the concentration of 4HOBP (Figure 11c).

By mere comparison with TD-DFT data, the 360/480 nm peak could be compatible with a $T_1 \rightarrow S_0$ or a $S_1 \rightarrow S_0$ transition. These transitions are calculated at, respectively, 521 and 504 nm. Although it is unusual to detect a radiative $T_1 \rightarrow S_0$ transition (phosphorescence emission) at room temperature in solution, the emission wavelength interval compares well with the vibrationally resolved spectra registered in ethanol glass at 77 K, which show peaks at 433, 450, 475, and 518 nm.[90] To better understand the nature of the 360/480 nm peak, its intensity was measured in air, in pure oxygen and in oxygen-free atmosphere at different concentration values of 4BPOH in ACN. The rationale is that the T_1 state of 4BPOH undergoes reaction with O_2, which is in competition with the emission of radiation. The more important is the reaction with O_2, the

faster is the deactivation of T_1 and the higher inhibition is expected for a $T_1 \rightarrow \cdot S_0$ radiative process. Indeed, the T_1 lifetime was about halved when passing from an O_2-free atmosphere to air, and it was decreased by an order of magnitude when passing from O_2-free to pure O_2 (see Figure 8c).[81] As a consequence, under the hypothesis that the 360/480 nm signal is due to a $T_1 \rightarrow \cdot S_0$ transition (phosphorescence process), one would expect the signal intensity to decrease by about one order of magnitude when passing from an O_2 - free to a pure O_2 atmosphere. The same effect would not necessarily occur if the 360/480 nm signal is due to a $S_1 \rightarrow \cdot S_0$ transition, also considering the very short lifetime of the excited singlet states of 4BPOH.[81] The oxygen effect on the 360/480 nm emission intensity is reported in Figure 12, which shows that the differences between O_2-free, aerated and pure-O_2 systems were within the experimental uncertainty.

Therefore, the unimportant effect of oxygen rules out the $T_1 \rightarrow S_0$ transition as the cause of the observed signal, and the 360/480 nm peak is thus rather assigned to a $S_1 \rightarrow S_0$ transition calculated at 504 nm, which alone is compatible with both the experimental emission wavelengths and the oxygen effect.

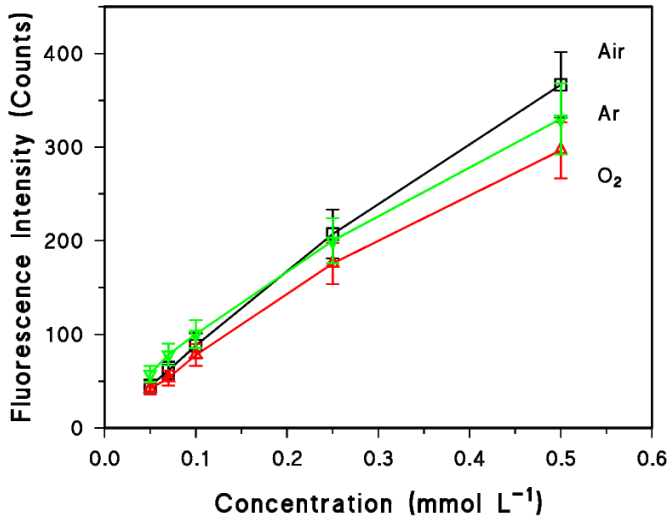

Figure 12

Figure 12. Fluorescence Intensity vs. Concentration of 4BPOH in acetonitrile solutions, in air (black), O_2 atmosphere (red) and argon atmosphere (green). The fluorescence signal was observed at Ex=360 nm / Em= 480 nm, using 10 nm slit widths in both excitation and emission.
Error bars represent the standard errors of replicate experiments

When considering the data shown in Figure 11c, at low 4BPOH concentration in the absence of inner filter effects the 230/330 nm peak was actually much more intense than the peak at 360/480 nm, in qualitative agreement with the calculated oscillator strengths for the $S_2 \rightarrow S_0$ and $S_1 \rightarrow S_0$ transitions (0.472 and 0.001, respectively).

The previous section reported that the state T_1 can be produced upon laser excitation at 355 nm.[3] The results shown here suggest that irradiation in that wavelength region can promote transition to S_1 and hence fluorescence emission (see Figure 11c). The center of the $S_0 \rightarrow S_1$ transition is actually predicted at 327 nm (Figure 10), but the absorption spectrum of 4BPOH is extended at longer wavelengths (Figure 9b). In this scenario, the laser would excite S_0 to S_1, followed by inter system crossing (ISC) to T_1. However, the absorption of radiation by 4BPOH at and above 320 nm is very low and the $S_0 \rightarrow S_1$ transition is thus very weak. A fortiori, the same is true at the laser excitation wavelength (355 nm). Interestingly, close to this value we calculated (see the table in the Appendix) two spin-forbidden absorptions from S_0 at 356 and 377 nm, respectively corresponding to $S_0 \rightarrow T_3$ and $S_0 \rightarrow T_2$ transitions. Being spin-forbidden, these transitions are also expected to be weak. Therefore, it is also possible that in the LFP experiments the state T_1 is generated without involving the S_1 state, perhaps through a $S_0 \rightarrow T_2/T_3$ spin-forbidden absorption, followed by $T_2/T_3 \rightarrow T_1$ spin-allowed internal conversions.
On the basis of our experimental and computational results, we can assess that: both excited states S_1 and T_1 can be reached by light absorption (the latter either from S_1 by ISC, or by internal conversion from T_2/T_3) and can decay to S_0 by non-radiative processes; S_1 can also decay to S_0 radiationally but T_1 does not, at least at room temperature. This scenario is also coherent with previous experimental findings: the lifetimes of T_1 in ACN at room temperature have been studied by using transient UV-Vis spectra (that our calculations quite well reproduce, see Figure 13 and compare it with Figure 4b).
The only phosphorescence experiment reported in the literature (emission from T_1) was performed in very different conditions, i.e. methylcyclohexane or alcohol glasses at 77 K.[90]

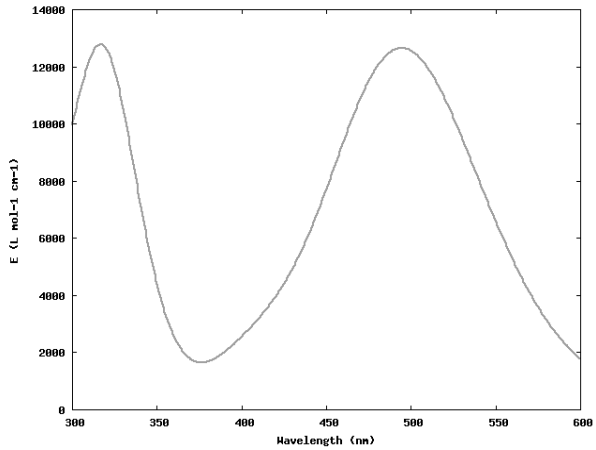

Figure 13

Figure 13. Calculated absorption spectra of 4BPOH triplet state T_1 in acetonitrile.

Electronic structure of the excited states

The nature of the first two singlet excited states S_1 and S_2 and of the first triplet state T_1 of 4BPOH was analyzed in terms of differential electronic density maps (Figure 14). The figure clearly shows that all of the three excited states correspond to charge-transfer from the hydroxyphenyl moiety, involving both the phenyl π and the hydroxyl lone-pair electrons, towards the anti-bonding orbitals located on the phenyl (π^*) and carbonyl group (π_{CO}^*). Some contribution of an excitation from the non-bonding/lone pair n_{CO} is also present. On the basis of these data we can assess that these excited states correspond to mixed n-π^* and π-π^* configurations. Therefore, the classical excited-state distinctions between n-π^* and π-π^* as reported in the past literature are clearly too clear-cut and only provide a very rough approximation of the actual nature of the relevant excited states. Differences can only be found by inspection of the coefficients and of the nature of the configurations, which are reported in the appendix.

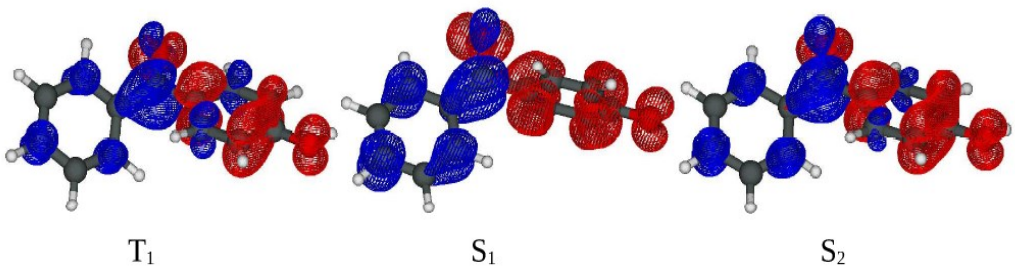

Figure 14

Figure 14. Differential electronic density maps for the states S_1 (left), T_1 (center) and S_2 (right), with respect to S_0. Red areas correspond to a reduction in the electronic density, blue areas correspond to an increase in the electronic density.

The electronic properties of the excited states are also well illustrated by the change in the electrostatic potential V compared to that of the ground state (Figure 15). Figure 15a (V in ACN) clearly shows that in all excited states, and particularly in S_1, the hydroxylphenyl moiety assumes an acid (and electrophilic) character while the benzoyl moiety (and particularly the carbonyl group) becomes more basic (more nucleophilic), as a result of the partial charge-transfer nature of these excited states. It is noticeable that the oxygen atom of the hydroxyl group, which shows a small basic character in S_0 (the small blue area opposite to the hydrogen and corresponding to the lone pair areas), becomes essentially neutral in S_1 (the blue area becomes white) or less basic in T_1 (the blue area becomes smaller). The changes in the chemical and electrostatic properties of the excited states are even more evident in water (Figure 15b). All the excited states show

more acidic hydroxyphenyl moieties, with a loss of the basic character of the hydroxyl oxygen atoms. Excited states in 2-propanol show similar behavior (see the Appendix). These electronic properties are expected to have consequences on the acid properties of the excited states.

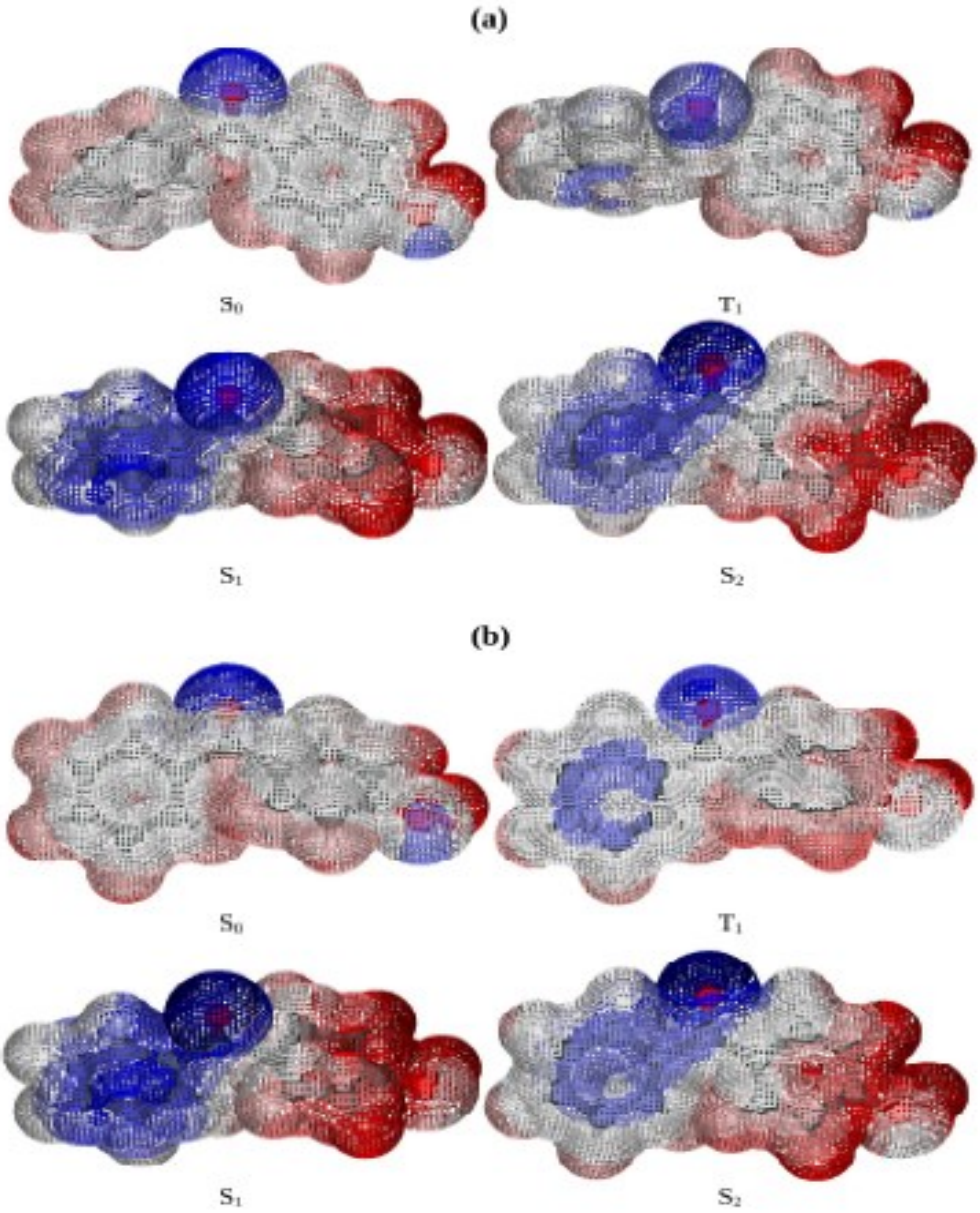

Figure 15

Figure 15 Electronic potential V on the Van der Waals surfaces of the S_0, T_1, S_1, and S_2 states in acetonitrile (a) and water (b). Red areas correspond to positive V values (acid/electrophilic character), blue areas correspond to negative V values (basic/nucleophilic character)..

Acid properties

The exact calculation of the pKa of an acid is quite a though challenge. Here we suggest a reasonable model that allowed us to calculate the pKa of the ground state of 4BPOH in water, in good agreement with the experimental findings. Our pKa value, 8.3, well compares with the values of 8.5 or 7.9 reported in the literature [82-90] A value of 8.21 can be estimated with the Hammett equation.[125] Our model consists in the use of the water complex of undissociated 4BPOH and of the anionic $4BPO^-$, together with a water molecule and an ossonium cation:

$$[4BPOH\ (H_2O)_3] + (H_2O)_4 \rightarrow [4BPO\ (H_2O)_3]^- + [H_3O\ (H_2O)_3]^+ \quad (20)$$

Figures of all complexes are reported in the Appendix. The same protocol was used to calculate the deprotonation equilibria for the S_1 and T_1 states. Using 2-propanol molecules, we calculated also the deprotonation equilibria of S_0, S_1 and T_1 in this alcoholic solvent. The results are collected in the following Table 2.

	Water	2-propanol
S_0	$9.0\ 10^{-11}$ (8.3)	$9.6\ 10^{-15}$ (12)
S_1	$1.5\ 10^{-1}$ (-0.9)	$2.4\ 10^{-1}$ (0.6)
T_1	$4.9\ 10^{-2}$ (-0.4)	$1.5\ 10^{-2}$ (1.8)

Table 2

Table 2 Equilibrium constants and pK_a values (in parenthesis) for the proton transfer from 4BPOH to the solvents 2-propanol and water.

Coherently with the previously-reported anticipations on the electronic structures of the excited states (Figure 15 and related discussion), both S_1 and T_1 show a strong increase of the acidity compared to the ground state: the first singlet state in water is one billion times more acidic than the ground state, and the effect is even larger in 2-propanol where S_1 is one hundred billion times more acidic than S_0. The triplet states show almost the same strong increase of the acidity. The calculation results are in reasonable agreement with the experimental findings reported for water, according to which both 4BPOH-S_1 and 4BPOH-T_1 have pKa < 0.8. In contrast, despite the strong effect of the electronic excitation, the excited states of 4BPOH in 2-propanol still behave as weak acids. Deprotonation of the 4BPOH-S_1 and 4BPOH-T_1 states in the alcoholic solvent does not seem to be competitive with the other decay processes, as testified by the similarity between the EEM spectra registered in 2-propanol and in acetonitrile where the deprotonation is not possible, being the latter solvent not basic. Note, however, that the observed quenching of 4BPOH luminescence and photosensitizing activity in 2-propanol compared to acetonitrile could also be due to a redox reaction between 4BPOH-T_1 and the alcoholic solvent.

The acidity of 4BPOH-S_1 compared to 4BPOH-S_0 has important implications for the fluorescence of 4BPOH in water. Indeed, in a wide range of pH conditions the ground state would be undissociated but the S_1 state, produced after radiation absorption, would quickly undergo deprotonation. The absorption spectra of 4BPOH at pH 1 (occurrence of the undissociated form), in ~neutral pH conditions (mixture of 4BPOH and $4BPO^-$, with a prevalence of the former) and at pH 10 ($4BPO^-$) are reported in Figure 16a. The occurrence of the anion $4BPO^-$ at pH 10 and its absorption spectrum agree well with the computational results: the calculated absorption spectrum (Figure 16b, blue line) shows two peaks at 346 and 257 nm that correspond to the experimental maxima found at 348 and 250 nm.

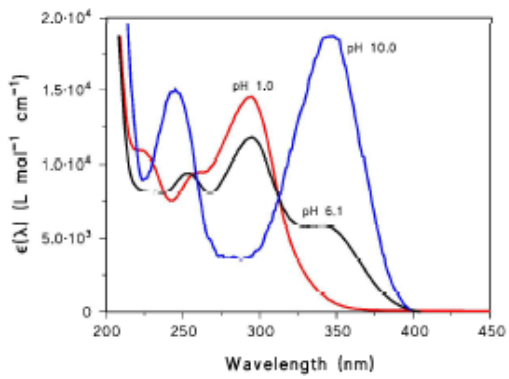

Figure 16a

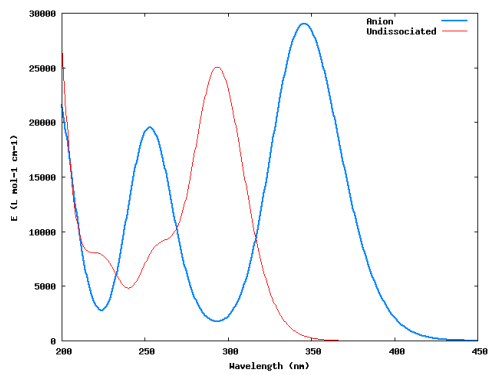

Figure 16b

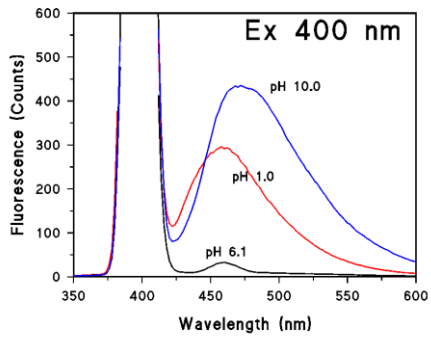

Figure 16c

Figure 16. (a) Absorption spectra of 0.1 mM 4BPOH in water, at different pH values: pH 1.0 (adjusted with $HClO_4$, red line), pH 10.0 (adjusted with NaOH, blue line) and natural pH (not adjusted, pH 6.1, black line).
(b) Calculated absorption spectra in water of the anion $4BPO^-$ (blue line) and of undissociated 4BPOH (red line).
(c) Fluorescence emission spectra of 0.1 mM 4BPOH in aqueous solution, excited at 400 nm at different pH values: pH 1.0 (adjusted with $HClO_4$, red line), pH 10.0 (adjusted with NaOH, blue line) and natural pH (6.1, not adjusted, black line).

Figure 16c reports the fluorescence spectra obtained upon 400-nm excitation of 4BPOH solutions at pH 1.0, 6.1 and 10.0. These spectra correspond to the "C-like" peak of 4BPOH, which is related to the $S_1 \rightarrow S_0$ transition. The high emission

peak at 400 nm is the Rayleigh signal of water, while the limited absorption of the solutions at and above 400 nm excludes significant inner-filter effects on either excitation or emission. The absence of the inner-filter effect was the main rationale for the choice of 400 nm as the excitation wavelength in these experiments. The fluorescence emission intensity was considerably higher under basic and acidic pH conditions than at ~neutral pH. Moreover, the 460-nm emission signal observed in ~neutral conditions was largely due to the Raman emission of water: the actual fluorescence emission is the very small signal that can for instance be appreciated with some difficulty around 500 nm. At pH 1, undissociated 4BPOH absorbs radiation and the fluorescence emission from 4BPOH-S_1 is in competition with the deprotonation of the excited state. However, the low pH value ensures that a significant fluorescence emission is still observed. This emission occurs at a different wavelength than the emission at pH 10 (vide infra), which suggests that 4BPOH-S_1 is involved rather than $4BPO^-$-S_1. At pH 10 the dissociated form $4BPO^-$ already occurs as the ground state, and no excited-state deprotonation will take place. In these conditions, $4BPO^-$ shows an intense fluorescence emission that likely involves the transition from $4BPO^-$-S_1 down to $4BPO^-$-S_0 (and that is different from 4BPOH-S_1 $\rightarrow$ 4BPOH-S_0 as far as the emission wavelength is concerned, as already highlighted).
The optimization in water of the structure of $4BPO^-$-S_1 allowed for the calculation of the electronic transitions from this state to the ground state $4BPO^-$-S_0. The relevant transitions correspond to the emission maximum of $4BPO^-$-S_1 that is calculated at 689 nm. The agreement is only very qualitative, although the emission from $4BPO^-$-S_1 $\rightarrow$ $4BPO^-$-S_0 is calculated at a longer wavelength (689 nm) compared to 4BPOH-S_1 $\rightarrow$ 4BPOH-S_0 (504 nm), as experimentally observed. However, the calculated $\Delta\lambda$ ~ 180 nm is much larger than the experimental $\Delta\lambda$ ~ 20 nm. The large deviation of the calculated emission wavelength from the experimental datum is possibly due to the large change in the structure of $4BPO^-$-S_1 compared to $4BPO^-$-S_0 (see the Appendix). Similarly to the case of 4BPOH-S_1, the largest variations concern the phenyl dihedral angles Θ_A and Θ_B.

Outcomes of the 4BPOH computational study

The fluorescence spectrum of 4BPOH shows signals at two different emission wavelengths, which is not typical and is accounted for by the fact that 4BPOH does not follow Kasha's rule. Actually, both the S1 and S2 excited singlet states account for the observed fluorescence emission, with S2 giving the most intense signal. The EEM spectrum shows three fluorescence peaks, and two of them are centered at emission wavelengths ~330 nm that correspond to a S2 $\rightarrow$ S0 transition. The former and most intense peak has Ex/Em ~230/330 nm, with the excitation wavelength corresponding to a transition from S0 to S6 or to a highly excited vibrational state of S2. The second peak has Ex/Em ~280/330 nm, and it corresponds to a S0 $\rightarrow$ S2 transition in excitation (as well as S2 $\rightarrow$ S0 in emission). The third fluorescence peak has Ex/Em ~360/480 nm, corresponding

to S0 → S1 in excitation and to S1 → S0 in emission. The latter peak is interesting, because is falls in the region of the "peak C" of humic substances. The interest of this finding can only be increased by the fact that aromatic carbonyls in general, and benzophenones in particular, are well-known components of humic matter.

The fluorescence of 4BPOH is observed in aprotic or poorly protic solvents, and also in aqueous solution but only at acidic or basic pH. The reason is that 4BPOH-S0 is a relatively weak acid (pKa ~8), while the corresponding excited states (and 4BPOH-S1 in particular) are strong acids with pKa < 0. Therefore, if in ~neutral aqueous solution the undissociated 4BPOH-S0 is excited to 4BPOH-S1, the latter undergoes quick deprotonation and deactivation to 4BPO−-S0 (followed by protonation back to 4BPOH-S0), without fluorescence emission. At acidic pH (e.g., pH 1) 4BPOH-S1 is still able to emit fluorescence photons because of understandably slower deprotonation, while in basic solution one has the occurrence of 4BPO−-S0 that, when excited to 4BPO−-S1, gives rise to a fluorescence emission at longer wavelengths compared to 4BPOH-S1. Within humic substances at reasonable pH values, a compound such as 4BPOH can be fluorescent if it is included in a hydrophobic environment out of contact with the water molecules. Considering that humic compounds are complex aggregates of molecules with different polarity, arranged in a pseudo-micellar fashion with hydrophilic surfaces and hydrophobic cores, poorly water-soluble molecules such as 4BPOH are likely to be found in the waterless inner compartment.

Phenol oligomers

As mentioned before there is a lack of knowledge about the structure of both the CDOM chromophores and its fluorophores. Despite the important knowledge gaps, routine analyses on natural water samples have been carried out in the fields of both limnology[126] and oceanography.[127]
This chapter reports the results of an investigation into a family of compounds that could derive from the degradation of lignin via biological transformation[128] or abiotic reactions.[129] In last years, HULIS (HUmic-Like Substances) have also been studied for their role in the atmospheric environment because the fluorescence properties of atmospheric aerosols have a certain resemblance with those of terrestrial and aquatic humic and fulvic acids.[130]
HULIS can reach the atmosphere as a consequence of primary (biomass burning, release of organic compounds from water and soil) and secondary processes (atmospheric reactions).[131]-[132] Several potential reactions that could generate HULIS have been studied in the laboratory. Among these, photochemical processes involving phenolic compounds in the presence of triplet sensitizers produce species with many humic-like properties (functional groups, absorption and fluorescence spectra, hygroscopic properties) that thus resemble atmospheric HULIS [133]. Interestingly, the same processes induce oligomerization of phenol through formation of the corresponding phenoxy radicals.[133] However, pristine phenols and HULIS emit fluorescence in clearly separated wavelength intervals,[134] and the photochemical and photosensitized transformation of phenolic compounds produces a gradual shift of the fluorescence emission range towards the HULIS region.[135]

To test the hypothesis that the humic-like fluorescence of HULIS is accounted for by phenol oligomers (trimers, tetramers and so on), one has to face the difficulty that these compounds are hardly available as commercial standards. To by-pass this problem, the present work carries out a comparison between the available experimental data (fluorescence emission of phenol and of 4-phenoxyphenol, hereafter 4PP, the smallest phenol oligomer) and a quantum mechanical assessment of the same properties. Subsequently, the computational techniques thus optimized and validated were used to predict the fluorescence behavior of larger compounds for which standards are not available, thereby carrying a comparison with the known HULIS emission. This study is useful in that it contributes at elucidating the nature of the fluorescence properties of both atmospheric HULIS and surface-water humic substances.

Optical Measurements

The absorption spectra of phenol and 4PP were measured with a Varian Cary 100 Scan UV–vis double-beam spectrophotometer, using quartz cuvettes (1.000 cm optical path length). The excitation-emission matrix (EEM) fluorescence spectra were taken with a VARIAN Cary Eclipse Fluorescence Spectrophotometer, with an excitation range from 200 to 400 nm at 10 nm steps, and an emission range from 200 to 600 nm with a scan rate of 1200 nm min^{-1}. Excitation and emission slits were set at 5 nm for 0.1 mM phenol, and at 20 nm for 0.1 mM 4PP. Spectra were taken in a fluorescence quartz cuvette (Hellma) with 1.000 cm optical path length on both relevant directions. The Raman signal of water was taken as a reference for lamp intensity and signal stability within different measurements.

Computational Simulations

Similarly to the case of 4BPOH, the computational study was performed within the Density Functional Theory (DFT) with the following procedure: we first optimized the geometries of the ground states, then we calculated the excitation energies with the Time-Dependent DFT (TD-DFT) [106-107]
. As in the case of 4BPOH the excitation energies calculated in this way correspond to the maxima in the absorption spectra, because this approach does not include vibrational contributions or dynamic solvent effects. Actually, our intent is not to fully reproduce the experimental absorption spectra, but only to identify the most important transitions and reproduce the fluorescence spectra. When more conformations are possible for a certain molecule, each set of transitions is reported and it is scaled by the weight of the corresponding conformation (see details in the Appendix). After excitation each molecule was re-optimized in its first excited singlet state, and the difference between the excited-state energy and that calculated for the ground state at the excited-state geometry was taken as emission (fluorescence) energy. Solvent effects (water) to the electronic energies were introduced in both geometry optimization and TD-DFT calculations by the Polarized Continuum Method (PCM) [110-111] within the universal Solvation Model Density [112-113]. A preliminary screening of DFT functionals was carried out, and 17 different functionals were tested in order to choose the best functional and basis set; "best" in this case means that it affords the nearest reproduction of the experimental fluorescence signal observed with phenol and 4PP. The mPWLYP functional (modified Perdew– Wang exchange functional)[136] and Lee–Yang–Parr correlation [137-138] with the Pople basis set 6-31 + G(d) [139-140] were chosen, because this set gives a suitable approximation of the experimental values and requests reasonable calculation time. Calculations were performed by using the quantum package Gaussian 09-A [121]

Comparison between Experimental Data and Theoretical Simulations

The absorption and fluorescence properties were calculated for a series of poly-para-phenoxyphenols, as shown in the next scheme. The relevant compounds are phenol, 4-phenoxyphenol (4PP), 4-(4-phenoxy)phenoxyphenol (4PPP) and 4-(4-(4-phenoxy)phenoxy)phenoxyphenol (4PPPP).

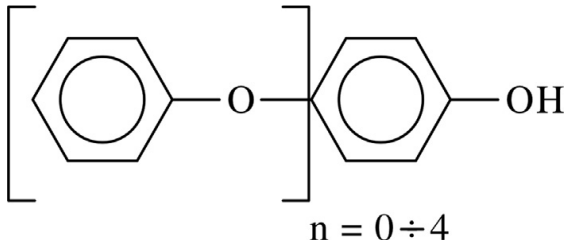

Scheme 2 The poly-*para*-phenoxyphenols studied

For phenol and 4PP, the predictions of calculations were compared with the available experimental data and this constituted the benchmark phase of the present study. To confirm the predicted trend of the fluorescence emission wavelengths, partial calculations were also carried out for a 5-ring system, The latter calculations were referred to one conformation only, due to remarkable computational costs.

Phenol

The absorption spectra were calculated in the first place. Phenol absorption bands were predicted at 230 and ~265 nm, in satisfactory agreement with the experimental data (see Figure 17a). As far as fluorescence is concerned, both the $S_2 \rightarrow \cdot S_0$ and $S_1 \rightarrow \cdot S_0$ transitions were calculated. For phenol, the predicted emission wavelengths (λ_{em}) were at 276 and 287 nm, respectively. Figure 17b reports the EEM spectrum of phenol, which shows fluorescence bands around excitation/emission (Ex/Em) wavelengths of ~220/ ~300 nm and ~270/~300 nm. The two bands with Ex/Em of ~220/~600 nm and ~270/~600 nm are the second harmonics of the bands with emission at ~300 nm. The excitation wavelengths correspond quite well to the experimental and calculated absorption bands of phenol, while there appears to be only one emission band (λ_{em} ~ 280-320 nm). This band is consistent with the $S_1 \rightarrow \cdot S_0$ transition, in agreement with Kasha's rule [122] according to which the S_2 state would quickly undergo radiationless deactivation to S_1, from where the fluorescence emission would take place. The spectroscopic properties of phenol have been the subject of several computational studies, the most recent of which has been performed by using high-level ab-initio methods.[141] However, the cited findings are not directly comparable with our results because all literature calculations have been carried out in the gas phase. For our purposes, it is more interesting to carry out a

comparison with experimental data [142] concerning the change in some structural parameters. The relevant experimental data are quite well reproduced, as reported in the Appendix.

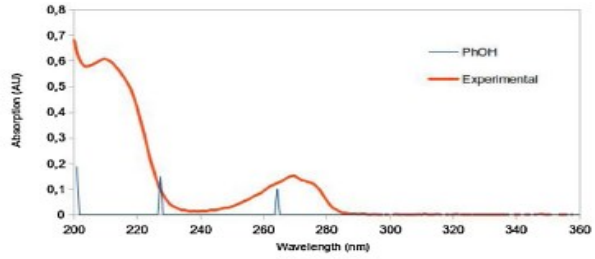

Figure 17 a

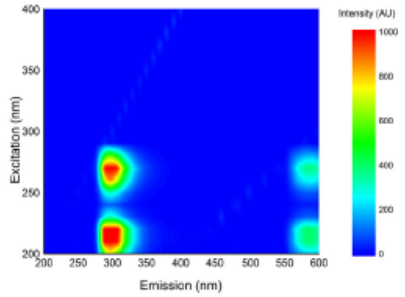

Figure 17 b

Figure 17 (a) Experimental absorption spectrum of phenol (0.1 mM solution), with overlapped calculated transitions. (AU = absorption units)
(b) EEM of phenol (0.1 mM aqueous solution). Both excitation and emission slits were set at 5 nm)

4-Phenoxyphenol (4PP)

Differently from phenol that has just one conformer, 4PP has three different stable conformations (here indicated as 2a, 2b and 2c, as shown in Figure 18). The main differences among the three 4PP conformers are the two dihedral angles between the aromatic rings, which show different reciprocal orientations.

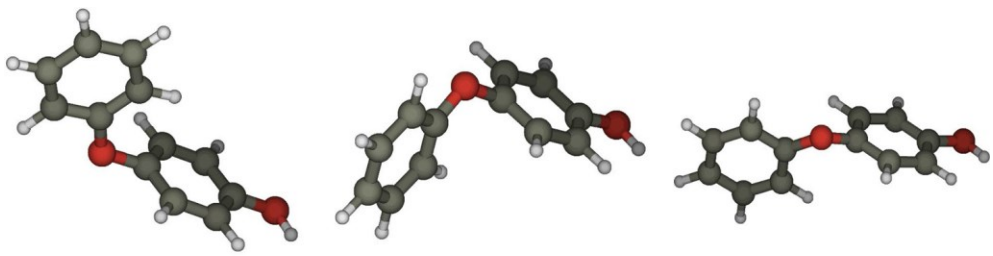

Figure 18 The three conformers of 4-phenoxyphenol (4PP).

Based on the stability of each conformer, the relative abundance is predicted to be 2b > 2a > 2c. Eighty transitions were calculated for each structure (see the Appendix), and they were superposed to the experimental absorption spectrum. Figure 19a shows the results of this procedure, and the comparison suggests that

the experimental absorption band of 4PP around 200 nm would derive from multiple transitions involving the three conformers. The experimental band around 230 nm is predicted to be due to several transitions occurring at 220–240 nm, while the observed band around 280 nm would be the consequence of transitions predicted at 260–270 and 290–300 nm. Overall, there is a good qualitative agreement between the calculated transitions and the experimental spectrum.

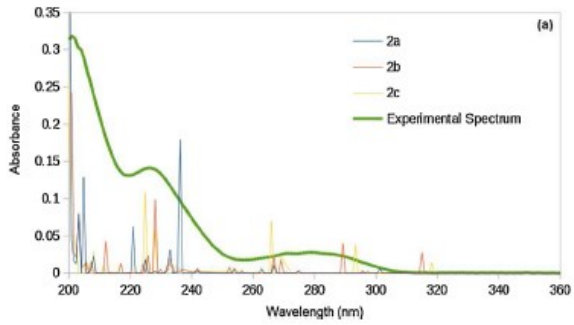

Figure 19 a

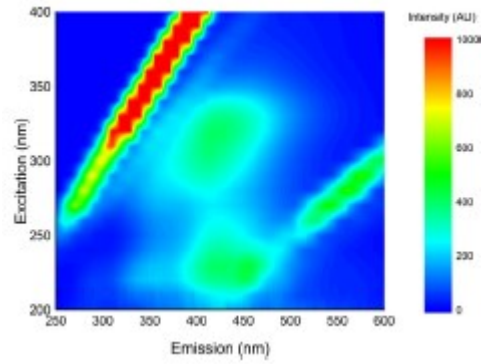

Figure 19 b

Figure 19 (a) Experimental absorption spectrum of 4-phenoxyphenol (0.1mM solution), with overlapped calculated transitions.
(b) EEM of 0.1 mM 4-phenoxyphenol in aqueous solution (both excitation and emission slits were set at 20 nm)

To investigate the fluorescence properties of 4PP, the geometry of the first excited state of each conformer was determined. Based on the results obtained with phenol and in agreement with Kasha's rule, only the $S_1 \rightarrow S_0$ transition was taken into account. Similarly to the ground state, the S_1 state presents, apparently, three conformations (2a-S_1, 2b-S_1, 2c-S_1: their structural parameters are reported in Figure 20 and Table 3). Again, the three conformers mainly differ for the values of the dihedral angles.

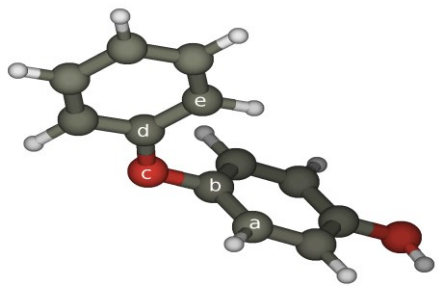

Figure 20

Figure 20. The theta (θ) dihedral angle is measured by considering two atoms on the first aromatic ring, as well as the oxygen and the carbon atom on the second ring (here identified as a-b-c-d atoms). In contrast, the omega (ω) angle is measured by considering one carbon atom on the first ring, the connecting oxygen and two atoms on the second ring (here identified as b-c-d-e atoms).

The first ring is that containing the OH function, the other is the second ring.

Parameters of 4PP ground state (S_0)				
Name	**(θ)**	**(ω)**	**ΔG (Kcal mol^{-1})**	**Weight**
2a	88	4	0.305	0.32
2b	-61	154	0	0.53
2c	-129	-152	0.764	0.15
Parameters of 4PP excited state (S_1)				
Name	**(θ)**	**(ω)**	**ΔG (Kcal mol^{-1})**	**Fluorescence (nm)**
2a	53	17	8.88	359
2b	-176	-109	0.040	425
2c	-4	104	0	425

Table 3 Structural parameter and relative energy of 4PP conformers in the states S_0 and S_1.

Predicted transitions for the emission are at ~355 nm (2a-$S_1 \rightarrow S_0$) and ~425 nm (both 2b- $S_1 \rightarrow S_0$ and 2c-$S_1 \rightarrow S_0$). The former emission is due to an electron transfer from the π framework of the phenoxy moiety to the π framework of the phenol, while the latter emissions are both due to an electron transfer in the opposite direction (see Figure 21).

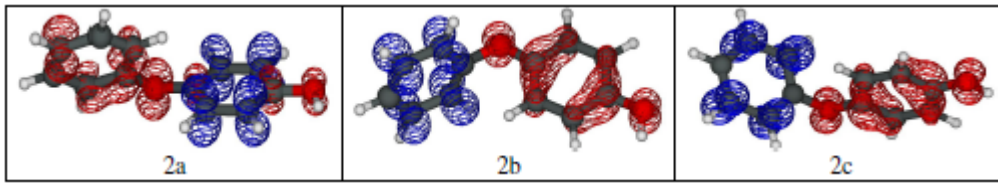

Figure 21 Differential electronic density maps between S_1 and S_0 in the different conformers of 4PP

The differential electronic density maps represent the difference in electronic densities between the ground and the first excited state responsible for the fluorescence. In other terms, the red areas are where the electron comes from (S_0), while the blue area is where the electron goes (S_1). These areas roughly correspond to the HOMO and LUMO in HOMO–LUMO dominated electronic transitions, as it is the case here.

The experimental fluorescence spectrum (EEM matrix) is reported in Figure 19b. It shows some linear features that do not depend on 4PP emission (they are the Raleigh scattering of the solution at $\lambda_{Em} = \lambda_{Ex}$, its second harmonic at $\lambda_{Em} = 2\lambda_{Ex}$, and the Raman signal of water at $\lambda_{Em} > \lambda_{Ex}$), two weak fluorescence bands at Ex/Em ~220/~350 nm and ~280/~350 nm, and two more intense bands at Ex/Em ~220/~425 nm and ~300/~425 nm. The excitation wavelengths roughly correspond to the two absorption bands of 4PP at ~225 and ~280 nm (corresponding to the transitions $S_0 \rightarrow S_2$ and $S_0 \rightarrow S_1$, respectively). Even more significantly, one observes a remarkably good agreement between the predicted and the observed wavelengths of fluorescence emission: a couple of weak bands

correspond to the 2a-$S_1 \rightarrow S_0$ transition, and the other couple to 2b- $S_1 \rightarrow S_0$ and 2c- $S_1 \rightarrow S_0$. The excited electronic states 2b-S_1 and 2c-S_1 are generated, respectively, from the 2b and 2c conformers that represent 70% of the excited 4PP population, while the electronic state 2a-S_1 is generated from 2a that makes up the remaining 30%. This calculation result can explain why the emission bands at ~350 nm (generated by 2a-S_1) are weaker than those found at ~425 nm (generated by the most abundant 2b-S_1 and 2c-S_1 conformers).

4-(4'-phenoxy)phenoxyphenol (4PPP)

In the case of the three-ring system 4PPP, three conformers (3a, 3b and 3c) were found. They are described by the dihedral angles between the three aromatic rings (each conformer is described by a total of four dihedral angles: θ and ω are the angles between the first aromatic ring (that beariung the OH function) and the second; θ' and ω' are the analogous angles between between the second and the third aromatic ring. The structures of 3a, 3b and 3c are reported in Figure 22, and their predicted order of stability and abundance is 3a > 3c ~ 3b.

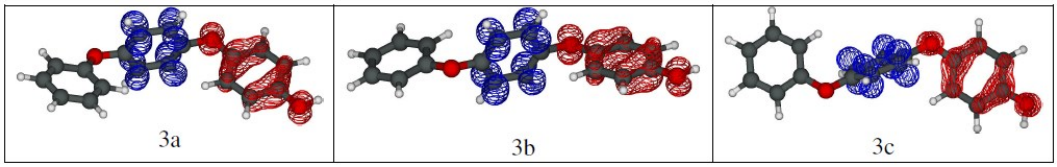

Figure 22 Differential electronic density maps between S_1 and S_0 in the different conformers of 4PPP

As before, eighty absorption transitions were calculated for each conformer (as reported in the Appendix), the main ones being shown in Figure 23a. When considering the band broadening that should take place in aqueous solution, one may predict that 4PPP would absorb radiation below 340 nm and that the identity/structure of the absorption bands would be partially lost as shown in Figure 23b.

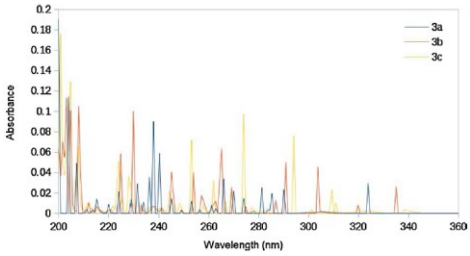

Figure 23a

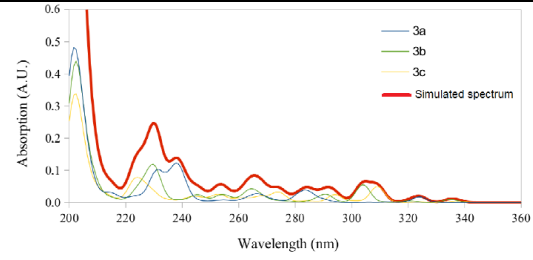

Figure 23b

Figure 23 (a) Main calculated transitions for 4PPP (b) Simulated absorption spectrum for 4PPP obtained by linear combination of the calculated absorption bands, weighted by the relative energies of the structures.

A S_1 state can be computed for each ground-state conformer, from which it mainly differs for the values of the dihedral angles (see the Table 4 for the

structural parameters, and the Appendix for the structures of 3a-S_1, 3b-S_1 and 3c-S_1).

Parameters of 4PPP ground state (S_0)						
Name	**(θ)**	**(ω)**	**(θ')**	**(ω')**	**ΔG (Kcal mol^{-1})**	**Weight**
3a	88	4	117	165	0	0.47
3b	-123	-159	-66	-20	0.607	0.25
3c	-60	159	129	156	0.513	0.28
Parameters of 4PPP excited state (S_1)						
Name	**(θ)**	**(ω)**	**(θ')**	**(ω')**	**ΔG (Kcal mol^{-1})**	**Fluorescence (nm)**
3a	3	83	117	162	0.071	447
3b	-3	97	69	163	0.024	448
3c	117	-106	-67	162	0	448

Table 4 Structural parameters and relative energies of the 4PPP conformers in the states S_0 and S_1

Interestingly, similar emission wavelengths (in the 447–448 nm range) are predicted for the three $S_1 \rightarrow S_0$ transitions. Coherently with this fact, we can observe that all the three transitions are due to an electron transfer from the π framework of the phenol moiety to the π framework of the adjacent phenoxyl moiety, as shown in Figure 22. Therefore, 4PPP would emit fluorescence radiation around 450 nm.

4-(4-(phenoxy)phenoxy)phenoxyphenol (4PPPP)

The four-ring system 4PPPP has six different stable conformers (4a–4f) with comparable abundance, a partial exception being 4f that is the least stable. The conformers differ for the six dihedral angles between the aromatic rings, as in previous cases. The absorption transitions of 4PPPP were derived with the same procedure described before and they are shown in Figure 24a.

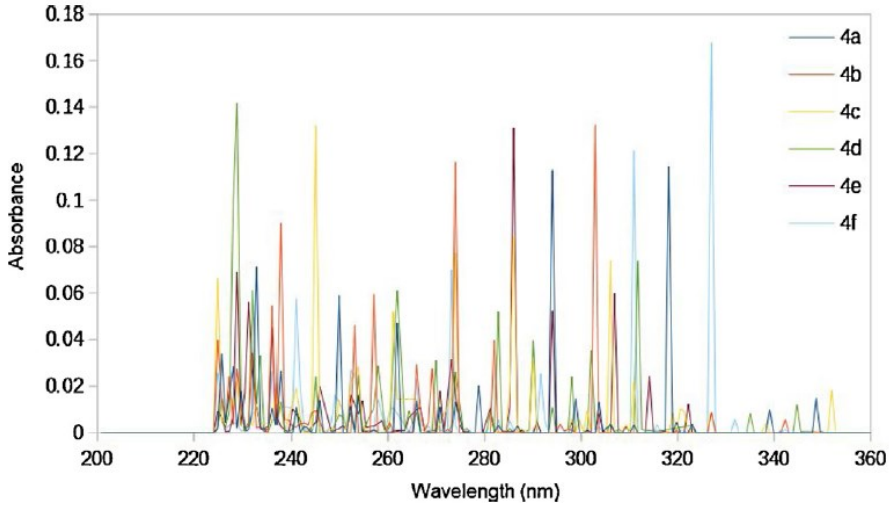

Figure 24°

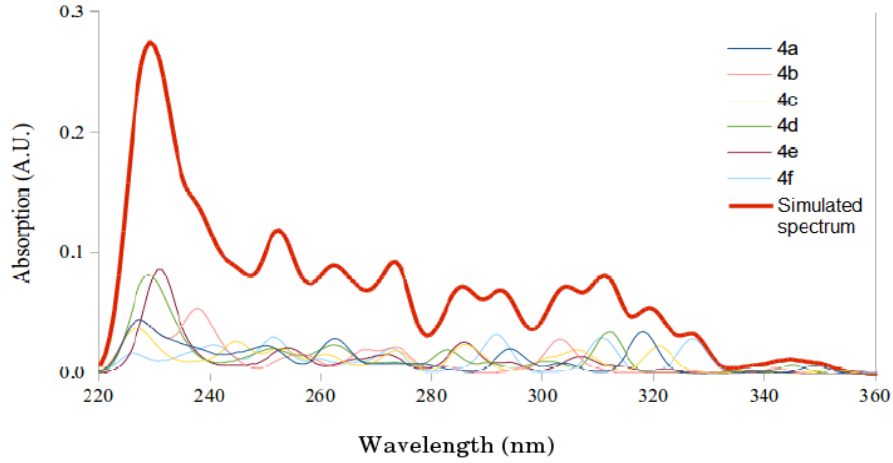

Figure 24b

Figure 24 (a) Main calculated transitions for 4PPPP (b) Simulated absorption spectrum for 4PPPP obtained by linear combination of the calculated absorption bands, weighted by the relative energies of the structures.

The large number of transitions covers with regularity the wavelength range up to at least 360 nm. Under these circumstances, the simulated absorption spectrum of 4PPPP would show an overall decrease of the absorption intensity with increasing wavelength, with limited spectral features (as shown in Figure 24 b). It might be tempting to draw a parallel between such conditions and the featureless pseudo-exponential decay with wavelength that is observed in the absorption spectra of humic substances in surface waters and of atmospheric HULIS. [143] Similarly to 4PP and 4PPP, also in the case of 4PPPP the S_1 conformers ($4aS_1$–$4fS_1$) mainly differ for the dihedral angles. The predicted emission wavelengths for five of the conformers are very similar and range from ~446 to ~448 nm, while for the conformer 4b, for which the state S_1 is higher in energy, the predicted fluorescence emission is at 434 nm.

Parameters of 4PPPP ground state (S_0)								
Name	**(θ)**	**(ω)**	**(θ')**	**(ω')**	**(θ'')**	**(ω'')**	**ΔG (Kcal mol^{-1})**	**Weights**
4a	109	-9	137	148	58	28	0.242	0.17
4b	93	-1	115	165	129	154	0.201	0.18
4c	-126	-156	130	152	-62	158	0.109	0.19
4d	-70	167	123	158	-121	-161	0.362	0.15
4e	-62	158	-76	-11	67	20	0	0.22
4f	-48	-36	-53	-33	55	27	0.878	0.09
Parameters of 4PPPP excited state (S_1)								
Name	**(θ)**	**(ω)**	**(θ')**	**(ω')**	**(θ'')**	**(ω'')**	**ΔG (Kcal mol^{-1})**	**Fluorescence (nm)**
4a	161	-41	-176	89	64	23	0	448
4b	53	35	103	-5	-14	-61	3.038	434
4c	-163	-141	4	89	119	-23	0.044	447
4d	-22	-46	-2	97	69	18	0.036	446
4e	22	41	-4	-87	-62	-24	0.038	446
4f	-19	-47	-4	102	73	14	0.017	448

Table 5 Structural parameters and relative energies of the 4PPPP conformers in the states S_0 and S_1

Considerations on the predicted fluorescence

The calculated wavelengths of fluorescence emission are in good or very good agreement with the experimental data, when available (i.e., in the cases of phenol and 4PP). Moreover, the computational results predict an increase of the fluorescence emission wavelengths when increasing the number of aromatic rings, as shown in Figure 25. 4PP was the only case where two considerably different emission wavelengths were predicted for the various conformers. Both emissions were actually observed in the experimental spectrum, although the emission corresponding to the conformer 2a was much weaker than the other

one (2b + 2c). Note that the conformer 2b would be the most stable and, therefore, the most abundant.

The trend reported in Figure 25 shows a plateau in the calculated fluorescence emission maxima near 450 nm, and there is very little difference between the emission wavelengths predicted for 4PPP and 4PPPP. This trend is confirmed by the emission at 444 nm calculated for one sample conformer of the five-ring system 4-(4-(4-(4- phenoxy)phenoxy)phenoxy)phenoxyphenol (4PPPPP), which is almost identical to the emission from 4PPPP. This issue can be reasonably explained when taking into account the nature of the excited states, looking at the differential electronic densities and particularly at the graphical representation of the differential electronic density maps. Figure 26a reports the differential electronic density map for the conformer 4d of 4PPPP (the maps for the other conformers are reported in the Appendix), from which one can deduce that the excited states (S_1) of the molecules with two or more rings show a charge-transfer (CT) character.

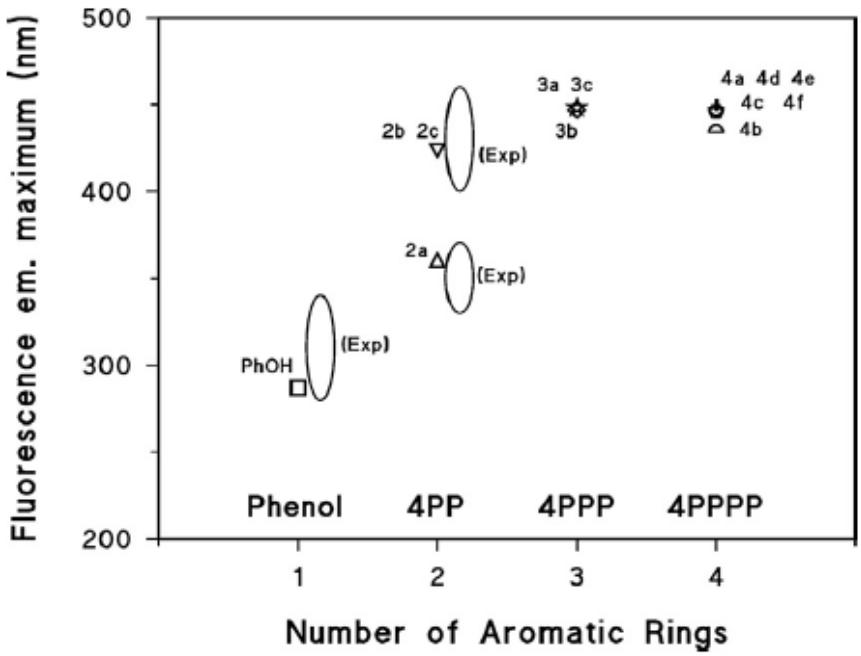

Figure 25

Figure 25. Trend of the calculated fluorescence emission maxima of the investigated compounds (their different conformers are indicated on the plot), as a function of the number of aromatic rings. The experimental data (Exp: wavelength range of the measured emission band) for phenol and 4PP are also reported as ellipses near the relevant calculation results.

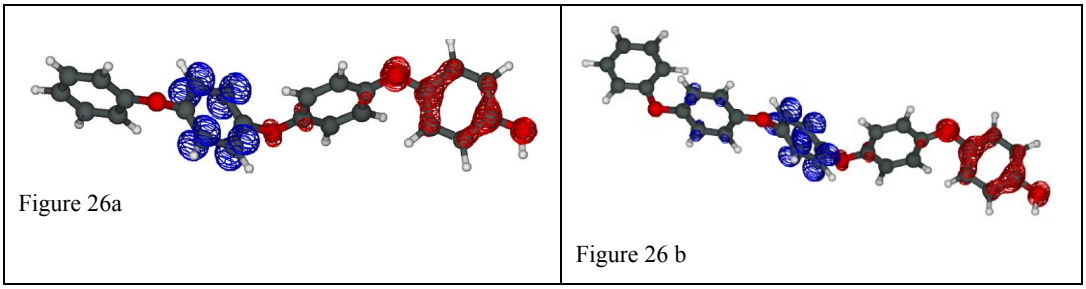

Figure 26. (a) Differential density map for the $S_1 \rightarrow S_0$ transition of the 4d conformer of 4PPPP. (b) Differential density map for the $S_1 \rightarrow S_0$ transition of the only five-ring conformer studied.

All the differential electron density maps show an electron transfer from the p orbitals of one aromatic ring to the π orbitals of a different aromatic ring (with some participation of the π orbitals located on the oxygen atoms). In particular, for all the molecules with calculated fluorescence around 446–448 nm (4PPPPP, five out of six conformers of 4PPPP as reported in the Appendix, and all the three conformers of 4PPP, as shown in Figure 22) the electronic transfer is from the first aromatic ring (that bearing the hydroxyl group) to the second or the third aromatic ring. By contrast, the 434 nm emission from conformer 4b corresponds to a CT from the third to the second ring. For 4PP, the excited states emitting at 425 nm (2b and 2c) correspond to a CT from the first ring to the second, while the conformer emitting at 359 nm (2a) corresponds to a CT from the second ring to the first (Figure 21).

It is interesting to point out that the predicted emission at ~450 nm is well within the fluorescence region of HULIS.[130] It is also very near the fluorescence signal observed upon phototransformation of phenolic compounds, under conditions where the formation of phenoxyl radicals and the subsequent dimerization/oligomerization processes are quite likely.[135-144] The computational results presented here give support to the hypothesis that the observed fluorescence in the mentioned systems is accounted for by phenol oligomers: an ongoing oligomerization process, with formation of progressively larger systems with an increasing number of aromatic rings, would produce a fluorescence signal at wavelengths approaching 450 nm. At that point, the possible formation of larger compounds is not expected to cause an important modification of the emission wavelengths. Another interesting issue concerns the absorption spectra, where a gradual shift of the absorption towards higher wavelengths is predicted for the oligomers with more aromatic rings, together with a loss of the individual features of the different bands. An absorbance increase at higher wavelengths has been reported under conditions where oligomerization is operational, both in gas-solid systems and in solution, together with the appearance of a featureless decay of the absorption with increasing wavelength.[144] However, differently from the case of phenol oligomers, the experimental absorption was extended into the visible, which is most likely due to charge-transfer bands caused by interaction

between electron donors and acceptors. Donors and acceptors might include phenols and aromatic carbonyls, respectively, that could be formed under oxidative conditions. The acceptor–donor inter-molecular interactions would be characterized by efficient processes of internal conversion, with an efficient quenching of the possible fluorescence emission.[23] Therefore, phenol oligomers could account for the observed fluorescence emission, but their contribution to the experimental absorption spectra is expectedly limited.

Outcomes of the Phenol Oligomers Study

Phenol dimers and oligomers are characterized by the presence of different conformers, which differ for the dihedral angles between the aromatic rings. Each conformer gives its own contribution to the absorption and fluorescence spectra of the investigated compounds. In particular, 4PP and 4PPP have three stable conformers each, while 4PPPP has six conformers. The predicted wavelengths of fluorescence emission, which correspond to $S_1 \rightarrow S_0$ transitions, increase up to a plateau when increasing the number of aromatic rings. Considering that the transitions producing fluorescence involve at most three aromatic rings, important changes in the emission wavelength are not expected when further increasing the molecular size. This issue is further supported by the calculated fluorescence emission of one of the conformers of 4PPPPP. The plateau in the predicted emission wavelengths is at around 450 nm, which is quite in the fluorescence range of HULIS and of the C-like peak of humic substances. The oligomeric compounds might thus account for the HULIS-type fluorescence, which has been observed under conditions where phenol oligomerization was operational due to the formation of phenoxy radicals.[135] Interestingly, the plateau in the emission wavelengths predicts that a mixture of phenol oligomers could not show fluorescence in a different spectral interval than that experimentally observed: an increasing molecular size would initially shift the fluorescence emission from the phenolic region to the HULIS one, but further increases of the ring number are not expected to produce important modifications in the wavelengths of the emission signal.

Section II - Pollutant phototransformation

The second part of this thesis work is dedicated to natural water systems in which photochemistry plays a significant role in the depletion of pollutants, especially the non-biodegradable ones. This section presents a study regarding propanil, an herbicide that is largely used in rice cultivation.

The case of Propanil in flooded paddy fields.

Propanil (N-(3,4-Dichlorophenyl)propanamide, hereafter PRP) is a post-emergence contact herbicide that is widely used in rice cultivation. It acts as an inhibitor of photosynthesis by blocking the electron-transfer processes involved in CO_2 reduction, killing weeds that, differently from rice, do not carry out fast PRP hydrolysis to 3,4-dichloroaniline (34DCA) with the enzyme arylacylamidase.[145] PRP is not very toxic to mammals,[146] but potentially lethal human poisoning during pesticide use may occasionally occur. Indeed, both PRP and its major metabolite 34DCA can cause methemoglobinemia.[147] PRP is a pollutant of concern for aquatic organisms such as crustaceans (acute toxic effects detected at mg L^{-1} levels)[148] and, most notably, algae (acute toxicity at tens μg L^{-1} levels)[148] and some fish (LC_{50} levels in the range of tens μg L^{-1} to tens mg L^{-1} depending on the species).[149-150] PRP undergoes relatively fast degradation in paddy water, and 34DCA is a major transformation intermediate that shows comparable or even longer persistence than the parent compound.[151-152] Similarly to PRP, 34DCA is acutely toxic at mg L^{-1} levels to fish, crustaceans, and algae,[146] but it can also interfere with the development of fish embryos and with the reproduction of crustaceans at μg L^{-1} levels.[153] Both PRP and 34DCA show some genotoxic effects, but none of them is classified as carcinogenic.[146]

The transformation of PRP into 34DCA is known to take place during PRP biological degradation, but it could also occur under some irradiation conditions.[154] The persistence of the parent compound and of its main metabolite suggests that a water-holding period of several days after PRP spraying and before paddy-water discharge into the receiving water bodies would minimize environmental contamination phenomena by either PRP or 34DCA.[151-152] The cited environmental effects have urged the introduction of some restrictions to PRP use in the U.S.,[155] and in the E.U. its use is permitted only under emergency conditions.[156] However, PRP is still manufactured and applied on a large scale worldwide.[157]

Several studies have focused on PRP biodegradation as the supposed main transformation pathway in paddy-field water.[158] However, PRP also undergoes photodegradation under sunlight,[158] and the kinetics of phototransformation might be comparable with those of biochemical transformation and with the overall field persistence.[154] Unfortunately, to date the photochemical degradation of PRP has been studied either in synthetic solutions (ultrapure water),[154-159] or upon irradiation of natural waters but without a distinction between direct and indirect photolysis processes, which prevents a generalization of laboratory results to field conditions.[160]
The photochemical fate of xenobiotics in sunlit surface waters depends on the occurrence of different processes such as the direct photolysis and the indirect photochemistry, where the latter involves reaction with reactive transient species such as ^{3}CDOM*, $^1O_2$, $^{\bullet}OH$ and $CO_3^{\bullet-}$.

Rice fields under study

The paddy water used in the present studywas collected in three conventional rice farms located in the municipalities of Rovasenda (45.536970° N; 8.298246° E, 220 m a.s.l), Santhià (45.377806° N; 8.201165° E, 179 m a.s.l), and San Germano Vercellese (45.356445° N; 8.244346°E; 165m a.s.l), all located in the province of Vercelli, Piemonte region, NW Italy. This is the most important rice growing area of Italy, where over 90% of the total Italian rice is grown. The rice field size was 0.9 ha, 1.1 and 0.7 ha in Santhià, San Germano Vercellese, and Rovasenda, respectively. The rice fields of Santhià and San Germano Vercellese were ploughed in autumn to incorporate crop residues, and broadcast seeded on flooded fields during the first days of May with *Sirio CL* and *Volano* rice varieties, respectively. The Rovasenda field was planted in autumn with a cover crop composed of a mixture of grasses and dicot species. The cover crop was shredded, a few days before broadcast sowing of the rice variety *Carnaroli* at the end of April. Seeding rate was of 150 kg ha^{-1} for *Sirio CL*, and 200 kg ha^{-1} for *Volano* and *Carnaroli*.
Paddy fields are flooded by means of an articulated system of ditches and channels that innerve the whole rice district. The paddy fields at Santhià and San Germano Vercellese are included in the West Sesia irrigation district and are flooded with waters from the Roggia Cavallera and the Roggia Molinara di San Germano, respectively. The paddy field of Rovasenda is fed with water from Roggia Bardesa, which is included in the East Sesia irrigation district.
Sampling took place in late May, 2016. Two one-liter glass bottles were filled starting from a bulk of 10 L paddy water collected in each rice field, by randomly filling a 10 L PTFE bucket. Samples were temporarily stored in a portable refrigerator until transfer to the laboratory, where they were vacuum filtered with polyamide filters (0.45 µm pore size) and kept refrigerated at ~5.5 °C until analysis or irradiation. At the time of sampling, the water level in each paddy field was around 5–7 cm and the crop was at 3–4 leaf stage (growth stage 13–14 on the BBCH scale).[161] At this stage the rice plants do not yet produce an important

shading of the paddy water, but later growth causes a considerable decrease of the light transmitted through the rice canopy as shown in Figure 27.

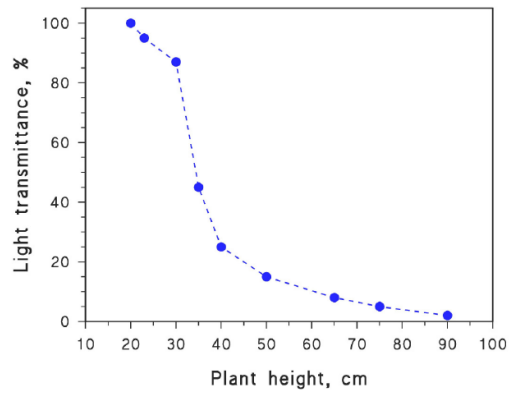

Figure 27 a

Figure 27 b

Figure 27 c

Figure 27. (a) Sunlight transmittance reaching the paddy-water surface as a function of the height reached by the rice plants. Note that the rice plants considerably shield light when reaching 35-40 cm height or above, and almost no light is transmitted for h = 90 cm.
(b) Photograph of a paddy field taken in Santhià, when the plants have grown up considerably and shade almost totally the paddy water. (c) The paddies at the time of our sampling in Rovasenda.

Irradiation Experiments

Solutions to be irradiated (5 or 20 mL total volume) were placed in the same cylindrical Pyrex glass cells described before. The solutions were irradiated mainly from the top. After the scheduled irradiation time, the whole solutions (5 mL case) or 1.2 mL solution aliquots (20 mL case) underwent analysis. The temperature of the irradiated solutions was ~30 °C.
Paddy-water samples (20 mL) were irradiated under a lamp spanning a wide spectral emission range, with the purpose of measuring the formation rates of $^{\bullet}OH$, $^{1}O_2$, and $^{3}CDOM^*$. The determination of the photochemical kinetics parameters of PRP (direct photolysis quantum yield and second-order reaction rate constants) involved experiments with systems based on ultra-pure water instead of paddy water (5 mL total volume). The relevant solutions were irradiated with lamps chosen to achieve selective excitation of the photoactive compounds. In these experiments, the standard initial concentration of PRP was 20 μmol L^{-1}, or less when required by the kinetic determinations. For instance, the reaction between PRP and $^{\bullet}OH$ was studied using nitrate photolysis as $^{\bullet}OH$ source and competition kinetics with 2-propanol as $^{\bullet}OH$ scavenger.[162] The

relevant solutions were irradiated under a 20 W Philips TL01 lamp, having an emission maximum at 313 nm and producing a 4.1 ± 0.1 W m^{-2} UV irradiance on top of the irradiated systems. The UV irradiance (290–400 nm) was measured with an irradiance meter by CO.FO.ME.GRA. (Milan, Italy). The same lamp was used to study the direct photolysis of PRP. The reaction between PRP and the triplet state of anthraquinone-2-sulfonate (^{3}AQ2S*) was studied using a UVA black lamp (Philips TL-D 18 W, emission maximum at 368 nm), producing a UV irradiance of 27.5 ± 0.6 W m^{-2} on top of the irradiated systems. AQ2S was chosen as CDOM proxy for experimental convenience, because it is virtually the only triplet sensitizer that allows for a straightforward determination of the triplet-state reaction rate constant by using steady irradiation alone. Unfortunately, ^{3}AQ2S* is sometimes more reactive than average ^{3}CDOM*,[163] thus additional rate constants of PRP triplet sensitization were obtained by using the laser flash photolysis technique as explained hereafter, with the same apparatus that was described before. The reaction between PRP and $^1O_2$ was studied using Rose Bengal as $^1O_2$ source, irradiating the solutions with a 18 W Philips TLD Yellow lamp with emission maximum at 545 nm. The emission spectra of the lamps were measured with an Ocean Optics USB 2000 CCD spectrophotometer and corrected for the transmittance of the Pyrex window of the irradiation cells. On the basis of these data, the actual spectral photon flux density of the lamps was then obtained by chemical actinometry with 2-nitrobenzaldehyde (NBA).[94] Because the Yellow lamp does not allow for NBA actinometry, its spectral photon flux density was calculated by taking into account the shape of the emission spectrum, the integral irradiance measured with a Testo 540 irradiance meter, the irradiation geometry, and the solution volume. The photon flux density thus obtained was only approximate, but that did not affect the measurement of the $^1O_2$ reaction rate constant. Indeed, the formation rate of $^1O_2$ by irradiated Rose Bengal ($R_{^1O_2}^{RB}$) was measured independently with furfuryl alcohol (FFA) as probe molecule, and only $R_{^1O_2}^{RB}$ was used in rate-constant calculations. The spectral photon flux densities of the used lamps and the absorption spectra of the photosensitizers are reported in Figure 28.

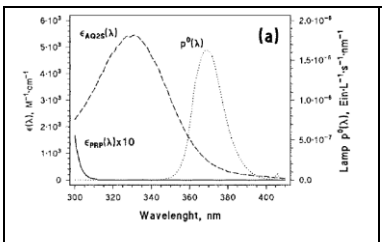

Figure 28 a

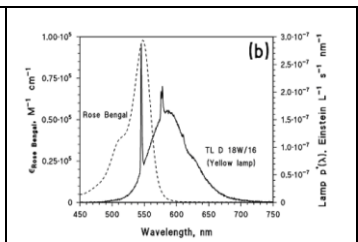

Figure 28 b

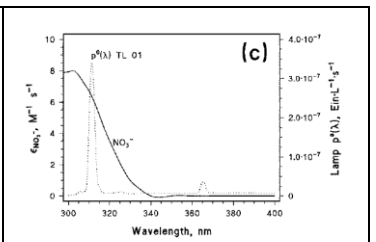

Figure 28 c

Figure 28. (a) Absorption spectra (molar absorption coefficients) of PRP and of antraquinone-2-sulphonate (AQ2S). Emission spectrum (spectral photon flux density in solution) of the UVA black lamp Philips TL-D 18W.

(b) Absorption spectrum of Rose Bengal. Incident spectral photon flux density of the lamp Philips TL D 18W/16 Yellow.
(c) Absorption spectrum of nitrate. Incident spectral photon flux density of the lamp Philips TL 01.

Liquid Chromatography Determinations

The time evolution of PRP, of the used probe molecules and of 34DCA was monitored by liquid chromatography, using the same apparatus described before. The used eluents were as follows: A = aqueous H_3PO_4 at pH 2.8; B = acetonitrile; C = Milli-Q water. The degradation of PRP was monitored in isocratic mode with a 45:55 B:C mixture (the retention time of PRP was R_t = 6.0 min), using 251 nm as the quantification wavelength. Under the same conditions, 3,4-dichloroaniline (quantified at 245 nm) had a retention time of 5.1 min. The time evolution of TMP was monitored by eluting with a 50:50 A:B mixture (R_t^{TMP} = 4.8 min, quantification wavelength λ = 270 nm), that of FFA with 90:10 A:B (R_t^{FFA} = 3.7 min, λ = 215 nm). Finally, the time evolution of phenol formed from benzene was monitored upon elution with 70:30 A:B (R_t^{Phenol} = 3.9 min, λ = 270 nm). Note that TMP, FFA and benzene were probe molecules added to paddy water (vide infra). The used chemicals (analytical grade) and the organic solvents (gradient grade) were used as obtained, without further purification. Ultra-pure water was produced with a Milli-Q system (Millipore).

Measurement of Photoinduced Transients upon Irradiation of Paddy-Field Water

Probe molecules were used to measure the photogeneration of transient species (^{3}CDOM*, $^1O_2$, $^\bullet$OH) [164]The paddy-water samples (20 mL) were put inside the irradiation cells, spiked with each probe molecule separately (the molecule was added as pure solid or liquid and let dissolve) and irradiated under a 40 W Philips TL K05 lamp, having emission maximum at 365 nm. This lamp spans the UVB, UVA and visible wavelength intervals: its spectral photon flux density is reported in Figure 29, together with the absorption spectra of the irradiated water samples. Dark experiments on paddy water were carried out under the same irradiation device, by wrapping the cells with aluminum foil.
Previous results suggest that the probe molecules used in this work (2,4,6-trimethylphenol, furfuryl alcohol, and benzene) do not directly photolyze under the TL K05 lamp (i.e., they are not degraded upon irradiation in ultra-pure water), basically because they do not absorb lamp radiation significantly.[165]

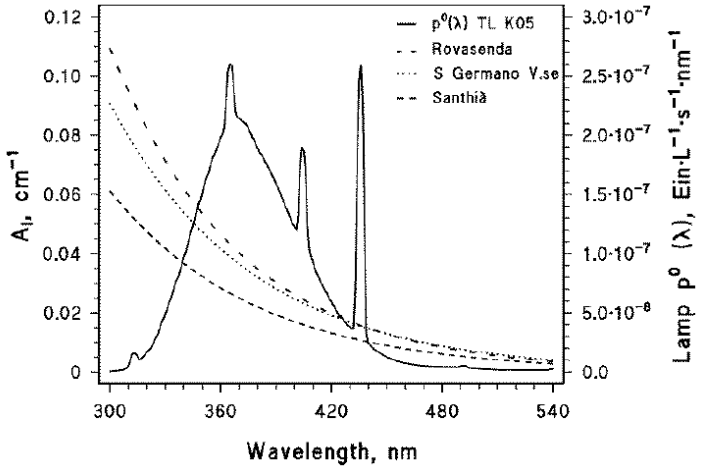

Figure 29

Figure 29. Left Y-axis shows the specific absorption spectra of the investigated water samples, referred to an optical path length of 1 cm, while the right Y-axis shows the emission spectrum (spectral photon flux density, $p°(\lambda)$) of the Philips TL K05 lamp (40 W) used for the irradiation experiments-

The formation of ^{3}CDOM* was monitored by using 2,4,6-trimethylphenol (TMP) as probe molecule. After photochemical production by CDOM, the transients ^{3}CDOM* can undergo either inactivation (by internal conversion or reaction with O_2) or reaction with TMP.

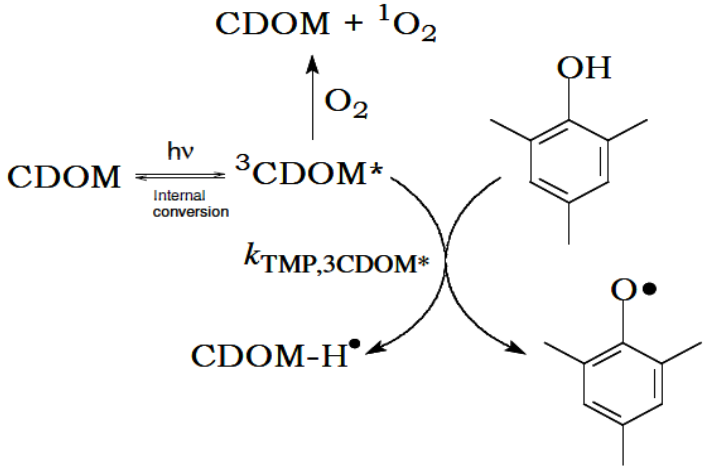

Scheme 3. Reaction processes involving TMP and ^{3}CDOM*

A reasonable literature value for the pseudo-first order inactivation rate constant of ^{3}CDOM* without TMP is k' ~5×10^5 s^{-1}, while the second-order reaction rate constant between TMP and ^{3}CDOM* is $k_{TMP,^3CDOM*}$ ~ (2-3)$\times10^9$ L mol^{-1} s^{-1}.[166]

Assume $R^{\bullet}_{^3CDOM}$ to be the formation rate of ^{3}CDOM* in each irradiated sample, R_{TMP} the experimental initial transformation rate of TMP in the same sample under irradiation, $R_{TMP,dark}$ the initial transformation rate of TMP without

irradiation, and $[TMP]_o$ the initial concentration of TMP spiked to the sample. By applying the steady-state approximation to ^{3}CDOM* one obtains the following equation:

$$R_{TMP} = R_{^3CDOM^*} \frac{k_{TMP,^3CDOM^*}[TMP]_o}{k_{TMP,^3CDOM^*}[TMP]_o + k'} + R_{TMP,dark} \qquad (21)$$

The calculated $\mathbf{R^{\bullet}_{^3CDOM}}$ depends on the assumed values of $\mathbf{k_{TMP,^3CDOM^*}}$ and k', for which there are literature data that are, however, affected by a considerable uncertainty. To minimize the uncertainty it was used $[TMP]_0$=1 mmol L^{-1}, so that one has $\mathbf{k_{TMP,^3CDOM^*}}$ $[TMP]_0 > k'$. In these conditions it is $\mathbf{R_{TMP} \sim R^{*}_{^3CDOM} + R_{TMP,dark}}$. To calculate $\mathbf{R^{\bullet}_{^3CDOM}}$ it was assumed $\mathbf{k_{TMP,^3CDOM^*}}$ = 2 10^9 L mol^{-1} s^{-1} and k' = 5 10^5 s^{-1},[167] but these assumptions have a limited impact on $\mathbf{R^{\bullet}_{^3CDOM}}$ when $[TMP]_0$ = 1 mmol L^{-1}. The steady-state ^{3}CDOM* concentration was determined as [^{3}CDOM*] = $\mathbf{R^{\bullet}_{^3CDOM}}$ $(k')^{-1}$. Given that ^{3}CDOM* is not a definite or univocal species, but rather a collection of diverse transients of still unknown nature with presumably different properties, the described procedure actually returns the triplet states that are reactive toward TMP. Anyway, the use of TMP as ^{3}CDOM* probe has become almost a standard procedure in recent studies. [59-94]

Furfuryl alcohol (FFA) was used as $^1O_2$ probe. Assume $\mathbf{R_{^1O_2}}$ as the $^1O_2$ formation rate in an irradiated sample, $\mathbf{R_{FFA}}$ as the FFA initial degradation rate in the same sample, $\mathbf{R_{FFA,dark}}$ as the FFA degradation rate in the absence of irradiation, and k'' = 2.5×10^5 s^{-1} as the pseudo-first order deactivation rate constant of $^1O_2$ in aqueous solution. By applying the steady-state approximation to $^1O_2$ one gets the following equation:

$$R_{FFA} = R_{^1O_2} \frac{k_{FFA,^1O_2}[FFA]_o}{k_{FFA,^1O_2}[FFA]_o + k''} + R_{FFA,dark} \qquad (22)$$

It is $\mathbf{k_{FFA,^1O_2}}$ = 1.2 10^8 L mol^{-1} s^{-1}, and $[FFA]_0$ = 0.1 mmol L^{-1} is the initial FFA concentration spiked to the sample. With the above equation one obtains $\mathbf{R_{^1O_2}}$, and the steady state [$^1O_2$] is calculated as [$^1O_2$] = $\mathbf{R_{^1O_2}}$ $(k'')^{-1}$.

The transformation reaction of benzene into phenol was used as $^{\bullet}$OH probe, with assumed yield η = 0.7. The key experimental parameter here was the initial formation rate of phenol, $R_{Phenol} = \eta R_{^{\bullet}OH}$ (note that in some experiments benzene was added in large excess to the paddy-water samples, so that it could be

assumed to scavenge virtually all of the photogenerated •OH). A scheme depicting the photochemical production of hydroxyl radicals and their reaction with the natural occurring scavengers (Scav) and with benzene is reported below, with the equation 23 used to obtain *η*.

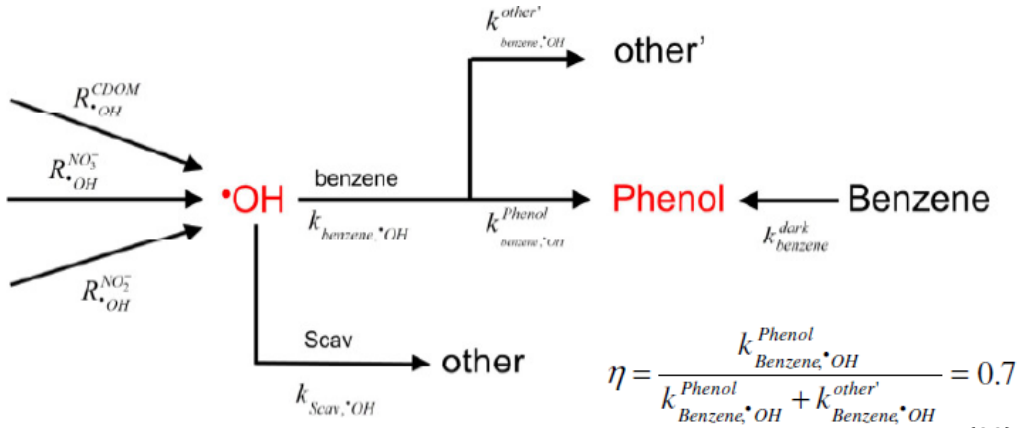

$$\eta = \frac{k^{Phenol}_{Benzene,^{\bullet}OH}}{k^{Phenol}_{Benzene,^{\bullet}OH} + k^{other'}_{Benzene,^{\bullet}OH}} = 0.7 \quad (23)$$

Scheme 4. Schematic of the reaction processes between benzene and •OH

The concentration of •OH varies with time according to the following equation:

$$\frac{d[^{\bullet}OH]}{dt} = R_{^{\bullet}OH} - k_{Scav,^{\bullet}OH}[^{\bullet}OH][Scav] - k_{benzene,^{\bullet}OH}[^{\bullet}OH][benzene] \quad (24)$$

where $R_{^{\bullet}OH} = R^{NO_2^-}_{^{\bullet}OH} + R^{NO_3^-}_{^{\bullet}OH} + R^{CDOM}_{^{\bullet}OH}$ is the total •OH formation rate in the irradiation sample. In steady-state conditions the •OH concentration is assumed not to vary with time ($\frac{d[^{\bullet}OH]}{dt} = \mathbf{0}$), so it is possible to obtain the •OH steady-state concentration as follows:

$$[^{\bullet}OH] = \frac{R_{^{\bullet}OH}}{k_{Scav,^{\bullet}OH}[Scav] + k_{benzene,^{\bullet}OH}[benzene]} \quad (25)$$

The phenol concentration changes with time according to the following equation:

$$R_{Phenol} = \frac{d[Phenol]}{dt} = k^{Phenol}_{Benzene,^{\bullet}OH}[^{\bullet}OH][Benzene] + k^{dark}_{Phenol}[Benzene] = k_{Benzene,^{\bullet}OH}\eta[^{\bullet}OH][Benzene] + R_{Phenol,dark} \quad (26)$$

When substituting [$^{\bullet}OH$] in equation (26) with the relevant expression taken from equation (25), one gets the following result:

$$\left(R_{Phenol} - R_{Phenol,dark}\right) = k_{Benzene,^{\bullet}OH}\,\eta[^{\bullet}OH][Benzene] = k_{benzene,^{\bullet}OH}\,\eta[Benzene]\frac{R_{^{\bullet}OH}}{k_{Scav,^{\bullet}OH}[Scav] + k_{benzene,^{\bullet}OH}[Benzene]} \quad (27)$$

By considering the contribution of each $^{\bullet}OH$ source to phenol formation and considering that [Scav] does not vary significantly during the irradiation experiments, one can assume $k'_{Scav} = k_{Scav\,,^{\bullet}OH}[Scav]$, where k'_{Scav} (s^{-1} units) is the pseudo-first order scavenging rate constant of $^{\bullet}OH$ by the natural components occurring in the sample. The following equation 28 can thus be obtained:

$$\left(R_{Phenol} - R_{Phenol,dark} - R_{Phenol}^{NO_2^-} - R_{Phenol}^{NO_3^-}\right) = \frac{k_{benzene,^{\bullet}OH}\,\eta[Benzene]}{k'_{Scav} + k_{benzene,^{\bullet}OH}[Benzene]}\,R_{^{\bullet}OH}^{CDOM} \quad (28)$$

In the presence of excess benzene ($[Benzene]_0$ = 2 mmol L^{-1}) one can assume that benzene itself scavenges the vast majority of $^{\bullet}OH$. The radical $^{\bullet}OH$ is photochemically produced by CDOM (with rate $R_{^{\bullet}OH}^{CDOM}$), nitrate and nitrite (with rates $R_{^{\bullet}OH}^{NO_3^-}$ and $R_{^{\bullet}OH}^{NO_2^-}$, respectively). Therefore, it is also important to assess the formation rate of phenol with 2 mmol L^{-1} benzene in ultra-pure water spiked with nitrate and nitrite at the same concentration values found in the samples ($R_{Phenol}^{NO_3^-}$ and $R_{Phenol}^{NO_2^-}$, respectively).

By so doing one can use the equation that follows to determine $R_{^{\bullet}OH}^{CDOM}$: $R_{Phenol} = 0.7R_{^{\bullet}OH}^{CDOM} + R_{Phenol}^{NO_2^-} + R_{Phenol}^{NO_3^-} + R_{Phenol,dark}$, where $R_{Phenol,dark}$ is the initial formation rate of phenol without irradiation. The experimental measurement of R_{Phenol}, $R_{Phenol,dark}$, $R_{Phenol}^{NO_3^-}$ and $R_{Phenol}^{NO_2^-}$ allows for $R_{^{\bullet}OH}^{CDOM}$ to be calculated. The steady-state [$^{\bullet}OH$] in the absence of benzene can be determined as $[^{\bullet}OH] = R_{Phenol}(0.7k'_{Scav})^{-1}$, where k'_{Scav} can be determined through a competition kinetics experiment in which different and relatively low $[Benzene]_0$ values are used. In this case one gets:

$$R_{Phenol} - R_{Phenol,dark} = 0.7\frac{k_{benzene,^{\bullet}OH}\,[benzene]_0}{k'_{Scav} + k_{benzene,^{\bullet}OH}\,[benzene]_0}R_{^{\bullet}OH}^{tot} \quad (29)$$

where $k_{benzene,^{\bullet}OH}$ =7.8 10^9 L mol^{-1} s^{-1}. By fitting the rate data obtained at different $[benzene]_0$ values, one can obtain both $R_{^{\bullet}OH}^{tot}$ (total formation rate of $^{\bullet}OH$) and k'_{Scav}.

With the values of the formation rates of ^{3}CDOM*, $^1O_2$ and $^\bullet$OH accounted for by CDOM, one can assess the corresponding quantum yields of transients photogeneration based on the lamp photon flux absorbed by CDOM itself:

$$P_a^{CDOM} = \int_\lambda p^0(\lambda)\left(1 - 10^{-A_1(\lambda)b}\right)d\lambda \quad (30)$$

where $p^0(\lambda)$ is the spectral photon flux density of the lamp, $A_1(\lambda)$ is the water sample absorbance over an optical path length of 1 cm, and b=1.6 cm is the optical path length inside the irradiated solutions (20 mL total volume). The quantum yields are calculated as follows: $\Phi_{^3CDOM^*} = R_{^3CDOM^*}(P_a^{CDOM})^{-1}$, $\Phi_{^1O_2} = R_{^1O_2}(P_a^{CDOM})^{-1}$, and $\Phi_{^\bullet OH} = R_{^\bullet OH}(P_a^{CDOM})^{-1}$. Note that CDOM is by far the main light absorber in natural waters between 300 and 500 nm, which is quite within the range of the used lamp, thus the measured paddy-water absorption spectrum is actually the absorption spectrum of paddy-water CDOM.[168]

Kinetic Data Treatment

The degradation of a given substrate S (either PRP or a probe molecule) was fitted with a pseudo-first order kinetic equation of the form $C_t^S = C_0^S e^{-k_d t}$, where C_t^S is the concentration of S at the time t, C_0^S the initial concentration, and k_d the pseudo-first order degradation rate constant.
The initial transformation rate of S is $R_0^S = k_d^S C_0^S$. The time evolution of phenol formed from benzene (used to measure $^\bullet$OH photogeneration) was fitted with the following equation:

$$C_t^P = \frac{k_f^P C_0^B}{\left(k_d^B - k_d^P\right)\left(e^{-k_d^P t} - e^{-k_d^B t}\right)} \quad (31)$$

where C_0^B and k_d^B are the initial concentration and the pseudo-first order degradation rate constant of benzene, respectively, C_t^P is the concentration of phenol at the time t, and k_f^P and k_d^P are, respectively, the pseudo-first order formation and degradation rate constants of phenol. The initial phenol formation rate is $R_o^P = k_f^P C_o^B$. Note that the formation yield of phenol from benzene is $\eta = 0.7 = k_f^P\left(k_d^B\right)^{-1}$. In some dark runs PRP had an initial lag time before the onset of degradation, which is usually associated with biological processes.[169] In these cases, the PRP time trend was successfully fitted with the following equation (32): [170]

$$C_t = C_0\, e^{-kt}\frac{e^{kL}}{1 + (e^{kL} - 1)e^{-kt}} \quad (32)$$

where C_t is PRP concentration at the time t, as before, C_0 its initial concentration, L the lag time, and k the pseudo-first order rate constant of PRP degradation.

Chemical and Spectroscopic Characterization of Paddy-Field Water

The absorption spectra were measured with a Varian Cary 100 Scan double-beam UV–visible spectrophotometer, using Hellma quartz cuvettes with 1 cm optical path length: The fluorescence EEM matrices were taken with a Cary Eclipse fluorescence spectrofluorimeter, using 10 nm slit width on both excitation and emission and a 1 cm fluorescence quartz cuvette.

The inorganic cations (Ca^{2+}, Mg^{2+}, Na^{+}, K^{+}, NH_4^{+}) were determined with a Dionex DX 500 ion chromatograph, equipped with Rheodyne injector (20 µL sample loop), LC-30 chromatography oven (operated at 30 °C), GP-40 pump for low-pressure gradients, Dionex IonPac CG-12A guard column (4 × 50 mm), Dionex IonPac CS12A column (4 × 250 mm), CERS 500 electrochemical suppression unit, and ED-40 conductometric detector. The eluent was a 20 mmol L^{-1} solution of methanesulfonic acid at 1 mL min^{-1} flow rate.

Inorganic anions (Cl^{-}, NO_3^{-}, SO_4^{2-}) were determined with the same instrument as above, equipped with Dionex IonPac AG9-HC guard column (4 × 50 mm), Dionex IonPac AS9-HC column (4 × 250 mm) and ASRS 300 electrochemical suppression unit. The eluent was a 9 mmol L^{-1} solution of K_2CO_3 at 1 mL min^{-1} flow rate.

Nitrite was determined by pre-column derivatization with 2,4-dinitrophenylhydrazine to produce the corresponding azide in acidic solution (10 min reaction time; the solution of the derivatizing agent in water + HCl + CH_3CN was previously purified by extraction with CCl_4).[171] The derivatized sample was analyzed by liquid chromatography using a reverse-phase C18 LiChroCART column, eluting with a 50:50 mixture of acetonitrile and water (pH 3 by H_3PO_4) at 1 mL min^{-1} flow rate, and using 305 nm as the quantification wavelength. Under these conditions, the retention time of the azide was 4.2 min.

The dissolved organic carbon (DOC) was determined as the difference between total (dissolved) carbon (TC) and inorganic carbon (IC), using a Shimadzu TOC-VCSH instrument. The TOC analyzer was equipped with an ASI-V autosampler and a TNM-1 module for the measurement of total nitrogen (TN), which was determined as well. The pH of the samples was measured with a combined glass electrode connected to a Metrohm 602 pH-meter.

Laser Flash Photolysis Experiments

Flash photolysis runs were carried out using the same apparatus already described (third harmonic -355 nm- Nd:YAG laser used in a right-angle geometry with respect to the monitoring light beam, single pulses energy set to 35 mJ). The triplet sensitization of PRP was studied using CDOM proxies such as 1-nitronaphthalene (1NN, 45.5 μmol L^{-1}), anthraquinone-2-sulfonate (AQ2S, 75.4 μmol L^{-1}), riboflavin (RF, 26.8 μmol L^{-1}), and 4-carboxybenzophenone (CBBP, 185 μmol L^{-1}), under conditions chosen on the basis of previous studies.[59-172-173-174] These compounds are well-known triplet sensitizers under 355 nm laser excitation. The triplet decay was monitored at different PRP concentration values, and the measured pseudo-first order decay constant k_{Sens} was plotted as a function of PRP concentration, as already done for 4BPOH. The concentration of PRP was varied within a maximum range of 0.05–1.25 mM, depending on the effect of PRP addition on k_{Sens}. The slopes of linearly fitted k_{Sens} vs [PRP] data were used to obtain the second-order quenching rate constants between PRP and the photosensitizer triplet states (^{3}1NN*, ^{3}AQ2S*, ^{3}RF*, and ^{3}CBBP*), according to a Stern–Volmer approach.

Photochemical Modeling.

The photodegradation of PRP in paddy water was modeled with the APEX software (Aqueous Photochemistry of Environmentally occurring Xenobiotics).[175] APEX predicts photochemical reaction kinetics from photoreactivity parameters (absorption spectrum, direct photolysis quantum yield and second-order reaction rate constants of a xenobiotic with the main photochemically produced transient species, as well as formation quantum yields and decay kinetics of photoreactive transients in natural water), and from data of water chemistry and depth. The photoreaction pathways modeled by APEX include the direct photolysis and the reaction with the transients $^{\bullet}OH$, $^1O_2$, $CO_3^{-\bullet}$, and ^{3}CDOM*. In this work, for the modeling we used chemical and photochemical paddy-water data, as well as PRP photoreactivity parameters. The used solar spectrum is referred to late May–early June at mid latitude,[176] when PRP is applied to paddy fields in the studied area and the water depth is around 5 cm.[152] The modeled lifetimes are referred to actual 24-h days (the day-night cycle is taken into account) under fair weather in the relevant season.

PRP Photochemical Reactivity

The reactivity of PRP by direct photolysis and upon reaction with $^{\bullet}OH$, $^1O_2$ and ^{3}AQ2S* was assessed by means of steady irradiation experiments, described in the previous paragraph. The results are reported hereafter.

Direct Photolysis

Propanil solutions with initial concentration C_0 = 20 μM and with pH ~ 7 were irradiated under a 20 W Philips TL01 UVB lamp (emission maximum at 313 nm). A control run was also carried out in the dark, by wrapping the cylindrical cells containing the solutions in double aluminum foil, and by placing them under the same lamp used for the irradiation experiments. In this way, comparable temperature and stirring conditions as for the irradiation experiments were achieved. The transformation of PRP in the dark was limited but not negligible.
Under the adopted conditions, irradiated PRP followed a first-order transformation kinetics as shown in Figure 30. The difference between the transformation rates in the dark and under irradiation was R_{PRP} = (8.43±0.77)×10^{-11} M s^{-1}. The photon flux absorbed by PRP can be expressed as usual with the following equation:

$$P_a^{PRP} = \int_\lambda p^0(\lambda)\left(1 - 10^{-\varepsilon_{PRP}(\lambda) b [PRP]}\right) d\lambda = (5.29 \pm 0.51)10^{-10} \quad \text{Einstein L}^{-1}\,\text{s}^{-1} \qquad (33)$$

where $p^0(\lambda)$ is the incident spectral photon flux density of the lamp, $\varepsilon_{PRP}(\lambda)$ the molar absorption coefficient of PRP (see Figure 28 c), b = 1.6 cm the optical path length in solution, and [PRP] = 20 μM. From these data it is possible to obtain the polychromatic photolysis quantum yield of PRP between 300 and 320 nm, where the spectra of the lamp and PRP overlap, as $\Phi_{PRP} = R_{PRP}\,(P_a^{PRP})^{-1}$ = 0.159±0.029.

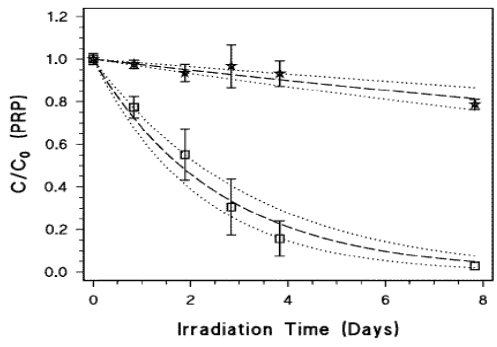

Figure 30

Figure 30. (□) Degradation of 20 μM PRP in Milli-Q water under irradiation. (★) Degradation of 20 μM PRP in Milli-Q water kept in the dark. The solution pH was around 7. Dashed curves are fit functions (Exponential first-order function for □ and linear for ★), while the dotted curves represents the 95% of confidence bands of the fit. The error bounds to the C/C_0 ratio represent ±σ for replicated experiments.

Reaction with •OH

The reaction rate constant between PRP and •OH was determined upon competition kinetics with 2-propanol, using the photolysis of nitrate as •OH source. Figure 31 reports the initial degradation rate R_{PRP} as a function of the molar concentration of 2-propanol, upon UV-B irradiation of 10 mM NO_3^- + 20 µM PRP at pH ~ 7. The trend of R_{PRP} vs. [2-propanol] shows a decrease as the alcohol concentration increases. The main reactions involved in PRP degradation are the following (reactions 34-36), where R• is a radical deriving from 2-propanol oxidation:

$$NO_3^- + h\nu + H^+ \rightarrow {}^\bullet OH + NO_2 \quad \Phi = 0.01 \qquad (34)$$

$$2\text{-propanol} + {}^\bullet OH \rightarrow R^\bullet \qquad k_2 = 1.9\times10^9\ M^{-1}\ s^{-1} \qquad (35)$$

$$PRP + {}^\bullet OH \rightarrow \text{Products} \qquad k_3 \qquad (36)$$

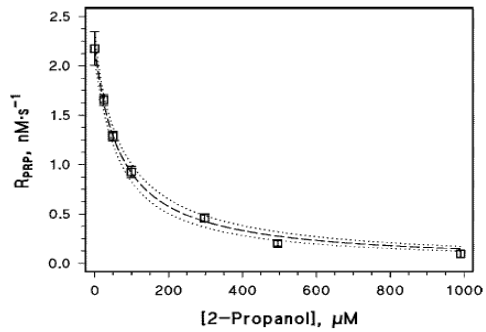

Figure 31

Figure 31. Initial transformation rates (R_{PRP}) of 20 µM PRP upon UV-B irradiation of 10 mM NO_3^-, as a function of the concentration of added 2-propanol. The solution pH was around 7. The dashed curve is the fit function (see equation 37), while the dotted ones represent the 95% confidence bands of the fit. The error bounds to the rate data represent ±σ.

Upon application of the steady-state approximation to •OH, one gets equation 37 for the initial transformation rate of PRP in the presence of 2-propanol, where $R_{\bullet OH}$ is the formation rate of •OH in reaction 34:

$$R_{PRP} = \frac{R_{\bullet OH}\, k_3[PRP]}{k_3[PRP] + k_2[2-propanol]} \qquad (37)$$

From the fit of the experimental data with equation 37 one gets $R_{\bullet OH}=(2.19\pm0.04)\times10^{-9}$ M s^{-1}. Most importantly, the fit yielded $k_3=(6.95\pm0.45)\times10^9$ M^{-1} s^{-1} as the reaction rate constant between PRP and •OH. The value of k_3 obtained here indicates that the reaction between PRP and •OH is not far from diffusive control in aqueous solution.[43]

Reaction with $^1O_2$

Figure 32 reports the initial transformation rate of PRP, as a function of its initial concentration, upon irradiation at pH ~7 of 10 μM Rose Bengal (hereafter RB), used as source of $^1O_2$ as per reaction 38. From the linear trend of the plot one derives R_{PRP} = (2.47±0.53)×10^{-7} [PRP], with R_{PRP} expressed in [M s^{-1}] units and [PRP] in molarity.

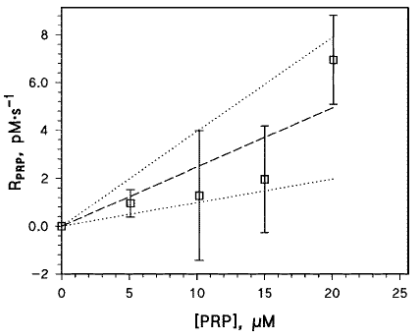

Figure 32

Figure 32. Initial PRP transformation rates (R_{PRP}) upon irradiation of 10 μM Rose Bengal (RB) under the yellow lamp (Philips TL D 18W/16), as a function of the initial PRP concentration. The solution pH was around 7. The linear fit line is dashed, while the dotted lines represents the 95% confidence bands of the fit. The error bounds to the rate data represent ±σ.

The reaction 39 between PRP and $^1O_2$ would be in competition with the thermal deactivation of singlet oxygen shown in reaction 40:

RB + $h\nu$ +O_2 → RB + $^1O_2$		(38)
PRP + $^1O_2$ → Products	k_6	(39)
$^1O_2$ → $^1O_2$	k_7 =2.5×10^5 s^{-1}	(40)

Upon application of the steady-state approximation to $^1O_2$, one gets the following expression for the initial transformation rate of PRP (R_{PRP}):

$$R_{PRP} = \frac{R_{^1O_2}\, k_6[PRP]}{k_7 + k_6[PRP]} \qquad (41)$$

where $R_{^1O_2}$ is the formation rate of $^1O_2$ by 10 μM RB under the used irradiation device. For very low [PRP] one gets that k_6 [PRP] « k_7 and, therefore:

$$\lim_{[PRP]\to 0}\{R_{PRP}\} = R_{^1O_2}\, k_6 k_7^{-1}[PRP] \qquad (42)$$

Equation 42 is consistent with the linear trend of R_{PRP} vs. [PRP] reported in Figure 32. The measurement of $R_{^1O_2}$ was carried out upon irradiation of 10 μM RB + 0.1 mM furfuryl alcohol (FFA), which reacts with $^1O_2$ with a rate constant k_{FFA} = 1.2×10^8 M^{-1} s^{-1}. The time evolution of FFA under irradiation is reported in Figure

33. The initial transformation rate of FFA was R_{FFA} = (4.02±0.13)×10^{-8} M s^{-1}. Photogenerated $^1O_2$ could undergo deactivation or reaction with FFA, and upon application of the steady-state approximation to [$^1O_2$] one obtains:

$$R_{^1O_2} = R_{FFA}\frac{k_7 + k_{FFA}[FFA]}{k_{FFA}[FFA]} \qquad (43)$$

From equation 43 one gets $R_{^1O_2}$ =(8.63±0.27)×10^{-7} M s^{-1}. From equation 38 and Figure 33 one derives $R_{PRP}[PRP]^{-1} = R_{^1O_2}\, k_6 k_7^{-1}$ =(2.47±0.53)×10^{-7} s^{-1}. From the known values of $R_{^1O_2}$ and k_7 one gets k_6 =(7.1±1.8)×10^4 M^{-1} s^{-1} as the reaction rate constant between PRP and $^1O_2$.

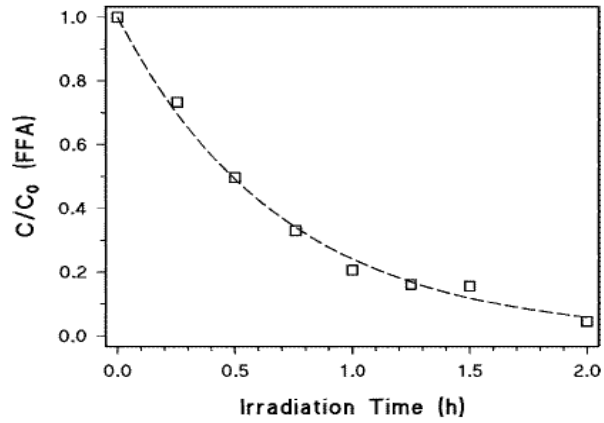

Figure 33

Figure 33. Time trend of FFA (initial concentration 0.1 mM) upon irradiation of 10 µM Rose Bengal under the used yellow lamp (Philips TL D Yellow) at pH 7.

Reaction with irradiated AQ2S

Figure 34 reports the initial transformation rates of PRP, as a function of its initial concentration, upon UV-A irradiation of 0.1 mM AQ2S at pH 7. The direct photolysis of PRP (irradiation without AQ2S) was negligible at the adopted irradiation time scale, up to 4.5 hours. The triplet state ^{3}AQ2S*, which is the main reactive species of AQ2S under irradiation, has a formation quantum yield $\Phi_{^3AQ2S^*}$ = 0.18, and a first-order deactivation rate constant $k_{^3AQ2S}$ =5.0×10^6 s^{-1}.[177] The formation rate of ^{3}AQ2S* is thus expressed as $R_{^3AQ2S^*} = \Phi_{^3AQ2S^*} Pa^{AQ2S}$ (where Pa^{AQ2S} is the photon flux absorbed by AQ2S, in units of Einstein L^{-1} s^{-1}). The transformation or deactivation of ^{3}AQ2S* is in competition with the reaction involving the substrate S (having rate constant $k_{^3AQ2S,S}$, as shown below in Scheme 5.[177] The unwanted reaction between ^{3}AQ2S* and ground-state AQ2S,

which would only complicate the kinetic model of the system, can be minimized by adopting an AQ2S initial concentration of 0.1 mM or lower.[172]

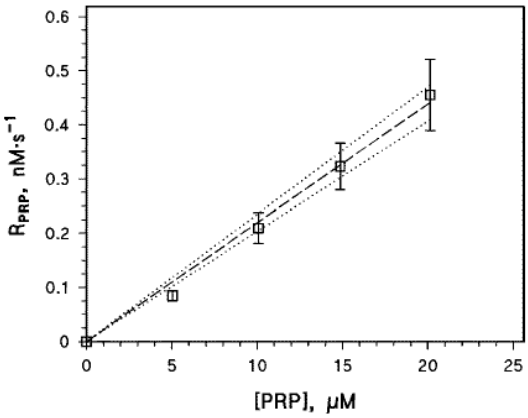

Figure 34

Figure 34. Initial transformation rates of PRP upon UV-A irradiation of 0.1 mM AQ2S, as a function of the initial PRP concentration. The solution pH was around 7. The fit line is dashed, the dotted lines represent the 95% confidence limits of the fit. The error bounds to the rate data represent ±σ.

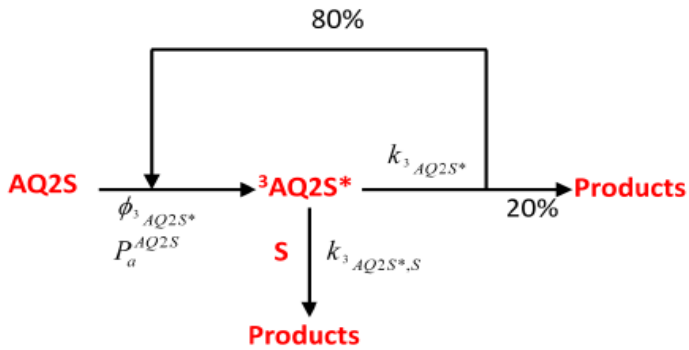

Scheme 5 Schematic of the processes involving the excited states of irradiated AQ2S

If S=PRP, and if the steady-state approximation is applied to ^{3}AQ2S*, the transformation rate of PRP by irradiated AQ2S can be expressed as follows:

$$R_{PRP} = \Phi_{^3AQ2S^*} \cdot P_a^{AQ2S} \cdot \frac{k_{^3AQ2S^*,PRP} \cdot [PRP]}{k_{^3AQ2S^*} + k_{^3AQ2S^*,PRP} \cdot [PRP]} \qquad (44)$$

Under the hypothesis that $k_{^3AQ2S^*,PRP}$ [PRP] « $k_{^3AQ2S^*}$, one gets:

$$R_{PRP} = \Phi_{^3AQ2S^*} \cdot P_a^{AQ2S} \cdot \frac{k_{^3AQ2S^*,PRP}}{k_{^3AQ2S^*}} \cdot [PRP] \qquad (45)$$

PRP absorbs a negligible fraction of the lamp radiation compared to AQ2S. For instance, at 370 nm (the emission maximum of the UVA lamp) the molar absorption coefficient of AQ2S is still significant while PRP does not absorb light as its absorbance signal is below the spectrophotometric limit of detection. Therefore, AQ2S can be safely considered as the only light-absorbing species in solution under the used lamp. The photon flux absorbed by AQ2S can thus be expressed in a reasonable easy way, avoiding the complications of absorption in mixtures: $P_a^{AQ2S} = \int_\lambda p^0(\lambda)\left(1 - 10^{-\varepsilon_{AQ2S}(\lambda)b[AQ2S]}\right)d\lambda$, where $p^o(\lambda)$ is the incident photon flux density of the lamp and $\varepsilon_{AQ2S}(\lambda)b[AQ2S]$ is the absorbance of AQ2S in the irradiated system, where *b* is the light path length, $\varepsilon_{AQ2S}(\lambda)$ is the molar absorption coefficient as a function of wavelength, and [AQ2S] is the molar concentration of AQ2S. In particular, with [AQ2S] = 0.1 mM one has Pa^{AQ2S}=1.22×10^{-6} Einstein L^{-1} s^{-1}.

From the experimental data one gets R_{PRP} = (2.19±0.06)×10^{-5} [PRP] and, upon comparison with equation 45, one derives that $\Phi_{^3AQ2S^*} P_a^{AQ2S} k_{^3AQ2S^*CLO} \left(k_{^3AQ2S^*}\right)^{-1}$ = (2.19±1.8)×10^{-5}. From the known values of $\Phi_{^3AQ2S^*}$ (0.18), $k_{^3AQ2S^*}$ (5.0×10^6 s^{-1}) and Pa^{AQ2S} (1.22×10^{-6} Einstein L^{-1} s^{-1}), one obtains $k_{^3AQ2S^*PRP}$ =(5.0±1.1)×10^8 M^{-1} s^{-1}.

The following Table reports the photoreactivity parameters of PRP, namely the direct photolysis quantum yield and the second-order reaction rate constants with the main photogenerated transient species.

Parameter	Units	mode	Value	pH	Technique
Φ_{PRP}	unitless		0.16 ±0.03	6.8	St. Irr.
$k_{(PRP,(^\bullet OH)}$	L M^{-1} s^{-1}		(7.0±0.5) 10^9	6.6	St. Irr.
$k_{PRP,^1O_2}$	L M^{-1} s^{-1}		(7.1±1.8) 10^4	6.7	St. Irr.
$k_{PRP,CO_3^{-\bullet}}$	L M^{-1} s^{-1}	Literature	(1.4±0.7) 10^7	8.0	LFP
$k_{PRP,^3AQ2S^*}$	L M^{-1} s^{-1}	Reaction	(5.0±1.1) 10^8	6.4	St. Irr.
$k_{PRP,^3AQ2S^*}$	L M^{-1} s^{-1}	quenching	(4.6±0.4) 10^9	6.4	LFP
$k_{PRP,^31N\ N^*}$	L M^{-1} s^{-1}	quenching	(3.6±0.3) 10^8	6.8	LFP
$k_{PRP,^31R\ F^*}$	L M^{-1} s^{-1}	quenching	(1.3±0.3) 10^8	6.6	LFP
$k_{PRP,^34CBB\ P^*}$	L M^{-1} s^{-1}	quenching	(4.9±0.9) 10^8	7.0	LFP

Table 6. PRP photoreactivity parameters. The table also reports the technique used to assess the parameters themselves, where St. Irr = Steady irradiation, LFP = Laser Flash Photolysis

The main advantage when using AQ2S as CDOM proxy is experimental convenience, because AQ2S does not yield important levels of $^{\bullet}OH$ or $^{1}O_2$ under irradiation, and because its second-order rate constants of triplet sensitization can be easily determined by steady irradiation experiment as shown above. However, ^{3}AQ2S* is often too reactive compared to ^{3}CDOM* and it may lead to an overestimation of the triplet-sensitization reactions triggered by ^{3}CDOM*.
Additional photosensitizers were thus chosen, and in particular 1-Nitronaphtalene (1NN), Riboflavine (RF) and 4-Carboxybenzophenone (CBBP). RF and CBBP have several analogies with known CDOM components, [45] while the 1NN triplet state is less reactive compared to ^{3}AQ2S* and it is very conveniently studied by laser flash photolysis.[45] Indeed, the study of the reactivity of ^{3}1NN*, ^{3}RF* and ^{3}CBBP* with PRP required the use of a laser apparatus, which was also used to measure again the second-order reaction rate constant between PRP and ^{3}AQ2S*. It has been reported that the measured laser and steady-irradiation ^{3}AQ2S* second-order rate constants are very similar, but the laser apparatus might also detect physical quenching phenomena that do not lead to chemical reactions and are not taken into account by steady irradiation.[178] Moreover, in some cases the initial substrate is reformed during steady irradiation by a combination of oxidation and reduction processes, which the laser flash photolysis measurements do not take into account. [179]
The experimental laser flash photolysis data obtained in this work are summarized in the following Figure 35.

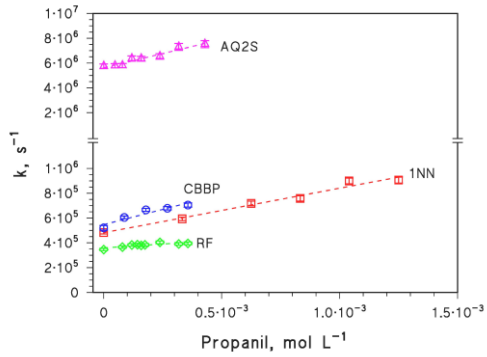

Figure 35

Figure 35 Pseudo-first order decay constants (k) of the triplet states of the investigated photosensitizers (AQ2S, 1NN, RF and; CBBP), as a function of propanil concentration. According to the Stern-Volmer approach, the slope of the linear regression equation gives the second-order reaction rate constant between the relevant triplet state and PRP. The error bars (±3σ) represent the goodness of the fit of the raw experimental data with an exponential function. Experiments were carried out by means of laser flash photolysis (355 nm excitation wavelength, 35 mJ energy per pulse). Note the break in the Y-axis (the triplet state of AQ2S was by far the one undergoing the fastest deactivation).

In the case of PRP + ^{3}AQ2S*, the steady-irradiation (reaction) rate constant was actually an order of magnitude lower than the laser (quenching) one (see Table 6). In contrast, the ^{3}AQ2S* reaction rate constant was not much different from the quenching constants measured with the other photosensitizers.

Figure 36 reports correlation plots of the measured rate constants of triplet sensitization, with the triplet-state energy and with the triplet reduction potential.[180]

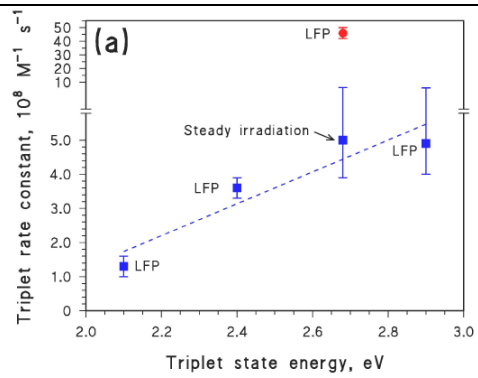

Figure 36 a

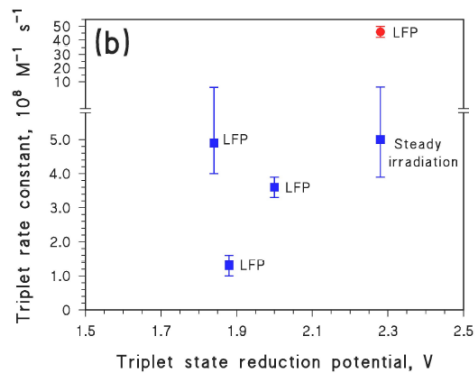

Figure 36 b

Figure 36 Correlation plots of the triplet sensitization rate constants of PRP measured in this work (a reaction rate constant measured by steady irradiation and the quenching rate constants measured by laser flash photolysis, LFP) with: (a) the energies of the triplet states of AQ2S, 1NN, 4CBP and RF; (b) the triplet-state reduction potentials.

The best correlation is obtained when taking the triplet energy into account, which might suggest that the reactions would at least partially involve an energy transfer from the sensitizer triplet states to PRP.[180] If an important fraction of the transferred energy is dissipated (for example by internal conversion), that might explain the difference between the measured quenching and reaction rate constants in the case of AQ2S. As a starting hypothesis, a PRP triplet sensitization rate constant of around 10^8 M^{-1} s^{-1} was assumed hereafter. If the difference between the ^{3}AQ2S* quenching and reaction rate constants is due to back-reduction processes, or if important energy dissipation pathways are operational, then there could be implications for the role of triplet-sensitized reactions in an environmental setting.[179]

The reactivity of PRP with $^1O_2$ is very low, ending up with $k_{PRP,^1O_2}$ ~ 10^5 M^{-1} s^{-1}. This is near the lower end of the rate constant values that can measured with the steady-irradiation methodology that uses RB as $^1O_2$ source. This is the most likely reason for which both the experimental data reported in Figure 32 and the $k_{PRP,^1O_2}$ values shown in Table 6 are affected by a non-negligible uncertainty.

Negligible formation of 34DCA from PRP was detected in the irradiation experiments, while almost quantitative formation of 34DCA was observed in the dark at pH 8 or lower, as shown in Figure 37. The time trend of PRP in the dark showed a clear lag time, which could suggest a biological process of PRP degradation [169-170] and would be consistent with the known PRP biodegradability.[181] The elevated formation yield of 34DCA from PRP observed in our dark experiments is consistent with the known pathways of PRP biodegradation, too.[150-152]

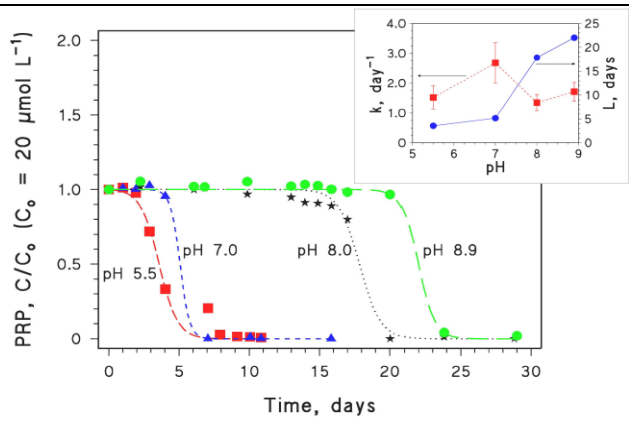

Figure 37

Figure 37 Time trend of 20 µmol L^{-1} PRP in the dark, in the presence of a phosphate buffer (50mmol L^{-1} total phosphate) at different pH values. The experimental curves were fitted with equation (32), and the values of *k* (pseudo-first order degradation rate constant) and L (lag time) as a function of pH are reported in the inset. The error bars (±σ) represent the uncertainty of the fit to the experimental data. In the case of L the bars were smaller than the symbols.

Chemical and Photochemical Characterization of Paddy-Field Water

The results of the chemical characterization of the paddy-field water samples are reported in Table 7. The data show low values of nitrate and nitrite and quite elevated DOC, which with appropriate substrates might produce potentially important degradation by ^{3}CDOM* and $^1O_2$.[9] The Rovasenda sample was also less rich in ionic species compared to the others. The fluorescence matrix (EEM) spectra reported in Figure 38 suggest the occurrence of humic materials [94] in all the investigated samples. The tentative humic abundance order Rovasenda > S.GermanoVC > Santhià is coherent with the absorption spectra (see Figure 29 above), because CDOM is the main radiation absorber and humic substances are major CDOM constituents.[9]

The degradation of TMP (^{3}CDOM* probe) spiked to the water samples under study was significant under irradiation and practically negligible in the dark (see Figure 39). The quantum yields of ^{3}CDOM* formation from irradiated paddy-field water, Φ_{3CDOM*}, are reported in Table 7 together with the corresponding steady-state [^{3}CDOM*] values. It is $\Phi_{3CDOM*} \sim 10^{-2}$, not far from the ^{3}CDOM* quantum yields measured upon irradiation of surface water samples under comparable conditions.[94] The time trend of FFA ($^1O_2$ probe) is also reported in Figure 39, which allows for a comparison with the ^{3}CDOM* production.

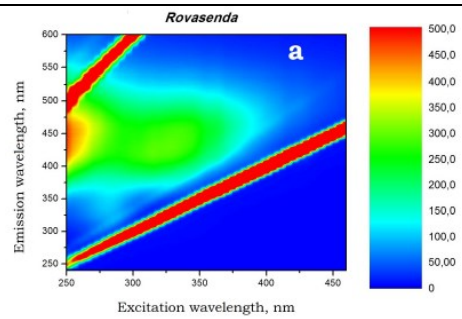

Figure 38 a

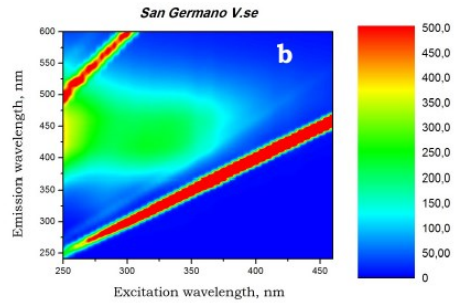

Figure 38 b

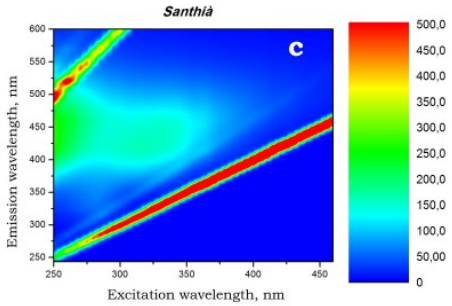

Figure 38 c

Figure 38 Excitation-Emission matrix (EEM) fluorescence spectra of the three studied paddy-field water samples: (a) Rovasenda, (b) San Germano Vercellese, and (c) Santhià. These spectra were taken by using 10 nm slit width for both the excitation and the emission beam.

Differently from TMP, the degradation of FFA in the dark was significant in two out of the three studied samples (Rovasenda and Santhià), thus the subtraction of the FFA transformation rate measured in the dark from that obtained under irradiation (R_{FFA}) had a non-negligible impact on the calculation of the $^1O_2$ formation rate. The quantum yields $\Phi_{^1O_2}$ are shown in Table 6 and, in this case as well ($\Phi_{^1O_2}$ = 10^{-3}–10^{-2}), they are similar to the quantum yields previously measured for lake water samples under a comparable irradiation setup.[94] Although our approach only measures the TMP-reactive triplet states, the fact that $\Phi_{^1O_2}$ <Φ_{3CDOM*}, with $\Phi_{^1O_2}$ not too far from Φ_{3CDOM*}, suggests an overall internal consistence of results obtained by using different probe molecules.[9-94] The values of $\Phi_{^{\bullet}OH}^{CDOM}$, $^{\bullet}$OH scavenging rate constant (k'_{Scav}) and steady-state [$^{\bullet}$OH] for the irradiated samples are reported in Table 6 as well. The measured $\Phi_{^{\bullet}OH}^{CDOM}$ in the 10^{-5} range is comparable to that found in irradiated surface waters.[94]

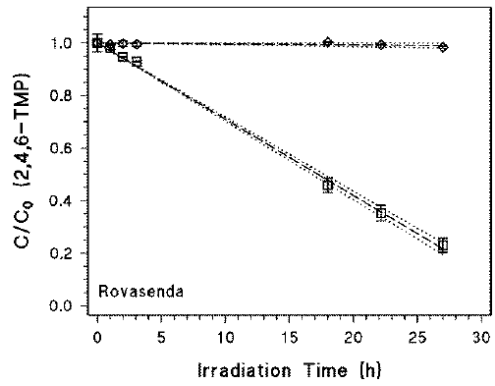

Figure 39 a

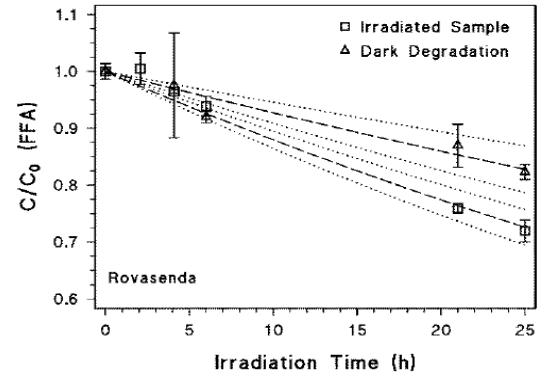

Figure 39 b

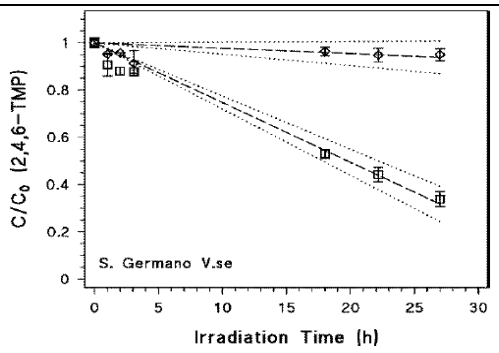

Figure 39 c

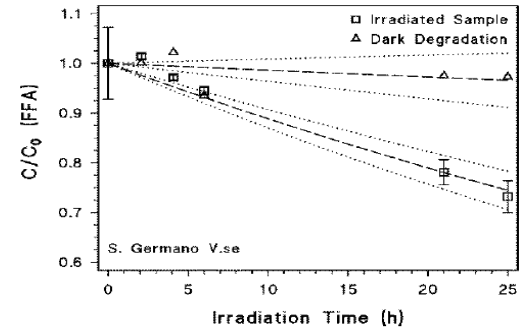

Figure 39 d

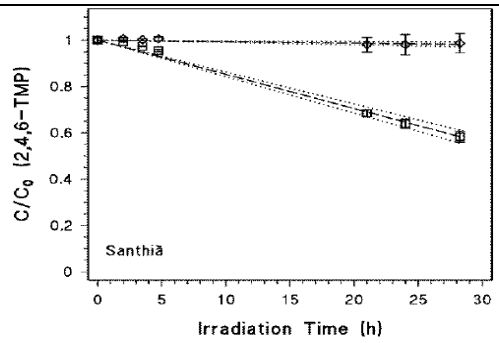

Figure 39 e

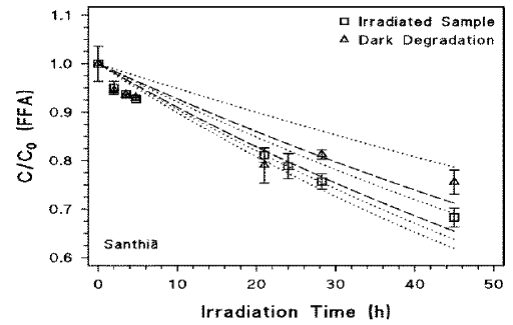

Figure 39 f

Figure 39 *Left side* In figure (a), (c) and (e) it is shown the time tend of 1 mM 2,4,6-trimethylphenol (TMP), the ^{3}CDOM* probe, spiked to the studied paddy-water samples, under irradiation (□) and in the dark (◊).

Right side In figure (b), (d) and (f) it is shown the time tend of 1 mM furfuryl alcohol (FFA), the $^1O_2$ probe, spiked to the studied paddy-water samples, under irradiation (□) and in the dark (◊).

Irradiation was carried out under the Philips TL K05 lamp (the emission spectrum of this lamp is reported above in Figure 29). Fit curves are dashed, while the dotted curves represent the 95% confidence limits of the fit.

Sample	TC (mgC L^{-1})	TC (mgC L^{-1})	IC (mgC L^{-1})	NO_3^- (mgN L^{-1})	NO_2^- (mgN L^{-1})	pH	$SUVA_{254nm}$ (L m^{-1} mgC^{-1})
Rovasenda	15.68±0.16	9.58±0.17	6.09±0.07	< LoD	< LoD	7.0	2.1
S.Germ.Verc.	24.92±0.44	6.80±0.54	18.11±0.31	< LoD	< LoD	8.2	2.4
Santhià	19.52±0.35	4.84±0.43	14.68±0.25	1.72±0.06	0.018±0.003	7.7	2.4

Table 7 Chemical Parameters of the paddy water samples under investigations. TC, DOC and IC were determined with the TOC analyzer, nitrate with ion chromatography, nitrite with HPLC-UV determination after pre-column derivatization. The specific UV absorbance at 254nm ($SUVA_{254nm}$) is the ratio between the paddy water absorbance at 254 nm (referred to a 1 m optical path length) and the DOC.

Sample	R_{TMP} (mol L^{-1} s^{-1})	$\Phi_{^3CDOM^*}$ (unitless)	[^{3}CDOM*] (mol L^{-1})	R_{FFA} (mol L^{-1} s^{-1})	$\Phi_{^1O_2}$ (unitless)	[$^1O_2$] (mol L^{-1})
Rovasenda	(1.34±0.10) 10^{-8}	(3.66±0.12) 10^{-2}	(3.33±0.03) 10^{-14}	(1.47±0.27) 10^{-10}	(6.96±1.47) 10^{-3}	(1.27±0.24) 10^{-14}
S.Germ.Verc.	(9.90±0.63) 10^{-9}	(2.93±0.26) 10^{-2}	(2.48±0.16) 10^{-14}	(2.91±0.33) 10^{-10}	(1.70±0.22) 10^{-2}	(2.82±0.29) 10^{-14}
Santhià	(4.89±0.25) 10^{-9}	(2.11±0.16) 10^{-2}	(1.22±0.06) 10^{-14}	(5.13±2.97) 10^{-11}	(3.91±2.35) 10^{-3}	(4.53±2.62) 10^{-15}

Sample	R_{Phenol} (mol L^{-1} s^{-1})	$\Phi_{^{\bullet}OH}^{CDOM}$ (unitless)	K'_{Scav} (s^{-1})	[$^{\bullet}$OH] (mol L^{-1})
Rovasenda	(9.41±0.62) 10^{-12}	(2.93±0.27) 10^{-5}	(1.36±0.09) 10^{6}	(9.88±1.30) 10^{-18}
S.Germ.Verc.	(4.63±0.85) 10^{-12}	(1.60±0.34) 10^{-5}	(9.77±1.79) 10^{5}	(6.77±2.48) 10^{-18}
Santhià	(7.88±0.23) 10^{-12}	(2.31±0.58) 10^{-5}	(1.12±0.03) 10^{6}	(1.01±0.06) 10^{-17}

Table 8 Photochemical Parameters of the paddy water samples under investigations. The initial degradation rates of TMP and FFA under irradiation (R_{TMP} and R_{FFA}), as well as the initial formation rate of phenol from benzene (R_{Phenol}) are reported, together with the other photochemical data mentioned in the text.

PRP (Photo)Degradation in Paddy-Field Water

Water samples (20 mL) from the three paddy-fields under study were spiked with 20 µmol L^{-1} PRP and irradiated under the TL K05 lamp. Dark control experiments were also carried out. The initial PRP photodegradation rate constants are reported in Figure 40.

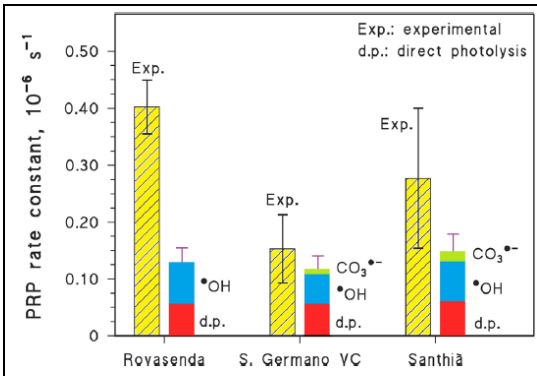

Figure 40

Figure 40 Experimental first order rate constants of PRP phototransformation in irradiated paddy water, compared to the predicted rate constant relative to photolysis, $^{\bullet}OH$ and $CO_3^{\bullet-}$ reactions. The error bars (±σ) represent the uncertainties of experiments and modeling.

The TL K05 lamp was previously used to measure ^{3}CDOM*, $^1O_2$ and $^{\bullet}OH$ photoproduction, thus the values already determined of [$^{\bullet}OH$], [$^1O_2$] and [^{3}CDOM*] in the same samples (see Table 8) are relevant to the measured PRP phototransformation. For $CO_3^{\bullet-}$ it was assumed production by $^{\bullet}OH+HCO_3^-/CO_3^{2-}$ and scavenging by DOM.[92]
The formation rate of $CO_3^{\bullet-}$ because of $^{\bullet}OH$ oxidation of HCO_3^- and CO_3^{2-} can be expressed as follows:

$$R_{CO_3^{\bullet-}} = R_{\bullet OH} \frac{k_{\bullet OH,HCO_3^-}[HCO_3^-] + k_{\bullet OH,CO_3^{2-}}[CO_3^{2-}]}{k_{\bullet OH,DOM}\,DOC + k_{\bullet OH,HCO_3^-}[HCO_3^-] + k_{\bullet OH,CO_3^{2-}}[CO_3^{2-}]} \quad (46)$$

The concentration values of carbonate and bicarbonate in each sample were calculated from the values of IC and pH reported in Table 7, and the steady-state [$CO_3^{\bullet-}$] was then calculated as follows:

$$[CO_3^{\bullet-}] = \frac{R^{\bullet OH}_{CO_3^{\bullet-}}}{k_{CO_3^{\bullet-},DOM}\,TOC} \quad (47)$$

The calculations yielded [$CO_3^{\bullet-}$] = 2.5×10^{-17}, 3.5×10^{-16} and 1.0×10^{-15} mol L^{-1} for Rovasenda, San Germano Vercellese and Santhià, respectively. For $k_{CO_3^{\bullet-},DOM}$, a mean value was used taken from the literature (2.35×10^4 L mg_C^{-1} s^{-1}).[92] The modeled first order rate constants of PRP phototransformation in each paddy-water sample were obtained as follows:

$$k_{PRP} = \frac{\Phi_{PRP} P_a^{PRP}}{[PRP]} + k_{PRP,I_{OH}}[^{\bullet}OH] + k_{PRP,^3CDOM^*}[^3CDOM^*] + k_{PRP,^1O_2}[^1O_2] + k_{PRP,CO_3^{\bullet-}}[CO_3^{\bullet-}] \quad (48)$$

where P_a^{PRP} was calculated by taking in account the competition for irradiance between PRP and CDOM, as follows:

$$P_a^{PRP} = \int_\lambda p^0(\lambda) \frac{A_{PRP}(\lambda)}{A_{PRP}(\lambda) + A_{CDOM}(\lambda)} \left(1 - 10^{-A_{PRP}(\lambda) - A_{CDOM}(\lambda)}\right) d\lambda \quad (49)$$

The $^1O_2$ process was found to be insignificant, while the modeled contributions of direct photolysis, $CO_3^{\bullet-}$ and $^\bullet OH$ to PRP phototransformation in irradiated paddy-field water are reported in Figure 40. Within the uncertainty associated with experimental data and model predictions, the sum of the $^\bullet OH$ and $CO_3^{\bullet-}$ reactions and of the direct photolysis could well account for the experimental phototransformation kinetics only in the case of San Germano Vercellese and, more marginally, for Santhià. In the case of Rovasenda, where additionally the $CO_3^{\bullet-}$ reactions were totally negligible, the three considered processes largely underestimated the PRP phototransformation. The ^{3}CDOM* reactions were intentionally excluded from these calculations because, when using the [^{3}CDOM*] values obtained with the TMP probe and assuming $k_{PRP,^3CDOM*}$ = 10^8 L mol^{-1} s^{-1}, one predicts in all the cases a phototransformation kinetics that is around an order of magnitude faster than the experimental one. Three possible explanations can be advanced: (i) the triplet states might react fast with TMP but much more slowly or not at all with PRP, in which case the measured [^{3}CDOM*] and/or the assumed $k_{PRP,^3CDOM*}$ might not apply to PRP photodegradation; (ii) the ~10^8 L mol^{-1} s^{-1} rate constants obtained by laser flash photolysis might considerably overestimate the actual reaction rate constants, for example because of physical quenching or energy dissipation; and (iii) PRP may undergo initial oxidation by reaction with ^{3}CDOM*, followed by back-reduction of partially-oxidized PRP to PRP by the antioxidant moieties occurring in DOM. This back-reduction process has already been observed with several substrates and, depending on the molecule, it can be irrelevant or extremely important. Interestingly, back reduction has been demonstrated to be insignificant in the case of the $^\bullet OH$ reactions.[179]

If $k_{PRP,^3CDOM*}$ < 10^8 L mol^{-1} s^{-1}, by using the TMP-derived [^{3}CDOM*] values one can compute which values of $k_{PRP,^3CDOM*}$ would be needed to match the experimental data. For Rovasenda one gets $k_{PRP,^3CDOM*}$ ~ 8 × 10^6 L mol^{-1} s^{-1} and, with very large error bars, 10^6 L mol^{-1} s^{-1} for San Germano Vercellese and 10^7 L mol^{-1} s^{-1} for Santhià. Excluding the case of San Germano Vercellese, it seems that $k_{PRP,^3CDOM*}$ ~ 10^7 L mol^{-1} s^{-1} might be used together with TMP-derived [^{3}CDOM*] to predict the PRP phototransformation kinetics. This $k_{PRP,^3CDOM*}$ value will thus be included hereafter in photochemical modeling.

The dark experiments showed an initially insignificant PRP degradation (lag phase of 10–15 h), followed by fast transformation. The trend was comparable to that of the dark experiments reported previously, except for the shorter lag time. The latter finding is reasonable for a microbiological process, which should be easier in filtered natural waters compared to ultra-pure laboratory water. Surprisingly, degradation was eventually faster in the dark than under irradiation. The dark PRP transformation produced 34DCA with 90–100% yield (lowest for Rovasenda

and highest for San Germano Vercellese), while the 34DCA yield under irradiation was only 13–19% (lowest for Santhià and highest for San Germano Vercellese). Considering that photochemical reactions do not appear to produce 34DCA, one has to conclude that photoinduced processes prevailed in the irradiated samples. For this to be possible (remember that PRP degradation in the dark was eventually faster than under irradiation), irradiation had to inhibit the dark PRP transformation. Under the hypothesis that the dark transformation was biological (which is reasonable in the presence of a lag time), an inhibition under irradiation would not be surprising because it is well-known for UV radiation to inactivate microorganisms.[182] The paddy water was filtered before irradiation or dark experiments, which would eliminate part of the microorganisms. Therefore, biological processes are expected to play a more important role in pristine paddy water than in the experimental conditions observed in this work.

Modelling of PRP Photochemical Transformation

The photochemical modeling used as input data the PRP photoreactivity parameters (Table 6), its absorption spectrum (Figure 28 a) and the paddy-water chemical and photochemical parameters (Table 7 and Figure 29). A water depth of 5 cm was assumed, which is typical of the period of PRP application and, for the same reason, a late May–early June fair-weather sunlight was used.[152] Because of the large spectral overlap between the TL K05 lamp and sunlight, the quantum yields measured under the lamp were used for modeling. On the basis of results obtained in the previous section, we considered direct photolysis, $^{\bullet}OH$ and $CO_3^{\bullet-}$ reactions, as well as triplet sensitization with $k_{PRP,3CDOM^*} \approx 10^7$ L mol^{-1} s^{-1}, as the important photodegradation pathways of PRP. To generalize on different paddy fields, a relationship was sought between the water absorption spectrum and the DOC, as already done for surface water.[176] The $A_1(\lambda)$ DOC^{-1} values of the paddy-water samples under study were very similar (as shown in Figure 41), which reflects the similar values of $SUVA_{254\ nm}$ (see Table 7).

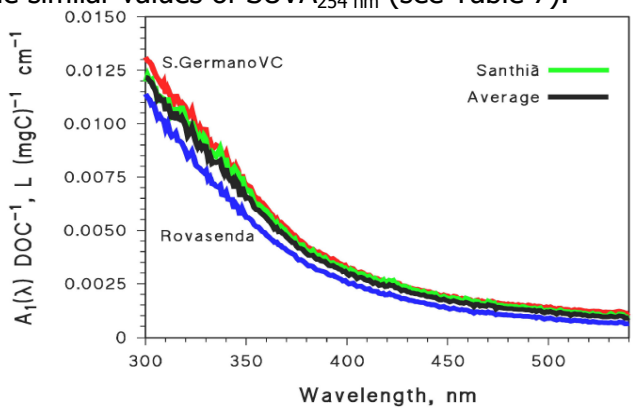

Figure 41

Figure 41 DOC-normalized absorption spectra ($A_1(\lambda)$ DOC^{-1}, where DOC = dissolved organic carbon) of the studied paddy-field water samples. The average of three spectra is

also reported, and the exponential fit of the average spectrum between 300 and 540 nm yielded.

$$A_1(\lambda)\ DOC^{-1} = (0.674 \pm 0.022)e^{-(0.013\pm0.001)\lambda}$$

The exponential fit of the average spectrum in the 300–540 nm wavelength interval yielded $A_1(\lambda)\ DOC^{-1} = (0.674 \pm 0.022)\ e^{-(0.013\pm0.001)\lambda}$. The latter function was used to model PRP photochemistry in paddy water with varying DOC. The pre-exponential factor is slightly larger but it is of the same order of magnitude as the surface water one, while the spectral slope (S = 0.013 ± 0.001) is slightly lower than that of surface waters.[175] Both issues suggest that paddy water may contain CDOM of comparable or slightly higher molecular weight than surface waters. An average of the experimental values was also taken for the transient formation quantum yields ($\Phi_{^{\bullet}OH}^{CDOM} = (1.68 \pm 0.49)\times10^{-5}$; $\Phi_{CDOM}^{^3CDOM^*} = (2.91 \pm 0.76)\times10^{-2}$) and for the pseudo-first order $^{\bullet}OH$ scavenging rate constant, $k'_{Scav} = [(1.55 \pm 0.22)\times10^5 L(mg_C)^{-1}s^{-1}]$ DOC. The expression of k'_{Scav} as a function of the DOC is justified by the fact that DOC measures DOM that is a major $^{\bullet}OH$ scavenger.[9] The proportionality factor $(1.55 \pm 0.22)\times10^5$ L $(mg_C)^{-1}$ s^{-1} found here for paddy water is significantly higher than that usually found in surface waters. The elevated biological activity in flooded paddies possibly causes DOM to be continuously produced and consumed. Not having enough time to undergo phototransformation, paddy-water DOM might well be more photolabile than surface water DOM. In fact, the latter becomes more photochemically stable when it undergoes photoprocessing in the natural environment.[183]

The PRP pseudo-first order phototransformation rate constants in flooded paddy fields, modeled for mid-latitude conditions, are reported in Figure 42a together with the corresponding half-life times. It is shown that for reasonable values of the DOC (which cannot be near zero due to the presence of the rice plants), the phototransformation can approach the typical PRP lifetimes of some days [152-154] only for elevated values of nitrate and nitrite (nearing 1 mmol L^{-1} and 10 μmol L^{-1}, respectively). In the paddy fields of the present study, having 0.1 mmol L^{-1} nitrate or less and DOC above 4 mg_C L^{-1}, the PRP half-life times would be longer than 15 days and could hardly compete with other processes including biodegradation.[152-154] However, flooded paddies are very effective denitrification reactors.[184] If they were irrigated with nitrate-rich water containing around 10^{-3} mol L^{-1} nitrate (corresponding to ~15 mg_N L^{-1} or ~60 mg NO_3^- L^{-1}), then in addition to achieving denitrification they would also divert a considerable PRP fraction away from 34DCA generation. In these conditions, an important fraction of PRP degradation is expected to take place by reaction with $^{\bullet}OH$ and $CO_3^{\bullet-}$ (Figure 42b). In contrast, in the presence of low nitrate and nitrite concentration values, the direct photolysis and, at high DOC, the ^{3}CDOM* reactions may be quite important for PRP phototransformation (Figure 42c).

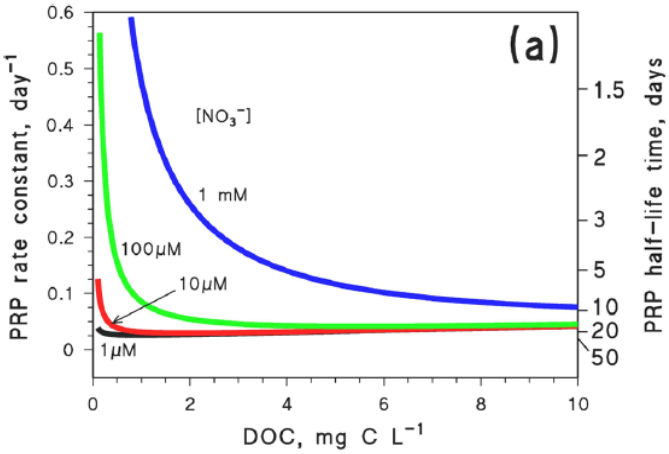

Figure 42 a

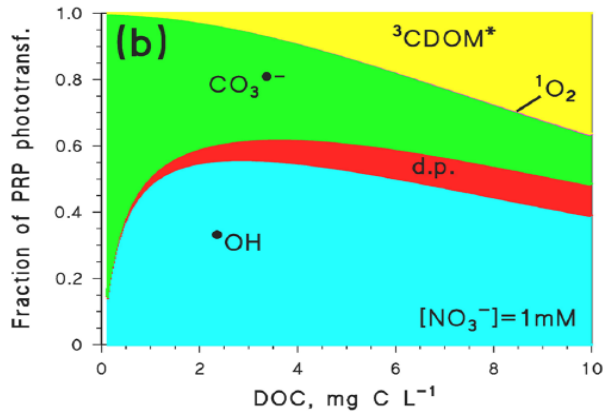

Figure 42 b

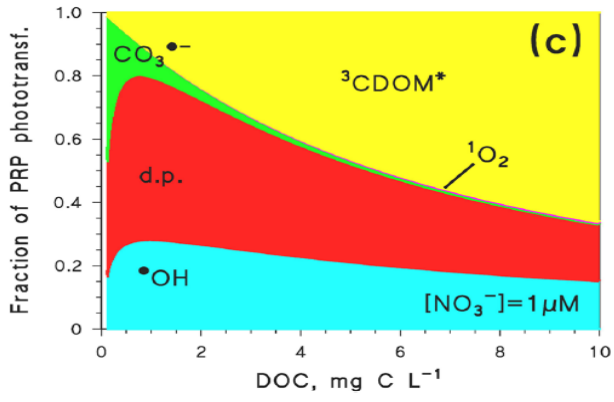

Figure 42 c

Figure 42 (a) APEX-modeled pseudo-first order rate constants of PRP phototransformation, and corresponding half-life times, in paddy-field water in late May-early June as a function of the DOC. (b,c) Modeled fractions of PRP phototransformation accounted for by direct photolysis (d.p.) and indirect photochemistry, as a function of the DOC for nitrate concentrations of (b) 1 mmol L^{-1} and

(c) 1 μmol L^{-1}. The nitrate concentration is reported over each plot. It was assumed $[NO_2^-] = 10^{-2}$ $[NO_3^-]$, which is often the case for environmental waters and also, approximately, for the Santhià sample in this work. Other water conditions: 5 cm depth, 1 mmol L^{-1} HCO_3^-, and 10 μmol L^{-1} CO_3^{2-}.

However, at low nitrate and nitrite the overall photodegradation would play a minor to negligible role in PRP attenuation. In contrast, PRP photodegradation would be important with elevated nitrate and nitrite, and in this case the $^{\bullet}OH$ and $CO_3^{\bullet-}$ processes would prevail over a wide range of DOC conditions (Figure 42b,c). Therefore, $^{\bullet}OH$ and $CO_3^{-\bullet}$ have a potentially elevated environmental significance in PRP phototransformation.

Outcomes of the Propanil Study – Environmental Implications

Depending on the conditions, the photochemical degradation of PRP can be a competitive pathway with respect to the dark processes, possibly microbiological. The most significant photoprocesses in environmental settings are those induced by $^{\bullet}OH$ and $CO_3^{\bullet-}$, because they would prevail with elevated nitrate and/or nitrite concentrations that would make PRP photodegradation to be about as important as biotransformation. In contrast, direct photolysis and ^{3}CDOM* reactions would prevail with low nitrate and nitrite, and in these conditions the photochemical reactions are unlikely to be important compared to the dark processes. The triplet-sensitized degradation of PRP in paddy water would be considerably slower than expected from experiments with model sensitizers. Despite the limited environmental significance of the process, further experiments will be required to elucidate this point. The photoreactions do not produce important amounts of 34DCA, while dark processes generate 34DCA with approximately quantitative yield. Elevated nitrate concentrations that enhance PRP photodegradation may occur if one wants to use flooded paddies as denitrification bioreactors, by irrigating them with water containing elevated nitrate levels. In this case an important fraction of PRP would be degraded without producing 34DCA, thereby gaining a further advantage in addition to denitrification.

Section III-Environmental Modeling

In this last section, natural lakes were taken in account and a mapping study on Swedish lake photochemistry is reported, with some simulations of the half-time life of specific pollutants, for which the needed photochemical parameters were available in literature.

Photoinduced reactions over large geographic regions: A phochemical mapping of Sweden

The photochemically induced processes discussed in this thesis are important for the attenuation of xenobiotics, but also for the modification and decomposition of dissolved organic matter in sunlit waters.[7] To protect resources such as plants, aquatic biota and drinking water, it is therefore crucial to understand the environmental fate and degradation pathways of pollutants.[7] However, little to nothing is known about the role of different photoreactions on large geographic scales, especially in boreal regions where the largest lake area on earth is located.[185] To gain first insight into the relevance of the different photoreactions in boreal lakes, a modeling study was conducted to obtain a large scale simulation of the likely photochemical behavior for a range of different compounds. The approach presented here has a number of assumption and uncertainties, but it provides an integrated method able to assess chemical persistence in aquatic biomes for different climate zones[186]. This study takes into account both direct processes (direct photolysis) and indirect photochemistry triggered by photogenerated transient species, as well as the depth of the water column.

In this work, a unique large-scale dataset was used that is made up of 1048 boreal lakes, distributed across 14 degrees of latitude. The available data included, for each lake, the TOC (useful to estimate DOM), nitrate, pH, inorganic carbon (sum of carbonic acid, carbonate and bicarbonate, which combined with pH can give the concentration of the three species) and CDOM absorption spectra, as well as the latitude and longitude coordinates.[187] With their comparatively high DOM concentration, the studied water environments are representative of boreal lakes in general.[188] Chemical measurements, atmospheric radiative transfer and aquatic photochemical kinetic data were merged in order to obtain a model able to resolve the environmental persistence of model

xenobiotics *via* the different photochemical reaction pathways, and to undersantd how the photoreaction pathways may change when browning and eutrophication occour.[69]

In this work we took into account five model anthropogenic compounds, namely APAP (Acethyl-Para-AminoPhenol, a common drug used to treat pain and fever),[163] DMM (DiMethoMorph, a fungicide used in agriculture),[189] EHMC (EthylHexyl Methoxy Cinnamate, a widely used UV-B filter),[48] FEN (FENuron, an erbicide),[56] and NIC (NICotine, the well-known alkaloid deriving mostly from tobacco)[54]. This list was chosen because these compounds are emerging pollutants, it is reasonable to find them in natural waters due to anthropogenic contamination and, most importantly, their photochemical behavior including the second-order rate constants with the modeled transients is reported in the literature.

Boreal Lake Dataset

Water chemical and chromophoric dissolved organic matter (CDOM) absorbance data from 1048 lakes, distributed across Sweden between latitudes from 55°N to 69°N, were obtained from the 2009 Swedish National Lake Inventory which is conducted by the Swedish University of Agricultural Sciences. Lake water had been sampled between 6 September and 24 November 2009, in most cases in the middle of the lake at 0.5 m depth. A summary of lake properties has been published earlier.[187]

Photon Absorption Calculations

For each lake, daily-integrated downwelling irradiation just below the water surface ($E_{od}^{Day}(\lambda,-0)$; Einstein m^{-2} day^{-1} nm^{-1}) was simulated for the autumnal equinox 2009 (Sep 22), as described previously.[187] Briefly, clear-sky downwelling spectra of global and diffuse irradiance reaching the water-air interface were derived for 280 to 600 nm with an hourly time step using the atmospheric radiative transfer model libRadtran 1.6.[190] The clear-sky irradiance spectra were corrected for attenuation by clouds using a cloud effect function,[191] which was parameterized using UV irradiance measurements from Norrköping, Sweden, during 2008 (n=2400). Total cloud cover data was retrieved from the archive of the operational mesoscale analysis system MESAN at the Swedish Meteorological and Hydrological Institute.[192] Transmittance of the above water surface irradiance across the air-water interface was calculated separately for the diffuse and direct fraction. The just below water surface hourly diffuse and direct irradiance spectra were converted to downwelling irradiance spectra and integrated to obtain daily irradiation spectra.

CDOM-absorbed photons ($P_a^{CDOM,Day}$; Einstein m^{-3} day^{-1}) were calculated for Sep 22, 2009 and 280 to 600 nm (with 1 nm resolution) from the surface of each lake in 0.005 m increments down to the target lake depths, as:

$$P_a^{CDOM,Day}(z) = \int_{\lambda_{min}}^{\lambda_{max}} E_{od}^{Day}(\lambda,-0)\, a_g(\lambda)\, e^{-(K_d(\lambda)z)}\, d\lambda \qquad (46)$$

where z is depth (m), λ_{min} and λ_{max} is the minimal and maximal wavelength (nm), $E_{od}^{Day}(\lambda,-0)$ is daily-integrated-downwelling scalar irradiation just below the water surface (Einstein m^{-2} day^{-1} nm^{-1}), a_g is the CDOM Napierian absorption coefficient (m^{-1}) and K_d is the vertical attenuation coefficient for downward irradiance (m^{-1}). a_g was calculated from measured CDOM absorbance, as the pre-exponential coefficient obtained when fitting the absorption spectrum.[117] K_d was estimated using regression relationships with a_g derived from literature data (n=565) for nine wavelengths between 300 and 400 nm, with subsequent fitting of an exponential function to obtain continuous spectra (spectral slope).[187]

Nitrate-absorbed photons ($P_a^{NO_3^-,Day}$; Einstein m^{-3} day^{-1}) were calculated as follows:

$$P_a^{NO_3^-,Day}(z) = \int_{\lambda_{min}}^{\lambda_{max}} \frac{\varepsilon_{NO_3^-}(\lambda)\, C_{NO_3^-}}{a_g(\lambda)}\, E_{od}^{Day}(\lambda,-0)\, a_g(\lambda)\, e^{-(K_d(\lambda)z)}\, d\lambda \qquad (47)$$

where $\varepsilon_{NO_3^-}$ is the molar absorption coefficient of nitrate (L μg N^{-1} m^{-1}) and $c_{NO_3^-}$ is nitrate concentration (μg N L^{-1}). The depth-specific CDOM- and nitrate-absorbed photons were integrated down to z = 0.05 m and down to the average depth (z_{avg}) of each lake using the trapezoid rule. Photon absorption by nitrite was not considered because its concentration is usually below the detection limit of the analytical method and, more importantly, because CDOM usually strongly prevailed over nitrate as $^{\bullet}OH$ source. Therefore, it is expected that CDOM out-competes also nitrite for $^{\bullet}OH$ generation

Photochemical modeling

To calculate the steady-state concentration of the photoreactive transient species, the photon fluxes absorbed by CDOM and nitrate were expressed as $P_a^i(z)$ (where *i* = CDOM or NO_3^-; Einstein L^{-1} s^{-1}). The formation rates of hydroxyl radicals ($^{\bullet}OH$) and singlet oxygen ($^1O_2$; mol L^{-1} s^{-1}) were calculated as follows:

$$R_{^{\bullet}OH}^{tot}(z) = R_{^{\bullet}OH}^{CDOM}(z) + R_{^{\bullet}OH}^{NO_3^-}(z) = \Phi_{^{\bullet}OH}^{CDOM}\ P_a^{CDOM}(z) + \Phi_{^{\bullet}OH}^{NO_3^-}\ P_a^{NO_3^-}(z) \qquad (48)$$

$$R_{^1O_2}^{tot}(z) = \Phi_{^1O_2}^{CDOM}\ P_a^{CDOM}(z) \qquad (49)$$

The formation quantum yields of photoreactive transient species by irradiated CDOM may vary among different aquatic environments, but such variations are

more limited than the environmental variability might suggest.[9] For our simulations, we used reasonable average values for lake water, namely $\Phi_{\bullet OH}^{CDOM}$ = 3 10^{-5} and $\Phi_{^1O_2}^{CDOM}$ = 1.2 10^{-3} (unitless). The value of $\Phi_{\bullet OH}^{CDOM}$, obtained experimentally upon irradiation of lake water samples, takes into account all known and poorly known processes of •OH photoproduction by CDOM, including the photo-Fenton reactions triggered by irradiation of Fe species.[9] For the photogeneration of •OH by nitrate we used

$$\Phi_{\bullet OH}^{NO_3^-} = (4.3 \pm 0.2) \cdot 10^{-2} \cdot \frac{[IC] + 0.0075}{2.25\,[IC] + 0.0075} \qquad (50)$$

where [IC] (mol L^{-1}) is the inorganic carbon concentration ($[H_2CO_3]$ + $[HCO_3^-]$ + $[CO_3^{2-}]$), derived from the available values of alkalinity and pH. The expression for $\Phi_{\bullet OH}^{NO_3^-}$ takes into account the effect of inorganic carbon species (mostly bicarbonate) on nitrate photochemistry, including reactions with geminate photofragments in the solvent cage.[35]

The steady-state $[^\bullet OH]_z$ (mol L^{-1}; day-averaged value referred to a water column of depth z) takes into account the scavenging of •OH by organic matter and inorganic carbon, expressed as:

$$[^\bullet OH]_z = \frac{R_{\bullet OH}^{tot}(z)}{k_{OM,\bullet OH}\,TOC + k_{HCO_3^-,\bullet OH}\,[HCO_3^-] + k_{CO_3^{2-},\bullet OH}\,[CO_3^{2-}]} \qquad (51)$$

where TOC is total organic carbon (mg C L^{-1}). Based on literature data, we used a reasonable value for the second-order reaction rate constant between •OH and lake-water organic matter, $k_{OM,\bullet OH}$ = $2 \cdot 10^4$ L mg_C^{-1} s^{-1},[176] and known literature values for the corresponding second-order reaction rate constants with bicarbonate and carbonate: $k_{HCO_3^-,\bullet OH}$ = $8.5 \cdot 10^6$ L mol^{-1} s^{-1}, $k_{CO_3^{2-},\bullet OH}$ = $3.9 \cdot 10^8$ L mol^{-1} s^{-1}.[43]

For $^1O_2$, one should consider its formation by irradiated CDOM (eq. 49) and its deactivation upon collision with the water solvent, which has a first-order rate constant of k_d = $2.5 \cdot 10^5$ s^{-1}.[86] Therefore, the steady-state $^1O_2$ concentration is calculated as follows:[86]

$$[^1O_2]_z = R_{^1O_2}^{tot}(z)\; k_d^{-1} \qquad (52)$$

The carbonate radical ($CO_3^{-\bullet}$) is produced by $^\bullet OH$ oxidation of inorganic carbon (HCO_3^- and CO_3^{2-}) and by $^3CDOM^*$ oxidation of CO_3^{2-}. The two pathways give the following formation rates for $CO_3^{-\bullet}$ (mol L^{-1} s^{-1}):

$$R_{CO_3^{-\bullet}}^{^\bullet OH}(z) = [^\bullet OH]_z \ (k_{HCO_3^-,^\bullet OH}[HCO_3^-] + k_{CO_3^{2-},^\bullet OH}[CO_3^{2-}]) \quad (53)$$

$$R_{CO_3^{-\bullet}}^{CDOM}(z) = \eta_{CO_3^{-\bullet}}^{CDOM}\ [CO_3^{2-}] P_a^{CDOM}(z) \quad (54)$$

where $\eta_{CO_3^{-\bullet}}^{CDOM}$ = 6.5·10^{-3} L mol^{-1}.[176] It is $R_{CO_3^{-\bullet}}^{tot}(z) = R_{CO_3^{-\bullet}}^{CDOM}(z) + R_{CO_3^{-\bullet}}^{^\bullet OH}(z)$ and, usually, $R_{CO_3^{-\bullet}}^{CDOM}(z) \ll R_{CO_3^{-\bullet}}^{^\bullet OH}(z)$. $CO_3^{-\bullet}$ is mostly scavenged by DOM, and its steady-state concentration (mol L^{-1}) was expressed as follows:

$$[CO_3^{-\bullet}]_z = \frac{R_{CO_3^{-\bullet}}^{tot}(z)}{k_{CO_3^{-\bullet},DOM}\ TOC} \quad (55)$$

where $k_{CO_3^{-\bullet},DOM}$ = 10^2 L (mg_C)$^{-1}$ s^{-1} .[43]

Finally, the CDOM triplet states ($^3CDOM^*$) are produced by CDOM irradiation and are deactivated by a number of processes, including internal conversion and reaction with dissolved O_2. These processes can be described by an overall first-order rate constant k' ≅ 5·10^5 s^{-1}.[43] The steady-state $[^3CDOM^*]_z$ (mol L^{-1}) was expressed as follows:

$$[^3CDOM^*]_z = \frac{\Phi_{^3CDOM^*}^{CDOM}\ P_a^{CDOM}(z)}{k'} \quad (56)$$

where $\Phi_{^3CDOM^*}^{CDOM}$ = 1.3·10^{-3} (unitless) is a reasonable average value for the behavior of CDOM in different lake environments.[175]

Kinetics of direct and indirect pollutant photolysis

Assume a pollutant substrate S at concentration [S] (mol L^{-1}), which can be degraded by direct photolysis and by reaction with $^{\bullet}OH$, $CO_3^{-\bullet}$, $^1O_2$ and $^3CDOM^*$. Assume also the following key parameters for S: photolysis quantum yield Φ_S, absorbed photon flux $P_a^S(z)$ (Einstein L^{-1} s^{-1}), and second-order reaction rate constants $k_{S,J}$ (L mol^{-1} s^{-1}), where J = $^{\bullet}OH$, $CO_3^{-\bullet}$, $^1O_2$ or $^3CDOM^*$. The degradation rate of S due to photochemical reactions is the following (mol L^{-1} s^{-1}):

$$R_S(z) = \Phi_S \, P_a^S(z) + [S] \sum_J k_{S,J} \, [J]_z \qquad (57)$$

where $[J]_z$ (mol L^{-1}) is the daily- and depth-averaged steady-state concentration of the transient species J (calculated as described above), referred to the depth z. The values of Φ_S and $k_{S,J}$ were parameterized according to each xenobiotic pollutant considered for the simulation, as reported hereafter. $P_a^S(z)$ (Einstein L^{-1} s^{-1}) was calculated as follows:

$$P_a^S(z) = [S] \int_{\lambda_{min}}^{\lambda_{max}} \frac{\varepsilon_S(\lambda)}{a_g(\lambda)} \cdot E_{od}^{Day}(\lambda,-0) \; a_g(\lambda) \; e^{-(K_d(\lambda) z)} \, d\lambda \qquad (58)$$

where $\varepsilon_S(\lambda)$ is the molar absorption coefficient of S (L mol^{-1} cm^{-1}). The pseudo-first order degradation rate constant is $k_S(z)=R_S(z)[S]^{-1}$. The value of $k_S(z)$ is independent of [S], provided that the latter is very low (usually below 1 µmol L^{-1}) and does not affect P_a^{CDOM} (the main light absorber in surface waters is CDOM, with usually negligible contributions from other solution constituents). The rate $R_S(z)$ is expressed in mol L^{-1} s^{-1} units, thus $k_S(z)$ has units of s^{-1}. More intuitive data can be obtained with units of day^{-1}, as $k_S^{Day}(z) = (8.5\ 10^4)^{-1}\ k_S(z)$. The half-life time of S in day units, in a water column of depth z, is given by the following equation:

$$t_{1/2}^{Day}(z) = \frac{\ln 2}{k_S^{Day}(z)} \qquad (59)$$

Model Assumptions

First of all, the phototransformation kinetics of the model compounds was determined under the assumption of thorough mixing of the lake water. For model parameterization, it was assumed that certain photochemical parameters are universally valid because they are referred to substances that do not vary in nature among different environments, and specifically: the quantum yield of $^{\bullet}OH$ by nitrate, the reaction rate constants of $^{\bullet}OH$ with carbonate and bicarbonate;[34-43] the reaction constants of APAP[163], DMM[193], EHMC[48], FEN[56] and NIC [54] with $^{\bullet}OH$, $CO_3^{-\bullet}$ and $^1O_2$, as well as the first-order inactivation rate constant of $^1O_2$ upon collision with the water solvent.[86] However, other photochemical parameters may depend on the environment such as the formation quantum yield of transient species from irradiated CDOM, the reaction rate constants of $^{\bullet}OH$ and $CO_3^{-\bullet}$with DOM, the first-order inactivation constant for ^{3}CDOM*, and the second-order reaction rate constants of ^{3}CDOM* with APAP, DMM, EHMC and FEN. These parameters were taken from the literature,[9-42-193-194] but all the cited studies were conducted on samples from temperate water bodies. Hence there is a degree of uncertainty of how appropriate is to use these values for boreal lakes. This model assumption is justified with the fact that DOM shows only a limited molecular and photochemical variability across inland waters worldwide. Specifically, ultrahigh-resolution mass spectrometry revealed a substantial overlap in molecular-level pattern of DOM in inland waters across different biomes and continents.[195] The individual compounds were largely overlapping between fresh DOM prior to substantial light exposure in boreal lakes and photolabile compounds from Congo River water, and *vice versa* (for example, DOM with substantial light exposure and photoresistant DOM).[195] Also, the wavelength-integrated apparent quantum yield for photochemical DOM mineralization varied by only a factor of 12 across a variety of boreal, polar, temperate and tropical lakes, including saline lagoons, which covered a very wide range in chemical and optical water properties.[196] Finally, considering that boreal lakes appear to be favorable environments for reaction triggered by ^{3}CDOM* and $^1O_2$, the values used for $\Phi^{CDOM}_{^3CDOM*}$ and $\Phi^{CDOM}_{^1O_2}$ are in the lower range of those reported for temperate water bodies.[9] Therefore, the formation of ^{3}CDOM* and $^1O_2$ in boreal lake water is here likely underestimated, which makes the present one a conservative calculation. [197]

Model Validation

The described approach to calculate the steady-state concentrations of photoreactive transients and the photochemical half-life times of xenobiotics has been previously validated by comparison with available field data of surface-water photoreactivity in European temperate lakes.[175] With respect to Swedish lakes, a half-life time of 1400 days has been measured for carbamazepine in Norra Bergundasjön in late spring (the corresponding 95% confidence interval was 780-

5700 days).[186] Using the Norra Bergundasjön water chemistry data measured during May to October 2015 (H. Olofsson, unpublished data), the irradiance spectra simulated for the measurement period,[187] as well as the lake average depth of 3.3 m, our model estimated $[^{\bullet}OH]_{ave}$ = (1-2)·10^{-18} mol L^{-1}. Assuming that carbamazepine mainly reacts with $^{\bullet}OH$ [187] and considering the reported second-order reaction rate constant of the process ($k_{Carbamazepine,^{\bullet}OH}$ = 8·10^{9} L mol^{-1} s^{-1})[198] gives a half-life time of 400-900 days, which is in reasonable agreement with the observations in Norra Bergundasjön. Moreover, the half-life time of ibuprofen was 4-10 days in lake Boren.[186] Ibuprofen is mainly transformed by $^{\bullet}OH$ and $^{3}CDOM^{*}$ reactions, and in both cases the reaction rate constants are ~1·10^{10} L mol^{-1} s^{-1} .[199] Using average Boren water chemistry data from 2013 to 2015 (http://ext-dokument.lansstyrelsen.se/Ostergotland/MSV/sjo/Mo03.pdf), irradiance spectra simulated for the measurement period [187] and the lake average depth of 5.4 m, we obtained $[^{\bullet}OH]$ = (5-15)·10^{-18} mol L^{-1} and $[^{3}CDOM^{*}]$ = (7-20)·10^{-17} mol L^{-1}. The resulting half-life times of ibuprofen (i.e. 3.5-10.6 days), mostly due to the reactions with $^{3}CDOM^{*}$, were almost exactly in the same range as the field observations. Hence, in both validation cases the model predictions derived from the steady-state concentrations of the photoreactive transient species were accurate within a factor of maximally two when compared to field data, which is a very reasonable result for the modeling of xenobiotics phototransformation.

Statistical analyses.

Principal components analysis (PCA) was carried out on column-autoscaled data using the chemometric software V-Parvus on the whole dataset (1048 samples, 18 variables). The percent explained variance on the first and second principal component was 38.9 and 23.2%, respectively. Loadings analysis emphasizes interrelationships among variables where correlations, anti-correlations and non-correlations correspond to parallel, anti-parallel and perpendicular loadings, respectively[200]. Relationships between the steady-state concentrations of the simulated photoreactive transients and the concentrations of total organic carbon and nitrate were analyzed using linear least square regression models. Right-skewed variables were logarithmically transformed before analysis, after adding a small constant value if the dataset included zero values. Model significance was assessed using regression analysis of variance. Differences were considered significant if P value ≤ 0.05. Linear regression lines are shown for the relationships where R^2>0.25. Analyses were conducted using R3.1.1[201]

Data representation

Color-coded maps visualizing patterns across the Swedish lakes were produced using the Sweden rds file provided in the Database of Global Administrative Areas (GADM) 2015 (http://gadm.org/country), and the function spplot of the R package sp in R3.1.[201]
Water chemical data from the Swedish National Lake inventory 2009 is available at the "Data host for inland waters" from the Swedish University of Agricultural Sciences.
The absorbance and irradiance spectra for each lake, used for the photochemical rate modeling are available from Birgit Koehler (University of Uppsala).

Concentration and control of reactive transient species

The spatial distribution of TOC was mirrored in the simulated steady-state concentration of DOM triplet states in the 5 cm upper layer of the water column, as well as the concentration of $^1O_2$ (as shown in Figures 43a and 43b, respectively). Coherently, a principal component analysis (PCA) reveal a strong correlation among [^{3}CDOM*], [$^1O_2$] and TOC, as shown in the next paragraph. Considering that high-TOC waters are generally rich in CDOM,[164-168] this correlation is simultaneously caused by elevated ^{3}CDOM* and $^1O_2$ formation rates, following photon absorption by CDOM in the surface water layer, and by deactivation of ^{3}CDOM* and $^1O_2$ that is largely independent of the TOC (see Figures 43a, 43c and 44a).[86]

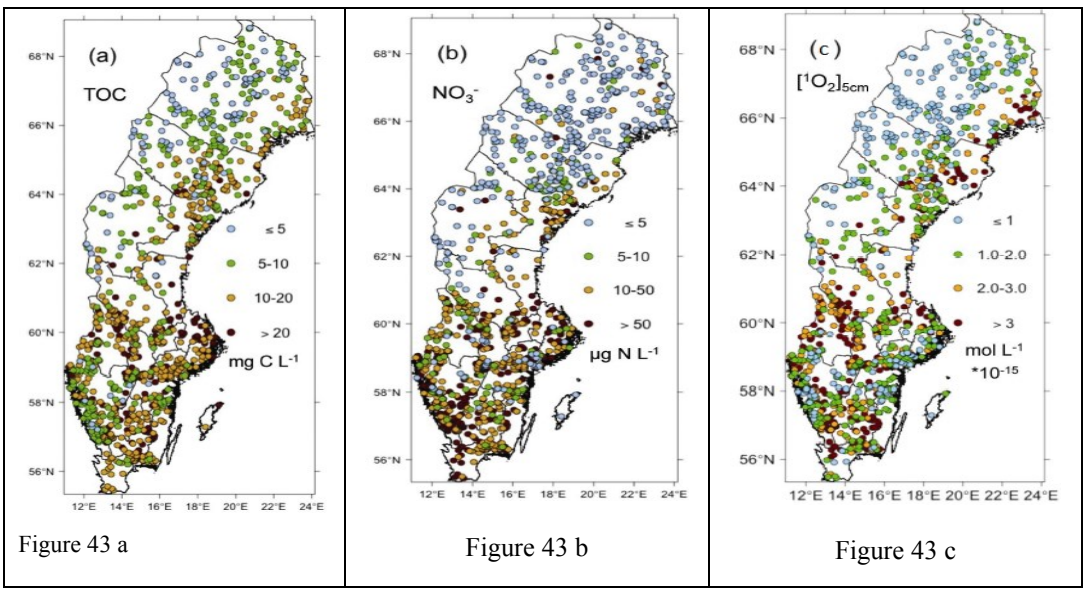

Figure 43 a

Figure 43 b

Figure 43 c

Figure 43 Map of Sweden showing the 1048 studied lakes (circles), color coded according the concentration of (a) TOC, (b) Nitrate, and (c) steady state concentration of $^1O_2$ down to 0.05m. Lines denote the counties of Sweden.

Both simulated $[^3CDOM^*]_{5cm}$ and $[^3CDOM^*]_{avg}$ values (avg is referred to the average lake depth) were lower in north-western Sweden, where TOC concentrations are usually low (often < 5 $mg_C\ L^{-1}$ as shown in Figure 43a). For $[^3CDOM^*]_{avg}$ the correlation with TOC is weaker compared to $[^3CDOM^*]_{5cm}$, likely because the photochemically active photons are largely absorbed by CDOM in the first upper meter upper of the water column across the studied lakes, *via* the absorption saturation phenomenon.[187] Consequently, photochemistry is inhibited in the poorly illuminated deeper water layers,[179] thereby dampening the TOC-$^3CDOM^*$ relationship. Only a small amount in the variability of the simulated photoreactive transients was explained by the photon flux as shown comparing figure 43 and figure 44. In the present case (fall equinox in Sweden) irradiance variations across the country were relatively limited and largely linked to the latitude, allowing other factors to play a more important role. Indeed the photochemical production of transient species in the present case depends not only on the irradiance, but most notably on the water chemistry and depth. In some cases ($^3CDOM^*$ and $^1O_2$) the chemistry only influences the photoproduction processes, while in other cases ($^{\bullet}OH$ and $CO_3^{-\bullet}$) it affects both formation and depletion of the transients.[134] In the water column of lakes, the irradiance absorption saturation induce a plateau in the formation rate of $^{\bullet}OH$ with increasing CDOM; in contrast, a similar effect does not take place for $^{\bullet}OH$ scavenging by DOM. [134] Consequently, $^{\bullet}OH$ scavenging is the major factor that controls $[^{\bullet}OH]_{avg}$ in the high-TOC lakes under study, producing low $[^{\bullet}OH]_{avg}$ levels compared to the temperate lakes.[55] In this study the lakes with the highest $[^{\bullet}OH]_{avg}$ values were the relatively low-DOC lakes of north-western Sweden, as shown in Figure 44d.

The radical $CO_3^{-\bullet}$ is mainly formed upon oxidation of inorganic carbon by $^{\bullet}OH$.[134] The simulated $[CO_3^{-\bullet}]_{5cm}$ and $[CO_3^{-\bullet}]_{avg}$ values were usually higher in the low-DOC lakes of north-western Sweden than in other parts of the country, as shown in Figures 44e and 44f, and they were low compared to temperate regions.[43-55]

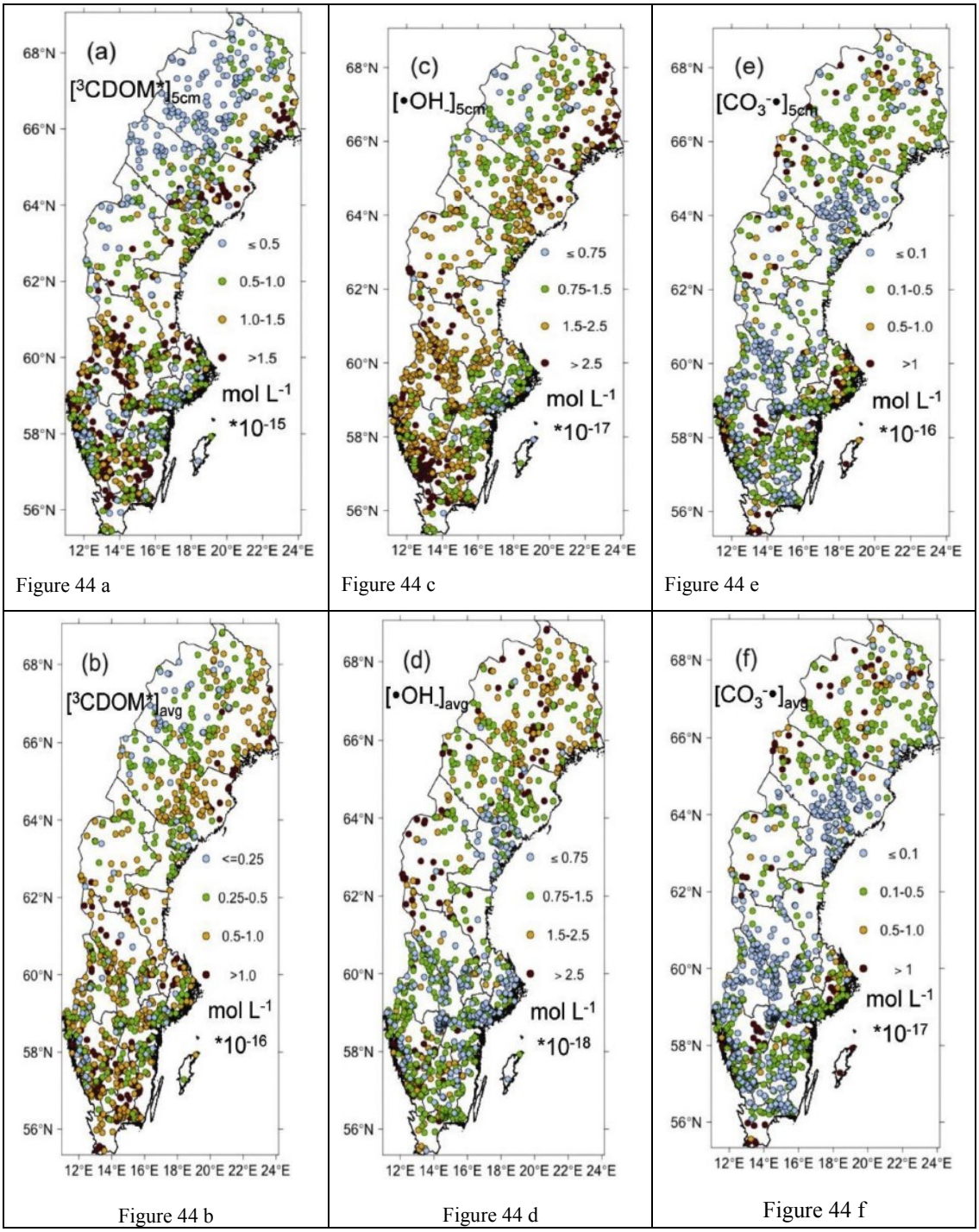

Figure 44 a

Figure 44 c

Figure 44 e

Figure 44 b

Figure 44 d

Figure 44 f

Figure 44 The location of the 1048 studied lakes (circles) across Sweden, color coded according to the simulated day-averaged steady state concentrations of the reactive transients: (a,b), [^{3}CDOM*] ,(c,d) [$^{\bullet}$OH] and (e,f) [$CO_3^{-\bullet}$], The upper maps (a,c,e) show mean concentration down to 0.05 m, while the lower maps (b,d,f) report the mean concentration down to the average lakes depth. All the values are reported in mol L^{-1}. Lines denote the counties of Sweden.

Indirect Pollutant Photodegradation

The quality of our modeling of pollutant photodegradation was assessed by comparing simulated vs. observed half-live times of two compounds (Ibuprofen and Carbamazepine) for two Swedish lakes as explained previously in the *Validation* section.

The five chosen model molecules (APAP, DMM, EHMC, FEN, and NIC) span a wide range of reactivity and allow, by photochemical fate modeling, for a thorough assessment of the main photoreaction pathways in Swedish lake water. The assessment was carried out by comparing our model predictions for boreal lakes with the well-known behavior of the chosen molecules in temperate environments. While our simulation study allowed for a first large-scale assessment of the likely photochemical behavior of a range of compounds in boreal lakes, laboratory and field studies are needed to provide detailed system and compound-specific observations and to substantiate the pattern found in this work with photochemical modeling.

	APAP	DMM	EHMC	FEN	NIC
Φ_S (unitless)	$4.6\ 10^{-2}$	$2.6\ 10^{-5}$	$3.8\ 10^{-2}$	$6\ 10^{-3}$	Not Available
$k_{S,^{\bullet}OH}$ (L mol^{-1} s^{-1})	$1.9\ 10^{9}$	$2.6\ 10^{10}$	$1\ 10^{10}$	$7\ 10^{9}$	$1.1\ 10^{9}$
$k_{S,^{3}CDOM^{*}}$ (L mol^{-1} s^{-1})	$1.1\ 10^{10}$	$1.6\ 10^{9}$	$5\ 10^{9}$	$2\ 10^{9}$	Not Available
$k_{S,^{1}O_2}$ (L mol^{-1} s^{-1})	$3.7\ 10^{7}$	$8.5\ 10^{5}$	$1.5\ 10^{7}$	$< 1\ 10^{6}$	$3.4\ 10^{6}$
$k_{S,CO_3^{\bullet-}}$ (L mol^{-1} s^{-1})	$3.8\ 10^{8}$	$< 1\ 10^{6}$	$< 1\ 10^{6}$	$6\ 10^{6}$	$< 1\ 10^{6}$

Table 9 Direct photolysis quantum yields (Φ_S) and second-order reaction rate constants ($k_{S,J}$) with the main photoinduced transients (J= $^{\bullet}$OH, ^{3}CDOM*, $^{1}O_2$, and $CO_3^{\bullet-}$) of the compounds modeled in this work (S=APAP,[163] DMM,[189] EHMC,[49] FEN [56] and NIC [64])

The generally high CDOM content in Swedish lakes, compared to temperate ones, restricts sunlight penetration into the water column and hence the direct photolysis of pollutants. This makes the simulated photoreactive transient species highly relevant for indirect photochemical degradation.[145-179] To gain insight into the photochemical reaction pathways prevailing in boreal lakes, the half-life times of APAP, DMM, EHMC, FEN, and NIC were considered as referred to the average lake depth. The simulated half-life times, which are inversely proportional to the photodegradation rate constants (see equation 59), ranged from weeks (EHMC and APAP) to months (DMM and FEN), as shown in Figure 46. The median water retention time of lakes in Sweden is 120 days, and it ranges from 7 days to 3.3 years. [202]Therefore, with the exception of NIC that has several years of photochemical lifetime, the predicted half-lives of the modeled compounds were within the short end of the typical water retention times in Swedish lakes. The longest half-life time values of APAP, DMM, and FEN were found in the north-western lakes, where the lowest $[^{3}CDOM^{*}]_{avg}$ values were predicted. In agreement, the pseudo first-order photodegradation rate constant for APAP, DMM

and FEN correlated positively with $[^3CDOM^*]_{avg}$, suggesting that their phototransformation was almost exclusively accounted for by $^3CDOM^*$. This is different from the general behavior of the same compounds in temperate water bodies, where $CO_3^{-\bullet}$ is a key photoreactive transient in the photodegradation of APAP,[163] and where $^\bullet OH$ plays important roles in DMM[189] and FEN[56] transformation. The simulated photochemical half-life of NIC, which mainly reacts with $^\bullet OH$,[64] reached up to years or even a few decades in high-TOC boreal lakes as shown in Figure 44 and in Table 9, in agreement with the low values of $[^\bullet OH]_{avg}$ expected to be found in these environments. This result actually means that biodegradation would be by far the main transformation pathway for Nicotine in Swedish lake water, with a mostly negligible contribution of photochemistry.[203] By comparison, photochemical half-lives of several months are expected for NIC in temperate lakes.[54] Overall, the general conditions that prevail in many of the studied Swedish lakes would favor the reactions induced by $^3CDOM^*$, to the detriment of processes induced by $^\bullet OH$ and $CO_3^{-\bullet}$.

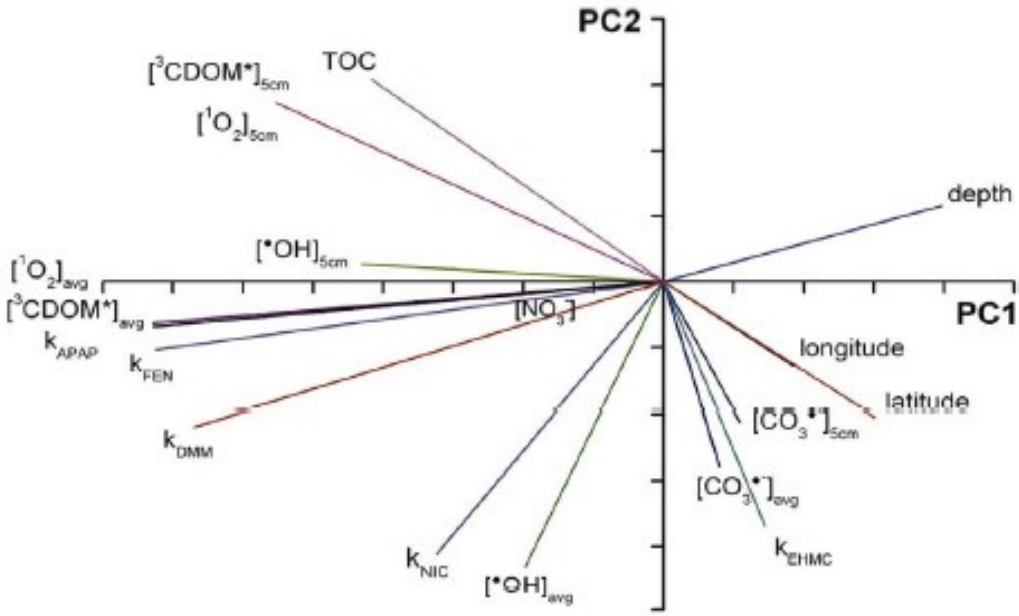

Figure 45

Figure 45 The loadings that resulted from the Principal Components Analysis (PCA) on the whole dataset. The percent explained variance on the first and second principal component was 38.9 and 23.2%, respectively. k_{APAP}, k_{DMM}, k_{EHCM}, k_{FEN} and k_{NIC} are the pseudo first-order kinetic constants for the photochemical degradation of the modeled compounds. They are related to the half-life times with the relationship shown in equation 59. $[J]_{avg}$ and $[J]_{5cm}$ are the steady-state concentrations of the photochemically generated J transients ($^\bullet OH$, $^3CDOM^*$, $^1O_2$, and $CO_3^{-\bullet}$), averaged down to the mean depth of each lake and in the first 5 cm of water, respectively.

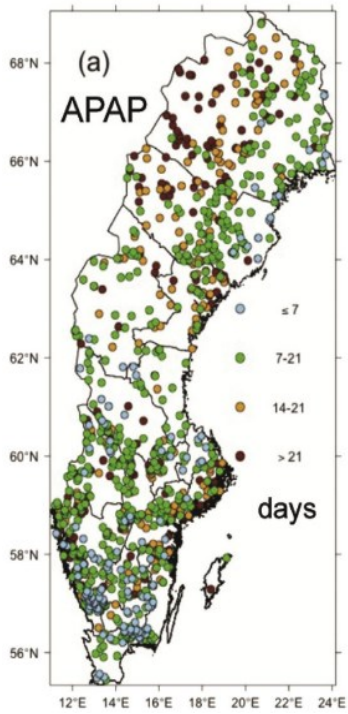

Figure 46 a

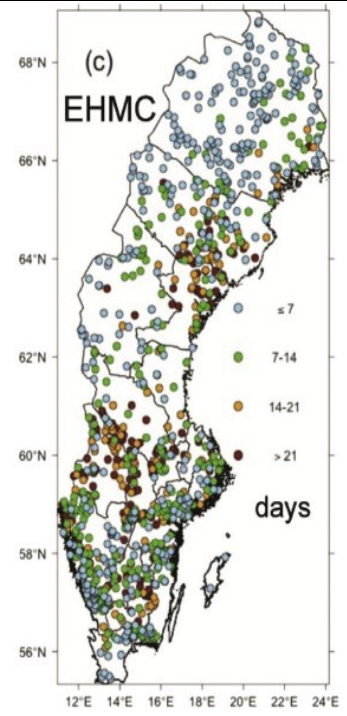

Figure 46 c

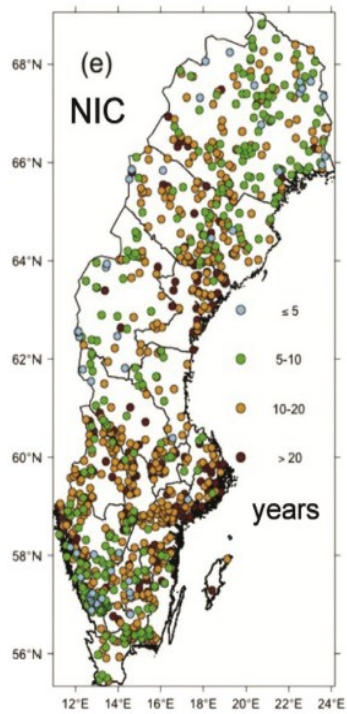

Figure 46 e

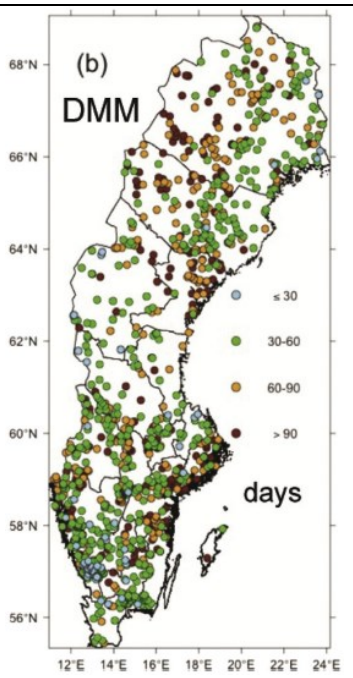

Figure 46 b

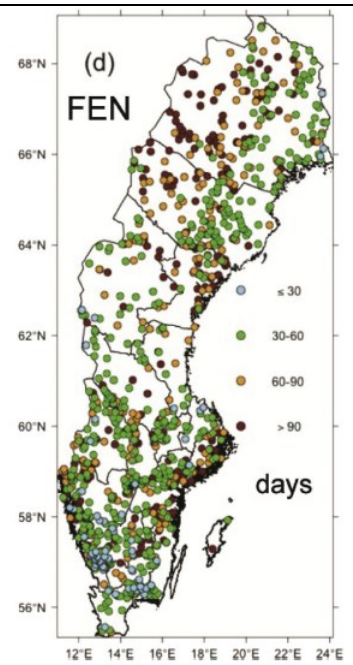

Figure 46 d

Figure 46 Maps of Sweden showing the location of the 1048 study lakes (circles), color coded according to the simulated half-time life of (a) APAP, (b) DMM, (c) EHMC, (d) FEN and (e) NIC. The lines denote the counties of Sweden.
The color coding of the classes are given in each panel, and the lifetimes are expressed in days (a-d) or years (e).

Photochemical Behavior of Boreal Lakes

The results of the above photochemical modeling can be extended to broader classes of naturally-occurring molecules and anthropogenic pollutants, as shown in Table 10 hereafter. Most notably, indirect reaction with ^{3}CDOM* can induce effective degradation of phenols and phenylurea erbicides.[204] High (C)DOM lakes would also be favorable environments for degradation processes induced by $^1O_2$, which has a similar geographic distribution as ^{3}CDOM* as shown in Figure 43c. Singlet oxygen is important in the phototransformation of anionic chlorophenols, commonly used as pesticides, herbicides and disinfectants.[205] In low-(C)DOM boreal lakes, $CO_3^{-\bullet}$ could induce significant photodegradation of aromatic amines and thiols, which are widely used for pesticides, pharmaceuticals, dyes and odors.[206] Moreover, $^\bullet$OH could significantly oxidize refractory pollutants such as the pharmaceutical carbamazepine (see the method validation section). The xenobiotics that would accumulate in high-CDOM boreal lakes are biorefractory compounds prevalently reacting with $^\bullet$OH or $CO_3^{-\bullet}$. However, due to similar reduction potential of ^{3}CDOM* and $CO_3^{-\bullet}$, [45-164]compounds are unlikely to react fast with $CO_3^{-\bullet}$ and be at the same time unreactive towards ^{3}CDOM*.[179] Therefore, accumulation is expected for biorecalcitrant xenobiotics that mainly react with $^\bullet$OH, such as some hydrocarbons and carbamazepine, the second most refractory pollutant in lake Norra Bergundasjön, located in southern Sweden.[186]

Sample compound	Major and (minor) photoreaction pathways in temperate lakes	Photochemical $t_{1/2}$ in temperate lakes (days)	Mean (±SE) Photochemical $t_{1/2}$ in boreal lakes (days)	Major photodegradation pathways for broader classes of dissolved compounds (main uses)
APAP	$CO_3^{-\bullet}$ (^{3}CDOM*, DP)	5-14	15.0±0.5	$CO_3^{-\bullet}$Aromatic Amines, thiols (pesticides, pharmaceuticals, dye and odors)
FEN	^{3}CDOM* ($^\bullet$OH)	10-50	73±2	^{3}CDOM* Phenylurea herbicides, phenols (plastic, medical drug, herbicides)
NIC	$^\bullet$OH ($^1O_2$)	50-300	5200±100	$^\bullet$OH Toluene (industrial feedstock and solvents) carbamazepine (medical drug)
EHMC	DP	< 2	12.0±0.3	DP Solar filters, triclosan (antibacterial and antifungal agent), some cephalosporine antibiotics, nitrobenzene(precursor to rubber chemicals, pesticides dyes, explosives and pharmaceuticals)
DMM	^{3}CDOM* and $^\bullet$OH (DP)	10-40	70.7±1.3	^{3}CDOM* Phenols, Phenylurea herbicides $^\bullet$OH Toluene carbamazepine

Table 10 Example compounds used to assess the photoreaction kinetics. For each compound, the main reaction pathways involved in phototransformation in temperate lake are listed. Earlier reported photochemical half-lives in temperate lake are included, for comparison with the half-lives obtained in this study for boreal lakes. The right column reports some compounds and compound classes that are expected to also undergo important phototransformation via the most relevant reaction pathway(s) highlighted in the previous column (SE=Standard Error, DP = Direct Photolysis)

Effect of Eutrophication and Browning

TOC and nitrate in a given lake may undergo long-term changes because of phenomena such as increasing CDOM concentration (browning)[69] and eutrophication. [207] Using a space-for-time replacement approach, the correlation plots of the simulated steady-state concentrations of the photoreactive transient species with TOC and nitrate give some insight into the possible impact of such increases (see figures 43, 47, 47bis and 48). Specifically, given that $[^3CDOM^*]_{5cm}$ and $[^1O_2]_{5cm}$ were positively correlated with TOC, TOC changes will proportionally modify these transients concentrations. The same correlation was weaker, but still significant for $[^3CDOM^*]_{avg}$ and $[^1O_2]_{avg}$. For instance, assuming irradiance and water depth do not undergo significant variations, a doubling of TOC (from 10 to 20 $mg_C\ L^{-1}$) would produce on average a ~60% increase of $[^3CDOM^*]_{avg}$ and $[^1O_2]_{avg}$. In contrast, the inverse relationship of TOC with $[^\bullet OH]_{avg}$ and $[CO_3^{-\bullet}]_{avg}$ suggests that the reactions triggered by $^\bullet OH$ and $CO_3^{-\bullet}$ would be further inhibited by browning. Differently from TOC, no strong relationship was found between the simulated photoreactive transients and nitrate. This result is expected for $^3CDOM^*$, because nitrate plays no role in $^3CDOM^*$ generation or deactivation. In the case of $^\bullet OH$, it indicates that CDOM strongly prevails over nitrate as $^\bullet OH$ source. Hence as opposed to TOC changes, nitrate changes (which are possibly due to eutrophication) should not modify photochemical reactions in boreal lakes.

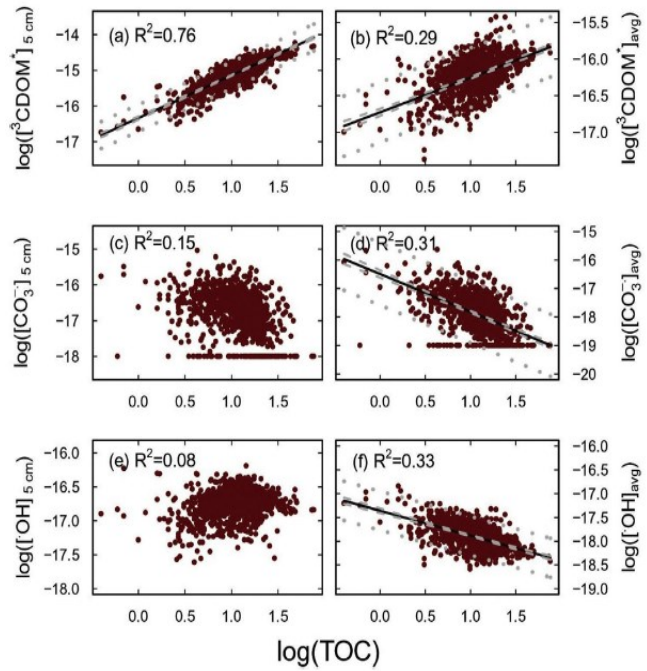

Figure 47

Figure 47 Scatterplot between the logarithmically transformed steady-state concentration of the simulated photoreactive transients (mol L^{-1}) and the logarithmically transformed Total Organic Carbon concentration (TOC, mg C L^{-1}), down to 0.05 m lake water depth for (a) $^3CDOM^*$, (c) $CO_3^{-\bullet}$ and (e) $^\bullet OH$, and down to the average depth of each lake for (b) $^3CDOM^*$, (d) $CO_3^{-\bullet}$ and (f) $^\bullet OH$. When R^2 exceeded 0.25 (cases (a), (b), (d) and (f)), linear regressions are included (solid black) with 95% confidence interval (dashed grey) and 95% prediction interval (dotted gray). The P-value was smaller than 0.05 for the other relationships as well, but given the small amount of explained variability (R^2) it was not considered. The dataset of $CO_3^{-\bullet}$ concentration included 116 zero values for the lakes with zero or negative alkalinity. In these cases a small positive constant value was added to the dataset before the log transformation (10^{-18} for (c) and 10^{-19} for (d)).

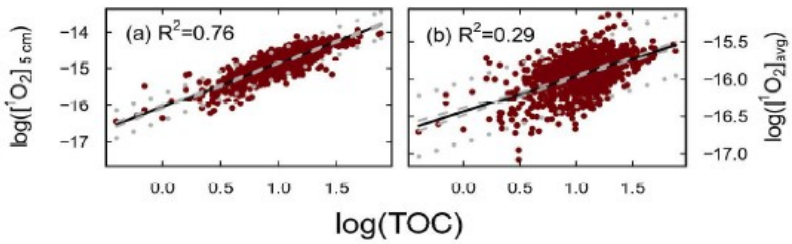

Figure 47 bis Scatterplots between the steady-state concentration of $^1O_2$ (mol L^{-1}) and the total organic carbon concentration (TOC, mg C L^{-1}), down to 0.05 m lake water depth (a) and down to the average depth of each lake (b). Because R^2 exceeded 0.25, linear regression lines are included (solid black) with 95% confidence intervals (dashed gray) and 95% prediction intervals (dotted gray). These figures are very similar to that obtained in Figure 47 for ^{3}CDOM*. This fact is due to the strong correlation between ^{3}CDOM* and $^1O_2$.

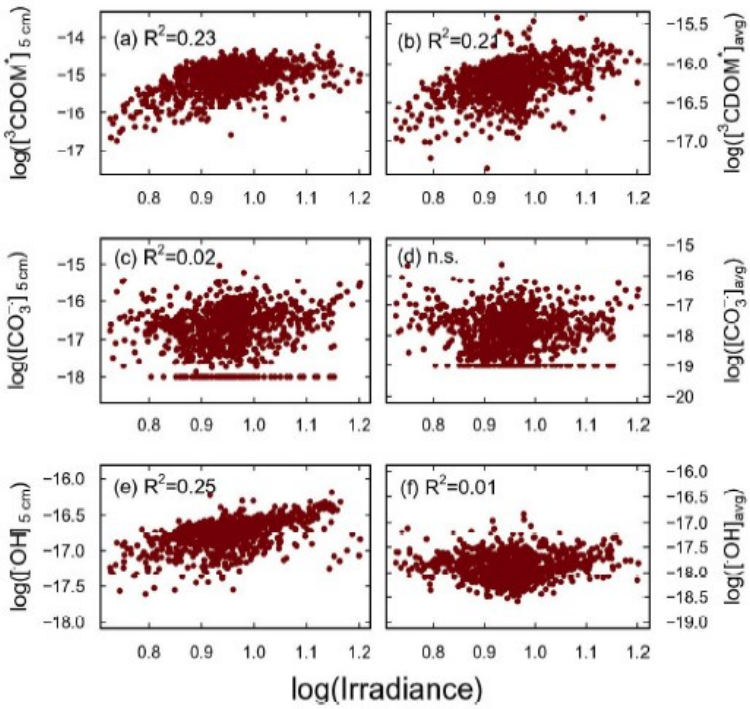

Figure 48 Scatterplots between the logarithmically transformed steady-state concentrations of the simulated photoactive transients (mol L^{-1}) and the logarithmically transformed downwelling scalar irradiance just below the water surface (280-600 nm; Einstein m^{-2} day^{-1}), down to 0.05 m lake water depth for (a) ^{3}CDOM*, (c) $CO_3^{-\bullet}$ and (e) $^\bullet$OH, and down to the average depth of each lake for (b) ^{3}CDOM*, (d; n.s.=not significant) $CO_3^{-\bullet}$ and (f) $^\bullet$OH. The P-value was smaller than 0.05 for all but one relationship (d), but given the small amount of explained variability (R^2) we did not consider these. The dataset of modeled $CO_3^{-\bullet}$ concentrations included 116 zero values, for the lakes with zero or negative alkalinity. In these cases, a small positive constant value was added to the dataset before transformation (10^{-18} in (c) and 10^{-19} in (d)). Plots with $^1O_2$ are not shown because they are very similar to those with ^{3}CDOM*.

Outcomes of Swedish Lake Modeling

Lakes are more numerous at boreal and artic latitudes than anywhere else on Earth,[185] and lakes in these areas commonly exhibit high CDOM concentrations, so ^{3}CDOM*-mediated photoreactions controlled by water chemistry are likely highly important processes behind the transformations of natural and anthropogenic organic compounds in these waters. The conditions in boreal lakes could favor the phototransformation of phenolic compounds, including chlorophenolates and phenylureas. With ongoing climate change, DOM and CDOM concentration, are expected to increase in northern inland waters,[68] so this change is expected to further facilitate the ^{3}CDOM* mediated photoreactions at the expense of direct photolysis and of processes mediated by $^{\bullet}OH$ and $CO_3^{-\bullet}$.

Conclusions

The multidisciplinary approach used in this work shows how different methods, technologies and practices can be focused on a huge environmental subject such as photochemistry, in order to increase the knowledge in the field from diverse points of view that range from molecular photochemistry and photophysics (4BPOH and Phenol-*p*-oligomers) to large-scale modeling (Swedish Lakes), passing through the study of a particular ecosystem (Propanil in paddy field).

The first part of this thesis was focused on the photochemistry of 4-hydroxybenzophenone and phenol oligomers, as particular *chromophores* that show typical humic-like fluorescence.

The computational approach in this case was extremely useful to explain the details of the fluorescence behavior of 4BPOH and, most of all to predict, the fluorescence signals even if the compound under investigation was not available for laboratory measurements. Moreover, with the computational approach it is also possible to investigate the nature of the transitions. For instance, we found that 4BPOH does not follow the Kasha's rule, as demonstrated by the occurrence of a $S_2 \rightarrow S_0$ emission transition. This compounds also shows different behavior in different solvents, in function of their polarity and proton affinity, because of the different acidity of the ground state (S_0-weak acid) and the excited states (S_1 and T_1-strong acids). It was thus proven that 4BPOH would not be fluorescent and would not produce $^1O_2$ in the presence of water, but would do so in its absence, thereby contributing to the occurrence of elevated $^1O_2$ levels in the hydrophobic cores of humic substances.

The computational approach is able to understand also the nature of the transitions, showing for instance by means of differential electronic density maps, the portion of the molecule interested in each electronic transition, which allowed for an explanation of why the fluorescence emission wavelength plateaus when increasing the number of aromatic rings.

The second part of this thesis was focused on natural water systems, in which the DOM plays for instance a key role in the fate of Propanil, an herbicide largely used in rice cultivations. In some specific water conditions, photodegradation could be competitive with dark reactions mediated by biota. The most significant photoprocesses in environmental settings are those induced by $^{\bullet}OH$ and $CO_3^{-\bullet}$, because they would prevail in the presence of elevated nitrate and/or nitrite concentrations that make PRP photodegradation to be about as important as biotransformation. In contrast, direct photolysis and ^{3}CDOM* reactions would prevail at low nitrate and nitrite, and in these conditions the photochemical

reactions are unlikely to be important compared to the dark processes. The photoreactions do not produce important amounts of toxic 34DCA, while dark (biological) processes generate 34DCA with approximately quantitative yield. Elevated nitrate concentrations that enhance PRP photodegradation may occur if one wants to use flooded paddies as denitrification bioreactors, by irrigating them with water containing elevated nitrate levels. In this case, an important fraction of PRP would be degraded without producing 34DCA, thereby gaining a further advantage in addition to denitrification.

The third part of this thesis reports the first example of a photochemical map, in which the steady-state concentrations of transient species are reported for a large geographic region. The map also allowed for the simulation of the half-lives of specific pollutants belonging to different compound classes, including paracetamol (APAP), dimethomorph (DMM), ethyl hexyl methoxycinnamate (EHMC), fenuron (FEN) and nicotine (NIC). Unlike temperate lakes, boreal and artic lakes commonly exhibit high CDOM concentrations that enhance ^{3}CDOM*-mediated photoreactions and make them likely highly important processes behind the transformations of natural and anthropogenic organic compounds. The predicted lifetimes range from weeks for APAP and EHMC that mainly react with ^{3}CDOM*, to several months for DMM and FEN that also react with ^{3}CDOM* but that in temperate lakes would mostly react with $^{\bullet}$OH and $CO_3^{-\bullet}$. Finally, NIC that mainly reacts with $^{\bullet}$OH has photochemical lifetimes of several years The conditions observed for boreal lakes, which favor the photoprocesses triggered by ^{3}CDOM* and $^1O_2$, enhance the phototransformation of phenolic compounds including chlorophenolates and phenylureas. In the relatively rare low-DOC lakes, the photoreactions involving hydroxyl and carbonate radicals could become important, especially in the degradation of biorefractory pollutants and, in the case of $CO_3^{\bullet-}$, of aromatic amines, phenolates and thiols/mercaptans. With ongoing climate change, DOM and CDOM concentrations are expected to increase in northern inland waters and this change is expected to further facilitate the ^{3}CDOM*- and $^1O_2$-mediated photoreactions at the expense of direct photolysis and of degradation reactions induced by $^{\bullet}$OH and $CO_3^{-\bullet}$.

Appendix

Section 1 - The case of 4-carboxybenzophenone

4-HYDROXYBENZOPHENONE BEHAVIOR IN DIFFERENT SOLVENTS

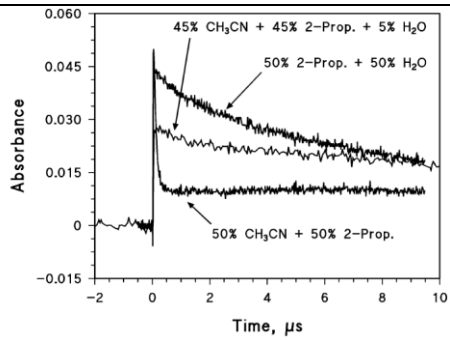

Time trend of the laser traces at 350 nm (355 nm laser irradiation, 94 mJ/pulse), in different mixtures of acetonitrile, 2-propanol and water (see the figure legends)..

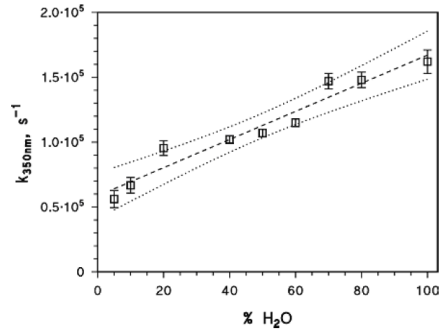

Trend of the first-order decay constant of the absorbance at 350 nm, as a function of the percentage of water in binary mixtures H2O/CH3CN. 4BPOH 0.1 mM, laser excitation at 355 nm, 94 mJ/pulse.

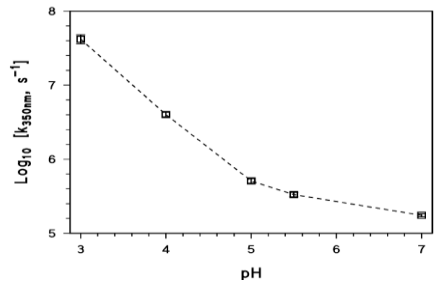

Trend of the first-order decay constant of the absorbance at 350 nm (decimal logarithm), as a function of the pH of the aqueous solution, adjusted with $HClO_4$.
4BPOH 0.1 mM, laser excitation at 355 nm, 94 mJ/pulse.

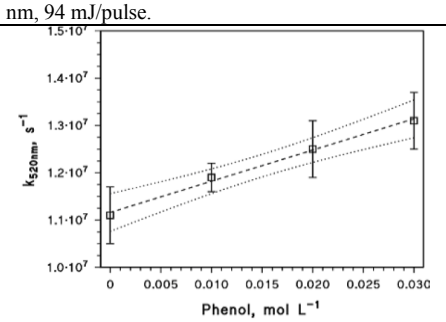

Trend of the first-order decay constant of the absorbance at 520 nm, as a function of phenol concentration in acetonitrile. 4BPOH 0.1 mM, laser excitation at 355 nm, 94 mJ/pulse.

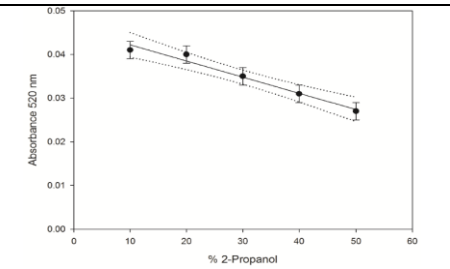

Trend of the Absorbance at 520 nm, as a function of the percentage of 2-propanol in binary mixtures 2-propanol/CH3CN. 4BPOH 0.1 mM, laser excitation at 355 nm, 94mJ/pulse.

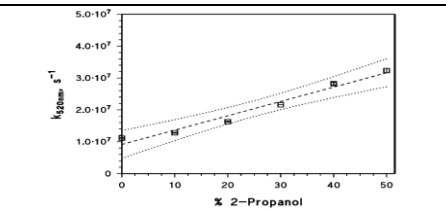

Trend of the first-order decay constant of the absorbance at 520 nm, as a function of the percentage of 2-propanol in binary mixtures 2-propanol/CH3CN. 4BPOH 0.1 mM, laser excitation at 355 nm, 94 mJ/pulse. The second-order reaction rate constant between 34BPOH* and 2-propanol was derived taking into account the fact that 100% 2-propanol is 13.1 M.

Computational study of 4-hydroxybenzophenone optical properties

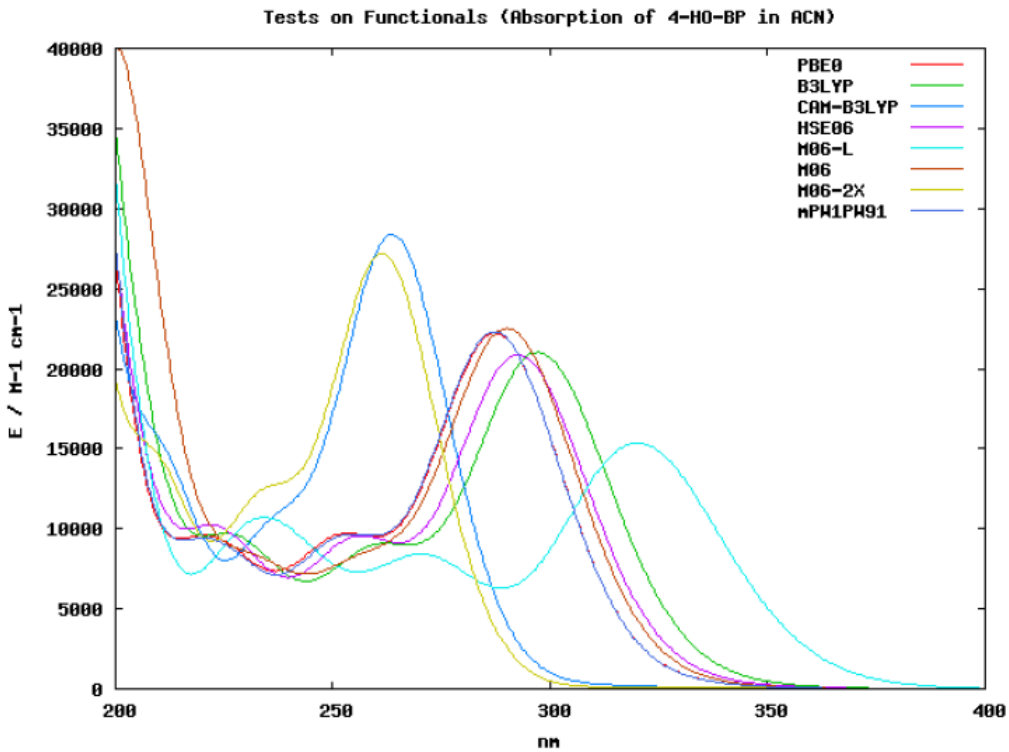

The choice of the functional is limited on the availability of the gradient for the excited states and its implementation in the program Gaussian 09A. Among the 8 functional tested (PBE0, B3LYP,CAM-B3LYP, HSE06, M06-L, M06, M06-2X, mPW91PW91) PBE0 and mPW91PW91 are the ones that better fit the experimental curve. PBE0 was chosen for its best fit. (Figure obtained with GNUPlot)

Note on Figure 10a

Figure 10a is intended to be purely illustrative. **R**, although related to the deformation of the structures with respect to the optimized geometries, is the same for all states and , indeed, dimensionless. All curves are parabolas whore parameters are defined as follows:

a. the parabola for the ground state is: $S_0(R) = k_0 (R-R_0)^2$ where $R_0 = 0$ and k_0 set arbitrarily to 0.82 in order to get a reasonable agreement between the value of $S_0(R_1)$ and the energies of the ground state at the excited states S_1 (see below)

b. the parabola for the excited state S_1 is: $S_1(R) = k_1 (R-R_1)^2 + c_1$ where the R_1 is set arbitrarily to1. c_1 is set to the value of the energy of state S_1 at its optimized

energy; $\mathbf{k_1}$ and $\mathbf{R_1}$ are found solving system of the equations defining the following conditions:

$S_1(R_1)$ is the energies of the **S_1** states at its optimized geometry;
$S_1(R=0)$ corresponds to the vertical excitation energy fro **S_0** to **S_1**.

c. the parabolas for the excited states **S_2** and **T_1** are: $\mathbf{S_2/T_1(R) = k_i (R-R_i)^2 + c_i}$ where the **R_i** are chosen so that the **$S_0(R_i)$** correspond to the energies of the ground state at the optimized geometries of the excited states **i**-esim. **k_i** and **c_i** are found solving system of the equations defining the following conditions:

$S_2/T_1(R_i)$ are the energies of the excited states at their corresponding optimized geometries.
$S_2/T_1(R=0)$ corresponds to the vertical excitation energies from **S_0** to **S_i**.

Despite of being far to be rigorous, this approach allowed us to get a semi-quantitative picture that quite well describe the electronic states of 4HOBP in Acetonitrile

Structure of the S_0, S_1, S_2 and T_1 states of 4BPOH optimized in acetonitrile

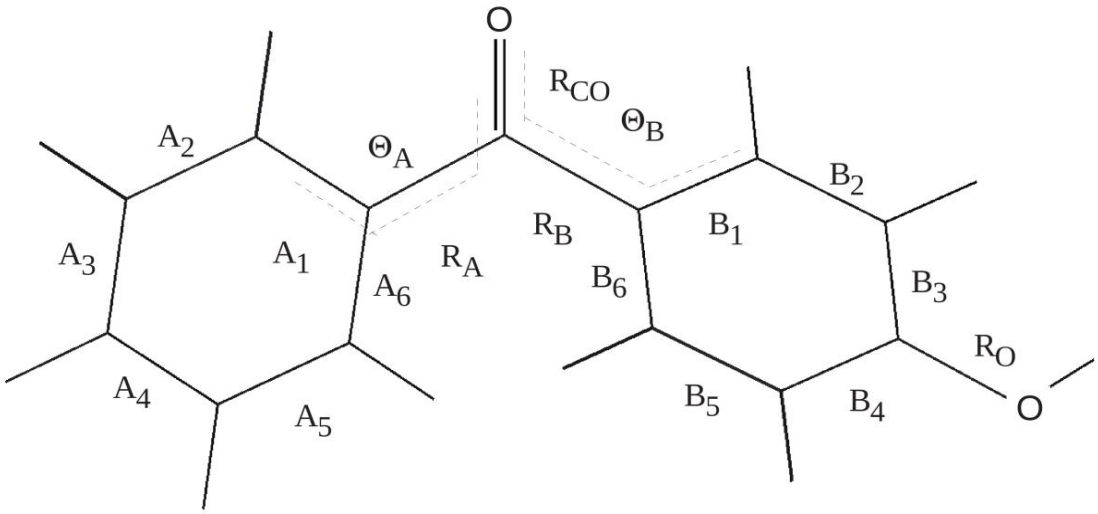

Coord	Values ----------				Deviations ----------		
	S_0	T_1	S_1	S_2	T_1	S_1	S_2
R_{CO}	1.230	1.294	1.293	1.275	**0.01**	**0.01**	**0.01**
R_A	1.494	1.467	1.408	1.448	0.00	**0.03**	**0.01**
R_B	1.483	1.431	1.480	1.495	**0.01**	0.00	0.00
R_O	1.352	1.347	1.332	1.329	0.00	0.00	0.00
A_1	1.402	1.410	1.427	1.430	0.00	0.00	0.00
A_2	1.391	1.391	1.386	1.383	0.00	0.00	0.00
A_3	1.397	1.397	1.403	1.405	0.00	0.00	0.00
A_4	1.395	1.398	1.404	1.403	0.00	0.00	0.00
A_5	1.394	1.391	1.385	1.386	0.00	0.00	0.00
A_6	1.401	1.409	1.426	1.429	0.00	0.00	0.00
B_1	1.403	1.454	1.418	1.425	**0.01**	0.00	0.00
B_2	1.386	1.372	1.376	1.375	0.00	0.00	0.00
B_3	1.401	1.414	1.411	1.417	0.00	0.00	0.00
B_4	1.398	1.428	1.411	1.417	0.00	0.00	0.00
B_5	1.388	1.367	1.375	1.375	0.00	0.00	0.00
B_6	1.404	1.444	1.418	1.422	**0.01**	0.00	0.00
Θ_A	-33.06	-22.71	0.02	-15.50	**0.03**	**0.33**	**0.09**
Θ_B	-23.90	-21.70	-86.87	-25.13	0.00	**1.21**	0.00
	Standard deviations from S_0 =				**0.068**	**0.297**	**0.083**

The following tables report energies, Cartesian coordinates and vertical transitions of the S_0, S_1, S_2 and T_1 states of 4BPOH in acetonitrile, obtained from the calculations.

```
*********************************************************************
4HOBP in ACN - S_0:
SCF Done: E(RPBE1PBE) = -651.149221428
Sum of electronic and thermal Free Energies= -650.991786
---------------------------------------------------------------------
1            6       0      -0.013953    -0.011151    -0.005343
2            6       0      -0.027235    -0.026449     1.395623
3            6       0       1.170919    -0.024324     2.108091
4            6       0       2.389133    -0.029206     1.429013
5            6       0       2.409349    -0.017071     0.032363
6            6       0       1.214689     0.006065    -0.680046
7            1       0      -0.971871    -0.012529     1.932811
8            1       0       1.151818    -0.019363     3.195144
9            1       0       3.322697    -0.038873     1.986577
10           1       0       3.357671    -0.021459    -0.499590
11           1       0       1.221950     0.027608    -1.766739
12           6       0      -1.268680     0.067781    -0.812779
13           8       0      -1.275479     0.721269    -1.854903
14           6       0      -2.493011    -0.634030    -0.357411
15           6       0      -2.456027    -1.786033     0.444446
16           6       0      -3.623780    -2.448800     0.795405
17           6       0      -4.858015    -1.954327     0.362292
18           6       0      -4.915244    -0.805590    -0.437710
19           6       0      -3.739975    -0.165397    -0.799175
20           1       0      -1.504444    -2.190900     0.777158
21           1       0      -3.592674    -3.350188     1.401664
22           8       0      -5.967339    -2.626414     0.742513
23           1       0      -5.878164    -0.422665    -0.770990
24           1       0      -3.780009     0.721373    -1.426074
25           1       0      -6.757766    -2.195369     0.373488
---------------------------------------------------------------------

---------------------------------------------------------------------

4HOBP in ACN - S_0 - Vertical transitions:

Excited State 1:     Singlet-A   3.7971 eV    326.52 nm     f=0.0047
Excited State 2:     Singlet-A   4.3082 eV    287.79 nm     f=0.4050
Excited State 3:     Singlet-A   4.6950 eV    264.08 nm     f=0.0191
Excited State 4:     Singlet-A   4.7923 eV    258.71 nm     f=0.0050
Excited State 5:     Singlet-A   4.9281 eV    251.59 nm     f=0.1505
Excited State 6:     Singlet-A   5.3913 eV    229.97 nm     f=0.0891
Excited State 7:     Singlet-A   5.6475 eV    219.54 nm     f=0.0684
Excited State 8:     Singlet-A   5.7063 eV    217.28 nm     f=0.0387
Excited State 9:     Singlet-A   5.7548 eV    215.44 nm     f=0.0134
Excited State 10:    Singlet-A   5.8921 eV    210.42 nm     f=0.0040
Excited State 11:    Singlet-A   5.9339 eV    208.94 nm     f=0.0127
Excited State 12:    Singlet-A   6.1057 eV    203.06 nm     f=0.0035
Excited State 13:    Singlet-A   6.1158 eV    202.73 nm     f=0.0476
Excited State 14:    Singlet-A   6.1740 eV    200.82 nm     f=0.0899
Excited State 15:    Singlet-A   6.3600 eV    194.94 nm    f=0.0587
Excited State 16:    Singlet-A   6.3802 eV    194.33 nm    f=0.2212
Excited State 17:    Singlet-A   6.4278 eV    192.89 nm    f=0.1384
Excited State 18:    Singlet-A   6.4819 eV    191.28 nm    f=0.0118
Excited State 19:    Singlet-A   6.5508 eV    189.27 nm    f=0.1360
Excited State 20:    Singlet-A   6.6536 eV    186.34 nm    f=0.0103
Excited State 21:    Singlet-A   6.6705 eV    185.87 nm    f=0.0182
Excited State 22:    Singlet-A   6.7138 eV    184.67 nm    f=0.4215
Excited State 23:    Singlet-A   6.7201 eV    184.50 nm    f=0.0178
```

```
Excited State 24:    Singlet-A   6.8002 eV    182.32 nm    f=0.2365
Excited State 25:    Singlet-A   6.8175 eV    181.86 nm    f=0.3821
Excited State 26:    Singlet-A   6.8718 eV    180.42 nm    f=0.0654
Excited State 27:    Singlet-A   6.9124 eV    179.37 nm    f=0.0685
Excited State 28:    Singlet-A   6.9622 eV    178.08 nm    f=0.0368
Excited State 29:    Singlet-A   7.0066 eV    176.95 nm    f=0.0299
Excited State 30:    Singlet-A   7.0493 eV    175.88 nm    f=0.0445
Excited State 31:    Singlet-A   7.0685 eV    175.40 nm    f=0.0032
Excited State 32:    Singlet-A   7.1050 eV    174.50 nm    f=0.0171
Excited State 33:    Singlet-A   7.1480 eV    173.45 nm    f=0.0083
Excited State 34:    Singlet-A   7.1869 eV    172.51 nm    f=0.0043
Excited State 35:    Singlet-A   7.2472 eV    171.08 nm    f=0.0111
Excited State 36:    Singlet-A   7.2976 eV    169.90 nm    f=0.0157
-----------------------------------------------------------------

-----------------------------------------------------------------

4HOBP in ACN - S_0 - Triplet Vertical transitions:

Excited State 1:     Triplet-A   3.0062 eV    412.43 nm    f=0.0000
Excited State 2:     Triplet-A   3.2868 eV    377.21 nm    f=0.0000
Excited State 3:     Triplet-A   3.4855 eV    355.71 nm    f=0.0000
Excited State 4:     Triplet-A   4.1007 eV    302.35 nm    f=0.0000
Excited State 5:     Triplet-A   4.1984 eV    295.32 nm    f=0.0000
Excited State 6:     Triplet-A   4.2965 eV    288.57 nm    f=0.0000
Excited State 7:     Triplet-A   4.4053 eV    281.44 nm    f=0.0000
Excited State 8:     Triplet-A   4.4133 eV    280.93 nm    f=0.0000
Excited State 9:     Triplet-A   4.8870 eV    253.70 nm    f=0.0000
Excited State 10:    Triplet-A   5.0392 eV    246.04 nm    f=0.0000
Excited State 11:    Triplet-A   5.2519 eV    236.07 nm    f=0.0000
Excited State 12:    Triplet-A   5.6520 eV    219.36 nm    f=0.0000
Excited State 13:    Triplet-A   5.6986 eV    217.57 nm    f=0.0000
Excited State 14:    Triplet-A   5.7870 eV    214.25 nm    f=0.0000
Excited State 15:    Triplet-A   5.8131 eV    213.29 nm    f=0.0000
Excited State 16:    Triplet-A   5.8692 eV    211.25 nm    f=0.0000
Excited State 17:    Triplet-A   5.9684 eV    207.74 nm    f=0.0000
Excited State 18:    Triplet-A   6.0289 eV    205.65 nm    f=0.0000
Excited State 19:    Triplet-A   6.0939 eV    203.46 nm    f=0.0000
Excited State 20:    Triplet-A   6.3076 eV    196.56 nm    f=0.0000
Excited State 21:    Triplet-A   6.3880 eV    194.09 nm    f=0.0000
Excited State 22:    Triplet-A   6.4157 eV    193.25 nm    f=0.0000
Excited State 23:    Triplet-A   6.4585 eV    191.97 nm    f=0.0000
Excited State 24:    Triplet-A   6.5077 eV    190.52 nm    f=0.0000
Excited State 25:    Triplet-A   6.5490 eV    189.32 nm    f=0.0000
Excited State 26:    Triplet-A   6.6453 eV    186.58 nm    f=0.0000
Excited State 27:    Triplet-A   6.6707 eV    185.86 nm    f=0.0000
Excited State 28:    Triplet-A   6.7792 eV    182.89 nm    f=0.0000
Excited State 29:    Triplet-A   6.8051 eV    182.19 nm    f=0.0000
Excited State 30:    Triplet-A   6.8217 eV    181.75 nm    f=0.0000
Excited State 31:    Triplet-A   6.8519 eV    180.95 nm    f=0.0000
Excited State 32:    Triplet-A   6.9139 eV    179.33 nm    f=0.0000
Excited State 33:    Triplet-A   6.9781 eV    177.68 nm    f=0.0000
Excited State 34:    Triplet-A   6.9821 eV    177.58 nm    f=0.0000
Excited State 35:    Triplet-A   7.0410 eV    176.09 nm    f=0.0000
Excited State 36:    Triplet-A   7.0529 eV    175.79 nm    f=0.0000
-----------------------------------------------------------------

*****************************************************************
4HOBP in ACN - S_1:
Total Energy, E(TD-HF/TD-KS) = -651.028704626
Energy, force constant and most relevant orbital transitions:
Excited State       1:      Singlet-A    2.4600 eV   503.99 nm f=0.0003
MO:     Occ          Virt                Coeff.
        50     ->     53                 0.18957
        52     ->     53                 0.67219
```

```
---------------------------------------------------------------------
1              6       0       0.011600      -0.167843     -0.061943
2              6       0      -0.106048      0.234081      1.301099
3              6       0       1.017057      0.573248      2.036815
4              6       0       2.298109      0.530604      1.462876
5              6       0       2.428468      0.136881      0.122881
6              6       0       1.319027     -0.206966     -0.632843
7              1       0      -1.08999       6 0.273369    1.764345
8              1       0       0.900444      0.876805      3.075532
9              1       0       3.173982      0.798403      2.047724
10             1       0       3.415642      0.099467     -0.334437
11             1       0       1.434811     -0.510359     -1.670563
12             6       0      -1.119687     -0.515543     -0.825558
13             8       0      -1.164742     -0.895318     -2.061140
14             6       0      -2.538273     -0.536339     -0.403394
15             6       0      -3.117414     -1.727141      0.104335
16             6       0      -4.430833     -1.745148      0.510758
17             6       0      -5.216737     -0.582866      0.357425
18             6       0      -4.677667      0.590694     -0.211151
19             6       0      -3.361808      0.597883     -0.614668
20             1       0      -2.500296     -2.615092      0.208032
21             1       0      -4.880246     -2.633310      0.945229
22             8       0      -6.484281     -0.656137      0.761120
23             1       0      -5.303425      1.472702     -0.327182
24             1       0      -2.932932      1.489919     -1.062326
25             1       0      -6.945904      0.188658      0.600725
---------------------------------------------------------------------

*********************************************************************
4HOBP in ACN - S_2:
Total Energy, E(TD-HF/TD-KS) = -651.004593591
Energy, force constant and most relevant orbital transitions:
Excited State       2:      Singlet-A    3.6801 eV   336.90 nm f=0.4715
MO:     Occ         Virt                 Coeff.
        49     ->    53                  0.14972
        51     ->    53                  0.35767
        52     ->    53                  0.58022
---------------------------------------------------------------------
1              6       0       0.014534      -0.135868     -0.040932
2              6       0       0.066878      -0.300509      1.377212
3              6       0       1.263743      -0.186355      2.067246
4              6       0       2.461881       0.104948      1.398881
5              6       0       2.427284       0.306101      0.009048
6              6       0       1.239348       0.210691     -0.692827
7              1       0      -0.839811      -0.483712      1.944673
8              1       0       1.264746      -0.316030      3.147795
9              1       0       3.397273       0.181945      1.947188
10             1       0       3.345839       0.539967     -0.526296
11             1       0       1.220340       0.369809     -1.766947
12             6       0      -1.181268      -0.199228     -0.855590
13             8       0      -1.191644       0.324146     -2.018498
14             6       0      -2.462023      -0.740197     -0.306836
15             6       0      -2.535151      -1.805577      0.631556
16             6       0      -3.745442      -2.341444      1.003479
17             6       0      -4.943037      -1.793567      0.480904
18             6       0      -4.900178      -0.715832     -0.437741
19             6       0      -3.681566      -0.194407     -0.803550
20             1       0      -1.625520      -2.254615      1.015264
21             1       0      -3.805717      -3.186442      1.683186
22             8       0      -6.083065      -2.347340      0.879155
23             1       0      -5.826410      -0.328290     -0.857102
24             1       0      -3.628226       0.615494     -1.524227
25             1       0      -6.850512      -1.895599      0.475080
---------------------------------------------------------------------
```

```
**********************************************************************
4HOBP in ACN - T_1:
Total Energy, E(TD-HF/TD-KS) = -651.049249622
Energy, force constant and most relevant orbital transitions:
Excited State       1:      Triplet-?Sym 2.3820 eV 520.51 nm f=0.0000
MO:     Occ          Virt                Coeff.
        51     ->     53                 0.18005
        52     ->     53                 -0.64038
        52     ->     54                 -0.14465
        52     ->     55                 -0.10040

----------------------------------------------------------------------
1            6       0      -0.018678     0.106712      0.038206
2            6       0      0.008482      0.097238      1.446630
3            6       0      1.208883      -0.057200     2.132650
4            6       0      2.412046      -0.193441     1.433934
5            6       0      2.401001      -0.161394     0.037069
6            6       0      1.204004      -0.006313     -0.654213
7            1       0      -0.911457     0.238165      2.008847
8            1       0      1.207908      -0.057986     3.220422
9            1       0      3.348691      -0.311743     1.973251
10           1       0      3.332234      -0.260031     -0.516514
11           1       0      1.199208      0.018355      -1.740497
12           6       0      -1.258001     0.315787      -0.717486
13           8       0      -1.189413     0.825581      -1.904982
14           6       0      -2.565772     -0.097588     -0.308957
15           6       0      -2.804002     -1.153777     0.647163
16           6       0      -4.076436     -1.508001     1.000330
17           6       0      -5.199421     -0.871834     0.389698
18           6       0      -4.999741     0.109835      -0.608057
19           6       0      -3.727286     0.478719      -0.966139
20           1       0      -1.961232     -1.676614     1.087452
21           1       0      -4.254880     -2.291986     1.731873
22           8       0      -6.419619     -1.274420     0.794278
23           1       0      -5.861571     0.575714      -1.083120
24           1       0      -3.567640     1.238121      -1.723230
25           1       0      -7.111068     -0.798712     0.299534
----------------------------------------------------------------------

----------------------------------------------------------------------

4HOBP in ACN - T_1 - Vertical transitions:

Excited State 1:      3.021-A      0.9563 eV    1296.53 nm    f=0.0212
Excited State 2:      3.023-A      1.3579 eV    913.07 nm     f=0.0563
Excited State 3:      3.029-A      1.8418 eV    673.16 nm     f=0.0002
Excited State 4:      3.045-A      1.9819 eV    625.59 nm     f=0.0024
Excited State 5:      3.059-A      2.4907 eV    497.79 nm     f=0.2209
Excited State 6:      3.037-A      2.5830 eV    480.01 nm     f=0.0050
Excited State 7:      3.055-A      2.8428 eV    436.13 nm     f=0.0284
Excited State 8:      3.038-A      3.0508 eV    406.40 nm     f=0.0288
Excited State 9:      3.290-A      3.5969 eV    344.70 nm     f=0.0195
Excited State 10:     3.042-A      3.7267 eV    332.69 nm     f=0.0054
Excited State 11:     3.077-A      3.7599 eV    329.75 nm     f=0.0095
Excited State 12:     3.363-A      3.8860 eV    319.05 nm     f=0.1863
Excited State 13:     3.220-A      4.0226 eV    308.22 nm     f=0.0091
Excited State 14:     3.378-A      4.1501 eV    298.75 nm     f=0.0023
Excited State 15:     3.251-A      4.1529 eV    298.55 nm     f=0.0205
Excited State 16:     3.343-A      4.1901 eV    295.90 nm     f=0.0122
Excited State 17:     3.239-A      4.2728 eV    290.17 nm     f=0.0287
Excited State 18:     3.324-A      4.3564 eV    284.60 nm     f=0.0043
Excited State 19:     3.060-A      4.4047 eV    281.48 nm     f=0.0006
Excited State 20:     3.440-A      4.4735 eV    277.15 nm     f=0.0516
Excited State 21:     3.043-A      4.5161 eV    274.54 nm     f=0.0050
Excited State 22:     3.091-A      4.6037 eV    269.31 nm     f=0.0055
```

```
Excited State 23:     3.555-A      4.6893 eV     264.40 nm     f=0.0018
Excited State 24:     3.509-A      4.6996 eV     263.82 nm     f=0.0022
Excited State 25:     3.142-A      4.7365 eV     261.76 nm     f=0.1369
Excited State 26:     3.083-A      4.8823 eV     253.95 nm     f=0.0340
Excited State 27:     3.348-A      4.9177 eV     252.12 nm     f=0.0004
Excited State 28:     3.069-A      4.9658 eV     249.68 nm     f=0.0164
Excited State 29:     3.498-A      5.0007 eV     247.93 nm     f=0.0079
Excited State 30:     3.182-A      5.0223 eV     246.87 nm     f=0.0156
Excited State 31:     3.104-A      5.1145 eV     242.41 nm     f=0.0046
Excited State 32:     3.052-A      5.1844 eV     239.15 nm     f=0.0027
Excited State 33:     3.083-A      5.2038 eV     238.26 nm     f=0.0032
Excited State 34:     3.947-A      5.3020 eV     233.84 nm     f=0.0044
Excited State 35:     3.241-A      5.3602 eV     231.30 nm     f=0.0155
Excited State 36:     3.057-A      5.4988 eV     225.48 nm     f=0.0081
-------------------------------------------------------------------
```

Structure of the S_0, S_1, S_2 and T_1 states of 4BPOH optimized in 2-propanol

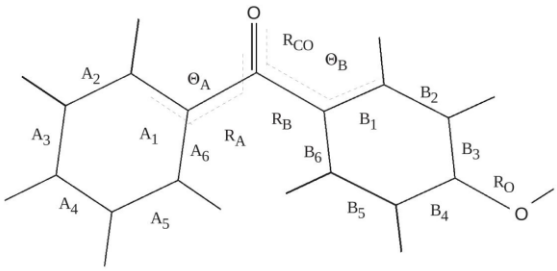

Coord	Values				Deviations		
	S_0	T_1	S_1	S_2	T_1	S_1	S_2
R_{CO}	1.234	1.285	1.298	1.283	0.01	0.01	0.01
R_A	1.492	1.477	1.409	1.449	0.00	**0.02**	0.01
R_B	1.479	1.432	1.478	1.485	0.01	0.00	0.00
R_O	1.353	1.346	1.328	1.328	0.00	0.00	0.00
A_1	1.402	1.406	1.426	1.428	0.00	0.00	0.00
A_2	1.391	1.391	1.385	1.383	0.00	0.00	0.00
A_3	1.397	1.396	1.402	1.403	0.00	0.00	0.00
A_4	1.395	1.396	1.404	1.402	0.00	0.00	0.00
A_5	1.393	1.393	1.385	1.386	0.00	0.00	0.00
A_6	1.401	1.405	1.426	1.426	0.00	0.00	0.00
B_1	1.404	1.463	1.420	1.431	0.01	0.00	0.00
B_2	1.386	1.367	1.374	1.374	0.00	0.00	0.00
B_3	1.401	1.419	1.414	1.416	0.00	0.00	0.00
B_4	1.398	1.436	1.414	1.420	0.01	0.00	0.00
B_5	1.387	1.363	1.373	1.374	0.00	0.00	0.00
B_6	1.404	1.451	1.420	1.424	0.01	0.00	0.00
Θ_A	-34.24	-29.19	0.57	-22.36	0.01	**0.37**	**0.04**
Θ_B	-23.46	-16.79	-84.98	-13.61	0.01	**1.15**	**0.03**
	Standard deviations from S_0 =				**0.062**	**0.296**	**0.076**

The following tables report energies, Cartesian coordinates and vertical transitions of the S_0, S_1, S_2 and T_1 states of 4BPOH in 2-propanol, obtained from the calculations.

```
*********************************************************************
4HOBP in 2-propanol - S_0:
SCF Done: E(RPBE1PBE) = -651.149703095
Sum of electronic and thermal Free Energies= -650.991777
---------------------------------------------------------------------
1              6       0      -0.004345     -0.009665     -0.000885
2              6       0      -0.005251     0.016421      1.402038
3              6       0      1.199115      0.005536      2.102915
4              6       0      2.410093      -0.035862     1.412468
```

5	6	0	2.417478	-0.047371	0.015987
6	6	0	1.217369	-0.010257	-0.686114
7	1	0	-0.944653	0.059205	1.947082
8	1	0	1.190939	0.028466	3.189952
9	1	0	3.348760	-0.056087	1.961326
10	1	0	3.360464	-0.081598	-0.524414
11	1	0	1.216228	-0.010036	-1.773212
12	6	0	-1.265592	0.097831	-0.790870
13	8	0	-1.277353	0.752098	-1.836643
14	6	0	-2.487087	-0.593520	-0.323605
15	6	0	-2.443825	-1.738642	0.488388
16	6	0	-3.608812	-2.395277	0.856170
17	6	0	-4.846467	-1.902605	0.430569
18	6	0	-4.909978	-0.761786	-0.380493
19	6	0	-3.737707	-0.126726	-0.758503
20	1	0	-1.489656	-2.143023	0.814300
21	1	0	-3.574682	-3.291156	1.470596
22	8	0	-5.951463	-2.571901	0.831686
23	1	0	-5.875828	-0.382185	-0.707371
24	1	0	-3.784471	0.756127	-1.390690
25	1	0	-6.750977	-2.149229	0.477676

4HOBP in 2-Propanol - S_0 - Vertical transitions:

Excited State 1:	Singlet-A	3.8637 eV	320.89 nm	f=0.0077
Excited State 2:	Singlet-A	4.2484 eV	291.84 nm	f=0.4416
Excited State 3:	Singlet-A	4.6358 eV	267.45 nm	f=0.0215
Excited State 4:	Singlet-A	4.7449 eV	261.30 nm	f=0.0051
Excited State 5:	Singlet-A	4.8685 eV	254.66 nm	f=0.1471
Excited State 6:	Singlet-A	5.3960 eV	229.77 nm	f=0.0980
Excited State 7:	Singlet-A	5.6684 eV	218.73 nm	f=0.0636
Excited State 8:	Singlet-A	5.7227 eV	216.65 nm	f=0.0283
Excited State 9:	Singlet-A	5.7856 eV	214.30 nm	f=0.0195
Excited State 10:	Singlet-A	5.9733 eV	207.57 nm	f=0.0058
Excited State 11:	Singlet-A	6.0114 eV	206.25 nm	f=0.0127
Excited State 12:	Singlet-A	6.1508 eV	201.57 nm	f=0.1388
Excited State 13:	Singlet-A	6.1852 eV	200.45 nm	f=0.0016
Excited State 14:	Singlet-A	6.2503 eV	198.36 nm	f=0.0347
Excited State 15:	Singlet-A	6.3900 eV	194.03 nm	f=0.3314
Excited State 16:	Singlet-A	6.3990 eV	193.76 nm	f=0.0188
Excited State 17:	Singlet-A	6.4490 eV	192.25 nm	f=0.0636
Excited State 18:	Singlet-A	6.5354 eV	189.71 nm	f=0.1097
Excited State 19:	Singlet-A	6.5631 eV	188.91 nm	f=0.0290
Excited State 20:	Singlet-A	6.6095 eV	187.58 nm	f=0.0187
Excited State 21:	Singlet-A	6.6248 eV	187.15 nm	f=0.0335
Excited State 22:	Singlet-A	6.7135 eV	184.68 nm	f=0.2713
Excited State 23:	Singlet-A	6.7649 eV	183.27 nm	f=0.2641
Excited State 24:	Singlet-A	6.8086 eV	182.10 nm	f=0.2447
Excited State 25:	Singlet-A	6.8369 eV	181.34 nm	f=0.3200
Excited State 26:	Singlet-A	6.9032 eV	179.60 nm	f=0.0669
Excited State 27:	Singlet-A	6.9409 eV	178.63 nm	f=0.0205
Excited State 28:	Singlet-A	6.9992 eV	177.14 nm	f=0.0164
Excited State 29:	Singlet-A	7.0146 eV	176.75 nm	f=0.0048
Excited State 30:	Singlet-A	7.0589 eV	175.64 nm	f=0.0309
Excited State 31:	Singlet-A	7.0976 eV	174.69 nm	f=0.0292
Excited State 32:	Singlet-A	7.1652 eV	173.04 nm	f=0.0128
Excited State 33:	Singlet-A	7.1765 eV	172.76 nm	f=0.0348
Excited State 34:	Singlet-A	7.2365 eV	171.33 nm	f=0.0041
Excited State 35:	Singlet-A	7.3415 eV	168.88 nm	f=0.0433
Excited State 36:	Singlet-A	7.3638 eV	168.37 nm	f=0.0004

****

4HOBP in 2-Propanol - S_1:
Total Energy, E(TD-HF/TD-KS) = -651.029413720
Energy, force constant and most relevant orbital transitions:
Excited State 1: Singlet-A 2.4547 eV 505.08 nm f=0.0011
MO: Occ Virt Coeff.
49 -> 53 0.18244
52 -> 53 0.67699

1	6	0	-0.001280	0.011052	-0.003728
2	6	0	-0.004402	-0.009508	1.421626
3	6	0	1.184807	-0.027971	2.131009
4	6	0	2.421904	-0.026724	1.467799
5	6	0	2.439946	-0.006428	0.065632
6	6	0	1.262722	0.012215	-0.664594
7	1	0	-0.952817	-0.012227	1.955613
8	1	0	1.155056	-0.044817	3.219002
9	1	0	3.350700	-0.042118	2.031965
10	1	0	3.392588	-0.005525	-0.461336
11	1	0	1.292378	0.028134	-1.751466
12	6	0	-1.201861	0.029100	-0.740342
13	8	0	-1.348363	0.037914	-2.030218
14	6	0	-2.586335	0.017183	-0.221753
15	6	0	-3.257493	-1.214023	0.003021
16	6	0	-4.537165	-1.228027	0.500137
17	6	0	-5.207395	-0.002597	0.721222
18	6	0	-4.583656	1.232046	0.430143
19	6	0	-3.300616	1.233999	-0.062272
20	1	0	-2.730416	-2.145790	-0.181687
21	1	0	-5.052760	-2.156721	0.726601
22	8	0	-6.444242	-0.077407	1.198791
23	1	0	-5.124447	2.160168	0.598129
24	1	0	-2.806162	2.172311	-0.297314
25	1	0	-6.836821	0.806807	1.312027

****

4HOBP in 2-Propanol - S_2:
Total Energy, E(TD-HF/TD-KS) = -651.007060603
Energy, force constant and most relevant orbital transitions:
Excited State 2: Singlet-A 3.6292 eV 341.63 nm f=0.5999
MO: Occ Virt Coeff.
48 -> 53 0.11232
49 -> 53 -0.11506
51 -> 53 0.29807
52 -> 53 -0.61561

1	6	0	0.000262	0.083561	0.048589
2	6	0	0.042418	0.048092	1.473517
3	6	0	1.247876	-0.053193	2.150752
4	6	0	2.463593	-0.115038	1.456060
5	6	0	2.447906	-0.045083	0.054548
6	6	0	1.253807	0.070309	-0.634453
7	1	0	-0.869316	0.154056	2.052682
8	1	0	1.244776	-0.070443	3.238862
9	1	0	3.403411	-0.205663	1.994923
10	1	0	3.383574	-0.085657	-0.499862
11	1	0	1.253297	0.120086	-1.719757
12	6	0	-1.200687	0.234812	-0.747355
13	8	0	-1.121236	0.769107	-1.911314
14	6	0	-2.551684	-0.129690	-0.249880
15	6	0	-2.803532	-1.010302	0.840946
16	6	0	-4.086162	-1.356189	1.192610
17	6	0	-5.186461	-0.798995	0.489686
18	6	0	-4.965876	0.077178	-0.600297
19	6	0	-3.678420	0.401248	-0.953434
20	1	0	-1.978905	-1.471968	1.371881

21	1	0	-4.281666	-2.056028	2.000118
22	8	0	-6.400716	-1.160126	0.888373
23	1	0	-5.817192	0.464443	-1.155806
24	1	0	-3.491977	1.050069	-1.803120
25	1	0	-7.093136	-0.707584	0.371387

****

4HOBP in 2-Propanol - T_1:
Total Energy, E(TD-HF/TD-KS) = -651.049250074
Energy, force constant and most relevant orbital transitions:
Excited State 1: Triplet-?Sym 2.4301 eV 510.21 nm f=0.000

MO:	Occ Virt	Coeff.
	51 -> 53	-0.11937
	52 -> 53	-0.65711
	52 -> 54	0.16123

1	6	0	-0.010908	0.031934	0.005809
2	6	0	-0.011005	0.043047	1.411045
3	6	0	1.186171	0.009251	2.121667
4	6	0	2.406612	-0.033889	1.445247
5	6	0	2.419321	-0.029282	0.048818
6	6	0	1.224954	0.010902	-0.663893
7	1	0	-0.950951	0.108389	1.954465
8	1	0	1.165808	0.027376	3.209171
9	1	0	3.340504	-0.061632	2.001775
10	1	0	3.365402	-0.057836	-0.487424
11	1	0	1.238856	0.017532	-1.750881
12	6	0	-1.256767	0.124342	-0.782199
13	8	0	-1.236321	0.727088	-1.916471
14	6	0	-2.493157	-0.491670	-0.403147
15	6	0	-2.593569	-1.566852	0.565924
16	6	0	-3.804206	-2.099833	0.895032
17	6	0	-5.002800	-1.633490	0.256544
18	6	0	-4.926274	-0.644862	-0.758983
19	6	0	-3.718740	-0.101923	-1.100765
20	1	0	-1.691889	-1.957535	1.025590
21	1	0	-3.883987	-2.899156	1.627704
22	8	0	-6.157973	-2.202962	0.646740
23	1	0	-5.838862	-0.323213	-1.257468
24	1	0	-3.651781	0.657438	-1.871251
25	1	0	-6.906954	-1.834015	0.147016

4HOBP in 2-Propanol - T_1 - Vertical transitions:

Excited State 1:	3.021-A	0.9677 eV	1281.22 n	m f=0.0288
Excited State 2:	3.021-A	1.3114 eV	945.42 nm	f=0.0585
Excited State 3:	3.028-A	1.7809 eV	696.18 nm	f=0.0002
Excited State 4:	3.044-A	1.9208 eV	645.49 nm	f=0.0025
Excited State 5:	3.052-A	2.4458 eV	506.93 nm	f=0.2312
Excited State 6:	3.034-A	2.5527 eV	485.70 nm	f=0.0020
Excited State 7:	3.056-A	2.8484 eV	435.28 nm	f=0.0267
Excited State 8:	3.039-A	3.0254 eV	409.80 nm	f=0.0377
Excited State 9:	3.269-A	3.5787 eV	346.45 nm	f=0.0236
Excited State 10:	3.043-A	3.7080 eV	334.37 nm	f=0.0052
Excited State 11:	3.072-A	3.7684 eV	329.01 nm	f=0.0131
Excited State 12:	3.300-A	3.9068 eV	317.36 nm	f=0.1658
Excited State 13:	3.198-A	3.9707 eV	312.24 nm	f=0.0015
Excited State 14:	3.328-A	4.0948 eV	302.78 nm	f=0.0001
Excited State 15:	3.512-A	4.1557 eV	298.35 nm	f=0.0466
Excited State 16:	3.095-A	4.2125 eV	294.33 nm	f=0.0013
Excited State 17:	3.223-A	4.2633 eV	290.82 nm	f=0.0292
Excited State 18:	3.363-A	4.3329 eV	286.15 nm	f=0.0031

```
Excited State 19:    3.064-A      4.4048 eV   281.47 nm     f=0.0006
Excited State 20:    3.464-A      4.4420 eV   279.12 nm     f=0.0483
Excited State 21:    3.052-A      4.5266 eV   273.90 nm     f=0.0028
Excited State 22:    3.112-A      4.6127 eV   268.79 nm     f=0.0143
Excited State 23:    3.070-A      4.6710 eV   265.43 nm     f=0.0032
Excited State 24:    3.202-A      4.7185 eV   262.76 nm     f=0.1363
Excited State 25:    3.853-A      4.7281 eV   262.23 nm     f=0.0183
Excited State 26:    3.073-A      4.8742 eV   254.37 nm     f=0.0311
Excited State 27:    3.324-A      4.9532 eV   250.31 nm     f=0.0031
Excited State 28:    3.196-A      4.9859 eV   248.67 nm     f=0.0172
Excited State 29:    3.276-A      5.0157 eV   247.19 nm     f=0.0049
Excited State 30:    3.133-A      5.0313 eV   246.43 nm     f=0.0147
Excited State 31:    3.309-A      5.0715 eV   244.47 nm     f=0.0092
Excited State 32:    3.067-A      5.1946 eV   238.68 nm     f=0.0020
Excited State 33:    3.069-A      5.2081 eV   238.06 nm     f=0.0041
Excited State 34:    3.934-A      5.3027 eV   233.81 nm     f=0.0052
Excited State 35:    3.263-A      5.3663 eV   231.04 nm     f=0.0138
Excited State 36:    3.054-A      5.4603 eV   227.06 nm     f=0.0079
-----------------------------------------------------------------------
```

Structure of the S_0, S_1, S_2 and T_1 states of 4BPOH optimized in water

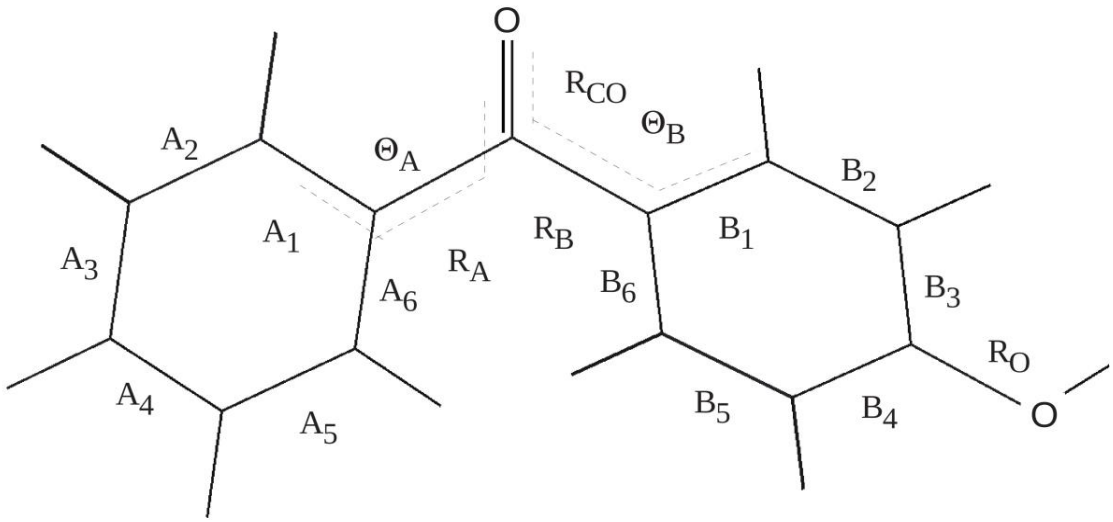

Coord	Values ----------				Deviations ----------		
	S_0	T_1	S_1	S_2	T_1	S_1	S_2
R_{CO}	1.237	1.286	1.305	1.292	0.01	**0.02**	0.01
R_A	1.490	1.478	1.410	1.450	0.00	**0.02**	0.01
R_B	1.477	1.434	1.477	1.476	0.01	0.00	0.00
R_O	1.359	1.349	1.328	1.332	0.00	0.00	0.00
A_1	1.402	1.405	1.426	1.427	0.00	0.00	0.00
A_2	1.391	1.392	1.386	1.384	0.00	0.00	0.00
A_3	1.397	1.396	1.402	1.402	0.00	0.00	0.00
A_4	1.395	1.396	1.403	1.401	0.00	0.00	0.00
A_5	1.393	1.393	1.385	1.387	0.00	0.00	0.00
A_6	1.401	1.405	1.425	1.424	0.00	0.00	0.00
B_1	1.405	1.464	1.421	1.433	0.01	0.00	0.00
B_2	1.385	1.366	1.372	1.374	0.00	0.00	0.00
B_3	1.401	1.421	1.415	1.415	0.00	0.00	0.00
B_4	1.398	1.437	1.415	1.420	0.01	0.00	0.00
B_5	1.387	1.362	1.373	1.374	0.00	0.00	0.00
B_6	1.405	1.451	1.421	1.427	0.01	0.00	0.00
Θ_A	-34.45	-29.11	0.80	-25.69	0.01	**0.38**	**0.02**
Θ_B	-23.20	-16.70	-84.96	-7.84	0.01	**1.16**	**0.07**
	Standard deviations from S_0 =				**0.061**	**0.297**	**0.084**

The following tables report energies, Cartesian coordinates and vertical transitions of the S_0, S_1, S_2 and T_1 states of 4BPOH in water, obtained from the calculations.

```
**********************************************************************
4HOBP in Water - S_0:
SCF Done: E(RPBE1PBE) = -651.143255699
Sum of electronic and thermal Free Energies= -650.984820
----------------------------------------------------------------------
1       6       0       -0.020554     0.000292     -0.004286
2       6       0       -0.034812     -0.007686    1.396927
3       6       0       1.163091      -0.019235    2.108391
4       6       0       2.380388      -0.047191    1.428215
5       6       0       2.400823      -0.045884    0.031743
6       6       0       1.207215      -0.007247    -0.681102
7       1       0       -0.979470     0.024092     1.932889
8       1       0       1.144984      -0.006808    3.195008
9       1       0       3.313810      -0.068863    1.985050
10      1       0       3.348495      -0.071671    -0.499930
11      1       0       1.217051      0.000385     -1.767884
12      6       0       -1.274832     0.090246     -0.802687
13      8       0       -1.282067     0.760222     -1.843037
14      6       0       -2.493190     -0.615024    -0.356699
15      6       0       -2.444005     -1.767589    0.444864
16      6       0       -3.604688     -2.442115    0.792830
17      6       0       -4.841838     -1.958619    0.357235
18      6       0       -4.912666     -0.810155    -0.441448
19      6       0       -3.744742     -0.157105    -0.800079
20      1       0       -1.488597     -2.162896    0.777006
21      1       0       -3.566340     -3.343136    1.398572
22      8       0       -5.950452     -2.647187    0.735643
23      1       0       -5.880912     -0.440967    -0.771806
24      1       0       -3.796388     0.732181     -1.422177
25      1       0       -6.745743     -2.224083    0.372589
----------------------------------------------------------------------

----------------------------------------------------------------------

4HOBP in Water - S_0 - Vertical transitions:

Excited State 1:      Singlet-A     3.9142 eV    316.75 nm     f=0.0106
Excited State 2:      Singlet-A     4.2198 eV    293.82 nm     f=0.4528
Excited State 3:      Singlet-A     4.5844 eV    270.45 nm     f=0.0221
Excited State 4:      Singlet-A     4.7020 eV    263.68 nm     f=0.0053
Excited State 5:      Singlet-A     4.8287 eV    256.77 nm     f=0.1369
Excited State 6:      Singlet-A     5.4150 eV    228.97 nm     f=0.0929
Excited State 7:      Singlet-A     5.6950 eV    217.71 nm     f=0.0564
Excited State 8:      Singlet-A     5.7276 eV    216.47 nm     f=0.0218
Excited State 9:      Singlet-A     5.8223 eV    212.95 nm     f=0.0167
Excited State 10:     Singlet-A     6.0443 eV    205.12 nm     f=0.0032
Excited State 11:     Singlet-A     6.0763 eV    204.05 nm     f=0.0296
Excited State 12:     Singlet-A     6.1838 eV    200.50 nm     f=0.1534
Excited State 13:     Singlet-A     6.2662 eV    197.86 nm     f=0.0019
Excited State 14:     Singlet-A     6.3130 eV    196.39 nm     f=0.0294
Excited State 15:     Singlet-A     6.4106 eV    193.40 nm     f=0.3061
Excited State 16:     Singlet-A     6.4188 eV    193.16 nm     f=0.0151
Excited State 17:     Singlet-A     6.4977 eV    190.81 nm     f=0.0488
Excited State 18:     Singlet-A     6.5434 eV    189.48 nm     f=0.0857
Excited State 19:     Singlet-A     6.5585 eV    189.04 nm     f=0.0265
Excited State 20:     Singlet-A     6.5853 eV    188.28 nm     f=0.0815
Excited State 21:     Singlet-A     6.6389 eV    186.75 nm     f=0.0059
Excited State 22:     Singlet-A     6.7224 eV    184.43 nm     f=0.2525
Excited State 23:     Singlet-A     6.7918 eV    182.55 nm     f=0.3294
```

```
Excited State 24:    Singlet-A    6.8284 eV   181.57 nm    f=0.3138
Excited State 25:    Singlet-A    6.8783 eV   180.25 nm    f=0.1886
Excited State 26:    Singlet-A    6.9363 eV   178.75 nm    f=0.0413
Excited State 27:    Singlet-A    6.9723 eV   177.82 nm    f=0.0310
Excited State 28:    Singlet-A    6.9970 eV   177.20 nm    f=0.0188
Excited State 29:    Singlet-A    7.0424 eV   176.05 nm    f=0.0192
Excited State 30:    Singlet-A    7.0629 eV   175.54 nm    f=0.0067
Excited State 31:    Singlet-A    7.1498 eV   173.41 nm    f=0.0494
Excited State 32:    Singlet-A    7.2215 eV   171.69 nm    f=0.0140
Excited State 33:    Singlet-A    7.2730 eV   170.47 nm    f=0.0345
Excited State 34:    Singlet-A    7.3023 eV   169.79 nm    f=0.0068
Excited State 35:    Singlet-A    7.3926 eV   167.71 nm    f=0.0445
Excited State 36:    Singlet-A    7.4417 eV   166.61 nm    f=0.0050
-----------------------------------------------------------------------

***********************************************************************
4HOBP in Water - S_1:
Total Energy, E(TD-HF/TD-KS) = -651.022471433
Energy, force constant and most relevant orbital transitions:
Excited State 1: Singlet-A 2.4846 eV 499.02 nm f=0.0013
MO:     Occ Virt            Coeff.
        48 -> 53            0.17382
        52 -> 53            0.67988
-----------------------------------------------------------------------
1       6       0       0.023987      -0.194206     -0.063875
2       6       0       -0.084481     0.055160      1.334858
3       6       0       1.035563      0.371389      2.086086
4       6       0       2.303810      0.454404      1.491135
5       6       0       2.425226      0.212401      0.115195
6       6       0       1.318175      -0.105747     -0.655159
7       1       0       -1.058899     -0.006036     1.815341
8       1       0       0.925950      0.555607      3.152759
9       1       0       3.177631      0.701569      2.087470
10      1       0       3.402726      0.273637      -0.359011
11      1       0       1.428234      -0.290619     -1.720757
12      6       0       -1.107119     -0.520563     -0.839041
13      8       0       -1.147310     -0.787754     -2.115574
14      6       0       -2.502600     -0.665998     -0.378590
15      6       0       -2.980584     -1.925711     0.074478
16      6       0       -4.272075     -2.061673     0.516426
17      6       0       -5.145648     -0.949949     0.449678
18      6       0       -4.709218     0.294173      -0.063853
19      6       0       -3.412505     0.419696      -0.496533
20      1       0       -2.298002     -2.769670     0.106688
21      1       0       -4.646829     -3.000709     0.911794
22      8       0       -6.389158     -1.140325     0.875788
23      1       0       -5.405366     1.127389      -0.108726
24      1       0       -3.058805     1.364181      -0.899256
25      1       0       -6.926335     -0.333405     0.776259
-----------------------------------------------------------------------

***********************************************************************
4HOBP in Water - S_2:
Total Energy, E(TD-HF/TD-KS) = -651.002739736
Energy, force constant and most relevant orbital transitions:
Excited State 2: Singlet-?Sym 3.5572 eV 348.54 nm f=0.686
MO:     Occ Virt            Coeff.
        48 -> 53            -0.15775
        51 -> 53            0.26620
        52 -> 53            0.62899
-----------------------------------------------------------------------
1       6       0       -0.054038     0.066689      0.063734
2       6       0       0.038957      -0.094685     1.475558
3       6       0       1.270225      -0.233955     2.097794
4       6       0       2.459370      -0.206975     1.357017
5       6       0       2.393239      -0.012565     -0.030317
```

```
6       6       0       1.171596        0.136875        -0.662944
7       1       0       -0.852652       -0.058263       2.092284
8       1       0       1.308461        -0.351424       3.178354
9       1       0       3.419262        -0.326966       1.852247
10      1       0       3.308145        0.014128        -0.617920
11      1       0       1.130756        0.276977        -1.739194
12      6       0       -1.287542       0.266381        -0.672593
13      8       0       -1.249692       0.966073        -1.758581
14      6       0       -2.600213       -0.248449       -0.237259
15      6       0       -2.795630       -1.197883       0.809589
16      6       0       -4.047951       -1.673460       1.113753
17      6       0       -5.180566       -1.190197       0.407600
18      6       0       -5.018805       -0.249236       -0.636732
19      6       0       -3.759874       0.203390        -0.948163
20      1       0       -1.947204       -1.608826       1.342946
21      1       0       -4.193072       -2.423580       1.885441
22      8       0       -6.367777       -1.682490       0.757975
23      1       0       -5.892247       0.082121        -1.193672
24      1       0       -3.624187       0.903810        -1.765082
25      1       0       -7.084765       -1.287203       0.228279
-----------------------------------------------------------------------

***********************************************************************
4HOBP in Water - T_1:
Total Energy, E(TD-HF/TD-KS) = -651.042787905
Energy, force constant and most relevant orbital transitions:
Excited State 1: Triplet-?Sym 2.4453 eV 507.03 nm f=0.000
MO:     Occ Virt            Coeff.
        51 -> 53            0.10320
        52 -> 53            -0.66036
        52 -> 54            -0.16632
-----------------------------------------------------------------------
1       6       0       0.001197        -0.009512       -0.006415
2       6       0       -0.004861       -0.013866       1.398641
3       6       0       1.189981        -0.005078       2.113993
4       6       0       2.413532        0.008665        1.442293
5       6       0       2.431583        0.026653        0.046085
6       6       0       1.239031        0.025237        -0.671077
7       1       0       -0.948119       0.005811        1.939026
8       1       0       1.164430        0.001229        3.200998
9       1       0       3.345084        0.013510        2.002537
10      1       0       3.379460        0.041609        -0.486513
11      1       0       1.257636        0.042426        -1.757627
12      6       0       -1.244425       0.048195        -0.799057
13      8       0       -1.241248       0.667253        -1.926244
14      6       0       -2.461576       -0.608325       -0.420683
15      6       0       -2.524754       -1.689769       0.545350
16      6       0       -3.716061       -2.261956       0.875639
17      6       0       -4.930958       -1.826393       0.244122
18      6       0       -4.890416       -0.827009       -0.765056
19      6       0       -3.702186       -0.247485       -1.108650
20      1       0       -1.609818       -2.053727       0.999581
21      1       0       -3.768752       -3.068332       1.602222
22      8       0       -6.071248       -2.434176       0.631270
23      1       0       -5.815918       -0.530998       -1.254517
24      1       0       -3.662792       0.519125        -1.873408
25      1       0       -6.829415       -2.077308       0.136292
-----------------------------------------------------------------------

-----------------------------------------------------------------------

4HOBP in Water - T_1 - Vertical transitions:

Excited State 1:      3.020-A       0.9896 eV   1252.87 nm    f=0.0340
Excited State 2:      3.019-A       1.2931 eV   958.78 nm     f=0.0564
Excited State 3:      3.028-A       1.7466 eV   709.84 nm     f=0.0004
```

```
Excited State 4:     3.043-A      1.8588 eV   667.01 nm    f=0.0024
Excited State 5:     3.046-A      2.4174 eV   512.88 nm    f=0.2235
Excited State 6:     3.033-A      2.5457 eV    487.03 nm   f=0.0018
Excited State 7:     3.056-A      2.8507 eV    434.92 nm   f=0.0254
Excited State 8:     3.041-A      3.0096 eV    411.96 nm   f=0.0454
Excited State 9:     3.254-A      3.5641 eV    347.87 nm   f=0.0235
Excited State 10:    3.046-A      3.6831 eV    336.63 nm   f=0.0054
Excited State 11:    3.069-A      3.7873 eV    327.36 nm   f=0.0155
Excited State 12:    3.110-A      3.9054 eV    317.47 nm   f=0.0688
Excited State 13:    3.264-A      3.9345 eV    315.12 nm   f=0.0661
Excited State 14:    3.321-A      4.0395 eV    306.93 nm   f=0.0061
Excited State 15:    3.570-A      4.1537 eV    298.49 nm   f=0.0574
Excited State 16:    3.207-A      4.2630 eV    290.84 nm   f=0.0262
Excited State 17:    3.042-A      4.2712 eV    290.28 nm   f=0.0006
Excited State 18:    3.401-A      4.3136 eV    287.43 nm   f=0.0019
Excited State 19:    3.520-A      4.4159 eV    280.77 nm   f=0.0385
Excited State 20:    3.035-A      4.4337 eV    279.64 nm   f=0.0026
Excited State 21:    3.068-A      4.5623 eV    271.76 nm   f=0.0012
Excited State 22:    3.128-A      4.6340 eV    267.55 nm   f=0.0309
Excited State 23:    3.054-A      4.6494 eV    266.66 nm   f=0.0044
Excited State 24:    3.156-A      4.7244 eV    262.44 nm   f=0.1650
Excited State 25:    3.848-A      4.7721 eV    259.81 nm   f=0.0058
Excited State 26:    3.068-A      4.9009 eV    252.98 nm   f=0.0169
Excited State 27:    3.308-A      4.9739 eV    249.27 nm   f=0.0053
Excited State 28:    3.178-A      5.0069 eV    247.63 nm   f=0.0237
Excited State 29:    3.179-A      5.0193 eV    247.02 nm   f=0.0013
Excited State 30:    3.130-A      5.0532 eV    245.36 nm   f=0.0010
Excited State 31:    3.455-A      5.0747 eV    244.32 nm   f=0.0212
Excited State 32:    3.119-A      5.2288 eV    237.12 nm   f=0.0024
Excited State 33:    3.072-A      5.2420 eV    236.52 nm   f=0.0043
Excited State 34:    3.876-A      5.3067 eV    233.64 nm   f=0.0051
Excited State 35:    3.301-A      5.3778 eV    230.55 nm   f=0.0093
Excited State 36:    3.055-A      5.4191 eV    228.79 nm   f=0.0065
-------------------------------------------------------------------------
```

Structures of the S_0 and S_1 states of $4BPO^-$ (anion) in Water

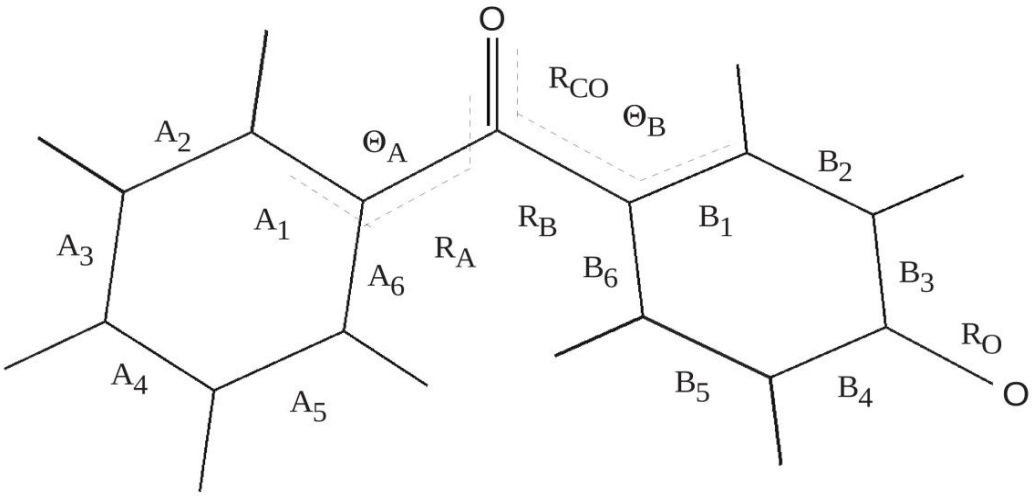

Coord	Values ----------		Deviations ----------
	S_0	S_1	S_1
R_{co}	1.250	1.303	0.01
R_A	1.496	1.421	**0.02**
R_B	1.452	1.486	0.00
R_O	1.285	1.260	0.00
A_1	1.416	1.429	0.00
A_2	1.376	1.385	0.00
A_3	1.436	1.404	0.00
A_4	1.433	1.404	0.00
A_5	1.379	1.386	0.00
A_6	1.415	1.428	0.00
B_1	1.403	1.422	0.00
B_2	1.386	1.368	0.00
B_3	1.401	1.449	0.01
B_4	1.398	1.449	0.01
B_5	1.388	1.368	0.00
B_6	1.404	1.422	0.00
Θ_A	-41.97	0.08	**0.54**
Θ_B	-13.55	-87.86	**1.68**
	Standard deviations from S_0 =		**0.357**

The following tables report energies, Cartesian coordinates and vertical transitions of the S_0 and S_1 states of $4BPO^-$ (anion) in water, obtained from the calculations.

```
*********************************************************************
4OBP Anion in Water - S_0:
SCF Done: E(RPBE1PBE) = -650.681535156
Sum of electronic and thermal Free Energies= -650.536616
---------------------------------------------------------------------
1       6       0       -0.019363       0.043007        0.048300
2       6       0       0.033662        0.052904        1.447963
3       6       0       1.261558        -0.005760       2.105392
4       6       0       2.444781        -0.095656       1.372594
5       6       0       2.399209        -0.107962       -0.022907
6       6       0       1.175395        -0.023205       -0.680813
7       1       0       -0.883850       0.132419        2.024992
8       1       0       1.292819        0.018985        3.191749
9       1       0       3.400909        -0.152535       1.886922
10      1       0       3.318941        -0.178965       -0.598199
11      1       0       1.137727        -0.021718       -1.767374
12      6       0       -1.309269       0.187156        -0.696483
13      8       0       -1.334182       0.979375        -1.662798
14      6       0       -2.478739       -0.573899       -0.296205
15      6       0       -2.413612       -1.704463       0.553025
16      6       0       -3.540272       -2.430672       0.875493
17      6       0       -4.838032       -2.071492       0.385232
18      6       0       -4.884871       -0.928895       -0.483627
19      6       0       -3.750358       -0.223148       -0.811926
20      1       0       -1.452149       -2.031436       0.941182
21      1       0       -3.461416       -3.305823       1.517971
22      8       0       -5.895244       -2.730993       0.701052
23      1       0       -5.853748       -0.627247       -0.877877
24      1       0       -3.825899       0.639149        -1.470890
---------------------------------------------------------------------

---------------------------------------------------------------------

4OBP Anion in Water - S_0 - Vertical transitions:

Excited State 1:      Singlet-A    3.5844 eV     345.90 nm     f=0.5361
Excited State 2:      Singlet-A    4.0415 eV     306.77 nm     f=0.0147
Excited State 3:      Singlet-A    4.2350 eV     292.76 nm     f=0.0032
Excited State 4:      Singlet-A    4.5098 eV     274.92 nm     f=0.0219
Excited State 5:      Singlet-A    4.7158 eV     262.91 nm     f=0.0016
Excited State 6:      Singlet-A    4.8204 eV     257.21 nm     f=0.2195
Excited State 7:      Singlet-A    4.8640 eV     254.90 nm     f=0.0416
Excited State 8:      Singlet-A    4.9507 eV     250.44 nm     f=0.0199
Excited State 9:      Singlet-A    5.1009 eV     243.06 nm     f=0.1417
Excited State 10:     Singlet-A    5.2429 eV     236.48 nm     f=0.0037
Excited State 11:     Singlet-A    5.4748 eV     226.47 nm     f=0.0009
Excited State 12:     Singlet-A    5.7060 eV     217.29 nm     f=0.0000
Excited State 13:     Singlet-A    5.7387 eV     216.05 nm     f=0.0309
Excited State 14:     Singlet-A    5.8095 eV     213.42 nm     f=0.0056
Excited State 15:     Singlet-A    5.8848 eV     210.69 nm     f=0.0021
Excited State 16:     Singlet-A    5.9896 eV     207.00 nm     f=0.0113
Excited State 17:     Singlet-A    6.0219 eV     205.89 nm     f=0.0430
Excited State 18:     Singlet-A    6.0543 eV     204.79 nm     f=0.0164
Excited State 19:     Singlet-A    6.0962 eV     203.38 nm     f=0.0325
Excited State 20:     Singlet-A    6.1736 eV     200.83 nm     f=0.0601
Excited State 21:     Singlet-A    6.1766 eV     200.73 nm     f=0.0847
Excited State 22:     Singlet-A    6.2473 eV     198.46 nm     f=0.0038
Excited State 23:     Singlet-A    6.3008 eV     196.78 nm     f=0.0378
Excited State 24:     Singlet-A    6.3289 eV     195.90 nm     f=0.0278
Excited State 25:     Singlet-A    6.3663 eV     194.75 nm     f=0.0012
Excited State 26:     Singlet-A    6.3936 eV     193.92 nm     f=0.0593
```

```
Excited State 27:    Singlet-A    6.4243 eV    192.99 nm    f=0.0049
Excited State 28:    Singlet-A    6.4421 eV    192.46 nm    f=0.0455
Excited State 29:    Singlet-A    6.5325 eV    189.80 nm    f=0.0032
Excited State 30:    Singlet-A    6.6424 eV    186.66 nm    f=0.0753
Excited State 31:    Singlet-A    6.6696 eV    185.89 nm    f=0.1882
Excited State 32:    Singlet-A    6.6882 eV    185.38 nm    f=0.0456
Excited State 33:    Singlet-A    6.7023 eV    184.99 nm    f=0.0318
Excited State 34:    Singlet-A    6.7065 eV    184.87 nm    f=0.1816
Excited State 35:    Singlet-A    6.7583 eV    183.45 nm    f=0.0563
Excited State 36:    Singlet-A    6.7913 eV    182.56 nm    f=0.1366
-----------------------------------------------------------------------

***********************************************************************
4OBP Anion in Water - S_1:
Total Energy, E(TD-HF/TD-KS) = -650.587126029
Energy, force constant and most relevant orbital transitions:
Excited State 1: Singlet-?Sym 1.7982 eV 689.48 nm f=0.000
MO:     Occ  Virt           Coeff.
        52 -> 53            0.70023
-----------------------------------------------------------------------
1       6       0       0.115300        -0.340743       -0.197365
2       6       0       -0.077480       -0.194482       1.210382
3       6       0       0.929797        0.297577        2.025691
4       6       0       2.175282        0.668228        1.495274
5       6       0       2.384749        0.529137        0.113621
6       6       0       1.390399        0.039493        -0.717313
7       1       0       -1.031602       -0.474239       1.652326
8       1       0       0.746979        0.396018        3.094197
9       1       0       2.960336        1.053774        2.139803
10      1       0       3.344927        0.810451        -0.315631
11      1       0       1.575075        -0.060149       -1.783809
12      6       0       -0.906084       -0.838612       -1.050398
13      8       0       -0.793965       -0.996018       -2.338577
14      6       0       -2.237841       -1.235686       -0.523866
15      6       0       -2.489958       -2.580494       -0.136960
16      6       0       -3.722325       -2.968144       0.313887
17      6       0       -4.816839       -2.020890       0.388729
18      6       0       -4.548933       -0.661989       -0.038381
19      6       0       -3.307476       -0.299837       -0.485275
20      1       0       -1.674978       -3.298700       -0.187861
21      1       0       -3.916283       -3.989631       0.630089
22      8       0       -5.955341       -2.365414       0.804992
23      1       0       -5.365211       0.053502        0.013609
24      1       0       -3.117152       0.723144        -0.801107
-----------------------------------------------------------------------
```

Electrostatic potential V on the Van der Waals surfaces of the S_0, T_1, S_1, and S_2 states in 2-Propanol

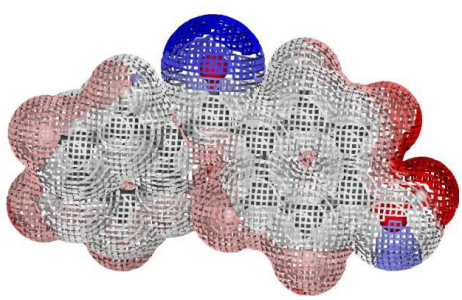

S_0

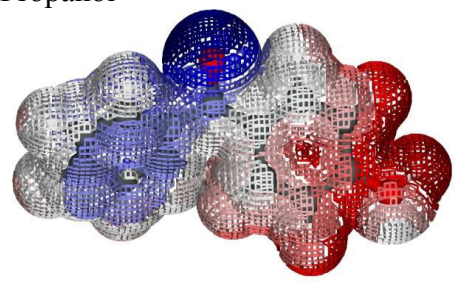

T_1

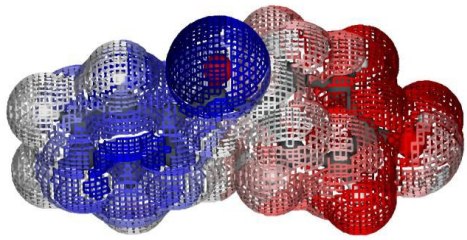

S_1

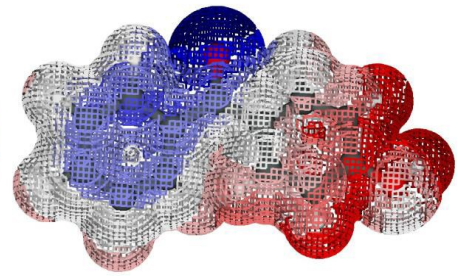

S_2

Deprotonation equilibrium of 4BPOH in 2-propanol

$[4HOBP\,(C_3H_8O)_3]\ +\ (C_3H_8O)_3\ \rightleftarrows\ [4OBP\,(C_3H_8O)_3]^-\ +\ [C_3H_9O\,(C_3H_8O)_2]^+$

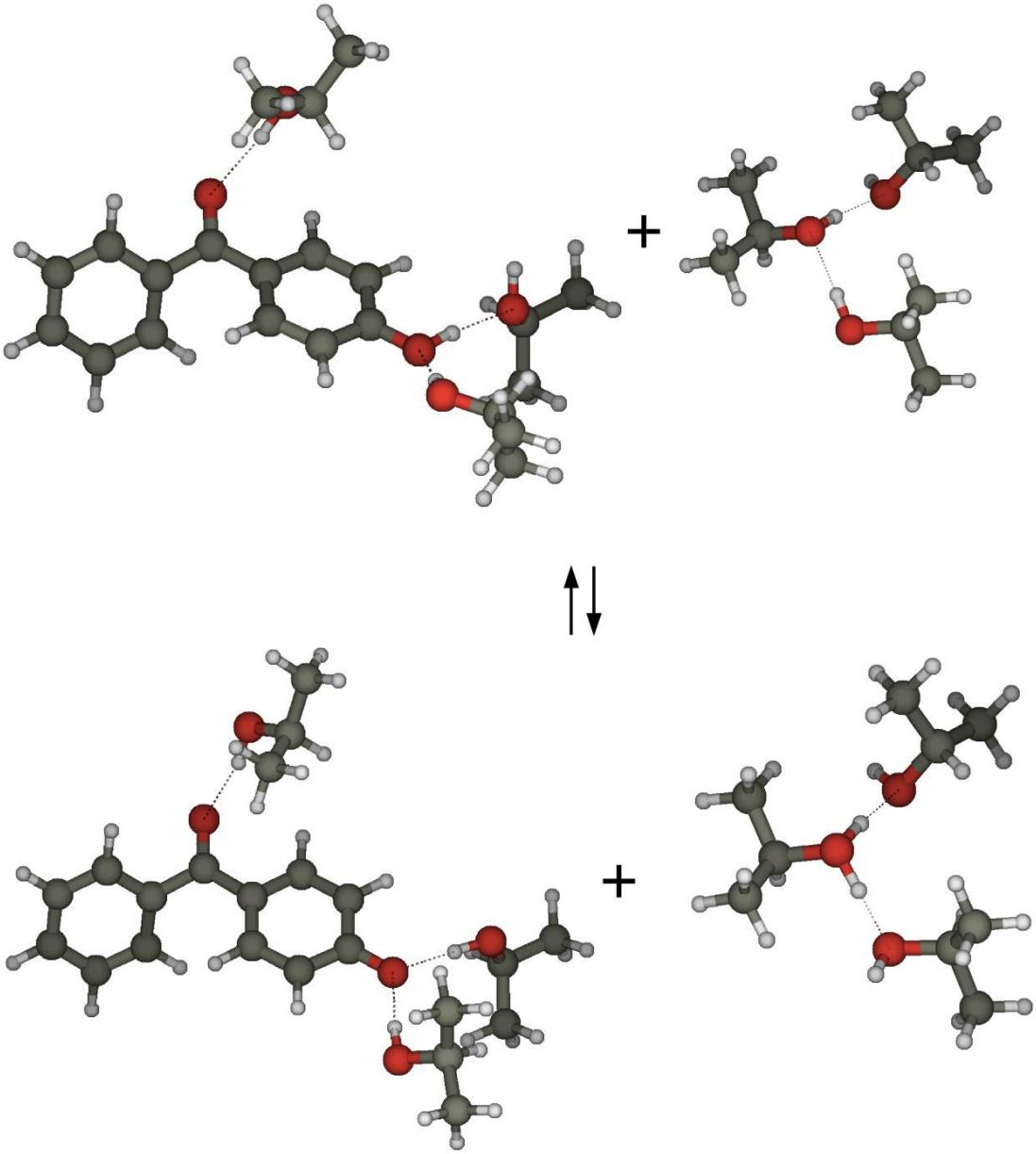

Section 1 – Phenol oligomers

Optimized structures of 4PP ground state conformations S_0 and excited states S_1

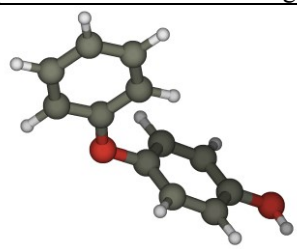	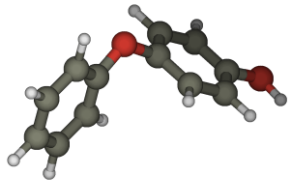	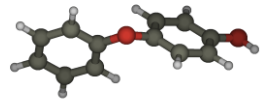
2a-S_0	2b-S_0	2c-S_0
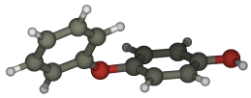	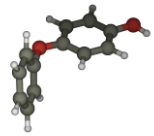	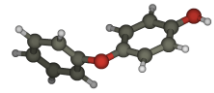
2a-S_1	2b-S_1	2c-S_1

The chart below shows the calculated transitions for the different conformers of 4PP (wavelengths and the force constants *f* are reported).

2a		2b		2c		2a		2b		2c	
λ (nm)	f	λ (nm)	f	λ (nm)	f	λ (nm)	f	λ (nm)	f	λ (nm)	f
301	0,027	315	0,028	318	0,025	202	0,141	202	0,060	201	0,094
297	0,007	296	0,012	296	0,021	201	0,083	201	0,449	200	0,257
275	0,009	289	0,105	293	0,117	200	0,659	198	0,150	198	0,146
273	0,001	271	0,003	272	0,001	197	0,031	196	0,005	196	0,027
267	0,033	269	0,024	269	0,030	197	0,026	196	0,003	196	0,090
263	0,023	267	0,072	266	0,075	196	0,034	195	0,179	195	0,008
257	0,001	258	0,001	261	0,001	196	0,007	195	0,022	195	0,108
254	0,008	256	0,014	255	0,021	195	0,049	194	0,038	194	0,015
252	0,001	252	0,024	251	0,020	194	0,144	194	0,009	194	0,050
247	0,005	243	0,016	243	0,003	193	0,054	193	0,024	193	0,022
242	0,010	243	0,005	243	0,025	192	0,103	193	0,046	192	0,021
242	0,001	240	0,003	239	0,001	191	0,007	191	0,016	191	0,001
236	0,302	237	0,005	238	0,001	191	0,026	189	0,022	190	0,016
235	0,016	235	0,003	237	0,003	188	0,012	189	0,016	189	0,018
233	0,032	233	0,020	233	0,013	188	0,006	188	0,016	189	0,016
232	0,017	232	0,005	231	0,008	187	0,002	188	0,001	189	0,026
228	0,003	230	0,014	229	0,015	186	0,001	187	0,004	187	0,001
227	0,004	228	0,135	228	0,080	185	0,003	186	0,009	186	0,127
225	0,020	226	0,078	226	0,014	184	0,010	186	0,106	185	0,011
222	0,004	224	0,016	225	0,118	184	0,000	184	0,082	184	0,021
221	0,073	221	0,001	221	0,002	183	0,000	184	0,002	184	0,083
221	0,000	217	0,003	217	0,015	183	0,002	183	0,017	183	0,001
219	0,002	217	0,014	215	0,006	182	0,020	181	0,000	181	0,003
214	0,004	214	0,001	214	0,003	181	0,003	180	0,001	180	0,006
214	0,001	213	0,010	214	0,001	180	0,003	180	0,010	180	0,003
213	0,001	212	0,002	213	0,002	180	0,001	179	0,009	179	0,014
210	0,002	212	0,043	211	0,028	179	0,008	179	0,039	178	0,003
208	0,024	210	0,013	210	0,004	178	0,040	178	0,001	178	0,011
207	0,017	207	0,030	208	0,030	177	0,003	178	0,003	178	0,003
206	0,000	207	0,007	207	0,002	177	0,006	177	0,001	178	0,019
205	0,181	206	0,129	206	0,140	177	0,007	177	0,005	177	0,005
205	0,031	204	0,006	206	0,018	176	0,010	176	0,004	177	0,001
203	0,169	203	0,150	202	0,316	176	0,032	176	0,004	176	0,004
202	0,042	202	0,252	202	0,215	175	0,017	175	0,025	175	0,007

Weight function and simulated spectra

The calculation of each structure required 80 transitions to be taken into account, starting from the lowest energy one. Such transitions were combined as Gaussian functions with the maximum on the wavelength of each transition. The combination was carried out by using the R language for statistical computing (R Development Core Team, 2008).
As an example, the R script used to combine the absorption spectra of the 2a conformation of 4PP is shown below.

```
a=c(0.0270,0.0068,0.0085,0.0007,0.0328,0.0232,0.0005,0.0079,0.0007
,0.0051,0.0100,0.0006,0.3019,0.0164,0.0318,0.0171,0.0033,0.0042,0.
0199,0.0039,
0.0729,0.0001,0.0015,0.0042,0.0014,0.0005,0.0019,0.0237,0.0165,0.0
001,0.1806,0.0307,0.1687,0.0421,0.1413,0.0833,0.6587,0.0310,0.0256
,0.0335,0.0071,0.0487,0.1438,0.0543,0.1029,0.0065,0.0258,0.0118,0.
0059,0.0023,0.0012,0.0025,0.0097,0.0001,0.0000,0.0021,0.0203,0.002
9,0.0027,0.0012,0.0076,0.0398,0.0030,0.0059,0.0073,0.0104,0.0324,0
.0173,0.0033,0.0023,0.0665,0.0266,0.0324,0.0017,0.0077,0.0024,0.01
68,0.0144,0.0057,0.0074)
b=c(301,297,275,273,267,263,257,254,252,247,242,242,236,235,233,23
2,228,227,225,222,221,221,219,214,214,213,210,208,207,206,205,205,
203,202,202,201,200,197,197,196,196,195,194,193,192,191,191,188,18
8,187,186,185,184,184,183,183,182,181,180,180,179,178,177,177,177,
176,176,175,174,173,173,173,172,172,171,171,170,170,169,169)
c=c(3.5)
xmin<c(200)
xmax<c(360)
x<seq(xmin,xmax,length.out=200)
nx=length(x)
ng=length(b)
y=data.frame(NULL)
for (i in 1:ng) {
for (j in 1:nx) {
y[i,j]=(a[i]*exp(((x[j]b[i])^2)/(c^2))) }}
colsum<colSums(y)
tabella<data.frame(x,colsum)
write.csv(tabella,file="PhOPhOH_acqua.csv")
```

The spectra of the different conformations were then linearly combined, by weighting for the different energy of the structures. The weight of each conformation was calculated as shown in the equation below:

$$w_i = \frac{e^{-\frac{E_i}{RT}}}{\sum e^{-\frac{E_i}{RT}}}$$

where E_i is the energy of the i^{th} conformation and N is the number of considered conformations, three in this case (2a, 2b and 2c). In this way one obtains the simulated absorption spectra, which give some insight into the possible absorption of radiation by compounds for which standards are not available. The figures 23b and 24 b, concerning 4PPP and 4PPPP, has been obtained with this approach.

Optimized structures of 4PPP ground state conformations S_0 and excited states S_1

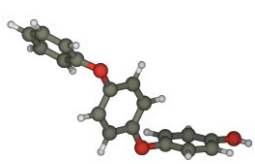	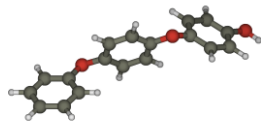	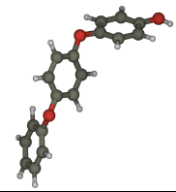
3a-S_0	3b-S_0	3c-S_0
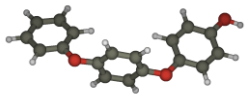	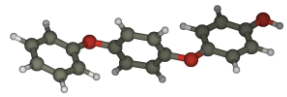	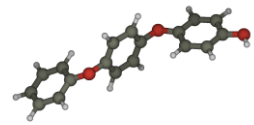
3a-S_1	3b-S_1	3c-S_1

The chart below shows the calculated transitions for the different conformers of 4PPP (wavelengths and the force constants ***f*** are reported).

3a		3b		3c		3a		3b		3c	
λ (nm)	f	λ (nm)	f	λ (nm)	f	λ (nm)	f	λ (nm)	f	λ (nm)	f
324	0,050	335	0,029	338	0,013	228	0,011	228	0,048	228	0,050
313	0,003	320	0,016	324	0,004	228	0,001	226	0,018	227	0,008
306	0,002	309	0,004	311	0,010	225	0,007	226	0,003	226	0,046
296	0,001	304	0,161	309	0,158	224	0,022	225	0,064	225	0,011
290	0,024	300	0,003	301	0,017	224	0,002	224	0,004	224	0,049
289	0,001	291	0,070	294	0,082	224	0,003	224	0,039	224	0,016
285	0,044	287	0,020	288	0,002	223	0,010	222	0,003	223	0,121
284	0,041	284	0,001	284	0,017	222	0,001	222	0,001	222	0,022
281	0,050	278	0,002	279	0,003	221	0,007	221	0,002	222	0,006
274	0,015	277	0,003	277	0,010	220	0,010	221	0,003	220	0,000
270	0,023	275	0,015	274	0,099	219	0,005	219	0,007	218	0,002
269	0,000	269	0,010	271	0,001	217	0,001	217	0,002	217	0,001
267	0,026	269	0,026	269	0,028	217	0,001	217	0,002	217	0,002
266	0,037	265	0,082	267	0,038	216	0,005	215	0,014	216	0,003
263	0,018	263	0,045	262	0,036	215	0,048	215	0,007	215	0,010
262	0,000	260	0,008	259	0,013	214	0,005	214	0,013	214	0,027
261	0,010	257	0,020	258	0,004	214	0,017	213	0,001	213	0,003
257	0,000	256	0,001	258	0,007	213	0,001	212	0,005	213	0,003
256	0,013	256	0,000	254	0,002	213	0,001	212	0,006	212	0,005
253	0,013	254	0,053	253	0,077	212	0,000	211	0,002	212	0,007
250	0,002	252	0,012	251	0,002	211	0,011	210	0,007	211	0,020
249	0,004	249	0,002	250	0,002	210	0,028	209	0,001	210	0,038
248	0,001	248	0,001	248	0,025	209	0,003	209	0,057	209	0,010
245	0,010	246	0,027	247	0,003	208	0,001	208	0,078	208	0,008
245	0,004	245	0,041	244	0,047	207	0,009	208	0,025	208	0,003
241	0,001	242	0,003	242	0,001	207	0,083	208	0,005	208	0,056
240	0,112	241	0,006	242	0,007	207	0,028	207	0,003	206	0,015
239	0,004	240	0,002	241	0,003	206	0,015	206	0,017	206	0,018
238	0,034	240	0,000	240	0,005	205	0,111	206	0,062	205	0,152
238	0,149	238	0,013	240	0,003	205	0,062	205	0,132	205	0,053
237	0,006	238	0,001	240	0,002	204	0,002	205	0,034	205	0,007
237	0,005	238	0,001	238	0,001	204	0,113	203	0,124	203	0,087
236	0,060	236	0,000	236	0,010	203	0,174	203	0,115	203	0,042
235	0,018	236	0,003	235	0,005	203	0,035	202	0,067	202	0,288
234	0,023	233	0,009	234	0,009	202	0,071	202	0,054	202	0,269
234	0,003	232	0,014	231	0,012	202	0,218	202	0,696	201	0,279
231	0,140	231	0,002	230	0,014	201	0,162	201	0,068	201	0,020

231	0,084	230	0,250	230	0,012	201	0,195	200	0,064	201	0,027
230	0,016	230	0,025	229	0,018	201	0,238	199	0,052	200	0,026
229	0,015	229	0,003	229	0,006	200	0,190	199	0,000	200	0,019

Optimized structures of 4PPPP ground state conformations S_0 and excited states S_1

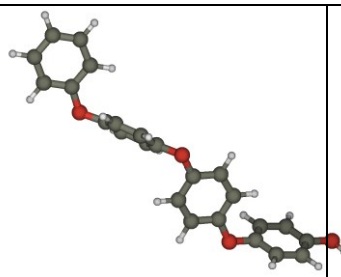	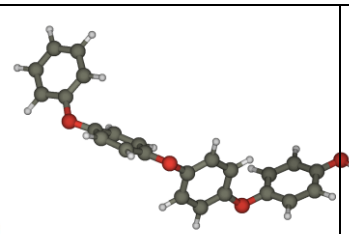	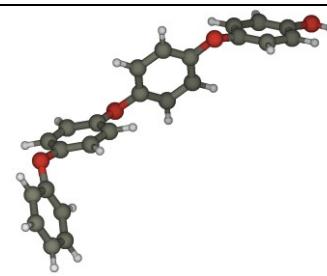
4a-S_0	4b-S_0	4c-S_0
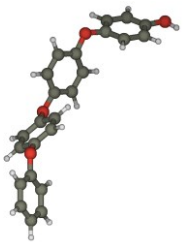	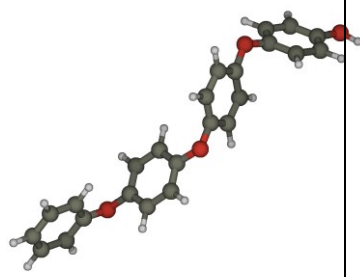	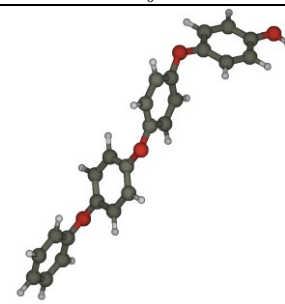
4d-S_0	4e-S_0	4f-S_0
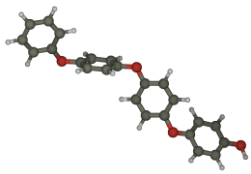	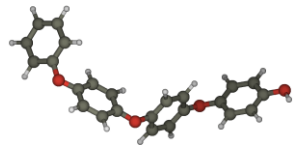	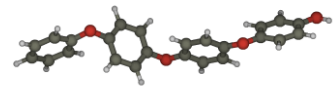
4a-S_1	4b-S_1	4c-S_1
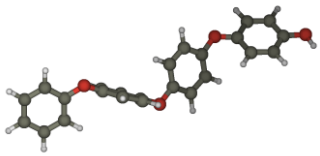	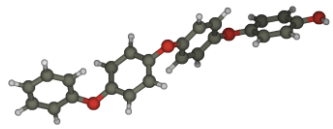	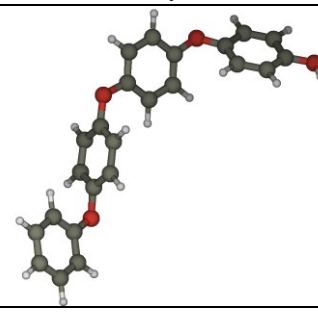
4d-S_1	4e-S_1	4f-S_1

Differential electronic density map between state S_1 and S_0 in the different conformations of 4PPPP.

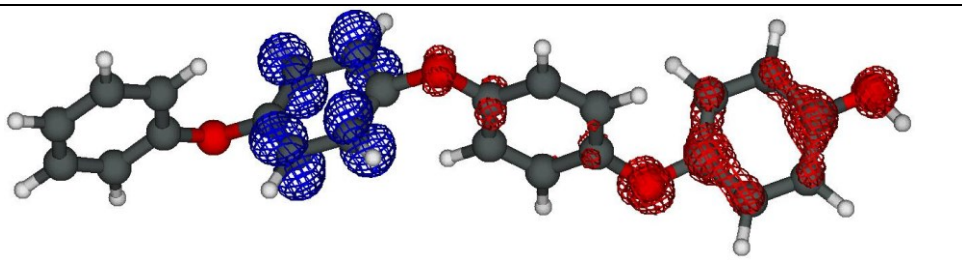	4a
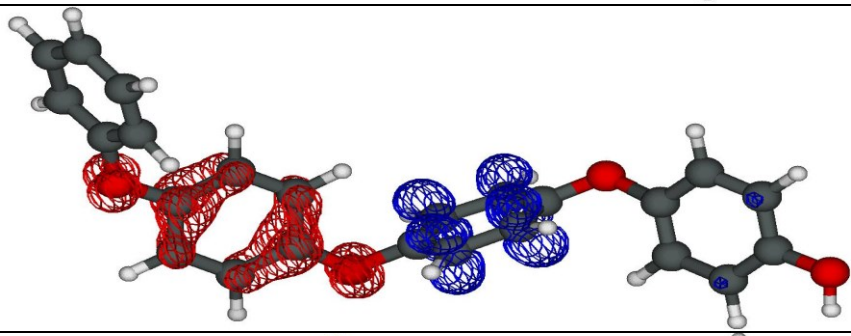	4b
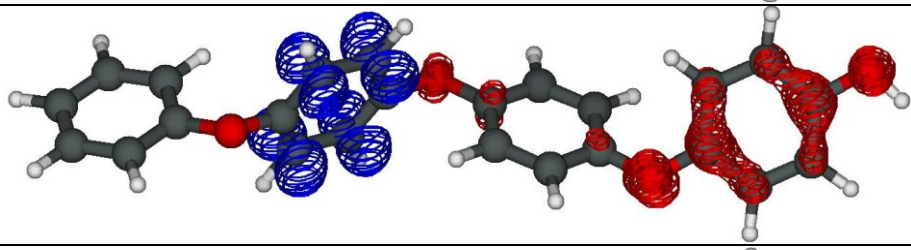	4c
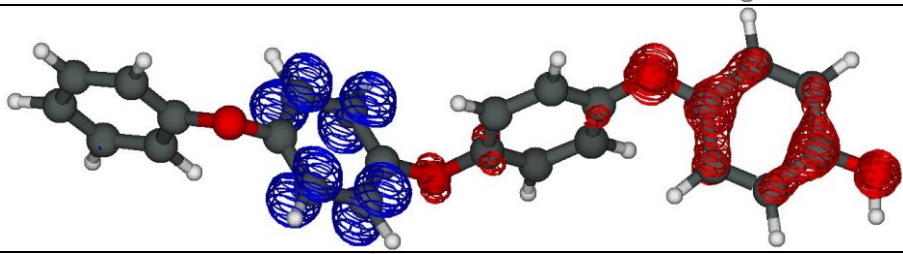	4d
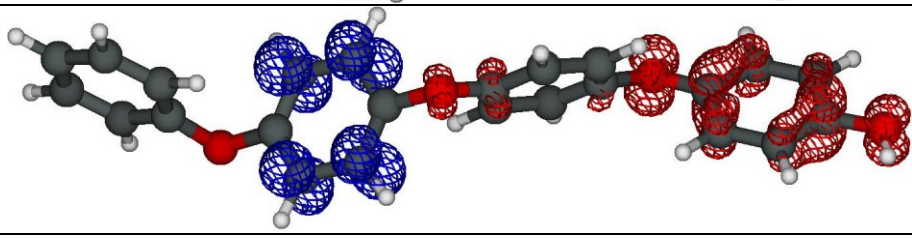	4e

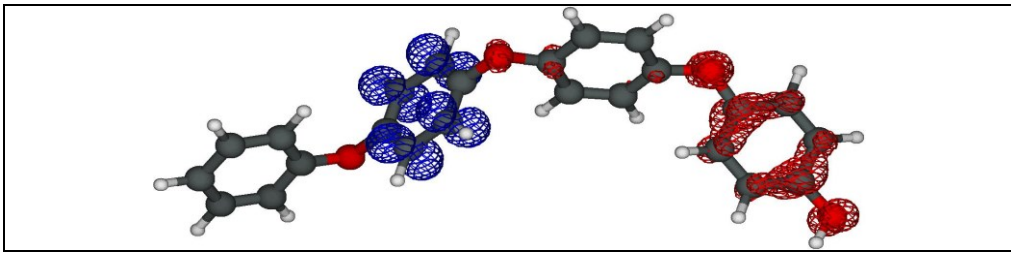

4f

The chart below shows the calculated transitions for the different conformers of 4PPPP (wavelengths and the force constants ***f*** are reported).

4a		4b		4c		4d		4e		4f	
(nm)	f		f	(nm)	f		f		f	(nm)	f
349	0,042	342	0,027	352	0,019	345	0,040	342	0,007	357	0,008
339	0,012	327	0,009	338	0,015	335	0,009	335	0,015	342	0,007
323	0,004	320	0,002	327	0,009	323	0,003	322	0,025	332	0,008
320	0,009	317	0,004	321	0,129	316	0,001	314	0,039	327	0,171
318	0,205	309	0,028	319	0,008	312	0,187	309	0,018	321	0,009
311	0,003	304	0,026	311	0,023	308	0,005	307	0,064	316	0,007
306	0,004	303	0,149	309	0,022	306	0,006	304	0,029	311	0,125
304	0,046	301	0,004	306	0,097	302	0,043	302	0,002	310	0,056
301	0,005	298	0,001	301	0,043	301	0,005	301	0,002	304	0,009
299	0,018	297	0,005	300	0,024	298	0,028	298	0,005	301	0,002
297	0,002	296	0,019	298	0,007	294	0,012	294	0,057	298	0,002
294	0,122	291	0,000	290	0,034	290	0,041	291	0,007	292	0,165
287	0,004	288	0,002	288	0,012	289	0,004	288	0,009	290	0,030
286	0,000	284	0,003	286	0,086	285	0,004	286	0,133	290	0,008
284	0,007	282	0,037	285	0,040	283	0,091	285	0,025	286	0,001
283	0,005	282	0,002	284	0,005	281	0,018	281	0,021	285	0,012
279	0,040	279	0,001	283	0,000	280	0,001	276	0,002	283	0,010
277	0,000	278	0,001	277	0,000	276	0,002	276	0,005	279	0,000
275	0,005	276	0,001	275	0,007	276	0,016	275	0,008	274	0,003
275	0,013	274	0,118	274	0,078	274	0,027	273	0,049	273	0,109
274	0,013	272	0,011	273	0,023	273	0,005	271	0,047	272	0,008
271	0,029	271	0,001	270	0,021	270	0,028	270	0,001	270	0,002
269	0,010	269	0,039	268	0,007	270	0,005	269	0,001	269	0,000
267	0,005	268	0,027	267	0,000	268	0,002	268	0,003	268	0,018
266	0,007	267	0,029	267	0,003	266	0,010	267	0,013	267	0,005
266	0,007	266	0,032	266	0,013	265	0,005	267	0,021	266	0,025
263	0,047	264	0,003	266	0,003	264	0,030	266	0,011	265	0,006
263	0,055	262	0,001	262	0,016	264	0,020	264	0,034	264	0,002
262	0,054	260	0,020	261	0,058	262	0,070	262	0,001	261	0,013
260	0,028	259	0,000	261	0,004	260	0,010	260	0,001	260	0,042
257	0,001	258	0,001	260	0,016	259	0,000	259	0,023	258	0,017
256	0,001	258	0,005	256	0,004	258	0,035	257	0,003	257	0,001
255	0,001	257	0,067	255	0,002	257	0,012	256	0,009	255	0,003
255	0,003	256	0,003	255	0,021	255	0,001	255	0,075	255	0,000
254	0,021	253	0,006	254	0,037	254	0,033	254	0,006	253	0,023
253	0,008	253	0,040	252	0,047	253	0,000	254	0,004	253	0,004
252	0,015	253	0,003	252	0,005	252	0,009	252	0,044	252	0,076
252	0,020	252	0,000	252	0,014	252	0,017	252	0,004	252	0,004
250	0,006	252	0,005	250	0,020	251	0,045	251	0,020	251	0,064
250	0,079	251	0,004	250	0,000	250	0,001	250	0,002	249	0,017
249	0,000	251	0,002	249	0,002	250	0,010	248	0,001	248	0,012
248	0,003	247	0,002	247	0,002	248	0,026	246	0,028	247	0,000
248	0,000	245	0,002	246	0,001	247	0,012	246	0,003	247	0,001
247	0,018	245	0,008	246	0,002	246	0,002	246	0,001	246	0,000
246	0,022	244	0,014	245	0,070	245	0,023	245	0,005	246	0,008
245	0,030	244	0,004	245	0,055	245	0,001	243	0,001	245	0,004
244	0,002	243	0,028	245	0,009	244	0,002	243	0,002	245	0,001
243	0,018	243	0,020	244	0,004	243	0,004	243	0,003	244	0,001
243	0,007	242	0,007	243	0,002	242	0,009	242	0,009	243	0,017
243	0,003	241	0,002	242	0,013	241	0,006	240	0,003	242	0,010
241	0,005	240	0,005	242	0,000	241	0,004	240	0,012	242	0,013
241	0,006	239	0,069	241	0,014	240	0,003	240	0,004	242	0,012

240	0,002	238	0,164	241	0,005	239	0,003	239	0,001	241	0,048
240	0,013	238	0,011	239	0,001	238	0,007	238	0,005	241	0,010
239	0,005	238	0,004	238	0,014	238	0,011	238	0,001	240	0,020
239	0,009	238	0,006	238	0,008	238	0,008	237	0,007	238	0,007
238	0,054	237	0,006	237	0,003	237	0,001	237	0,000	238	0,014
237	0,003	236	0,001	237	0,002	237	0,002	236	0,015	238	0,002
236	0,018	236	0,001	237	0,012	237	0,003	236	0,062	237	0,004
235	0,013	236	0,001	236	0,006	236	0,009	235	0,004	236	0,032
235	0,013	236	0,089	236	0,001	235	0,002	235	0,005	236	0,010
234	0,004	234	0,004	234	0,009	234	0,078	235	0,003	236	0,003
233	0,017	234	0,002	233	0,003	233	0,012	235	0,002	235	0,001
233	0,056	233	0,002	233	0,007	233	0,001	234	0,005	235	0,002
232	0,013	232	0,041	233	0,003	232	0,048	233	0,012	234	0,015
232	0,003	232	0,011	232	0,000	232	0,041	232	0,026	233	0,005
231	0,007	231	0,010	232	0,004	232	0,003	232	0,013	233	0,007
231	0,002	231	0,023	231	0,029	231	0,021	231	0,142	231	0,007
230	0,003	230	0,014	231	0,007	230	0,041	231	0,225	231	0,014
230	0,043	230	0,001	230	0,008	229	0,030	231	0,063	231	0,002
230	0,003	230	0,015	229	0,022	229	0,026	230	0,009	230	0,002
229	0,002	229	0,012	229	0,001	229	0,077	229	0,046	229	0,004
228	0,008	229	0,016	228	0,005	229	0,016	229	0,005	227	0,008
228	0,014	228	0,005	228	0,011	228	0,121	229	0,021	227	0,013
228	0,018	227	0,121	227	0,077	228	0,016	228	0,001	226	0,009
227	0,102	227	0,028	227	0,032	227	0,049	228	0,008	226	0,036
226	0,047	226	0,000	227	0,002	227	0,007	227	0,003	226	0,005
226	0,008	226	0,027	226	0,019	226	0,042	226	0,018	225	0,001
226	0,055	226	0,018	225	0,031	226	0,006	226	0,003	225	0,027
225	0,002	225	0,044	225	0,041	225	0,002	225	0,010	225	0,001

References

[1] Atkins, P.W. Physical-Chemistry, (2012), Oxford University Press

[2] Remucal, C.K., Environmental. Sciences: Processes Impacts, (2014) **16**, 628

[3] Challis, J.K., Hanson, M.L., Friesen, K. J., Wong, C.S. Environmental Sciences: Processes Impacts, (2014), **16**, 672

[4] Mottes, C., Lesueur-Jannoyer, M,. Le Bail, M., Malezieux, E., Agronomy for Sustainable. Development., (2014), **34**, 229.

[5] Ryberg, K.R., Gilliom, R.K., Science Total Environment., (2015) **538**, 431

[6] Zafirious O, Joussot-Dubien J., Zepp R. and Zika R., Environmental Science & Technology.(1984),. Vol 18**,** **12**,358A-370A.

[7] Vione, D., Maurino, V., Minero, C., and Pelizzetti, E. (2005) in Environmental Photochemistry Part II (The Handbook of Environmental Chemistry), Vol. 2M (eds P. Boule, D. Bahnemann, and P.J.K. Robertson), Springer, Berlin, pp. 221 – 253.

[8] Vione, D., Minella, M., Maurino, V., Minero, C., Chemistry European Journal (2014) **20**, 10590-10606

[9] Fenner, K., Canonica, S.,. Wackett, L.P., Elsner, M., Science, (2013) **341**, 752

[10] Richard, C. Canonica, S. (2005) in Environmental Photochemistry Part II (The Handbook of Environmental Chemistry), vol. 2M (eds P. Boule, D. Bahnemann, and P.J.K. Robertson), Springer, Berlin, pp. 299–323 .

[11] Loiselle, S.,Bracchini,L., Dattilo, A.M., Ricci,M., Tognazzi, A., Cozar, A., Rossi, C., Limnology and Oceanography. (2009), **54**, 590– 597.

[12] Hoigne, J., Formulation and calibration of environmental reaction kinetics: Oxidations by aueous photooxidants as an example. In Aquatic Chemical Kinetics; (1990), Stumm, W. , Ed.; Wiley: New York,; pp 43-70.

[13] Oliveira, J.L., Boroski, M., Azevedo, J.C.R., Nozaki, J., Acta Hydrochimica et. Hydrobiologica. (2006), **34**, 608–617

14 Brinkmann T, Hoörsch P, Sartorius D and Frimmel F.H, Environmental Science & Technology. (2003), **37**, 4190-4198

15 Walker C.H, Hopkin S.P, Sibly R.M and Peakall D.B (2006) Principles of Ecotoxicology, 3rd ed. Taylor & Fancis

16 Comoretto L, Arfib B and Chiron S, Science Total Environment. (2007), **380**, 124 – 132.

17 Kuivila K.M and Jennings B.E, International Journal of Environmental. Analytical Chemistry (2007), **87**, 897 – 911.

[18] H. D. Burrows, M. Canle, J. A. Santaballa and S. Steenken, Journal of Photochemistry and Photobiology B: Biology.(2002) **67**, 71

[19] Bonnichon, F., Richard, C., Grabner, G., Chemical Communications (2001) 73-74.

[20] Vione, D., Minero, C., Al Housari, F., Chiron, S., Chemosphere (2007) **69**, 1548.

[21] Madronich, S., Flocke, S., The Handbook of Environmental Chemistry vol. 2L (Environmental Photochemistry), P. Boule (ed.), (1999) Spinger, Berlin

[22] Pilewskie, P., Rottman, G., Richard, E., Solar Physics. (2005) **230**, 55

[23] Sharpless, C. M., Blough, N. V., Environmental Science: Processes & Impacts (2014) **16**, 654 - 671

[24] N. Chaichitehrani, N., D'sa, E. J., Ko, D. S., Walker, N. D., Osburn, C. L., Chen, R. F., Journal of Coastal Research. (2014) **30**, 800

[25] Sun, D. Y., Hu, C. M., Qiu, Z. F., Wang, S. Q., Optics Express, (2015) **23**, A718

[26] Loiselle, S. A., Bracchini, L., Cozar, A., Dattilo, A. M., Tognazzi, A., Rossi, C., Journal of Photochemistry and Photobiology: B: Biology (2009) **95**, 129.

[27] B. D. Shaw, B.D., Wei, J. B., Tuli, A., Campbell, J., Parikh, S. J., Dabach, S., Buelow, M., Hopmans, J. W., Vadose Zone Journal. (2014) **13**, 12

[28] Helms, J. R., Stubbins, A., Ritchie, J.D., Minor, E. C., Kieber, D.J., Mopper, K., Limnology and Oceanography (2008) **53**, 955-969.

[29] Galgani, L., Tognazzi, A., Rossi, C., Ricci, M., Galvez, J. A., Dattilo, A. M., Cozar, A., Bracchini, L., Loiselle, S. A., Journal of Photochemistry and Photobiology B: Biology (2011) **102**, 132

[30] Lin, A. Y. C., Wang, X. H., Lee, W. N., Environmental Science & Technology (2013) **47**, 4104

[31] Schubert, H., Sagert, S., Forster, R. M., Helgoland Marine Research (2001) **55**, 12

[32] Warneck, P., Wurzinger, C., Journal of Physical Chemistry (1988) **92**, 6278

[33] Nissenson, P., Dabdub, D., Das, R., Maurino, V., Minero C., Vione, D. Atmospheric Environment. (2010) **44**, 4859

[34] Vione, D., Khanra, S., Man, S. C., Maddigapu, P. R., Das, R., Arsene, C., Olariu, R. I., Maurino V., Minero, C., Water Research (2009) **43**, 4718

[35] Chiron, S., Minero, C., Vione, D., Environmental Science & Technology (2007) **41**, 3127

[36] Chiron, S., Comoretto, L., Rinaldi, E.,Maurino, V., Minero, C., Vione, D., Chemosphere (2009) **74**, 599

[37] Canonica, S., Chimia (2007) **61**, 641

[38] Tai, C., Li, Y. B., Yin, Y. G., Cai, Y., Jiang, G. B., Progress in Chemistry.(2012) **24**, 1388

[39] Chiwa, M., Higashi, N., Otsuki, K., Kodama, H., Miyajima, T., Takeda, k., Sakugawa, H., Chemosphere, (2015) **119**, 1386

[40] Page, S. E., Arnold, W. A., McNeill, K., Environmental Science & Technology (2012) **45**, 2818

[41] Lee, E., Glover, C. M., Fernando-Ortiz, F.L., Environmental Science & Technology (2013) **47**, 12073

[42] Canonica, S., Kohn, T., Mac, M., Real, F. J., Wirz, J., Von Gunten, U., Environmental Science and Technology (2005) **39**, 9182-9188

[43] Buxton, G. V., Greenstock, C. L., Helman, W. P., Ross, A. B., Journal of Physical and Chemical Reference Data (1988) **17**, 1027-1284

[44] Nakatani, N., Hashimoto, N., Shindo, H., Yamamoto, M., Kikkawa, M., Sakugawa, H., Analytica Chimica Acta (2007) **581**, 260

[45] Wenk, J., Eustis, S.N., McNeill, K., Canonica, S., Environmental Science & Technology (2013) **47**, 12802

[46] Latch, D. E., Stender, B. L., Packer, J. L., Arnold, W. A., McNeill, K., Environmental Science & Technology (2003) **37**, 3342

[47] Calza, P., Vione, D., Galli, F., Fabbri, D., Dal Bello, F., Medana, C., Water Research (2016) **88**, 235.

[48] Vione, D., Calza, P., Galli, F., Fabbri, D., Santoro, V., Medana, C., Science Total Environment (2015) **537**, 58

[49] Fabbri, D., Minella, M., Maurino, V., Minero, C., Vione, D., Chemosphere (2015) **119**, 601-607

[50] Huang, J.P., Mabury, S.A., Environmental Toxicology and Chemistry (2000) **19**, 1501

[51] Huang, J.P., Mabury, S.A., Environmental Toxicology and Chemistry (2000) **19**, 2181

[52] Czaplicka, M., Journal of Hazardous Matererials (2006) **134**, 45

[53] Hatipoglu, A., Vione, D., Yalcin, Y., Minero, C., Cinar, Z., Journal of Photochemistry and Photobiology A: Chemistry.(2010) **215**, 59

[54] Passananti, M., Temussi, F., Iesce, M. R., Previtera, L., Mailhot, G., Vione ,D., Brigante, M., Water Research (2014) **55**, 106

[55] Minella, M., Leoni, B., Salmaso, N., Savoye, L., Sommaruga ,R., Vione, D., Science Total Environment (2016) **541**, 247

[56] Fabbri, D., Minella, M., Maurino, V., Minero, C., Vione, D., Chemosphere (2015) **134**, 452

[57] Tixier, C., Sancelme, M., Bonnemoy, F., Cuer, A., Veschambre, H., Environmental. Toxicology and Chemistry (2001) **20**, 1381

[58] Ruggeri, G., Ghigo, G., Maurino, V., Minero, C., Vione, D., Water Research (2013) **47**, 6109

[59] De Laurentiis, E., Chiron, S, Kouras-Hadef, S., Richard, C., Minella, M., Maurino, V., Minero, C., Vione, D., Environmental Science & Technology (2012) **46**, 8164

[60] Cermola, M., Della Greca, M., Iesce, M. R., Previtera, L., Rubino, M., Temussi, F., Brigante, M., Environmental Chemistry Letters (2005) **3**, 43

[61] Isidori, M., Nardelli, A., Pascarella, L., Rubino, M., Parrella, A., Environmental International (2007) **33**, 635

[62] Wang, X. H., Lin, A. Y. C., Environmental Science & Technology (2012) **46**, 12417.

[63] Latch, D. E., Packer, J. L., Stender, B. L., VanOverbeke, J., Arnold, W. A., McNeill, K., Environmental Science & Technology (2005) **24**, 517

[64] Bianco, A., Fabbri, D., Minella, M., Brigante, M., Mailhot, G., Maurino, V., Minero, C., Vione, D., Water Research (2015) 72, 271

[65] Wetzel, R. G., Limnology: Lake and River Ecosystems. (2001) – Third Edition Academic Press

[66] Minella, M., Rogora, M., Vione, D., Maurino, V., Minero, C., Science Total Environment (2011) **409**, 3463

[67] Schindler, D. W., Hydroogical. Processes (1997) **11**, 1043

[68] Larsen, S., Andersen, T., Hessen, D. O., Global Change Bioology (2011) **17**, 1186

[69] Tang, Z. S., An, H., Shangguan, Z. P., Ecological Engineering (2015) **84**, 92

[70] Osburn, C. L., Morris, D. P., Thorn, K. A., Moeller, E. E., Biogeochemistry (2001) **54**, 251-278

[71] Morris D. P., Hargreaves B. R., (1997) Limnology and Oceanography (1997) **42**(2): 239–349

[72] Cammack, W. K., Kalff, J., Prairie, Y. T., & Smith, E. M.. Limnology and Oceanography, (2004) **49**(6), 2034-2045

[73] Coble, P. G., Nature (1990) **348** 432–435

[74] Coble, P. G., Marine Chemistry (1996) **51** 325-346

[75] Canonica, S., Hellrung, B., Mueller, P., Wirz, J., Environmental Science & Technology (2016) **40**, 6636–6641

[76] Golanoski, K. S., Fang, S., Del Vecchio, R., Blough, N. V., Environmental Science & Technology (2012) **46**, 3912–3920.

[77] Sharpless ,C. M., Blough, N. V., Environmental Science: Processes Impacts, (2014) **16**, 654–671.

[78] Palit, D. K., Research on Chemical Intermediate (2005) **31**, 205–225

[79] Sancho, M. I., Jubert, A. H., Blanco, S. E., Ferretti ,F. H., Castro, E. A., (2008) Canadian Journal of Chemistry (2008) **86**, 462-469

[80] Du, Y., Xue, J. D., Ma, C. WS., Kwok, W. M., Phillips, D. L., Journal of Raman Spectroscopy (2008) **39**, 1518-1525.

[81] Barsotti, F., Brigante, M., Sarakha, M., Maurino, V., Minero, C., Vione, D., Photochemical & Photobiological Sciences (2015) **14**, 2087-2096.

[82] Porter, G., Suppan, P., Transactions of the Faraday Society (1965) **61**, 1664-1673

[83] Das, P. K., Encinas, M. V., Scaiano, J. C., Journal of the American Chemical Society (1981) **103**, 4154-4162

[84] Murphy, K. R., Stedmon, C. A., Waite ,T. D., Ruiz, G. M., Marine Chemistry, (2008) **108**, 40-58.

[85] Peuravuori, J., Environmental Science & Technology (2005) **39**, 5541-5549

[86] Latch, D. E., McNeill, K., Science (2006) **311**, 1743-1747

[87] Appiani, E.,. McNeill, K., Environmental Science & Technology (2015) **49**, 3514-3522**.**

[88] Canonica, S., Jans,U., Stemmler ,K., Hoigne, J., Environmental Science & Technology (1995) **29**, 1822-1831

[89] Beckett, A., Porter, G. Transactions of the Faraday Society (1963) **59**, 2051–2057

[90] Bhasikuttan, A. C.,Singh, A. K., Palit, D. K., Sapre, A. V., Mittal, J. P. Journal of Physical Chemistry. A (1998) **102**, 3470–3480

[91] Franco, C., Olmsted, J., Talanta, (1990) **37**, 905–909

[92] Wilkinson, F., Helman, W. P., Ross, A. B., Journal of Physical and Chemical Reference Data, (1993) **22**, 113–262

[93] Li,D. D., Han, R. M., Liang, R., Chen, C. H., Lai, W. Z., Zhang, J. P., Skibsted, L. H., Journal of Physical Chemistry B (2012) **116**, 7154–7161

[94] Marchisio, A., Minella, M., Maurino, V.,Minero C.,Vione, D., Water Research (2015) **73**, 145–156.

[95] Maus, M., Rurack, K., New Journal of Chemistry (2000) **24**, 677–686

[96] Hoshino, M., Journal of Physical Chemistry (1987) **91**, 6385–6388

[97] Hoshino, M., Koizumi, M., Bullettin of the Chemical Society of Japan (1972) **45**, 2731–2736

[98] Natarajan, P., Journal of Chemical Education. (1976) **53**, 200–201

[99] Porter, G., Wilkinson, F., Transactions of the Faraday Society (1961) **57**, 1686–1691.

[100] Godfrey, T. S., Hilpern, W., Porter, G., Chemical Physics Letters (1967) 490–492.

[101] . Braslavsky,S. E., Glossary of terms used in photochemistry, 3rd edition, Pure and Applied Chemistry (2007) **79**, 293–465

[102] Das, T. N., Journal of Physical Chemistry A (2005) **109**, 3344–3351.

[103] Wilkinson, F., Brummer, J. G., Journal of Physical Chemistry Reference Data (1981) **10**, 809–999

[104] Martire, D. O., Evans, C., Bertolotti, S. G., Braslavsky, S. E., Garcia, N. A., Chemosphere, (1993) **26**, 1691–1701

[105] Palumbo, M. C., Garcia, N. A., Toxicology Environmental Chemistry (1988) **17**, 103–116

[106] Jensen, F., Introduction to Computational Chemistry, (1999) John Wiley & Sons, NY

[107] Kohn, W., Becke, A. D., Parr, R. G., Journal of Physical Chemistry (1996) **100**, 12974-12980

[108] Hehre, W. J., Ditchfield, R., Pople, J. A., The Journal of Chemical Physics (1972) **56**, 2257-2261**.**

[109] Clark, T., Chandrasekhar, J., Spitznagel, G.W., Schleyer, P.v.R., Journal of Computational Chemistry (1983) **4**, 294-301

[110] Mennucci, B., Tomasi, J., The Journal of Chemical Physics (1997) **106**, 5151-5158.

[111] Cossi, M., Rega, N., Scalmani, G., Barone, V., The Journal of Chemical Physics (2001) **114**, 5691-5570

[112] Marenich, A. V., Cramer, C. J., Truhlar, D. J., Journal of Physical Chemistry B (2009) **113**, 6378–6396.

[113] Marenich, A. V., Cramer, C. J., Truhlar, D. J., Journal of Physical Chemistry B (2009) **113,** 4538-4543

[114] Bauernschmitt, R., Ahlrichs, R., Chemical Physics Letters (1996) **256**, 254- 464.

[115] Dreuw, A., Head-Gordon, M., Chemical Reviews (2005) **105**, 4009-4037

[116] Jacquemin, D., Perpete, E. A., Vydrov, O. A., Scuseria, G. E., Adamo, C., The Journal of Chemical Physics (2007) **127**, 094102.

[117] Charaf-Eddin, A,. Planchat, A., Mennucci, B., Adamo, C., Jacquemin, D., Choosing a The Journal of Chemical Theory and Computation (2013) **9**, 2749-2760

[118] Perdew, J. P., Burke, K., Ernzerhof, M., Physical Review Letters (1996) **77**, 3865-3868

[119] Adamo, C., Barone, V., The Journal of Chemical Physics (1999) **110**, 6158-6169**.**

[120] McLean, A. D., Chandler, G. S., The Journal of Chemical Physics (1980) **72**, 5639-5348**.**

[121] Frisch, M. J., Trucks, G. W., Schlegel, H. B.., Scuseria, G. E., Robb, M. A., Cheeseman, J. R., Scalmani, G., Barone, V., Mennucci, B., Petersson, G. A., Nakatsuji, H., Caricato, M., Li, X., Hratchian, H. P., Izmaylov, A. F., Bloino, J., Zheng, G., Sonnenberg, J. L., Hada, M., Ehara, M., Toyota, K., Fukuda, R., Hasegawa, J., Ishida, M., Nakajima, T., Honda, Y., Kitao, O., Nakai, H., Vreven, T., Montgomery J. A. Jr., Peralta, J. E., Ogliaro, F., Bearpark, M., Heyd, J. J., Brothers, E., Kudin, K. N., Staroverov, V. N., Kobayashi, R., Normand, J., Raghavachari, K., Rendell, A., Burant, J. C., Iyengar, S. S., Tomasi, J., Cossi, M., Rega, N., Millam, J. M., Klene, M., Knox, J. E., Cross, J. B., Bakken, V., Adamo, C., Jaramillo, J., Gomperts, R., Stratmann, R. E., Yazyev, O., Austin, A. J., Cammi, R., Pomelli, C., Ochterski, J. W., Martin, R. L., Morokuma, K.., Zakrzewski, V. G., Voth, G. A., Salvador, P., Dannenberg, J. J., Dapprich, S., Daniels, A. D, Farkas, O., Foresman, J. B., Ortiz, J. V., Cioslowski, J., Fox, D. J Gaussian 09, Gaussian, Inc., Wallingford, CT, 590 2009.

[122] Kasha, M., Discussions of the Faraday Society (1950) **9**, 14-19

[123] Itoh, T., Chemical Reviews(2012) **112**, 4541-4568

[124] Nagaoka, S., Fujita, M,. Takemura, T., Baba, H., Chemical Physics Letters (1986) **123**, 489-492

[125] Hansch,C., Leo, A., Taft, R. W., Chemical Reviews (1991) **91**, 165-1951

[126] Hudson, N., Baker, A., Reynolds, D., River Research and Applications (2007) **23** 631-649

[127] Green, S. A., Blogh, N. V., Limnology and Oceanography (1994) **39** (8) 1903-1916

[128] Kirk, T. K., Farrell, R. L., Annual Reviews in Microbiology (1987) **41** (1), 465-501

[129] Brebu, M., Vasile, C., Cellulose Chemistry and Technology (2010) **44** (9) 353-363

[130] Graber, E. R., Rudich, Y., Atmospheric Chemistry and Physics (2006) **6** 729-753

[131] Simoneit, B. R. T., A.G. Douglas, J.R. Maxwell (Eds.), Advances in Organic Geochemistry,(1980) Pergamon Press, Oxford, pp. 343–352.

[132] Tolocka, M. P., Jang, M., Ginter, J. M., Cox, F. J., Kamens, R. M., Johnston, M. V., Environmental Science & Technology (2004) **38** 1428–1434.

[133] Net, S., Nieto-Gligorovski, L., Gligorovski, S., Temime-Rousell, B., Barbati, S., Lazarou, Y. G, Wortham, H., Atmospheric Environment (2009) **43** 1683–1692.

[134] Vione, D., Maurino, V., Minero, C., Environmental Science and Pollutant Research (2014) **21** 11614–11622.

[135] De Laurentiis, E.,Sur, B., Pazzi,M., Maurino, V., Minero, C., Mailhot, G., Brigante, M., Vione, D., Atmospheric Environment (2013) **70** 318–327

[136] Adamo, C., Barone, V., The Journal of Chemical Physics (1998) **108** 664–675.

[137] Lee, C., Yang, W., Parr, R. G., Physical Review B (1988) **37** (1988) 785–789.

[138] Miehlich, B., Savin, A., Stoll, H., Preuss, H., Chemical Physics Letters. (1989) **157** 200–206.

[139] Hehre, W. J.,Ditchfield, R., Pople, J. A., The Journal of Chemical Physics (1972) **56** 2257–2261..

[140] Clark, J., Chandrasekhar, G. W., Journal of Computational Chemistry (1983) **4,** 294–301.

[141] Jones, D. B., Da Silva, G. B., Neves, R. F. C., Duque, H. V., Chiari, L., De Oliveira, E. M., Lopes, M. C. A., Da Costa, R. F., Varella, M. T., Bettega, M. H. F., Lima, M. A. P., Brunger, M. J., The Journal of Chemical Physics (2014) **141** 74314.

142 Ratzer, C., Kupper, J., Spangenberg, D., Micheal-Schmit, Chemical Physics (2002) **283** 153–169.

[143] Albinet, A., Minero, C., Vione,D., Science Total Environment (2010) **408**, 3367–3373.

[144] Bianco, A., Minella, M., De Laurentiis, E., Maurino, V., Minero, C., Vione, D., Chemosphere (2014) **111** 529–536.

[145] Devine, M. D., Duke, S. O., Fedtke, C. Physiology of Herbicide Action; (1993) Prentice Hall: New Jersey

[146] Aldrich Material Safety Data Sheets (MSDS), last revision 2016

[147] Eddleston, M., Rajapakshe, M., Roberts, D., Reginald, K., Rezvi Sheriff, M. H., Dissanayake, W., Buckley, N., Journal of Toxicology: Clinical Toxicology (2002) **40**, 847−854

[148] Pereira, J. L., Antunes, S. C., Castro, B. B., Marques, C. R., Gonçalves, A. M. M., Gonçalves, F., Pereira, R. Ecotoxicology (2009) **18**, 455−463

[149] Okayi, R. G., Tachia, M. U., Ataguba, G. A., Dikwahal, S. H., Journal of Fishes and Aquatic Science. (2013) **8**, 233−237.

[150] Sancho, E., Fernández-Vega, C., Andreu, E., Ferrando, M. D., Ecotoxycology and Environmental Safety (2009) **72** 704-713

[151] Primel, E. G., Zanella, R., Kurz, M. H. S., Gonçalves, F. F., Martins, M. L., Machado, S. L. O., Marchesan, E, Journal of the Brazilian Chemical Society (2007) **18**, 585−589.

[152] Milan, M., Vidotto, F., Piano, S., Negre, M., Ferrero, A., Journal of Environmental Quality (2012) **41**, 1487−1496

[153] Trubetskova, I., Lampert, W., Archives of Environmental Contaminants Toxicology (2002) **42**, 193−198.

[154] Santos, T. C. R., Rocha, J. C., Alonso, R. M., Martinez, E., Ibanez,C., Barcelo, D., Environmental Science & Technology (1998) **32**, 3479−3484

[155] State of California, Department of pesticide regulation, PR-ENF-013a (REV. 12/08).

[156] European Food Safety Authority (EFSA). Conclusion on the peer review of the pesticide risk assessment of the active substance propanil. EFSA Journal (2011) **9** 2085.

[157] CCM. Production and Market of Propanil in China, 2nd ed. (2013) 47

(18)

158 Kanawi, E., Van Scoy, A. R., Budd, R., Tjeerdema, R. S., Toxicology Environmental Chemistry (2016) **98**, 689−704.

[159] Moilanen, K. W., Crosby, D. G., Journal of Agricultural and Food Chemistry (1972) **20**, 950−953.

[160] Konstantinou, I. K., Zarkadis, A. K., Albanis, T. A., Journal of Environmental Quality (2001) 30, 121−130.

[161] Lancashire, P. D., Bleiholder, H., Van den Boom, T., Annals of Applied Biology (1991) **119**, 561−601.

[162] Mack, J., Bolton, J. R., Journal of Photochemistry and Photobiology A: Chemistry (1999) **128**, 1−13.

[163] De Laurentiis, E., Prasse, C., Ternes, T. A., Minella, M., Maurino,V., Minero, C., Sarakha, M., Brigante, M., Vione, D., Water Research (2014) **53**, 235−248.

[164] Rosario-Ortiz, F. L., Canonica, S., Probe compounds to assess. Environmental Science & Technology (2016) **50**, 12532−12547.

[165] Minella, M., Merlo, M. P., Maurino, V., Minero, C., Vione, D., Chemosphere (2013) **90**, 306−311

[166] Halladja, S., Ter Halle, A., Aguer, J. P., Boulkamh, A., Richard. C., Environmental Science & Technology (2007) **41** 6066-6073.

[167] Al Housari, F., Vione, D., Chiron, S., Barbati. S., Photochemical & Photobiological Sciences (2010) **9** 78-86.

[168] Loiselle, S. A., Azza, N., Cozar, A., Bracchini, L., Tognazzi, A., Dattilo, A., Rossi, C., Freshwater Biology (2008) **53**, 535−545.

[169] Findlay, M., Smoler, D. F., Fogel, S., Mattes, T. E., Environmental Science & Technology (2016) **50**, 3617−3625.

[170] Maraccini, P. A., Mattioli, M. C. M.; Sassoubre, L. M.; Cao, Y. P.;Griffith, J. F., Ervin, J. S., Van De Werfhorst, L. C., Boehm, A. B., Environment Science & Technology (2016) **50**, 5068−5076

[171] Kieber, R. J., Seaton, P. J., Analitical Chemistry (1995) **67**, 3261−3264.

[172] Bedini, A., De Laurentiis, E., Sur, B., Maurino, V., Minero, C.,Brigante, M., Mailhot, G., Vione, D., Photochemical & Photobiological Sciences (2012) **11**, 1445−1453.

[173] Sur, B., Rolle, M., Minero, C., Maurino, V., Vione, D., Brigante, M., Mailhot, G., Photochemical & Photobiological Sciences (2011) **10**, 1817−1824.

[174] De Laurentiis, E., Socorro, J., Vione, D., Quivet, E., Brigante, M., Mailhot, G., Wortham, H., Gligorovski, S., Atmospheric Environment (2013) **81**, 569−578

[175] Bodrato, M., Vione, D., Environmental Science: Processes & Impacts (2014) **16**, 732−740.

[176] Frank, R., Klöpffer, W., Chemosphere (1988) **17**, 985−994.

177 Maddigapu, P. R., Bedini, A., Minero, C., Maurino, V., Vione, D., Brigante, M., Mailhot, G., Sarakha, M., Photochemical & Photobiological Sciences (2010) **9** 323-330.

[178] Swgartz, A. M., Patton, V., Heppleston, M. J., Barra, M., International Journal of Chemical Kinetics. (2008) , **40**, 839−844.

[179] Wenk, J., Von Gunten, U., Canonica, S., Environmental Science & Technology (2011) **45**, 1334−1340.

[180] McNeill, K., Canonica, S., Environmental Sciences: Processes Impacts (2016) **18**, 1381−1399.

181 Herrera-González, V. E., Ruiz-Ordaz, N., Galíndez-Mayer, J., Juárez-Ramírez, C., Santoyo-Tepole, F., Montiel, E. M.,. World Journal of Microbiology and Biotechnology (2013) **29**, 467−474.

[182] Piiparinen, J., Enberg, S., Rintala, J. M., Sommaruga, R., Majaneva, M., Autio, R., Vahatalo, A. V., Photochemical & Photobiological Sciences (2015) **14**, 1025−1038.

[183] Berto, S., Isaia, M., Sur, B., De Laurentiis, E., Barsotti, F., Buscaino, R., Maurino, V., Minero, C., Vione, D., Journal of Photochemistry and Photobiology: A Chemistry (2013) **251**, 85−93.

[184] Takahashi, T., Inagaki, H., Fukushima, T., Oishi, T.; Matsuno, K. Soil Science and Plant Nutrition (2010) **56**, 163−167.

[185] Verpoorter, C., Kutser, T., Seekell, D. A., Tranvik, L. J., Geophysical Research Letters (2014) **41**, 6396–6402

[186] Zou, H., Radke, M., Kierkegaard, A., MacLeod, M., McLachlan, M. S., Environmental Science & Technology (2016) **49** 1646-1653

[187] Koehler, B, Landelius, T, Weihenmeyer, G. A., Machida, N, Tranvik, L. J., Global Biogeochemical Cycles (2014) **28** 696-711

[188] Sobek, S., Tranvik, L. J., Prairie, Y. T., Kortelainen, P., Cole, J. J. Limnology and Oceanography (2007) **58**, 1208–1219

[189] Avetta ,P., Marchetti, G., Minella, M., Pazzi, M., De Laurentiis, E., Maurino, V., Minero, C., Vione, D., Science Total Environment (2014) **500** 351-360

[190] Mayer, B., Kylling, A., Emde, C., Hamann, U., Buras, (2011) R. libRadtran user's guide.

[191] Kasten, F., Czeplak, G. Solar Energy(1980) **24**, 177–189

[192] Hāggmark, L., Ivarsson, K. I., Gollvik, S. Olofsson, P. O., Tellus A dynamic Meteorology and oceanography (2000) **52**, 2–20

[193] Canonica, S., Freiburghaus, M., Environmental Science & Technology (2001) **35** 690-695

[194] Brezonik, P. L., Arnold, W. A., McNeill, K., Environmental Science & Technology (1998) **35** 3004-3010

[195] Kellerman, A. M., Dittmar, T., Kothawala, D. M., Tranvik, L. J., Nature Comunications (2014) **5** 3804

[196] Koehler, B, Broman, E., Tranvik, L. J., Limnology and Oceanography (2016) **6** 2207-2221

[197] Koehler, B, Barsotti, F., Minella, M., Landelius, T., Minero, C., Tranvik, L. J., Vione, D., Water Research (2018) **129** 94-104

[198] Wols, B., Hofman-Caris, C. Water Research (2012) **46**, 2815–2827

[199] Vione, D., Maddigapu, P. R., De Laurentiis E., Minella, M., Pazzi, M., Maurino, V., Minero, C., Kouras, S., Richard, C., Water Research (2011) 6725-6736

[200] Forina, M., Lanteri, S., Armanino, C., Oliveros, M. C., Casolino, C. (2008) V-PARVUS. An extendable package of programs for explorative data analysis, classification and regression analysis. Dip. Chimica e Tecnologie Farmaceutiche ed Alimentari, University of Genova

[201] R Development Core Team (2014), R: A language and environment for statistical computing, edited. R Foundation for Statistical Computing, Vienna, Austria.

[202] Müller, R. A., Futter, M. N.,Sobek, S., Nisell, J., Bishop, K, Weyhenmeyer, G. A., Aquatic Sciences (2013) **75** 535-545

[203] Benotti, M. J., Brownawell, B. J., Environmental Pollution (2009) **157** 994-1002

[204] Gerecke ,A. C., Canonica, S., Müller, S. R., Shärer, R., Schwarzenbach, R., P., Journal of Photochemistry and Photobiology A:Chemistry (2001) **35** 3915-3923

[205] Gerdes, R., Wöhrle, D., Spiller, W., Schneider, G., Schnurpfeil, G., Schulz-Ekloff, G., Journal of Photochemistry and Photobiology A:Chemistry (1997) **111** 65-74

[206] Larson, R. A., Zepp, R. G., Environmental Toxicology and Chemistry (1988) **7** 265-274

[207] Quiròs, R., Limnetica (2003) **22** 37-50